DEVELOPMENT OF NANO HALL SENSORS FOR HIGH RESOLUTION SCANNING HALL PROBE MICROSCOPY

A DISSERTATION SUBMITTED TO THE DEPARTMENT OF PHYSICS AND THE INSTITUTE OF ENGINEERING AND SCIENCE OF BİLKENT UNIVERSITY IN PARTIAL FULFILLMENT OF THE REQUIREMENTS FOR THE DEGREE OF DOCTOR OF PHILOSOPHY

By
Münir Dede

September 2008

I certify that I have read this thesis and that in my opinion it is fully adequate, in scope and in quality, as a dissertation for the degree of doctor of philosophy.

Prof. Dr. Ahmet Oral (Supervisor)

I certify that I have read this thesis and that in my opinion it is fully adequate, in scope and in quality, as a dissertation for the degree of doctor of philosophy.

Prof. Dr. Atilla Aydınlı

I certify that I have read this thesis and that in my opinion it is fully adequate, in scope and in quality, as a dissertation for the degree of doctor of philosophy.

Prof. Dr. Ömer Dağ

I certify that I have read this thesis and that in my opinion it is fully adequate, in scope and in quality, as a dissertation for the degree of doctor of philosophy.

Assoc. Prof. Dr. Oğuz Gülseren

I certify that I have read this thesis and that in my opinion it is fully adequate, in scope and in quality, as a dissertation for the degree of doctor of philosophy.

Assist. Prof. Dr. H. Özgür Özer

Approved for the Institute of Engineering and Sciences:

Prof. Dr. Mehmet Baray

Director of the Institute of Engineering and Sciences

ABSTRACT

DEVELOPMENT OF NANO HALL SENSORS FOR HIGH RESOLUTION SCANNING HALL PROBE MICROSCOPY

Münir Dede
Ph.D in Physics
Supervisor: Prof. Dr. Ahmet Oral
September 2008

Scanning Hall Probe Microscopy (SHPM) is a quantitative and non invasive method of local magnetic field measurement for magnetic and superconducting materials with high spatial and field resolution. Since its demonstration in 1992, it is used widely among the scientific community and has already commercialized. In this thesis, fabrication, characterization and SHPM imaging of different nano-Hall sensors produced from heterostructure semiconductors and Bismuth thin films with effective physical probe sizes ranging between 50nm-1000nm, in a wide temperature range starting from 4.2K up to 425K is presented.

Quartz crystal tuning fork AFM feedback is demonstrated for the first time for SHPM over a large temperature range. Its performance has been analyzed in detail and experiments carried with 1×1μm Hall probes has been successfully shown for a hard disk sample in the temperature range of 4.2K to 425K. Other samples, NdFeB demagnetized magnet, Bi substituted iron garnet and, single crystal BSCCO(2212) High Temperature superconductor were also imaged with this method to show the applicability of the method over a wide range of specimens. By this method, complex production steps proposed in the literature to inspect the non-conductive samples were avoided.

A novel Scanning Hall probe gradiometer has also been developed and a new method to image x, y & z components of the magnetic field on the sample surface has been demonstrated for the first time with 1µm resolution. 3D field distribution of a Hard Disk sample is successfully measured at 77K using this novel approach to prove the concept.

Keywords: Scanning Hall Probe Microscope, Hall Probe, Probe microscopy, SHPM, SOI, GaN, InSb, Quantum well, Bismuth, Quartz tuning fork, STM feedback, AFM feedback, Hall gradiometer, 3D field measurement.

ÖZET

YÜKSEK ÇÖZÜNÜRLÜKLÜ TARAMALI HALL AYGITI MİKROSKOBU İÇİN NANO HALL ALGILAYICILARIN GELİŞTİRİLMESİ

Münir Dede
Fizik Doktora
Tez Yöneticisi: Prof. Dr. Ahmet Oral
Eylül 2008

Taramalı Hall Aygıtı Mikroskobu (THAM), manyetik ve süperiletken malzemeleri yüksek uzaysal ve manyetik alan çözünürlüğü ile inceleyebilen tahribatsız ve nitel bir manyetik görüntüleme yöntemidir. İlk olarak 1992 yılında gösterilen yöntem hızla gelişerek etkin bir manyetik görüntüleme yöntemi olarak kabul görmüş ve ticari ürün haline de getirilmiştir. Bu tezde çeşitli çok katmanlı yarıiletken malzemeler ve Bizmut ince film kullanılarak 50-1000nm aktif fiziksel alana sahip Hall algılayıcıların üretimi, karakterizasyonu ve 4.2-425K sıcaklık aralığında THAM görüntülemesi başarılmıştır.

Elektriksel iletkenliği olmayan örneklerin incelenmesine olanak sağlayan Atomik Kuvvet Mikroskobu (AKM) geri beslemesini kullanmak için Hall aygıtlarının kuvartz kristal çatallara entegrasyonu geniş bir sıcaklık aralığında ilk defa gösterilmiştir. Yöntemin performansı ve çalışma kararlılığı 4.2-425K sıcaklık aralığında fiziksel aktif alan büyüklükleri 1×1μm olan farklı Hall aygıtlarla sabit disk örneği kullanarak başarılı bir biçimde gösterilmiştir. Benzer şekilde Fe katkılı Bizmut, termal olarak de-manyetize edilmiş NdFeB mıknatıs ve BSCCO(2212) tek kristal yüksek sıcaklık süperiletkeni de aynı yöntem ile görüntülenerek yöntemin çok değişik numunelerin incelenmesinde uygulanabilirliği ispatlandı. Geliştirdiğimiz bu yöntem sayesinde literatürde elektriksel

iletkenliği olmayan örnekleri incelemek için önerilen karmaşık mikro-yay üretim yöntemlerine olan gereksinim ortadan kalkmıştır.

Yüzey manyetik alanlarının uzaysal değişimini gözlemlemek için kullanılabilecek özgün bir gradyometre yöntemi ilk defa gösterilmiş ve bu yöntem manyetik alan dağılımının her üç uzaysal bileşenini, x, y ve z, 1µm'lik Hall algılayıcılar yardımı ile görüntülemek için kullanılmıştır. Yöntemin geçerliliğini göstermek için bir sabit disk örneğin manyetik alan profili 77K sıcaklıkta üç boyutlu (3B) olarak haritalandırılmıştır.

Anahtar Sözcükler: Taramalı Hall Aygıtı Mikroskobu, Hall algılayıcı, THAM, Uç mikroskobu, SOI, GaN, Bizmut, InSb, Kuvantum kuyu, Kuvartz kristal çatal, Atomik Kuvvet Mikroskobu (AKM) geri beslemesi, Taramalı Tünelleme Mikroskobu (TTM) geri beslemesi, Hall gradyometre, 3B görüntüleme.

ACKNOWLEDGEMENTS

It is my pleasure to express my sincere gratitude to my supervisor, Prof. Dr. Ahmet Oral for his invaluable guidance, support and opportunities provided beyond the scope of this study.

I also express my deep appreciation to Dr. Rızwan Akram for the scientific discussions and contributions he made to my Ph.D. work.

I would like to thank the members of my thesis committee, Prof. Dr. Atilla Aydınlı, Prof. Dr. Ömer Dağ, Assoc. Prof. Dr. Oğuz Gülseren and Assist. Prof. Dr. H. Özgür Özer for their comments on this thesis.

I am especially thankful to Assoc. Prof. Dr. İsmet İnönü Kaya of Sabancı University for his invaluable help about the e-beam writing system. I also would like to thank to Anıl Günay and Selda Sonuşen of Sabancı University for SEM images.

I would like to thank to Orhan Akar and Prof. Dr. Tayfun Akın of Metu Met for chip dicing.

I like to acknowledge Assoc. Prof .Dr. Marco Affronte and his group members, Alberto Ghirri and Andrea Candini, of University of Modena, Gian Carlo Gazzadi of INFM for the FIB work and the PPMS setup.

I would like to deeply thank to Prof. Dr. Ekmel Özbay and Evren Öztekin of Bilkent Nanotam for their help on wafer dicing.

I also like to acknowledge Prof. Dr. Kazuo Kadowaki of Tsukuba University for BSCCO samples.

I would like to thank to Dr. Ian Farrer and Prof. Dr. David A. Ritchie of Cambridge University for the GaAs HEMT wafers.

I also would like to thank to Prof. Dr. Adarsh Sandhu of Tokyo Institue of Technology, for the InSb wafers and his collaboration on Bismuth FIB milling.

I am thankful to Dr. Jeffrey McCord of IFW Dresden, for the NdFeB sample.

I would like to acknowledge Prof. Dr. Mustafa Ürgen and his group members for their help on FIB milling and hospitality.

I am obliged to thank Assist. Prof. Dr. Hidayet Çetin for his friendship, comments on thin film growth and collaboration on graphene samples.

I am also thankful to Çağrı İşeri for his detailed work on quartz tuning forks and Cosmos simulations.

I am thankful to, The Scientific and Technological Research Council of Turkey (TÜBİTAK), for sponsoring the thesis through the grants 105T473 and 105T501.

I would like to thank our group members Mehrdad Atabak, Özge Girişen, Sevil Özer, Aslı Elidemir and Dr. Özhan Ünverdi, for creating an enjoyable and unique working environment. I would like to acknowledge all the employees of NanoMagnetics Instrument Ltd. for the SHPM setups and for their close collaboration and assistance whenever I needed.

I would also like to thank to Bilkent ARL technicians Murat Güre and Ergün Karaman for their continuous effort in up keeping the clean room setups.

I am indebted to my family for their continuous support, and prayers. And finally, I thank my dearest wife Gülden as she was always beside me. I would like to devote this work to her and my parents.

Contents

Chapter 1 : Introduction & Background **1**

1.1 Introduction 1

1.2 Classical Hall Effect 3

1.3 Magnetoresistance Effects 9

1.4 Bitter Decoration 10

1.5 Lorentz Microscopy 12

1.6 Magneto-Optical (MO) Imaging 14

1.7 Spin Stand Microscopy 14

1.8 Scanning Superconducting Quantum Interference Device (SQUID) Microscopy 16

1.9 Magnetic Force Microscopy (MFM) 17

1.10 Scanning Hall Probe microscopy (SHPM) 18

Chapter 2 : The Microscope **20**

2.1 Introduction 20

2.2 The Microscope Body 21

2.3 The Hall Probe 23

2.4 Approach Mechanism 27

2.5 Scanner 29

2.6 SHPM Control Electronics & Software 32

2.6.1 Head Amplifier 33

2.6.2 Power Supply 34

2.6.3 Scan DAC 34

2.6.4 High Voltage Amplifier (HV Amps) 35

2.6.5 DAC Card 36

2.6.6 Slider Card 37

2.6.7 MicroController & A/D Card 38

2.6.8 Controller Card 39

2.6.9 Hall Probe Amplifier Card 40

2.6.10 Phase Locked Loop (PLL) Card 41

2.6.11 Spare A/D Card 43

2.6.12 PCI bus Digital I/O Card 43

2.6.13 Software 44

Chapter 3 : Fabrication & Characterization 45

3.1 Introduction 45

3.2 Sample Preparation 45

3.3 Active Area Definition 47

3.4 Mesa Step Definition 53

3.5 Recess Etch 54

3.6 Ohmic Contact Metallization 55

3.7 STM Tip Metallization 58

3.8 Metallization for Bonding 60

3.9 Packaging 60

3.10 GaN Hall Probes for SHPM 61

3.10.1 Introduction 61

3.10.2 Fabrication 62

3.10.3 Characterization 64

3.10.4 Experiments 70

3.11 InSb Based Quantum Well Hall Sensors 78

3.11.1 Introducion 78

3.11.2 Fabrication 79

3.11.3 Characterization 81

3.11.4 Experiments 84

3.12 SOI Hall Sensors for SHPM 89

3.12.1 Introduction 89

3.12.2 Fabrication 90

3.12.3 Characterization 92

3.12.4 Experiments 99

3.13 Bismuth Thin Film Hall Sensors 103

3.13.1 Introduction 103

3.13.2 Fabrication & Characterization 104

Chapter 4 : Quartz Crystal AFM Feedback for SHPM 127

4.1 Introduction 127

4.2 Sensor Preparation 131

4.3 Characterization 133

4.4 Experiments 139

Chapter 5 : Hall Probe Gradiometry 146

5.1 Introduction 146

5.2 Novel Hall Probe Gradiometry 150

5.3 Three Dimensional Magnetic Field Imaging 159

Chapter 6 : Conclusions 169

List of Figures

Figure 1.1: Schematic layout of the Hall effect on a slab geometry. 4

Figure 1.2: Schematic representation of the Hall effect considering the n type carriers. **E** and $\mathbf{E_H}$ are the external electric field and Hall field, respectively. 8

Figure 1.3: Electron deflection through the sample in Lorentz microscopy...................13

Figure 1.4: Schematic layout of the Scanning hall Probe Microscope. The common elements of the SPM family can clearly be distinguished. 19

Figure 2.1: The design representation of the SHPM with close up details of the scanner head. 22

Figure 2.2: Picture of the microscope. The shield, puck & sample holder, slider glass and the piezos are shown. 23

Figure 2.3: The alignment of the Hall probe with respect to the sample surface (b). The Hall probe (bottom part) and its reflection of the sample surface first made parallel by alignment screws (a), then the desired angle is given by loosening the screws on the corner of the chip. By this, the same angle is obtained on both sides. Mesa etch can be distinguished on the corner of the chip (a)...25

Figure 2.4: Effect of the sample-probe separation on the resolution when the sample is (b) 2.8μm, (c) 1.6μm and (d) 0.4μm. The dependency of the separation (*d*) with respect to the placement of the Hall cross about the mesa corner (*l*) is also shown in part (a)...26

Figure 2.5: Scope trace of high voltage pulse sent to the slider pizeo to slide the puck over the quartz tubing used as a guide. Each square has 50V vertical 2.5ms lateral scale...28

Figure 2.6: Schematic representation of the raster scan over the sample. 31

Figure 2.7: The SHPM Control Electronics..32

Figure 2.8: The Hall voltage amplifier..33

Figure 2.9: The frequency dependent gain response of OPA111 current to voltage converter. The measurement cycle used while obtaining the graph is shown above......34

Figure 2.10: Block diagram of Scan DAC card. 35

Figure 2.11: Block diagram of HV Amps. 36

Figure 2.12: Block diagram of DAC card...37

Figure 2.13: Block diagram of slider card 38

Figure 2.14: Block diagram of microcontroller A/D card 39

Figure 2.15: The block diagram of controller card. 40

Figure 2.16: Block diagram of Hall voltage amplifier card. 41

Figure 2.17:Block diagram of PLL card 42

Figure 2.18: Block diagram of spare A/D card..43

Figure 2.19: Screenshot of the SPM control program 44

Figure 3.1: Mask designs for Hall cross definition. The whole chip with ohmic pad extensions (a), close up appearance 10µm × 10µm e-beam/FIB template (b), and two different designs of 1µm Hall crosses (c) & (d) are shown. In first generation mask (c), Hall cross and tip separation is 14µm, whereas, in second generation mask (d) this distance is reduced to 8.5µm. The distances are measured from the center of the cross to the mesa corner. Reduction due to side etch is not included. 50

Figure 3.2: Examples of Hall cross definitions. A 1µm Hall probe after the develop (a) and when etched (b) is shown. Similarly (c) & (d) show developed and etched probes, respectively, where the probe size is 0.5µm. Given sizes are physical. 1µm probe defined using AZ-MIR701 whereas 0.5µm one is using AZ-1505. In both cases etching is done by CCl_2F_2 plasma with an etch depth of ~1.2µm 51

Figure 3.3: A 10μm × 10μm area isolated by etching for further e-beam process. The four pads have to be separated further until a Hall cross with desired size is obtained. The isolated lead, which appears on the upper left side of the image, is the tip pad. If needed it has to be connected to the corner of the active region where an isolated tip can be fabricated. 52

Figure 3.4. Schematic representation of Hall probe alignment......................................53

Figure 3.5: Mesa etch. 54

Figure 3.6: Recess etch mask design (a), and etched wafer (b). 56

Figure 3.7: Ohmic contacts without (a) and with (b) RTP. The Kirkendall effect after RTP can be seen in part (b). The RTP process was done at 450ºC for 45 sec under forming gas (95%N_2, 5%H_2) environment. An Ohmic metallization was done to a 2DEG HEMT GaAs sample evaporating 27nm Ge/ 54nm Au/ 6nm Ni /100nm Au. 58

Figure 3.8: Tip definition lithography (a) and the tip after lift-off (b) 10nm Cr /50nm Au evaporated for the tip. Connection between the tip lead and the tip is maintained via mesa etch. 59

Figure 3.9: Diced & packaged Hall probe. 61

Figure 3.10: Schematic diagram of the layer configuration of the AlGaN/GaN heterostructure used 64

Figure 3.11: Effect of Hall current on Hall coefficient, R_H., as a function of the temperature. 66

Figure 3.12: Effect of Temperature on Hall coefficient, R_H. as a function of the Hall current, I_H. 66

Figure 3.13: Hall coefficient for negative drive currents at high temperatures. 67

Figure 3.14: Hall coefficient for positive drive currents at high temperatures 67

Figure 3.15: Hall voltage (V_H) is measured as a function of Hall current (I_H), varying the temperature from 22ºC to 150ºC 69

Figure 3.16 Effect of temperature on the dynamic resistances for low current (r_{HLC}) and high current (r_{HHC}) regions. 69

Figure 3.17: Noise power spectrum of GaN probes at 300K for different drive currents. 70

Figure 3.18: Hall coefficient stability over time at different ambient temperatures 71

Figure 3.19: Hall voltage stability over time at different ambient temperatures. 72

Figure 3.20: Serial resistance measured at different ambient temperatures. 72

Figure 3.21: SHPM image of hard disk sample at Liquid helium temperature (4.2K) & Liquid Nitrogen Temperature (77K) obtained with GaN Hall probe. 73

Figure 3.22: SHPM image of hard disk sample at high temperatures. Scanning speed was 5μm/s. Distortions at 425K are most probably to be due to degradation of epoxy between the HP and tuning fork. 75

Figure 3.23: Effect of environment temperature on the resonance frequency and quality factor of the quartz tuning fork. 76

Figure 3.24: Stability comparison with respect to the electrical characteristics before and after the scan. 77

Figure 3.25: Stability comparison with respect to the electrical characteristics before and after the scan. 77

Figure 3.26: InSb quantum well wafer structure and band diagram. 80

Figure 3.27: Change of Hall coefficient (R_H) as a function of different drive currents with respect to the temperature for 1μm × 1μm. sized Hall probe. 82

Figure 3.28: Noise spectrum of InSb QW Hall probes at 300K for different bias currents. 83

Figure 3.29: Change of Hall coefficient (R_H) and the serial resistance (R_S) as a function of the temperature for fixed drive current I_H=100 μA 84

Figure 3.30: Resonance frequency curve of the 32.768kHz quartz crystal tuning fork loaded with 1.25 mm. × 1.25 mm. × 0.5 mm. InSb QW Hall sensor. 85

Figure 3.31: HDD SHPM scan image obtained at room temperature. The magnetic field profile (a) and the surface topography (b) obtained simultaneously. The scan parameters are; area: 55µm × 55µm, speed: 5µm/sec., resolution: 256×256 pixels, mode: AFM tracking 86

Figure 3.32: NdFeB permanent magnet image scanned at room temperature. The scan parameters are; area: 55µm × 55µm, speed: 5µm/sec., resolution: 256×256 pixels, mode: lift off 87

Figure 3.33: High temperature scan of Hard disk sample (a) 25ºC (b) 125ºC................88

Figure 3.34: Effect of material thickness on Hall coefficient with respect to the carrier density, calculated based on the parameters of the used SOI wafer. 92

Figure 3.35: Effect of device thickness on the magnetic flux noise spectrum vs. frequency at 25°C with fixed bias current of 500µA. 93

Figure 3.36: Effect of bias current on the magnetic flux noise spectrum vs. frequency at 25°C............................94

Figure 3.37: Effect of the temperature on the magnetic flux density noise spectrum vs. frequency with fixed bias current of 500µA. 95

Figure 3.38: Effect of Temperature on the V_H vs. I_H characteristics. r_{HHC} and r_{HLC} is the dynamic resistance defined as the slope of curve in high current (I_H> 100µA) and low current (I_H<100µA) regime. 96

Figure 3.39: Effect of device thicknesses on the V_H vs. I_H characteristics. 96

Figure 3.40: Change of series resistance R_s with respect to temperature for a Hall device thickness of 405nm. 97

Figure 3.40: Effect of Temperature on the Hall coefficient vs. Hall current. 98

Figure 3.42: Effect of device layer thickness on the Hall coefficient vs. Hall current characteristics. 98

Figure 3.43: SHPM image of hard disk sample using (a) QTF AFM and (b) STM feedback at 25°C, with scanning speed of 5μm/s. Device thickness was 405nm. 100

Figure 3.44: SHPM image of hard disk drive sample at high temperatures (50-100°C) using QTF AFM feedback. 102

Figure 3.45: Change in resonance frequency and the quality of the quartz crystal tuning fork loaded by a 1 mm × 1mm × 0.5 mm Si Hall probe. 102

Figure 3.46: Ohmic contact metallization with (a) and without (b) mesa step. 107

Figure 3.47: Image reversal lithography for active area definition (a) and the thin film obtained by thermal evaporation followed by lift off (b). 108

Figure 3.48: STM tip metallization. 109

Figure 3.49: SEM images of FIB patterned typical 50nm × 50nm Bi Hall probe. The STM tip Hall cross center distance is ~4μm. 110

Figure 3.50: RT-SHPM image of Bi substituted iron garnet sample obtained by 50nm sized Bi Hall probe. Image size is 8×8μm and the vertical scale from bright to dark is ±55G. 111

Figure 3.51: Mounting Hall sensors on a 1” sized sample holder. PCBs were mounted by double sided carbon tape. Grounding between the top layer of the PCBs and the holder was obtained by aluminum tape pieces and carbon paste. 112

Figure 3.52: Effect of charging. The line definitions were not sharp as the beam profile could not be adjusted sharp enough and had a wide Gaussian shape. 113

Figure 3.53: Accumulation of Gallium on the surface due to overexposure. Bubble formation around the exposed areas is the sign of accumulation. 113

Figure 3.54: Images of a typical FIB patterned Hall probe at ×1000 (a), ×5000 (b), ×20000 (c), and ×50000 (d) magnifications. Overall chip, mesa, Ohmic pads and the STM tip can be seen. 114

Figure 3.55: Image of FIB patterned Hall probe at ×20000 (a), with close up display of Hall cross (b) 115

Figure 3.56: Temperature depended change in Hall coefficient of ~100nm sized Bi Hall probes. 116

Figure 3.57: Noise spectral density pattern of the probes measured through the scope 117

Figure 3.58: Noise spectrum of the ~80nm thick ~100nm sized Bi hall probe at 200K as a function of the frequency. 118

Figure 3.59: Noise spectrum of the ~80nm thick ~100nm sized Bi hall probe at 100K as a function of the frequency. 119

Figure 3.60: Minimum detectable magnetic field of ~100nm sized Bi probe as a function of the applied bias current at 200K 120

Figure 3.61: Minimum detectable magnetic field of ~100nm sized Bi probe as a function of the applied bias current at 100K 120

Figure 3.62: Solid drawing of the e-beam pattern designed for 100nm wide Hall probes. The shape composed of 23 individual rectangles. Different index colors gives ability to expose at different dose values in a single drawing. 122

Figure 3.63: 100nm Hall probe fabricated by e-beam lithography and Bizmuth thermal evaporation & lift-off. 126

Figure 4.1: Top (a) ands side (b) view of the quartz tuning fork Hall probe combined sensor after packaging. 132

Figure 4.2: One prong free (a) and two prongs free (b) configurations of combined sensors. 134

Figure 4.3: First 5 vibration modes of two prongs free configuration obtained by finite element analysis. 135

Figure 4.4: First 5 vibration modes of one prong free configuration obtained by finite element analysis. 136

Figure 4.5: Frequency response of 32kHz Quartz Tuning fork with integrated Hall probe under fix prong and free prong configuration. The effect of scan piezo is also shown. 137

Figure 4.6: Side view (a) and corner view (b) of the sample-probe alignment 140

Figure 4.7: Autotune curves of the tuning forks. 140

Figure 4.8: SHPM image of (a) iron garnet crystal and (b) NdFeB demagnetised magnet obtained in AFM Tracking mode at 300K. Size of the images and vertical scale of the images are (a) 40×40µm & 62 Gauss and (b) 52×30µm & 12,868 Gauss, respectively 142

Figure 4.9: SHPM image of (a) Hard disk specimen and (b) simultaneously obtained topography at 300K. Size of the images are 50×50µm and vertical scales are (a) 209 Gauss and (b) 127nm. Vertical scale for the topography shows the relative values.... 143

Figure 4.10: SHPM image of Hard disk specimen gathered by AFM tracking at 4.2K. Sizes of the images are 16 µm × 16µm and vertical scales are 312 Gauss and 170nm for magnetic (a) and topographic (b) images respectively. 144

Figure 4.11: SHPM image of single crystal BSCCO 2212 specimen at 4.2K obtained in lift-off mode. Scan area is 16×16µm and vertical scale is 1.65 Gauss. Image shown is the average of 25 images........ 145

Figure 5.1: A Hall plate in the integrated circuit technology. A magnetic field perpendicular to the chip surface generates a Hall voltage between the two voltage electrodes of the Hall sensor [95]. 147

Figure 5.2: Cut through of a 1D integrated vertical Hall device. This sensor is sensitive to a magnetic field parallel to the chip surface [95]........ 148

Figure 5.3: Two vertical Hall sensors placed in a cross shape (2D), used to measure a magnetic field in X and Y directions. 148

Figure 5.4: Hall gradiometer. 151

Figure 5.5: Hall effect with non-perpendicular current and voltage leads with different configurations under uniform magnetic field. 152

Figure 5.6: Hall effect with non-perpendicular current and voltage leads with different configurations under non-uniform magnetic field. 153

Figure 5.7: Orientation of the Hall sensor, over the sample, with respect to the scan direction of the microscope: Hall cross has 45° alignment. 155

Figure 5.8: SHPM scan of a Hard disk sample at 77K with normal Hall sensor configuration of mutually perpendicular current and voltage leads. Hall cross diagram shows the relative alignment of the probe over the sample and the leads' positions. ..155

Figure 5.9: Calculated $\partial \mathbf{B_z}/\partial \mathbf{x}$ from the measured $\mathbf{B_z(x,y)}$ data matrix by forward differences. 157

Figure 5.10: Calculated $\partial \mathbf{B_z}/\partial \mathbf{y}$ from the measured $\mathbf{B_z(x,y)}$ data matrix by forward differences. 157

Figure 5.11: SHPM scan of a HDD at 77K with Hall sensor configuration shown in the diagram. The image represents $\partial \mathbf{B_z}/\partial \mathbf{x}$ due to the relative positions of current and voltage leads 158

Figure 5.12: SHPM scan of a HDD at 77K with Hall sensor configuration shown in the diagram. The image represents $\partial \mathbf{B_z}/\partial \mathbf{y}$ due to the relative positions of current and voltage leads. 158

Figure 5.13: Visualization of incremental scan for $B_z(x,y,z)$, $\partial B_z(x,y,z)/\partial x$ and $\partial B_z(x,y,z)/\partial y$ 161

Figure 5.14: SHPM image of Hard disk sample, (a) forward scan (in the tunneling range) and (b) backward scan (3.5µm away from the surface). Both images were

obtained with STM feedback. Scan speed was 5µm/s, resolution set to 256 × 256 pixels, -100mV bias voltage applied to the sample and the tunneling current of 1nA maintained during the scan. 163

Figure 5.15: SHPM images of Hard disk sample obtained at room temperature showing effect of the thermal drift. Pictures are the forward scans of probe above the sample with a height of (a) 0.5µm, (b) 1.5µm, (c) 2.5µm, (d) 3.5µm respectively. Field decay is not seen as the offset is only given during the backward scan. Approximately 4 hours of time passed between the shown images. The shift is towards the bottom left corner. All images were obtained with STM feedback using a 1µm PHEMT sensor. Scan speed was 5µm/s, resolution set to 256 × 256 pixels, -100mV bias voltage applied to the sample and the tunneling current of 1nA maintained during the scan. 164

Figure 5.16: SHPM images of Hard disk sample obtained at 77K showing effect of the thermal drift. Pictures are the scans of probe levels above the sample with a height of (a) 0.25 µm, (b) 1.25µm, (c) 2.5µm, (d) 3.75µm respectively. Approximately 10 hours passed between the first and the last images. There is a very little drift which becomes insignificant after thermal stabilization. All images were obtained using a 1µm PHEMT sensor. Scan speed was 5µm/s, resolution set to 256 × 256 pixels. The decay of the magnetic field can also be seen as the sensors moves away from the sample. 165

Figure 5.17: SHPM image of Hard disk sample, shows the $\mathbf{B_z}$ of the field (a), obtained at 77K in the feedback tracking zone. Image was obtained using a 1µm PHEMT sensor. Scan speed was 5µm/s, resolution set to 256×256 pixels. $\partial \mathbf{B_z}(x,y)/\partial \mathbf{x}$ (b) and $\partial \mathbf{B_z}(x,y)/\partial \mathbf{y}$ (c) are calculated from $\mathbf{B_z}$ image by differentiating rows and columns of the image matrix respectively. 166

Figure 5.18: $\mathbf{B_y}$ field calculated by integrating $\partial \mathbf{B_z}/\partial \mathbf{y}$ over a finite range. Each image file used in calculation was obtained using the same 1µm PHEMT sensor. Scan speed was 5µm/s, resolution set to 256×256 pixels. The increments along the z-direction, ***h***, is set to 0.25µm in the range of [0, 6.5µm] 167

Figure 5.19: $\mathbf{B_x}$ field calculated by integrating $\partial\mathbf{B_z}/\partial\mathbf{x}$ over a finite range. Each image file used in calculation was obtained using the same 1μm PHEMT sensor. Scan speed was 5μm/s, resolution set to 256×256 pixels. The increments along the z-direction, $\boldsymbol{h}$, is set to 0.25μm in the range of [0, 6.5μm]..168

List of Tables

Table 1.1: Worldwide production of original information, if stored digitally, in terabytes circa 2002. Upper estimates assume information is digitally scanned, lower estimates assume digital content has been compressed [20]. 15

Table 3.1: Process parameters of the photoresists used in active area definition 49

Table 3.2: Typical Channel Electron Properties at 295K [54] 79

Table 3.3: RIE etch parameters for InSb 81

Table 4.1: Summary of the used parameters and calculation / simulations results for QTFs. 138

Chapter 1 : Introduction & Background

The purpose of this chapter is to give an overview about a number of existing and commonly used techniques for magnetic characterization and magnetic imaging, along with the underlying physical interactions in a non comprehensive way. The methods mentioned are not necessarily a probing technique. For the methods used in domain observation “Magnetic Domains: The analysis of Magnetic Microstructure” by Hubert & Schafer has an excellent and detailed discussion addressing the relevant literature [1]. A review paper by Simon J. Bending [2] describes the local probing methods used for vortex imaging in superconductors. The “Magnetic Imaging” Chapter edited by Wolfgang Kuch of the book “Magnetism: A Synchrotron Radiation Approach” [3] and the relevant chapter of the book “Methods in materials research : a current protocols publication” [4] can be also consulted for more detailed information.

1.1 Introduction

The history of the Scanning Probe Microscopes (SPMs) started with the invention of Scanning Tunneling Microscope (STM) in 1981 by Binnig and Rohrer [5]. In this technique an atomically sharp conductive tip is brought in to close proximity of a conductive sample. Classically electrons are not expected to overcome the potential barrier. But, we know, from the quantum mechanics, that there exist a non zero possibility for electrons to tunnel the air or vacuum gap between the tip and the sample. The tunneling current is exponential function of the height of the tip over the sample. Thus, if the current is fed in to a control circuit it is possible to control the height of the tip. By this way a sample surface could be scanned with atomic resolution. This invention not only made it possible to resolve the atoms at the surfaces, but also brought new possibilities to the investigation of the surfaces using different probe-sample interactions. Shortly after the invention of STM, a new method, the Atomic Force

Microscope (AFM) , utilizing force interactions between tip and sample, has been invented [6]. In AFM the conductive tip is replaced by a non- conductive tip attached to the end of a cantilever. The AFM is sensitive to the forces between the tip and the sample, which deflects the cantilever and is measured through an optical system . After AFM many different methods developed to examine different properties through various tip-surface interactions.

Probing techniques have also found applications in magnetism studies. Although it is possible to get information about the magnetic properties of the materials with macroscopic measurements, it is only possible to interpret them further with the aid of local measurement techniques done at the microscopic level. Especially, the measurements performed on magnetic domains on the local scale helps to link the basic physical properties of the matter to its macroscopic properties and the practical applications. The analysis of magnetization curve of a material, for example, requires a basic understanding of the domain structure, that is microscopic regions of identical magnetization direction, of that material [1]. Magnetic imaging techniques allow the most direct visualization of magnetic properties on a microscopic scale and material properties can be studied.

Different classifications can be done for the magnetic imaging techniques considering the way in which depth sensitivity is achieved; the way in which the lateral information is acquired and the physical interaction with the sample magnetization [3]. The first two classification schemes are not interesting in the context of this thesis. The depth sensitivity is a measure of how deep the surface penetrated, and the information extracted from that depth, by the technique used. In other words it represents the probing depth. The way in which the lateral information is acquired, on the other hand, is relevant whether the sample surface is scanned or directly imaged. Classification with respect to the physical interaction includes the physical phenomenon which lies behind the measurement.

The scanning quantum interference device, SQUID, microscope for example, measures magnetic flux, the Hall probe measures magnetic stray field, and the magnetic force microscope (MFM) measures the gradient of the magnetic field convolved with the magnetic moment of the cantilever tip. Since, the force on the electrons due to the stray fled of the sample is the physical interaction in Scanning Hall Probe Microscopy (SHPM), first a simple background information about the underlying physics is needed.

1.2 Classical Hall Effect

The Hall effect is a charge transport phenomenon discovered by an American physicist Edwin Herbert Hall in 1879 [7] during his PhD thesis work and named after him. Before we examine the underlying physics behind the effect, a historical background can help to understand the scientific environment in which the discovery is done. First of all, despite to the fact that it was proposed by Greek scientists two millennia ago and George Johnstone Stoney [8] in 1874 as the minimum quantity of the electricity, the electrons were not known to exist at the time of the discovery. They are later discovered by Joseph John Thomson in 1897 at Cavendish Laboratory [9]. Electron charge is first quantified by Robert Andrews Millikan in 1909 with his famous oil drop experiment [10] and the results are further improved later in 1913 [11]. (For the full history of discovery of electron, the paper by Robotti [12] gives an excellent review). The force on the current carrying conductors, under the magnetic field was formulated by Andre Marie Ampere, Felix Savart, and Jean Baptiste Biot, well before the discovery of the Hall effect.

Edwin Hall found a contradictory sentence while reading James Clerk Maxwell's classical book Electricity and Magnetism [13]. There was a sentence stating that the magnetic force on the current carrying conductors does not act on the electric current but, on the conductor which carries the current. However, this was against to the very practical observation that conductors generally are not affected by a magnet while not

bearing a current. Also, the strength of the effect is directly proportional to the amount of the current passed. Hence, for a double conclusion, Hall proposed an experiment suggesting "If the current of the electricity in a fixed conductor is itself attracted by a magnet, the current should be drawn to one side of the wire, and therefore the resistance experienced should be increased". Motivated with this; Hall, conducted series of experiments finally concluding that current tends to move towards the side of the conductor.

In order to examine the physics of the classical Hall effect, charge carrier slab, as shown in Fig. 1.1, with the dimensions $l \times w \times d$ can be considered. When a current passes through a conductor in the $-y$ direction, placed in a uniform external magnetic field perpendicular to the direction of the current, charges are deflected due to the Lorentz Force under the presence of this magnetic field.

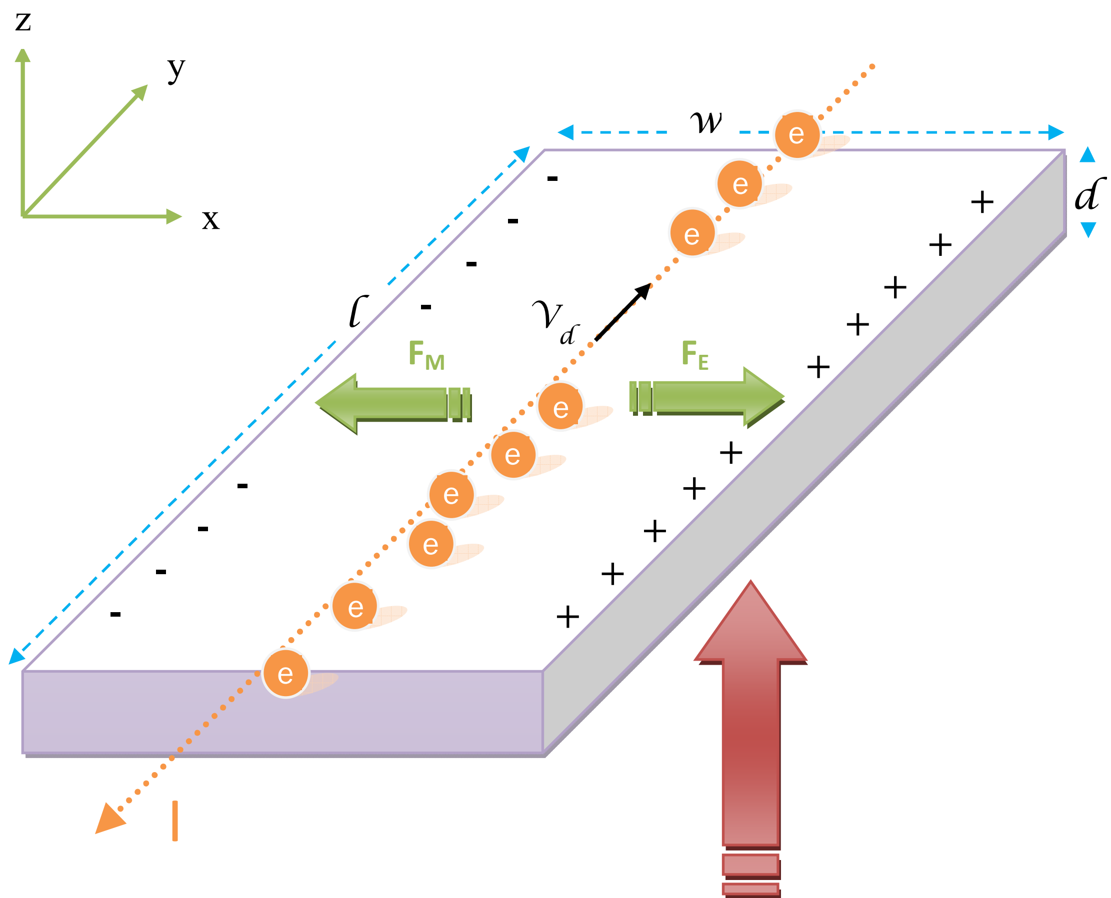

Figure 1.1: Schematic layout of the Hall effect on a slab geometry.

Electrons flow is in opposite direction to the current flow, in +*y* direction. Thus, as the current flows from high to low potential, electrons will flow from low to high electric potential. While flowing through the conductor, the presence of the external magnetic field deflects the electrons towards the left side of the slab with the Lorentz force

$$\vec{F}_M = -e(\vec{v} \times \vec{B}) \tag{1.1}$$

Accumulation of electrons on the left hand side of the slab creates a charge imbalance, which in turn makes that side negatively charged. This will in turn generate an electric field until the electric force due to the field balances the magnetic force. The total force on the electron can be written as the total Lorenz Force,

$$\vec{F} = q\vec{E} + q(\vec{v}x\vec{B}) \tag{1.2}$$

which should become zero. For the sake of simplicity we can assume all the carriers to be the electrons with a charge –*e* and they all move with the same average drift velocity, v_d. Thermal effects can also be excluded for the time being. The electrons are also treated as point particles. Equipped with these, the drift velocity can be visualized as the speed of electrons passing through the cross-section of the conductor with a cross-sectional area A, ($w \times d$) and length *l* in a time *t*. So,

$$v_d = \frac{l}{t} \tag{1.3}$$

Total charge, Q, in that slab is,

$$Q = lwdN(-e) \tag{1.4}$$

where N is the number of electrons per unit volume in the slab. The current, by definition, is the flow of total charge per unit time,

$$I = \frac{Q}{t} \tag{1.5}$$

then,

$$t = \frac{l}{v_d} \tag{1.6}$$

Thus, current flowing through the slab can be written as,

$$I = (-e)NAv_d \tag{1.7}$$

$$v_d = \frac{I}{(-e)NA} \tag{1.8}$$

$$v_d = \frac{j}{(-e)N} \tag{1.9}$$

where j is the current density. However, in general the drift velocity also depends on the other parameters. To have the charges flow, there must be a potential difference across the charge holding material. This potential difference creates an electric field E defined by,

$$\vec{E} = \frac{V}{l} \tag{1.10}$$

And the drift velocity can be defined as average velocity gained by the current carrying particles due to the presence of the electric field. The proportionality constant of the linear relation between the drift velocity and the electric field known as the mobility, μ. Mobility is defined by the scattering mechanisms (defects, impurities, phonons etc.) of the material and has unique characteristics. Electron mobility, or the mobility itself in general, is the proportionality constant between the charge density and conductivity.

$$(-e)N_{3D}\mu = \sigma \tag{1.11}$$

$$\mu = \frac{1}{(-e)N_{3D}\rho} \tag{1.12}$$

Mobility is strong function of the defects and the temperature (lattice vibrations). Matthiessen's rule formulizes that relation as

$$\frac{1}{\mu} = \frac{1}{\mu_{impurity}} + \frac{1}{\mu_{lattice}} \tag{1.13}$$

This is an empirical rule, stating that the resistivity is sum of the resistivity due to the impurities and the resistivity due the lattice.

Going back to the Hall effect, we see that the Lorentz force creates an accumulation of electrons on one side of the conductor. As the charge neutrality condition should be satisfied, accumulated electrons will induce positive charges at the other side of the slab and these will create a potential difference across the width of the sample and thus an electric field which is called as Hall field, $\mathbf{E_H}$ (Fig. 1.2). Presence of this field forces the excess charges to decrease at that side of the slab and eventually a balance between transverse electric and magnetic forces nulls the net force. Hence,

$$\vec{F} = (-e)\overrightarrow{E_H} + (-e)\mu\left(\vec{E} \times \vec{B}\right) \tag{1.14}$$

$$\vec{F} = (-e)\overrightarrow{E_H} + (-e)\left(\overrightarrow{v_d} \times \vec{B}\right) = 0 \tag{1.15}$$

$$\overrightarrow{E_H} = \left(\overrightarrow{v_d} \times \vec{B}\right) \tag{1.16}$$

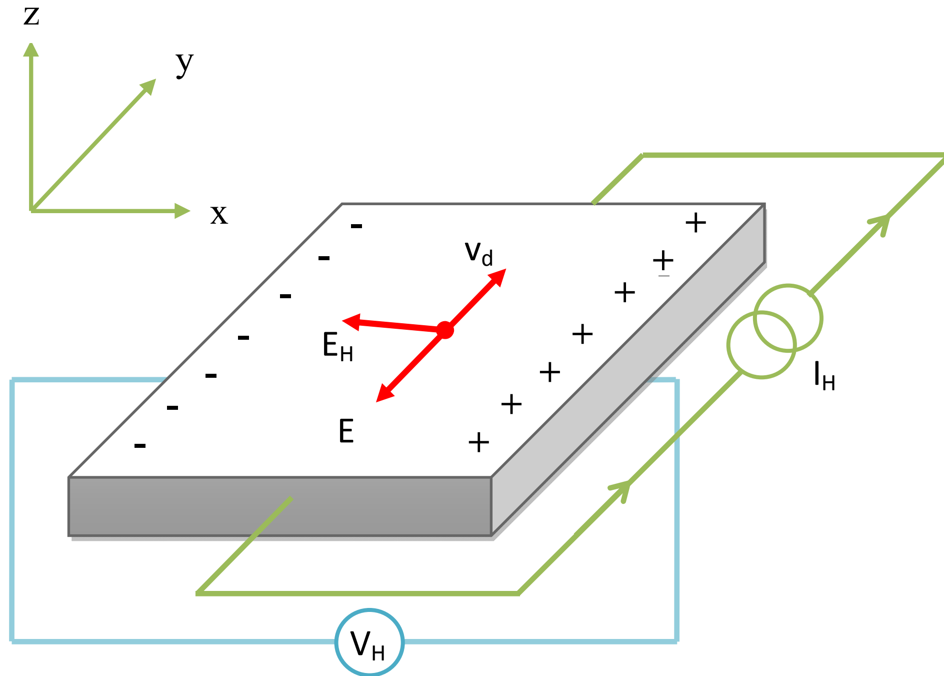

Figure 1.2: Schematic representation of the Hall effect considering the n type carriers. **E** and $\mathbf{E_H}$ are the external electric field and Hall field, respectively.

$$\frac{V_H}{w}\hat{x} = v_d B(\hat{y} \times \hat{z}) \tag{1.17}$$

$$\frac{V_H}{w} = v_d B \tag{1.18}$$

$$\frac{V_H}{w} = -\frac{I}{eNwd}B \tag{1.19}$$

$$V_H = -\frac{I}{en}B \tag{1.20}$$

$$V_H = R_H I B \tag{1.21}$$

R_H, the proportionality factor of the equation, is called as the Hall coefficient. It depends on the free carrier concentration in the material. Measurement of coefficient by applying a know magnetic field, **B** perpendicular to the slab and measuring the Hall voltage V_H and its polarity , enable us to obtain free charge density and its type (n or p-type) of the material. The sign of the Hall coefficient represents the majority of the charge carriers.

1.3 Magnetoresistance Effects

Magnetoresistors are a class of the materials which undergo a resistance change with the applied magnetic field. If the variation of the resistance can be calibrated with respect to the applied field strength they can be used as a magnetic field gauge or sensor. This dependence is generally non-linear [14]. Fabrication of small probes allows this method to be useful at local magnetization measurements. All the current Hard Disks use Giant Magnetoresistance (GMR) sensors for read heads and the discovery of this effect by Albert Fert and Peter Grünberg were awarded with the Nobel Prize in Physics in 2007. Tunneling magnetoresistance (TMR) Sensors are estimated to replace the GMR sensors, as they show much higher change in resistance, as high as 450%, compared to the GMR sensors.

GMR is based on the weak coupling between thin ferromagnetic films separated by a normal non-magnetic metal in which the resistance of certain materials drops dramatically as a magnetic field is applied. The effect is usually seen in magnetic multilayered structures, where two or more magnetic layers are closely separated by a thin spacer layer a few nm thick. An electron with certain spin state is allowed to pass through the first magnetic layer. If the second magnetic layer is aligned in a similar way then that electrons can easily pass through the structure, and the resistance is low. If the second magnetic layer is misaligned then neither spin channel can get through the structure easily so the electrical resistance is high. This can be repeated by successive

stacking of more than two layers. So, when an external field is applied to ferromagnetic stacks oriented anti-parallel, that shows a high resistance in the absence of the field, becomes parallel exhibiting the same direction of magnetization with a low resistance. Electrons spin in one of two directions, up or down, which corresponds to the North and South poles of a magnetic field.

Anisotropic magnetoresistance (AMR) on the other hand, depends on the angle between magnetisation and current density in a thin permalloy film. The physical origin of AMR effect is the different shift of the energy levels of electrons with a positive and negative spins, respectively, under the influence of a magnetic field. This leads to a shift in the Fermi levels [15].

Extraordinary magnetoresistance (EMR) is produced by sandwiching a thin layer of highly conducting metal like gold between layers of nonmagnetic semiconducting materials. The EMR effect is due to the magnetic field induced current redistribution between the semiconductor and the metal [16]. The change of the resistance was as high as 100 – 75,0000 % in fields ranging from 0.05 to 4T for symmetric van der Pauw disk at room temperature [17].

Ballistic magnetoresistance is produced at the junction of two nanowires. Because the junction is only a few hundred atoms wide, electrons flow straight through rather than bouncing from side to side the way electrons flow through larger wires. The change in resistance is greater than 3,000 percent, and the small size of the sensor makes it possible to read tiny, closely-packed bits [18]

1.4 Bitter Decoration

Bitter or powder pattern imaging of domain structures is the oldest imaging technique proposed by Bitter in 1931 [19]. Bitter used Fe_2O_3 particles of ~1µm in size suspended

in ethyl acetate to observe the stray fields on different ferromagnetic substances. The technique is based on covering the surface with a colloidal suspension of magnetic particles. The particles collect and agglomerate in regions where large stray fields from the sample are present, typically over domain walls. Then the pattern can be imaged using an optical microscope or an electron microscope depending on the size of the patterns. Success of the method mainly depends of the preparation of the magnetic colloids. A good colloid can have particles of ~10nm enriched by various surfactants to aid better surface adhesion [1]. Another method to cover the surface with fine particles consist of evaporation of ferromagnetic particles from a filament [2]. A filament made of ferromagnetic materials, usually iron, nickel or cobalt, placed a few centimeters away from the sample used to form a magnetic vapor in a low pressure helium environment. The particles in the vapor travel to the sample surface and arrange themselves according to the present inhomogeneous field distribution. Since the spatial resolution is limited by the particle size in colloid, we can say that the resolution can be ~10nm theoretically. Usually 100nm spatial resolution is practically achievable. Note that, although the bittern decoration gives a direct visualization of the size and shape of the domain patterns, no information can be extracted about the magnitude and the direction of magnetization. Another difficulty should be highlighted is related to the sample preparation. The technique cannot distinguish between the real topography and the stray field distribution of the sample. Thus, fine polishing or chemical treatment of the specimen is necessary. The ferrofluid or evaporated ferromagnetic particles can stick to the surface and may prevent further use of that sample or it might be required to re-clean the sample before it is used for another experiment. In that sense bitter decoration is an invasive imaging method. The Bitter decoration is limited to low field values, typically less than 10mT [2] and only works if the sample has stray field [1].

1.5 Lorentz Microscopy

Lorentz microscopy is a special type of the imaging that uses transmission electron microscopy (TEM). While use of conventional SEM requires no special sample preparation, for TEM the samples must be thinned to ~70nm (depends on the acceleration voltage used) and the samples must be conductive up to some degree as required in most of electron based techniques. In electron microscopy the electrons emitted from the filament are accelerated to high energies of 100-200keV in the standard TEMs. These energies can go up to 1MeV in some high voltage transmission electron microscopes [1]. Electrons also has the wave nature and their wavelength can be as small as 0.0123 Å, which is much smaller than inter atomic spacing [1]. Thus, while analyzing, it is possible to use the particle or wave aspect of the electrons. If we consider the particle aspect than classically the electron will interact with magnetic field according to well known Lorentz force and they will be deflected. In that case only the perpendicular component of the magnetic field to the direction of motion of electrons is effective on the deflection. The Lorentz microscopy is based on these deflections along the path of the electrons due to magnetic fields in the specimen. However the interpretation of this deflection may be different depending on the used method. First method is defocused or Fresnel mode Lorentz imaging. The name is given because the magnetic contrast obtained is based on the Fresnel effect. While electrons are passing through the sample they are deflected in directions depending on the magnetization direction of each domain. Thus, the distribution of the domains throughout the sample consequently deflects and superposes the electrons in constructive or destructive manner creating bright or dark parts due to the wave nature of the electrons. This effect can be observed while the microscope is defocused since, only defocused images contain angular information. Note that the method only works if the domain walls are parallel to the magnetization axis. When they are perpendicular no net deflection can be achieved. In other method used, instead of defocusing the image diffraction pattern is formed at one of the aperture planes of the microscope which is called in focus or Foucault

method. A selective imaging can be obtained by changing the position of the aperture. This will allow electrons deflected only with certain angle to form the bright or dark field. Hence, prediction about the magnetization direction is possible

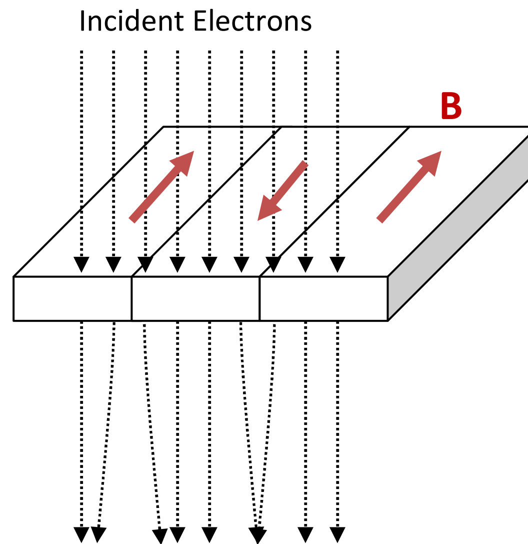

Figure 1.3: Electron deflection through the sample in Lorentz microscopy

Differential phase microscopy, on the other hand, is a special case of the Lorentz technique which can achieve ~2 nm resolution [4]. To use this technique a TEM should be modified to measure the Lorentz deflection with quadrant electron detector. The deflection is measured through the differences of the currents created on the quadrants of the detector, which gives the name to the method.

Common to all the Lorentz Microscopy methods described above, we can say that they all give high resolution images are sensitive to small variations of the magnetization. However, the limitations or the negative aspects have to be considered as well. First of all the method require a huge amount of investment on the microscopes. Sample preparation is difficult and may require special tools as well which in turn increases the budget further. The magnetic fields used to deflect or condense the electron beams

should have a special arrangement not to interfere with the surface magnetization of the samples so that the electron beams are not affected by these fields.

1.6 Magneto-Optical (MO) Imaging

Magneto-optical imaging is a general term used for broad family of magnetic imaging methods that are based on the small rotations of the polarization plane of the polarized light and only visible when viewed with a polarization microscope. The interaction of polarized light with the magnetization structure of the material causes the plane of polarization to rotate. If the rotation of the polarization plane happens due to reflection of light then this is the Kerr effect. On the contrary, if the rotation of the linearly polarized light is in transmission, than the effect is called Faraday effect. The sensitivity of this method is mainly limited by the optical parts of the used microscope. Other limitation comes from the MO material and how good they are brought into contact with the sample. If a laser is used instead of the conventional optical system, this can increase the resolution and can give better flexibility in terms of the post processing. But they are slower compared to the classical systems and heating of the sample due to higher power can be a problem [1]. But modern pulsed lasers have made it possible to capture images at rates of 10 ns frame [4]. Typical resolution is around 0.3μm [1, 4] in a high quality optical microscope using an oil immersion objective and blue light illumination [4]. Sample preparation is also important. To enhance the resolution samples must be optically flat and damage free. Nevertheless, MO is more or less a non-invasive technique which gives direct and fast observation of the magnetization.

1.7 Spin Stand Microscopy

A study carried out by the faculty and students at the School of Information Management and Systems at the University of California at Berkeley shows that about 5 exabytes (1 exabyte = 10^{18} bytes) of new information was created in 2002 and 92% of

this information is stored in magnetic media [20]. To rationalize the number it worth to note that Library of Congress contain about 136 terabytes of information; five exabytes of information is equivalent in size to the information contained in 37,000 new libraries the size of the Library of Congress book collections! Table 1.1 summarizes yearly worldwide production of original stored content.

Table 1.1: Worldwide production of original information, if stored digitally, in terabytes circa 2002. Upper estimates assume information is digitally scanned, lower estimates assume digital content has been compressed [20].

Storage Medium	*2002 Terabytes Upper Estimate*	*2002 Terabytes Lower Estimate*	*1999-2000 Upper Estimate*	*1999-2000 Lower Estimate*	*% Change Upper Estimates*
Paper	1,634	327	1,200	240	36%
Film	420,254	76,69	431,690	58,209	-3%
Magnetic	5187130	3,416,230	2,779,760	2,073,760	87%
Optical	103	51	81	29	28%
TOTAL:	5,609,121	3,416,281	3,212,731	2,132,238	74.5%

From this table, we can conclude that currently, hard disk drives are the dominant magnetic storage devices because they offer the best overall combination in non-volatility, reliability, large capacity, high data transfer rate, and low production cost. The development in hard disk drive (HDD) industry brings the technological advancement of hard disk drives. A hard disk is composed of many parts having different functions which require a joint study of different branches of science and engineering to continue advancement. This multi-disciplinary scheme contains studies from physics, material science, aeronautical engineering, computer sciences etc. One of the important aspects about developing the HDDs is the control of data writing on the ferromagnetic material used for data storage in hard disk. Inspection done on this subject can help to improve the new materials to be employed as a storage medium, to

characterize write/read heads. In that sense, the spin stand microscopy is one of the methods specifically developed to serve the HDD research and industry. The imaging is done with a sensor brought in to very close proximity of the HDD while the disk is mounted on a spin stand. Visualization of the bits is done with high speed at a few hundred nanometer scale resolution. In fact it is very similar to the real working principle of an HDD. The sensor used in spin-stand microscopy technique is a conventional magnetoresistive read/write head. Images are acquired by scanning a certain portion of the rotating disk in the along-track and cross-track directions [21]. If the along-track direction is scanned, while the disk is rotated, cross-track direction scanning is performed by using radial displacements of the head with the voice coil.

1.8 Scanning Superconducting Quantum Interference Device (SQUID) Microscopy

The superconducting quantum interference device, SQUID, is by far the most sensitive sensor of magnetic flux reaching a resolution of 10^{-21} Wb(Tesla m^2). Magnetic field resolution of SQUIDs can be as low as $fT/\sqrt{Hz}$ with a pickup coil are of a few square millimeter [22].

There are two main types of SQUIDs, which are DC and RF SQUIDs. The distinction comes from the number of Josephson junctions used. RF SQUIDs can work with only one Josephson junction, whereas DC SQUIDs need two junctions. Josephson junctions are the weak links separating a superconducting loop which form the detection part of the device.

When it is brought close to the sample, external flux generated by the specimen penetrates the SQUID loop. To maintain the flux quantization condition the SQUID loop should generate a current which circulates through the loop. This circulating current will cause one of the Josephson junctions to exceed its critical current, and a

voltage will develop across the SQUID. This voltage triggers the feedback systems and a current $I_{feedback}$ is supplied by the feedback circuit with a known mutual inductance L. The feedback flux $\Phi_{feedback} = L \times I_{feedback}$ required to keep voltage generated through the loop minimized is equal to the applied flux through the SQUID that generated the signal [23]. The SQUID should be positioned as close as possible to the sample to achieve a high spatial resolution [24, 25]. It is also important to have a small effective area of the loop. A recently reported nano-SQUID has a spatial resolution of substantially less than 0.5μ m with field resolution of ~10 nT [26].

1.9 Magnetic Force Microscopy (MFM)

Magnetic force microscopy is a modified atomic force microscope sensitive to the magnetostatic forces instead of atomic forces (AFM). A first demonstration of MFM goes back to 1987 [27, 28]. In this method forces are measured by a deflection of magnetically coated cantilever very similar to the conventional AFM [6]. Deflection of the cantilever can be measured in several ways including the use of piezoresistive cantilevers or by optically deflecting a laser beam from the back of the cantilever. The difference to AFM comes with the tip which is coated with a ferromagnetic material. The coating must be optimized in accordance with the inspected sample. The sample and tip brought together with the aid of the usual AFM approach techniques. When the surface is reached, the designated area can be scanned with the help of the piezo scanners. Usually a lift off technique developed by Digital Instruments is employed. In this scan method first the surface topography is scanned by AFM feedback along the forward scan. Then up on completion of the topographic profiling a certain height is given to lift the scanner and the surface is scanned again following its texture with the given offset in the backward scan direction. By this way the effect of the short range forces are eliminated and the van der Walls forces are kept at constant level. Interaction between the tip and the sample is not very straightforward. It includes magnetization distribution of the tip that interacts with the stray field of the sample. However, it can be

hard to quantify the components of the interactions as the tip itself may be dominating over the samples stray field due to its high magnetization. So it is not straightforward to obtain quantitative images. Nevertheless, although the information about the magnetization distribution in a sample is only indirect, MFM is probably the most widely used magnetic imaging method. Main reason for this is ease use of the microscope under various environmental conditions, its high spatial resolution, which also gives topographic information, and the commercial availability of instruments.

1.10 Scanning Hall Probe microscopy (SHPM)

The first realization of this method is given by Chang *et al.* in 1992 [29]. Since then the methods is spreading among the science community and already commercialized [30].

In SHPM as shown in Figure 1.4, a Hall probe integrated with an STM tip is brought in to close proximity of the sample under inspection using the course approach mechanism. The sample is tilted ~1-2º about the probe to have the STM tip at the highest position. Integrated STM tip keeps track of the surface just like in the case of STM seeking a tunneling current. The tunneling current is fed into a control electronic to maintain a constant current changing the height of the sensor with respect to the topography of the sample using a piezo tube scanner. The simultaneous topography and magnetic imaging can be accomplished while scanning the designated area within the scan range of the piezo. Overall control of approach and scan is maintained via dedicated SHPM control electronic and software. It is also possible to use AFM feedback as explained in Chapter 4, which makes it possible to scan non-conductive samples for simultaneous topography and magnetic data. Integration of Hall probes with quartz tuning fork force sensors are demonstrated here.

The technique can give quantitative data with a high spatial resolution [31]. Microscope can work in a wide temperature range under high magnetic fields [32]. The detailed

description of the method and sensor fabrication is given in Chapter 2 and Chapter 3 respectively. Achievement of 50nm spatial resolution using Bismuth thin film and FIB milling is described in Chapter 3 together with the fabrication of other semiconducting materials selected as candidates for SHPM imaging. Chapter 5, on the other hand shows the first demonstration of the novel Hall gradiometer and its use to obtain all the spatial components of the magnetic field over a hard disk sample with 700nm spatial resolution.

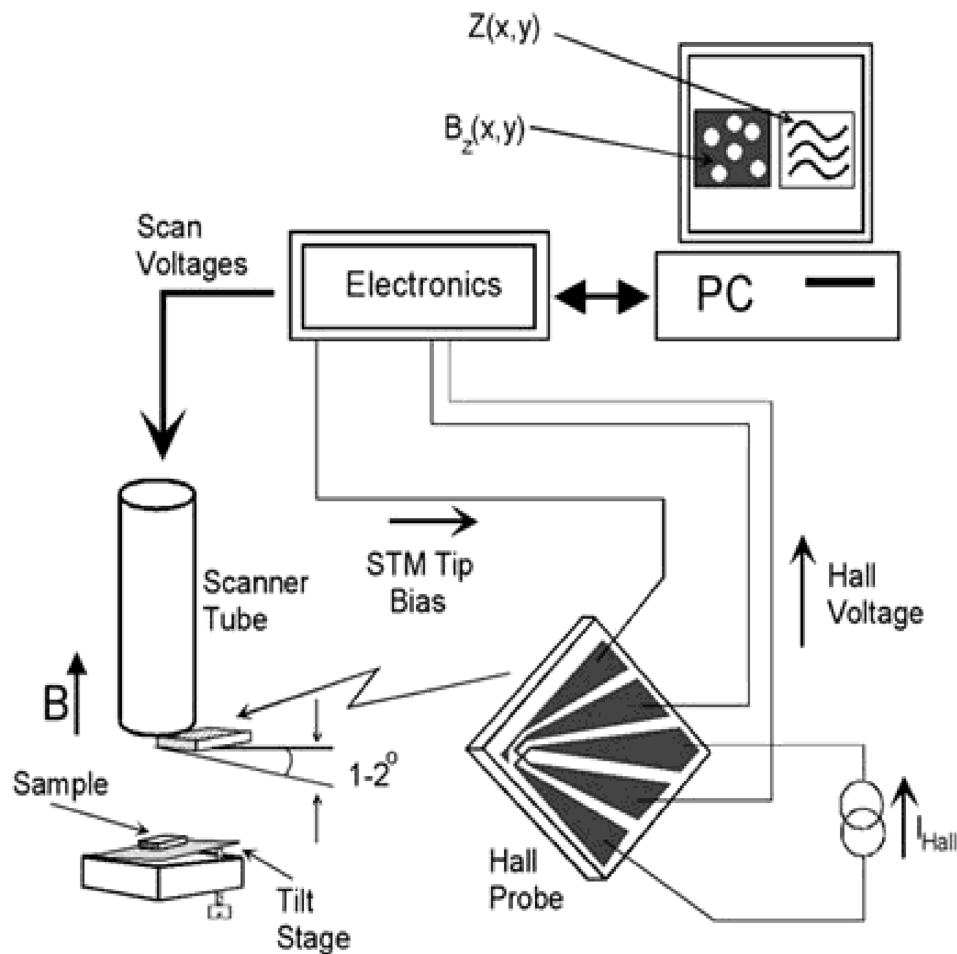

Figure 1.4: Schematic layout of the Scanning hall Probe Microscope. The common elements of the SPM family can clearly be distinguished.

Chapter 2 : The Microscope

This chapter explains the details of the Scanning Hall Probe Microscope (SHPM) used in this thesis. The microscope body, electronic control unit and the acquisition & control software are introduced. The details of the electronics are kept brief aiming to guide the reader in a general sense of functionality. The details of the sensor, coarse approach and scan mechanisms are also given.

2.1 Introduction

Scanning Hall Probe Microscope SHPM is a member of the Scanning Probe Microscopy (SPM) family and shares the common characteristics of these instruments. Although different subfield classifications are possible with respect to the interaction used or property measured, SPM in general, refers to techniques that use the interaction of a probe (or sensor) with the surface of a sample to measure various characteristics; surface conductivity, static charge distribution, localized friction, magnetic fields, elastic moduli etc, of the sample at nanometer scale, in some cases atomic resolution. Thus, whatever the technique is used or property is inspected, there are a set of common elements used in all the SPMs. These common properties can be listed as,

1. The Probe (sensor),
2. Coarse approach Mechanism,
3. Scanner Mechanism,
4. Control Electronics & Software.

The following sections briefly explain these particular elements in general sense with details specific to the microscope employed in this thesis. The microscope used is

commercially available [30] Scanning Hall Probe Microscope (SHPM), developed in collaboration with our group.

2.2 The Microscope Body

The microscope body is an assembly housing all the mechanical parts, moving or stationary, which forms the microscope. Scanner and coarse approach mechanisms, electrical connectors and cabling are all brought together to form the microscope. The microscope has been shaped according to the application requirements. The microscope used in this study has a compact form in order to fit in to cryostat systems for low temperature applications. Radiation baffles decrease the effect of the radiation from 300K reaching the head and help preserve the cryogen. The extension tube is designed to bring the scan head to the magnet center of the cryostat. It also houses all the cables used to carry the signal in and out to the SHPM head. Approach and scanner elements are located on the head as shown in Fig. 2.1 & 2.2. The sample is placed on the sample holder facing towards the sensor, which is mechanically attached to the slider puck. The puck is, then, engaged over the slider glass tube by properly tightened the leaf spring. The puck, which is held by static friction, is free to move along the slider tube. The hollow cylindrical shield is placed around the whole head to mechanically protect the scanner, to help maintaining the temperature stability and it shields the system from the electromagnetic noise.

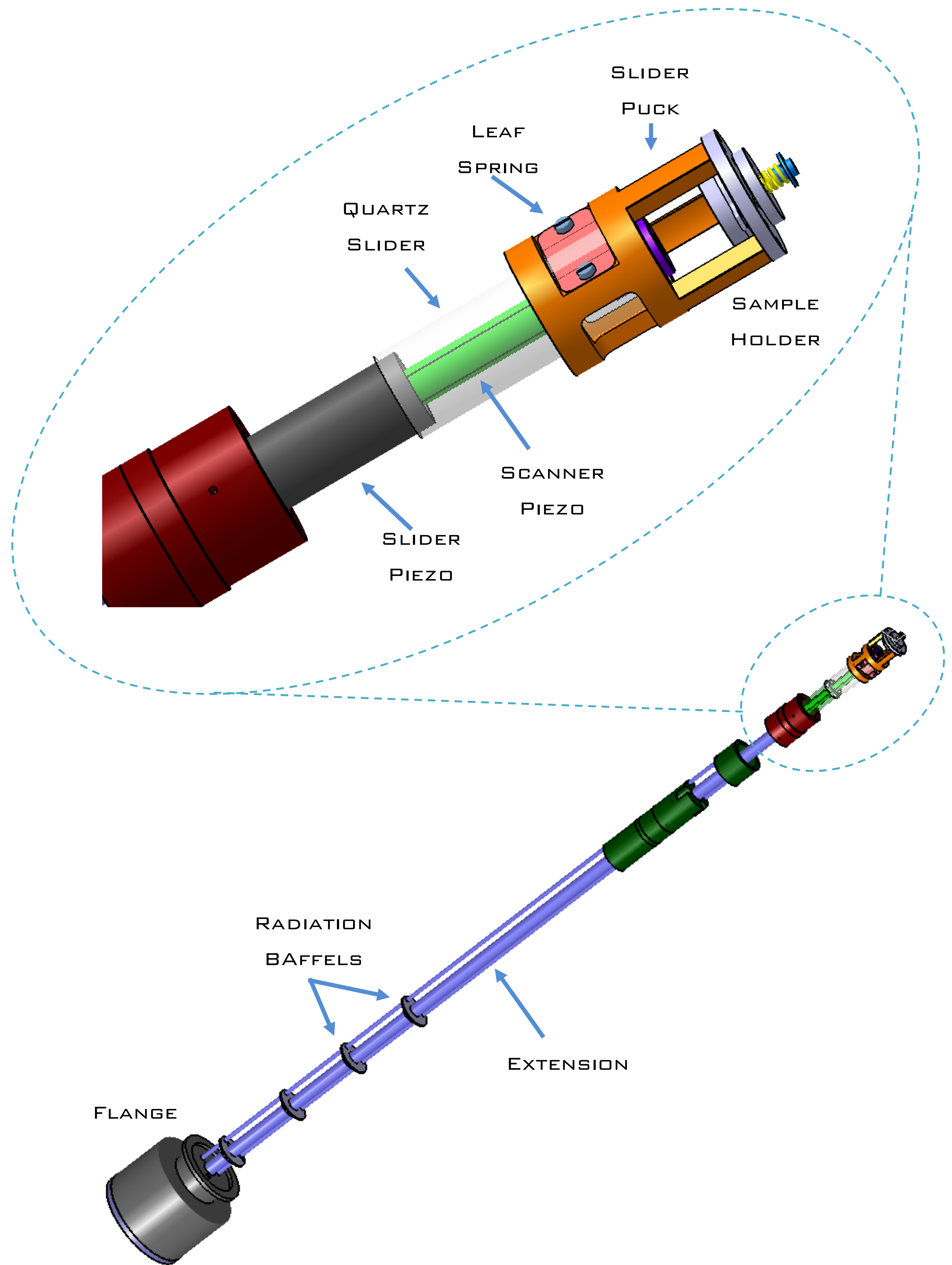

Figure 2.1: The design representation of the SHPM with close up details of the scanner head.

Figure 2.2: Picture of the microscope. The shield, puck & sample holder, slider glass and the piezos are shown.

2.3 The Hall Probe

The first, and may be the most important, element is the sensor. The probe is specially fabricated to be sensitive to a specific property aimed for measurement and interfaces the sample with the rest of the microscope. The probe, in this application, is a Hall sensor, which is sensitive to the perpendicular component of the stray magnetic field on the surface of the magnetic or superconducting samples. The working principle and the production details of Hall sensors are given in related sections of the thesis. Use of other type of sensors is also possible depending on the property need to be measured provided that the right electrical connections are done. We can use the microscope as STM, AFM and MFM, replacing the Hall probe with appropriate sensor. The fabricated Hall sensors

are mounted on a non magnetic printed circuit board (PCB) that has suitable electrical connections to the rest of the microscope cabling with spring probes mating at the back of the PCB. The PCB sensor holder and the sensor isolated electrically by placing a piece of alumina ceramic sheet in between. Electrical connections from the probe to PCB are achieved by 12μm gold wires using ultrasonic wedge bonder. The sensor holder is, then screwed at the end of a piezoelectric scanner to map the field over the sample. To pick a proper magnetic signal the probe should be as parallel as possible to the sample. On the other hand the mesa corner, which is used as a crude STM or AFM tip, must be in closest position to the sample. To satisfy both requirements, the sample is tilted 1-1.5° with respect to the probe. There are set of three screws on the sample puck to achieve this. Increasing the tilt angle more than ~3° may cause the chip edges to touch the sample. Also, increasing the angle increase the separation of the active region and decrease the magnetic signal. On the other hand if the angle is set lower than 1°, defects or spikes left from the fabrication can touch the surface and create unwanted signals by shorting the current or voltage leads of the Hall sensor to the sample bias voltage or can increase the probe–sample separation.

Probe-sample separation is important in terms of both spatial resolution and field sensitivity. Spatial sensitivity is the ability to resolve the fine magnetic structures on the sample. In that sense, the smaller the Hall probe size, the better resolution is obtained. Nevertheless, if the probe sample separation is bigger than the size of the cross, that is the size of active Hall area, aimed structural resolution cannot be obtained. In addition to that, the field decays with the distance and quantification of it is not possible when the probe is far from the sample. This distinction can clearly be seen in the images given in Fig. 2.4, where a thermally demagnetized NdFeB permanent magnet is imaged at various probe sample separations. The probe separation is higher when the Hall cross is away from the tip corner. Thus to increase the resolution the Hall cross must be brought as close as possible to the mesa corner of the chip. Field resolution, on the other hand, does not depend on the probe sample separation. Existence of an external magnetic field creates

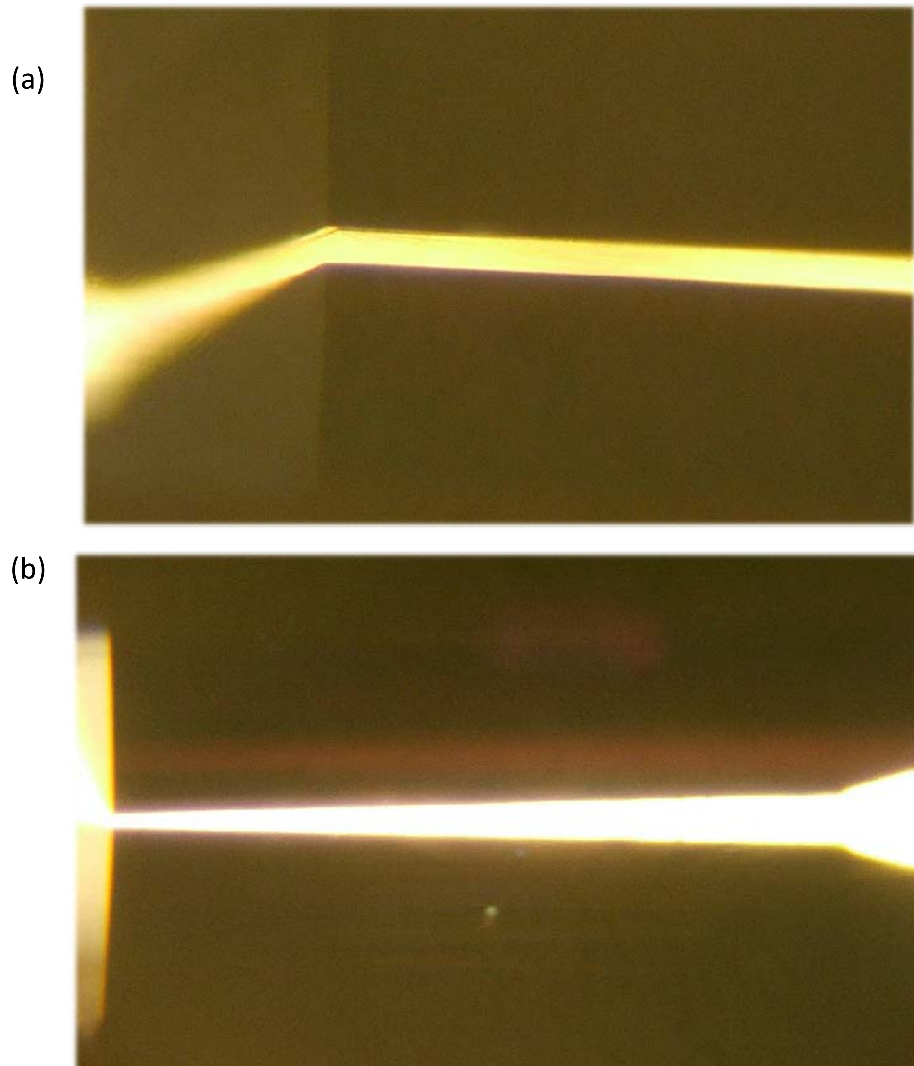

Figure 2.3: The alignment of the Hall probe with respect to the sample surface (b). The Hall probe (bottom part) and its reflection of the sample surface first made parallel by alignment screws (a), then the desired angle is given by loosening the screws on the corner of the chip. By this, the same angle is obtained on both sides. Mesa etch can be distinguished on the corner of the chip (a).

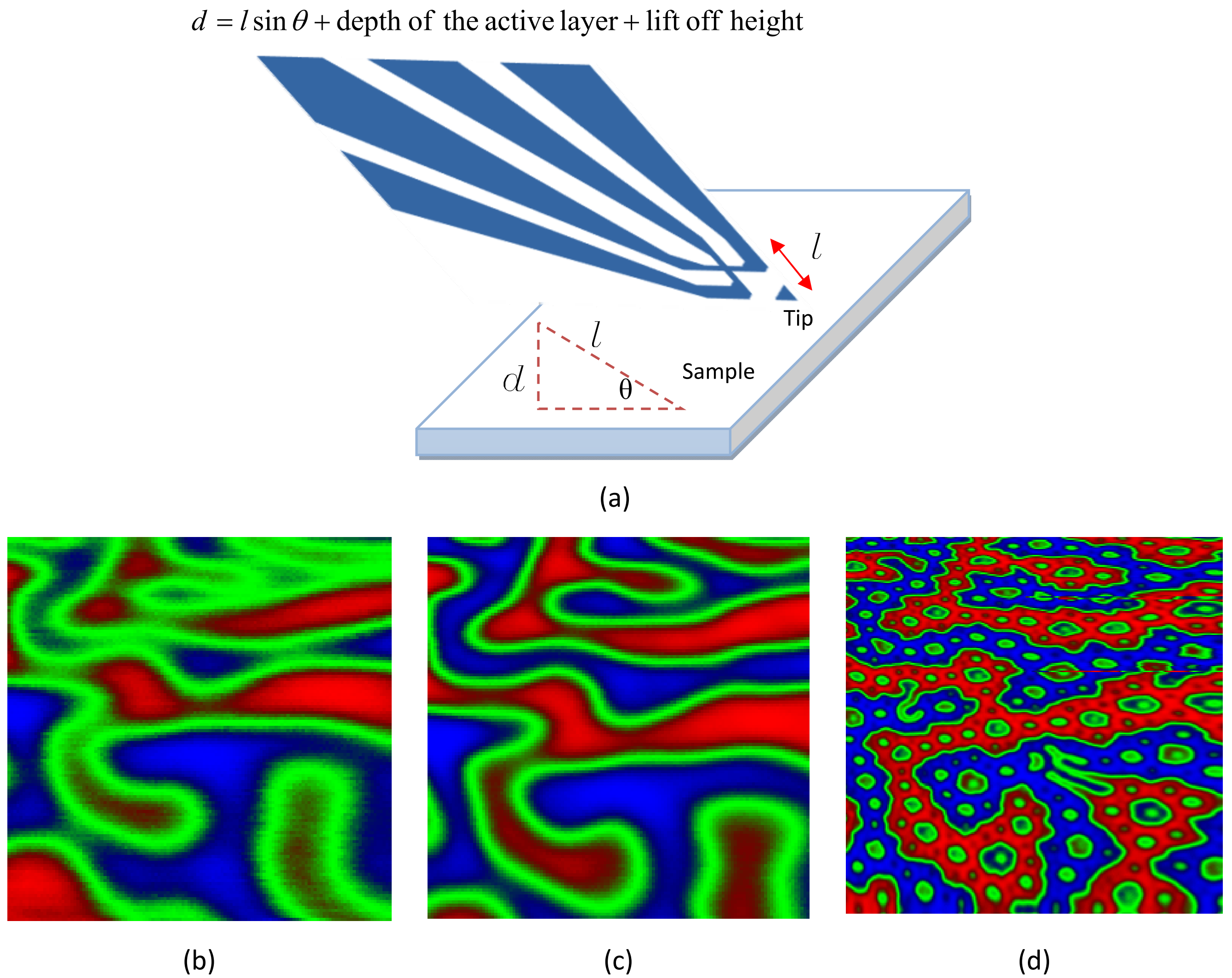

Figure 2.4: Effect of the sample-probe separation on the resolution when the sample is (b) 2.8μm, (c) 1.6μm and (d) 0.4μm. The dependency of the separation (*d*) with respect to the placement of the Hall cross about the mesa corner (*l*) is also shown in part (a).

the Hall voltage signal. The main noise component of this signal comes from the Johnson noise which is generated by the thermal agitation of the charge carriers [33]. Johnson noise is defined by

$$V_n = (4k_B T R_S \Delta f)^{1/2} \tag{2.1}$$

where k_B, T, R_S and Δf are the Boltzmann constant, temperature, series resistance and the measurement bandwidth respectively. The signal to noise ratio (SNR) has to be maximized for a better performance.

$$SNR = \frac{I_{Hall}\, R_H B}{\sqrt{4 k_B T R_S \Delta f}} \tag{2.2}$$

I_{Hall} cannot be increased indefinitely due to the Joule heating. To maximize SNR the material should have low serial resistance, low carrier density and high carrier mobility in order to minimize the resistance and maximize the Hall coefficient.

2.4 Approach Mechanism

Since the magnitude of the interaction between the sensor and the sample and the property aimed to be measured varies as a function of the probe-sample distance, the probe and the sample had to be brought in to close proximity of each other for a proper mapping. Thus an approach mechanism is needed in order to do this in a controlled manner. A simple stick-slip coarse approach mechanism [34, 35] is incorporated in our microscope. The basic principle of the motion provided by this coarse approach is based on the control of the inertia with piezoelectric ceramic element to direct the motion of a slider. The slider puck is attached to the quartz tube using a leaf spring. The quartz tube is glued to a slider piezo tube. The slider is mechanically clamped to the quartz tube using a leaf spring, whose tightness is adjusted to hold the slider puck even in vertical position by frictional force (Fig. 2.1). To move the slider puck a rapid asymmetric voltage pulse is applied to the piezo over a short period of time. This voltage pulse, as shown in Fig. 2.5, gives a small acceleration which is *not* enough to overcome the static friction and the carrier (puck) moves together with the quartz tube attached to the piezo. This small acceleration is followed by a large deceleration on the opposite direction, which is so rapid that the puck overcomes the static friction and remains stationary for a short time while the quartz tube is contracted. The sliding puck can move in both

directions, up and down. To reverse the direction an opposite polarity pulse is is applied. Step size can be varied by adjusting the magnitude of the voltage pulse. The tightness of the leaf spring, can change the frictional force of the slider puck on the quartz tube. Thus, it may not be possible to obtain exactly the same step size over a certain motion length. Also when the microscope is vertical, backward and forward step sizes are different due to the mass of the slider puck.

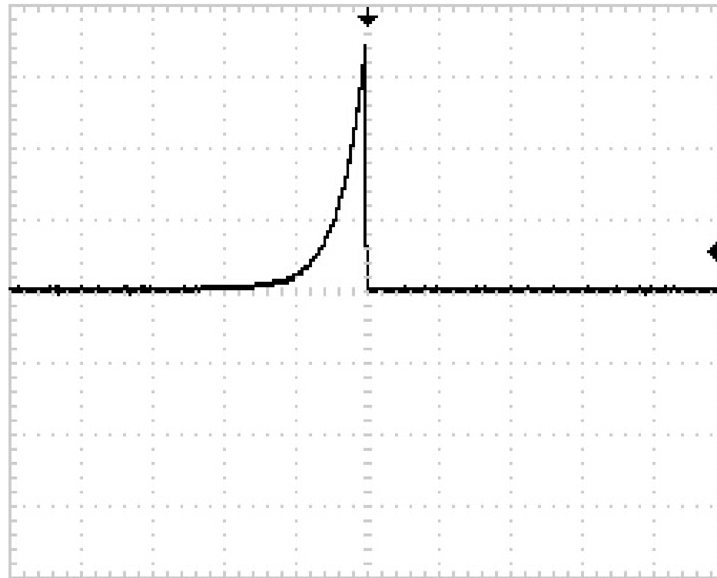

Figure 2.5: Scope trace of high voltage pulse sent to the slider pizeo to slide the puck over the quartz tubing used as a guide. Each square has 50V vertical 2.5ms lateral scale.

Before scanning the sample is approached by course approach mechanism towards the probe until a set feedback parameter (tunnel current or force) is successfully maintained. The feedback control is done by lowering the sample towards the sample extending the scanner piezo right after the forward step of the slider. The extension of the piezo is limited to approximately 4.8μm at room temperature. Thus, if the feedback signal level is not reached in the range of the scanner piezo, it is retracted back and another forward step is done by stick-slip motion. Different approach mechanism, like mechanical

screws and capacitance detection used by Moler group [36], piezoelectric detection of the shear forces [37] used together with the step motors are also applicable. It is also possible to move the sample laterally within 3mm diameter using the XY slider in our microscope.

2.5 Scanner

The precise position control of the probe over the surface, both vertically and laterally, is done by a piezoelectric scanner. This scanner is in tubular form composed of four outer segments (quadrants) electrically isolated from each other end one inner electrode. They are produced from artificial ferroelectric PZT ceramics. Application of voltage with right polarity to the designated electrodes results in dipole arrangement with respect to the field created. So, when a voltage is applied they change their shape; contracted or extended (elongated). The high voltage signals sent by the electronics drive the scanner and the attached probe over the sample in a raster scan in two dimensional pattern. An image of the sample is obtained, depending on the nature of the interaction, representing the topography, magnetic properties, or any other physical, morphological or structural property. While scanning the sensor, the SHPM feedback control circuit maintains the scanner to be in a proper z-position tracking the surface topography. This is done by continuously measuring the electrical error signal picked by the probe and comparing it with the set value. The feedback control changes the high voltage signals to elongate or contract the scanner in z direction until a match is obtained between the read and set values. The sensitivity of the analog z-feedback is software adjustable by changing its loop gain. Proper selection of feedback gain is important as it can affect the overall image quality. When the feedback gain is too high, this may cause the scanner to oscillate at the system resonant frequency. On the other hand if the gain is too small, it cannot react to the error signal changes quick enough and the topography appears to be smoother than it actually is. This can also damage the probe. It is also possible to scan while the feedback is disabled if the examined surface

is extremely smooth and has no slope. Generally, a scan without feedback is faster but, the scanner has to be lifted off for some height to ensure no obstacles will be present during the scan, which decreases the sensitivity of detection. Both, STM [29] and AFM [38-40] feedback is used for imaging during this study.

To scan the sample, alternating voltages are applied to the outer electrodes. As the applied voltage difference induces strain (or stress) it causes the tube to bend back and forth in X & Y directions. While bending the piezo in one quadrant, high voltage is applied to opposite electrodes has the same magnitude but in opposite polarity. By this way a designated area can be scanned. In our system X is chosen to be the fast scan direction. While the scanner is moving along a scan line data sampling is done at equally spaced points. This spacing between the consequent data points is called the pixel size and can be adjusted in the software. The pixel size determines the resolution of the image and the incremental change in high voltage applied to the scanner electrodes. Although usually a square image, with equal number of pixel sizes on both fast and slow scan directions, is taken; any step and scan size within the limits of the scanner can be set.

The maximum scan size that can be achieved with a particular piezoelectric scanner depends upon the length of the scanner tube, the diameter of the tube, its wall thickness, and the piezoelectric coefficients (d_{31}) of the particular piezoelectric ceramic used in the microscope. Usually, the lateral scan sizes of scanners are a few ten microns, whereas, the z range is of the order of a few microns. While scanning the measured signal is stored in an array whose dimensions are given by the set resolution or the step size. The elements of this matrix are used to generate false image of the scanned property on the computer.

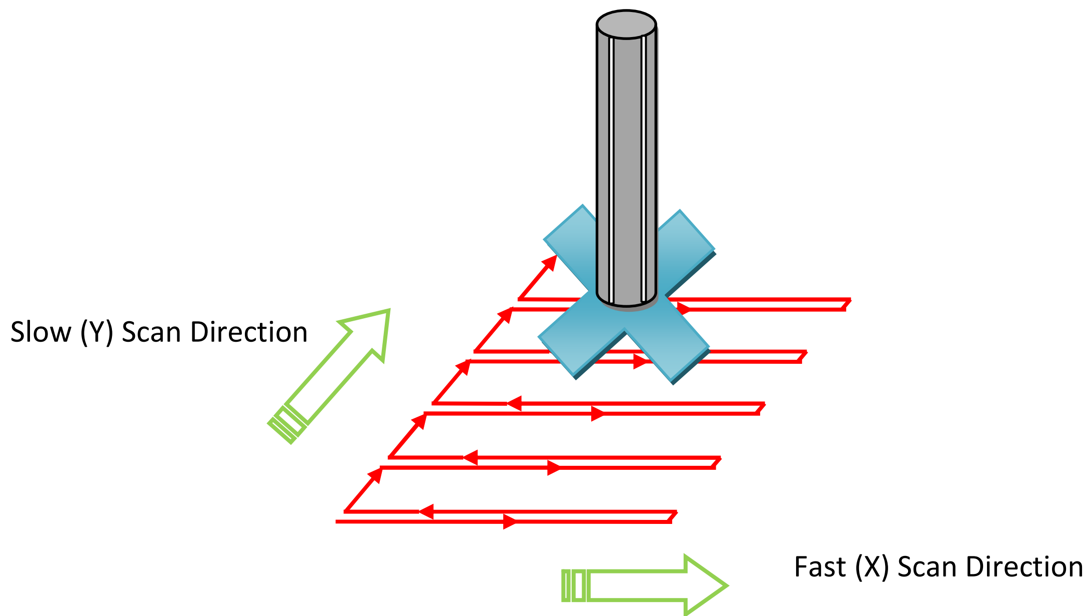

Figure 2.6: Schematic representation of the raster scan over the sample.

The microscope can be run in different scan modes. The first one is the tracking mode in which surface texture is followed by the probe for simultaneous topographic and magnetic detection. In the tracking mode, either the tunnel current between the STM tip (the gold coated corner of the mesa at the Hall sensor chip) and the sample is measured and used to drive the feedback loop or, AFM feedback where the magnitude change or frequency shifty in resonance of a cantilever due to the interaction with the sample is detected. This mode of operation gives the highest sensitivity because of the smallest probe-sample separation is achieved, albeit being slow. Also, the rough surfaces can slightly affect the magnetic image quality since the probe will move up and down while following the texture and its local Hall sensor height will not be the same from point to point. The second mode is the lift-off mode, where the Hall sensor is lifted off to a certain height above the sample ensuring there is no obstacle in the scan area and the head can then be scanned extremely fast to measure the local magnetic field distribution. As the sample-probe distance is increased the resolution also decreases. However, this mode gives opportunity to scan many images in shorter time. Thus, images can later be averaged to enhance the sensitivity and decrease the effect of *1/f*

noise. The signal bandwidth should be chosen accordingly not to lose any data. The third mode is the real time scan mode. This mode is the same as the lift off mode except the image is shown after the scan is completed. However, only one channel can be recorded in this mode. The fourth scan is the lift-off scan mode. In this mode feedback is on and the surface topography is followed stored during the forward scan. Then the head is lifted off at certain set value and the registered line profile is followed with this given offset during backward scan.

2.6 SHPM Control Electronics & Software

The SPM Controller Electronics interfaces the microscope the control software running on the personal computer. Signal acquisition & amplification, XYZ piezo motor movements, feedback control, data acquisition, scanning etc. are all controlled by the electronics. The electronics used is composed of modular cards with different functions. Some modules are functional all the time, whereas, some of them are specific to the application. The functions of the modules will briefly be given in the following sections.

Figure 2.7: The SHPM Control Electronics.

2.6.1 Head Amplifier

This amplifier is housed in a small box and attached to the microscope head through the dedicated Lemo connector. The other end of the card has D-15 type connector for input/output power supply, and ±15V connections. The head amplifier has a differential input, low noise Hall amplifier with a gain of 1,001. The output voltage of the Hall sensor is amplified through this fixed gain differential amplifier, which uses the classical three operational amplifier topology as shown in Fig.2.8. STM current or AFM Force is amplified using a -100mV/nA gain current to voltage converter.

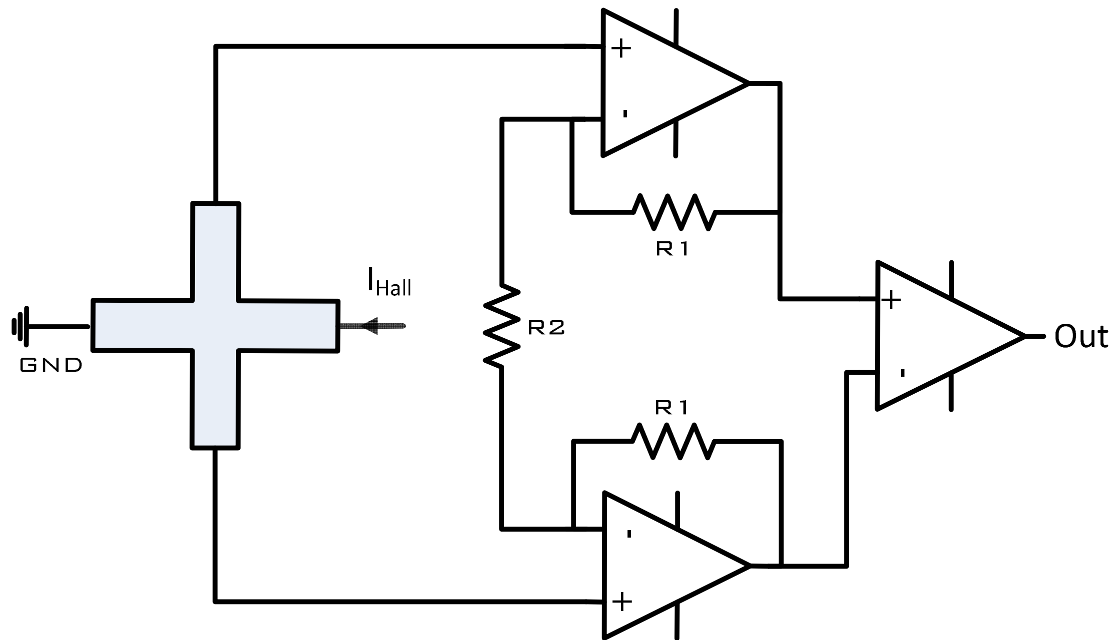

Figure 2.8: The Hall voltage amplifier.

The frequency dependent gain of the amplifier depends on the operational amplifier used. OPA111 for instance, exhibits the behavior given in the Figure 2.9 and has ~3kHz 3dB bandwidth. If OPA637 is used, than, the 3dB bandwidth is 30kHz.

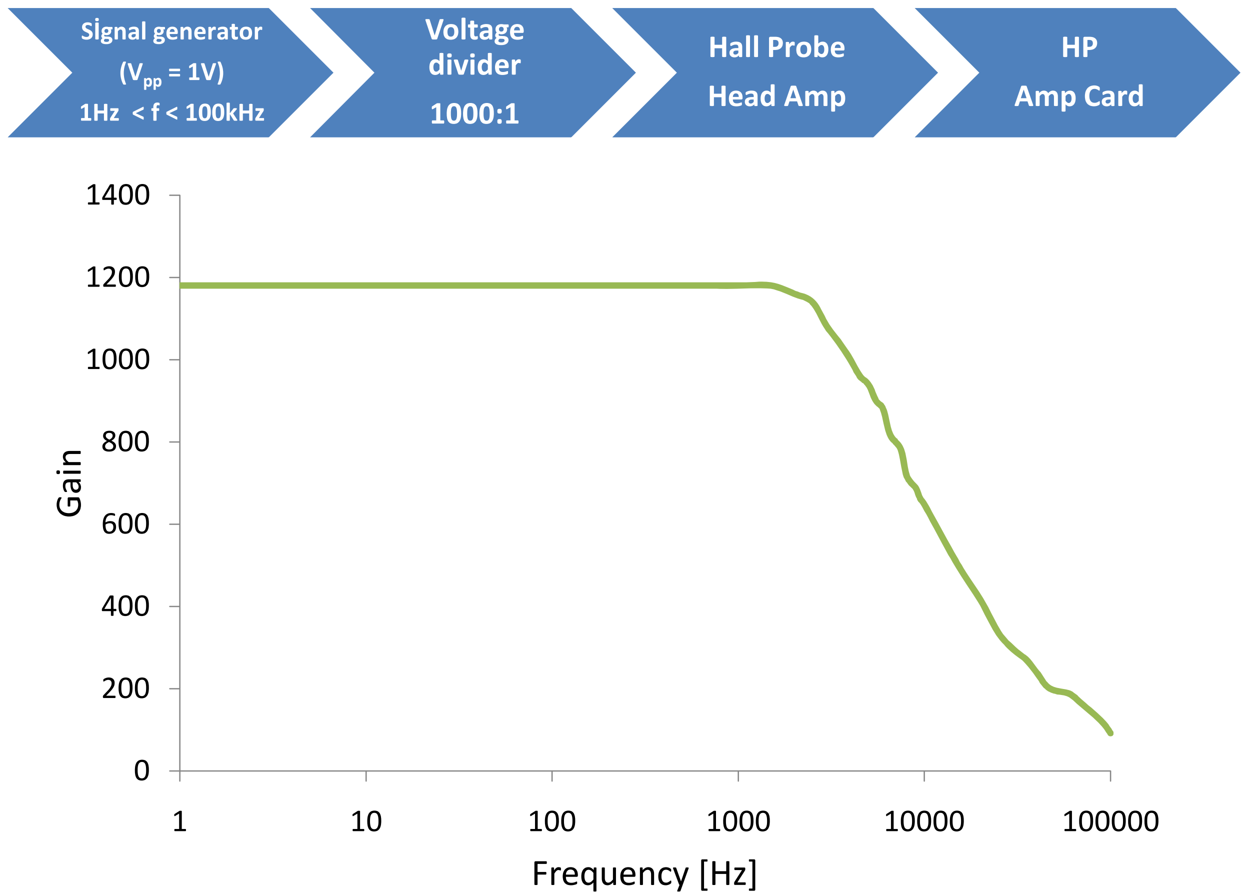

Figure 2.9: The frequency dependent gain response of OPA111 current to voltage converter. The measurement cycle used while obtaining the graph is shown above.

2.6.2 Power Supply

This card generates all the relevant regulated voltages for the SPM Controller (+220V, -200V, +15V, -15V, +5V, +8V, -8V and +420V).

2.6.3 Scan DAC

This card generates the scan voltages V_X and V_Y used for scanning the piezo tube. The output range and the resolution are ±10V and 18/20bits, respectively. These voltages are sent to High Voltage amplifier (HV) card through the backplane. The block diagram is

given in Fig. 2.10. Pixelization in XY scans affects the resolution such that features smaller than the pixel size of the image cannot be resolved. Thus the voltage sent to the XY scanner is important. The relationship between the movement of the piezo and the applied voltage is nonlinear. This causes the forward and reverse scan directions to behave differently and display hysteresis between the two scan directions. This anomaly can be corrected with appropriate non-linear voltage application to compensate the movement of piezo. The recent software that we have used can handle this.

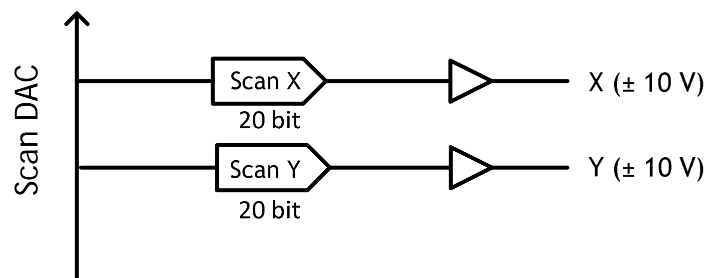

Figure 2.10: Block diagram of Scan DAC card.

2.6.4 High Voltage Amplifier (HV Amps)

This card combines and amplifies X & Y scan voltages (from Scan DAC card) with the Z-voltage (from control card) and generates N,S,E & W voltages to drive the scan piezo. It supplies the piezo drive signals for the quadrant electrodes of the tube piezo as follows:

$$S\ (\text{South}) = -10 \times (V_Z + V_Y)$$
$$N\ (\text{North}) = -10 \times (V_Z - V_Y)$$
$$E\ (\text{East}) = -10 \times (V_Z - V_X)$$
$$W\ (\text{West}) = -10 \times (V_Z + V_X)$$

where V_X , V_Y and V_Z can take values within ±10V. Therefore the outputs of the HV Amp card should be able to swing ±200V.

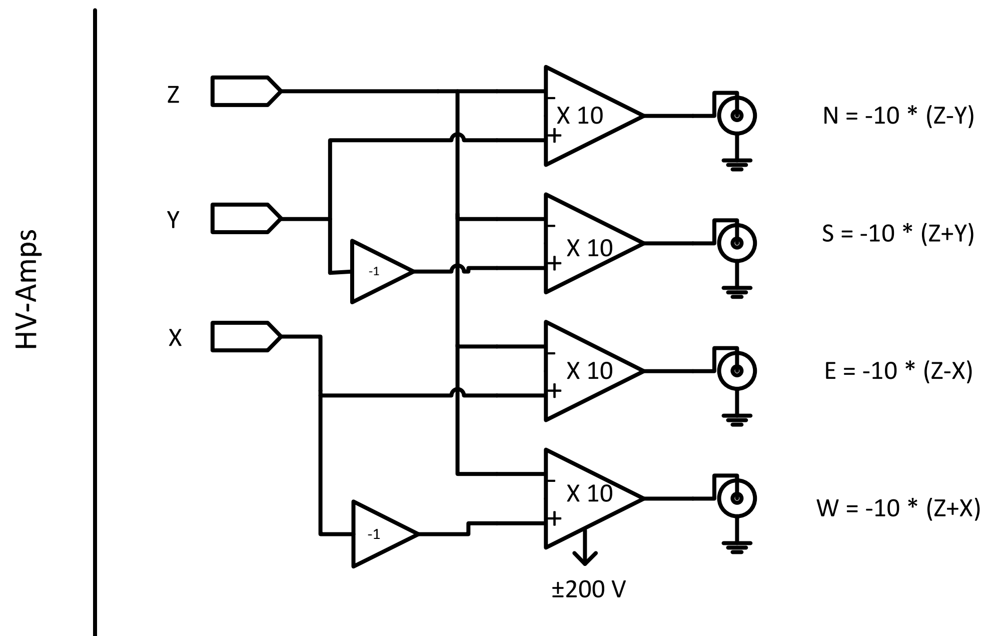

Figure 2.11: Block diagram of HV Amps.

2.6.5 DAC Card

This card has four 16bit DACs which supplies V_{Bias}, Z_{offset}, V_{coil} & I_{SET} for the SPM Controller as shown in Fig. 2.13. Output range of these voltages can be selected by jumpers on the card, ±10V (default), ±5V, ±3.3V and ±2.5V. The coil voltage output can supply up to ±1A to drive the small test coil wound up at the LT-SHPM head directly.

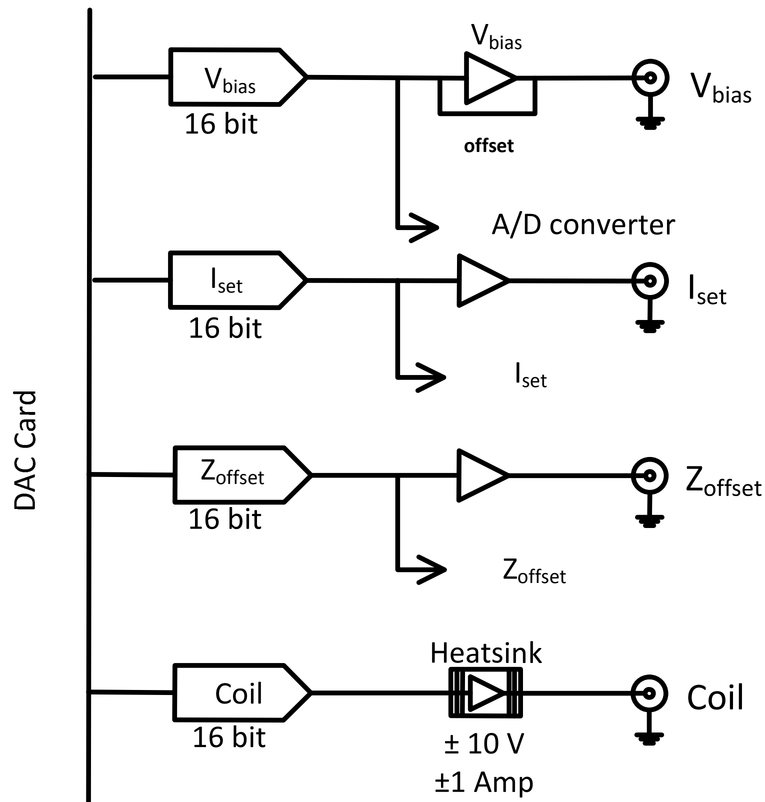

Figure 2.12: Block diagram of DAC card

2.6.6 Slider Card

This card is used to drive the stick-slip piezo sliders. The card generates a specially optimized high voltage pulse, which is multiplexed to the relevant electrodes by relays under software or keypad/keyboard control. Outputs are short circuit protected.

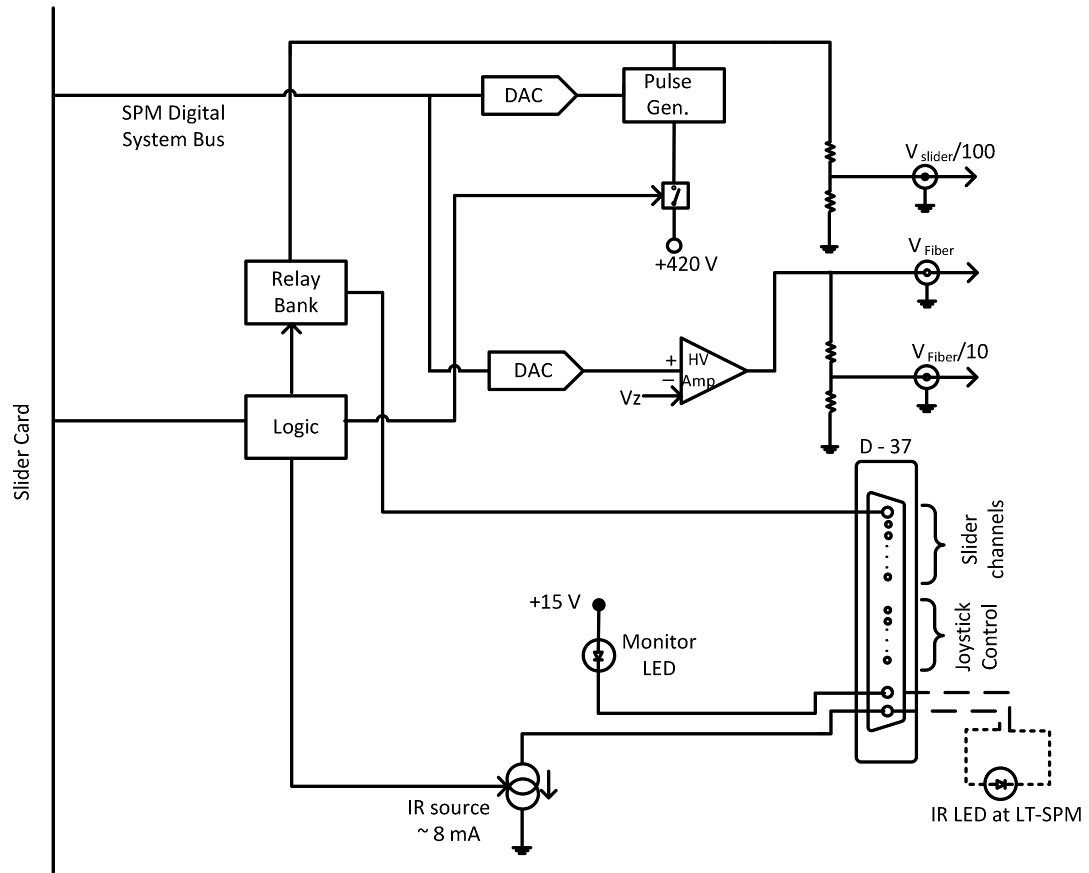

Figure 2.13: Block diagram of slider card

2.6.7 MicroController & A/D Card

This card facilitates the computer interface using RS-232 serial port and PCI I/O Card. It measures the relevant 8-channels of voltages with 16 bit resolution at a maximum speed of 200kSamples/s. The serial port can be used alone to control the electronics. The PCI I/O can also be used alone with much faster speed. The channel gain can be selected from 1,2,4 & 8.

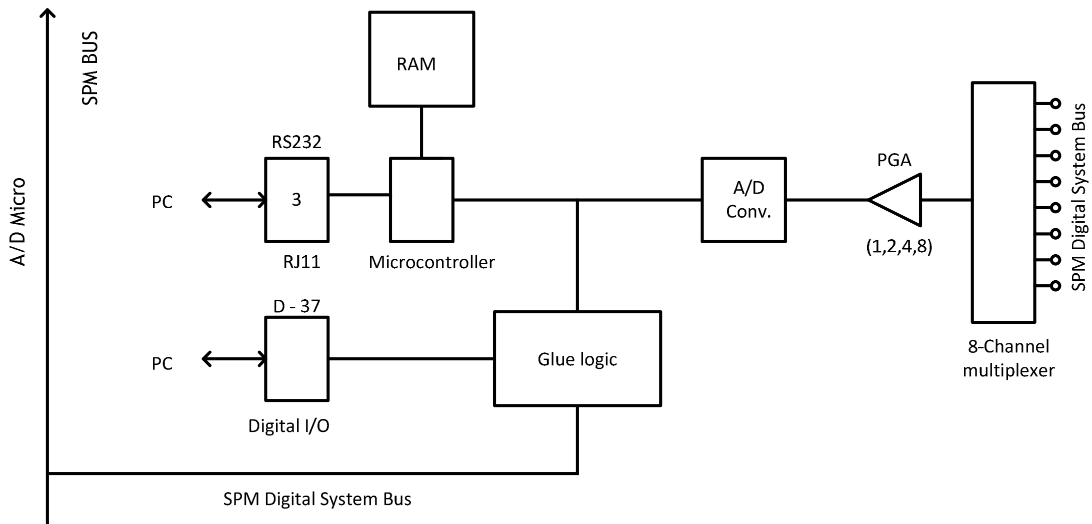

Figure 2.14: Block diagram of microcontroller A/D card

2.6.8 Controller Card

In LT-STM Mode, the Controller Card achieves tunneling feedback and keeps tunnel current constant by adjusting the tip-sample separation. There is a –100mV/nA gain current to voltage converter at the Head Amp box attached to the head. Output of this I–V converter should be connected to I_T in of the card. In AFM Mode, the external input (Ext in) is used for reading any voltage value into the card and for AFM feedback. In STM mode, tunnel current input is first rectified, then passed through a logarithmic converter (to linearise the exponential I_T – distance relation), then compared with a set current value. The output of this comparator is amplified and integrated to give the voltage output to be sent to the HV amplifier. V_Z output at the front panel is buffered output of the control card. The set tunnel current and gain of the loop can be set by software. +10V at the V_Z means the scan PZT is fully extended, –10V at the V_Z means the scan PZT is fully retracted. There is a ×10 gain at the HV amp card, so the full range is ±100V for the Z-motion. X&Y scan signals are added electronically, they give

another ±100V. Therefore resultant voltages applied to the scanner piezo electrodes are ±200V.

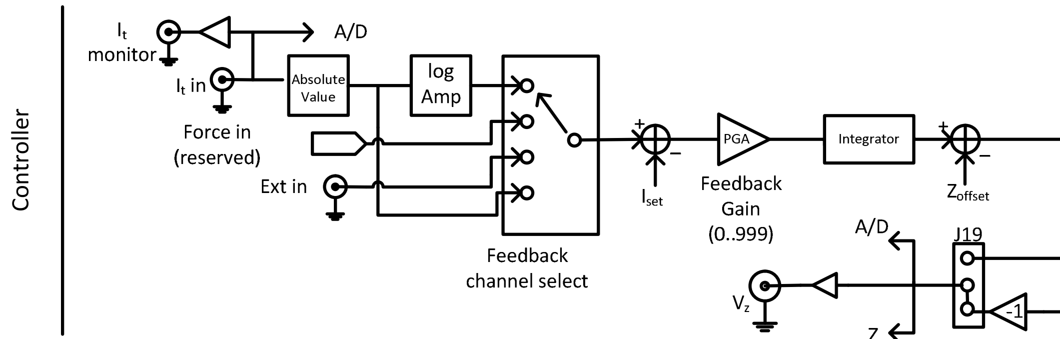

Figure 2.15: The block diagram of controller card.

The resolution in the vertical direction is primarily determined by the resolution of the vertical scanner movement. How fine the number of data points in the vertical dimension can be set is calculated by the conversion of 16 bits over the full vertical range of the scanner which is ±100V.

2.6.9 Hall Probe Amplifier Card

The DC Hall current, (I_{Hall},) to drive the Hall sensor, and the amplified Hall voltage, V_{Hall} , is further processed (amplified, shifted & filtered) by this card. The range of I_{Hall} can be jumper selected to be ±100μA or ±1000 μA. The software automatically detects the jumper setting and adjusts itself accordingly. The Hall current can be switched on or off under SPM Software control. When switched off, the current leads are short-circuited to each other. There is a ×1001 gain Hall probe amplifier at the Amplifier box attached to the head. Output of this amplifier should be connected to V_H in on the HP AMP card. This input is further amplified, subtracted by an offset value (set by the software), filtered by the card, and output to the front panel. V_H out is used to monitor the microscope. The software sets post-amplifier gains (×1,10,100,1000) and filter cut-

off frequencies opf the low pass filter (0.1kHz, 1kHz, 10kHz & 100kHz). There is also a voltage limiter connected to the I_{Hall+} & I_{Hall-} leads of the Hall sensor enabled by J2. This protects the Hall probe for accidental over voltages and high currents. The limiting voltage is ~±2.7V.

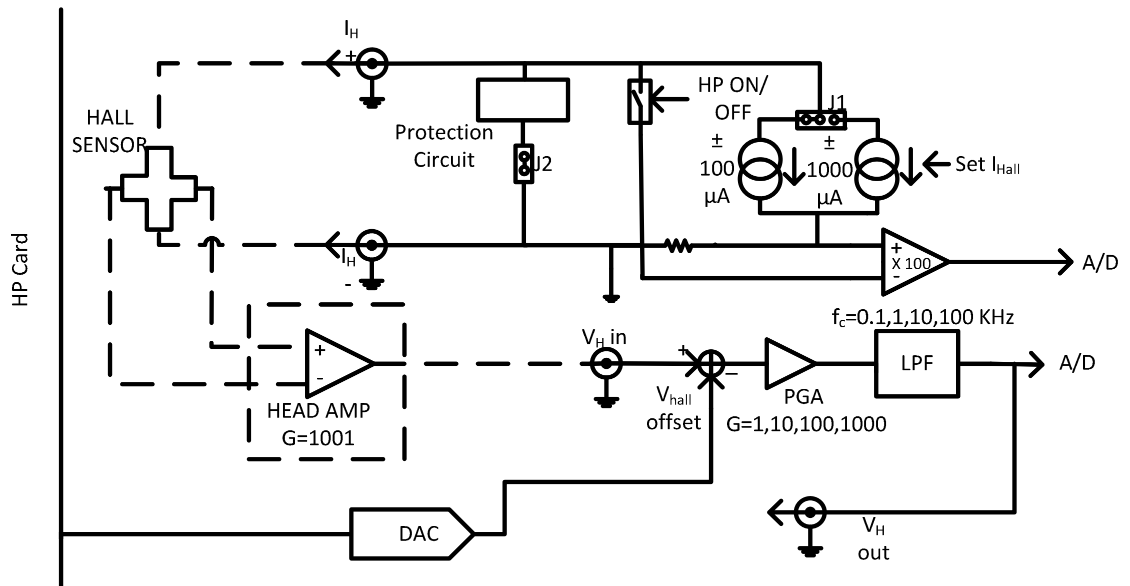

Figure 2.16: Block diagram of Hall voltage amplifier card.

2.6.10 Phase Locked Loop (PLL) Card

In Low Temperature Atomic Force Microscope (LT-AFM) Mode, Phase Locked Loop (PLL) Card sets the Quartz Crystal Tuning Fork Force sensor into oscillation and measures the changes in its resonance frequency, Δf (Freq. Out) and amplitude (A). The range of operation is between 10-1,000 kHz with 4 measurement range: ±150Hz, ±300Hz, ±450Hz and ±600Hz. The firmware of the PLL Card can field upgraded using the SPM Control Software. The PLL card generates the excitation signal applied to dither piezo. Dither piezo shakes the quartz force sensor generating a voltage at the same frequency. This signal is amplified by the Head Amplifier and fed into *Signal in*

input of the card. The PLL Card adjusts the frequency/phase of the oscillator to set the system into resonance and the digital Phase Locked Loop measures the frequency shifts. When the AFM tip attached to one of the quartz prongs gets close to specimen surface, the resonance frequency shifts. This shift, Δf, is measured by the PLL card. The centre frequency, lock range of the PLL, amplitude and the phase of the oscillator can be all adjusted using the SPM Control Software. The software can find the resonance frequency, quality factor and locks the Quartz Crystal tuning fork automatically at the resonance frequency. The PLL Card can also be used tapping mode AFM, as a Dual Channel Lock-in, where amplitude and phase of input signal is measured.

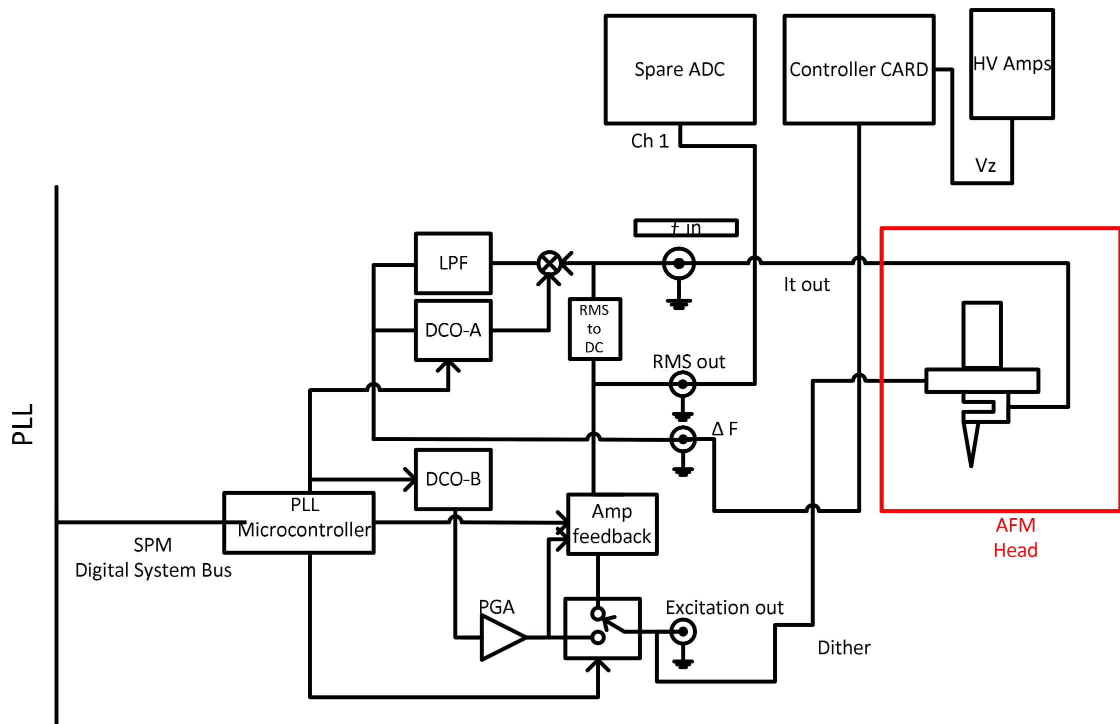

Figure 2.17:Block diagram of PLL card

2.6.11 Spare A/D Card

Spare A/D Card lets the SPM Controller to digitize up to 8-channels of more input signals with 16 bit resolution at a maximum speed of 200k samples/s. The channel gain can be selected from 1,2,4 & 8. The inputs are differentially buffered.

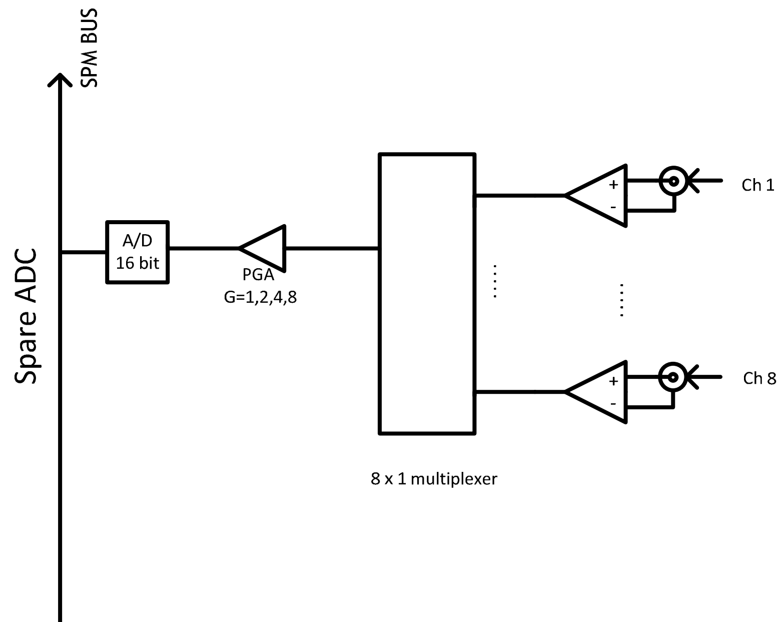

Figure 2.18: Block diagram of spare A/D card

2.6.12 PCI bus Digital I/O Card

This card, which is mounted on the PC, facilitates high speed digital data acquisition.

2.6.13 Software

All the parameters of the microscope controlled by the electronics are set through the software. Furthermore the image signal are stored, displayed, filtered or modified by the software.

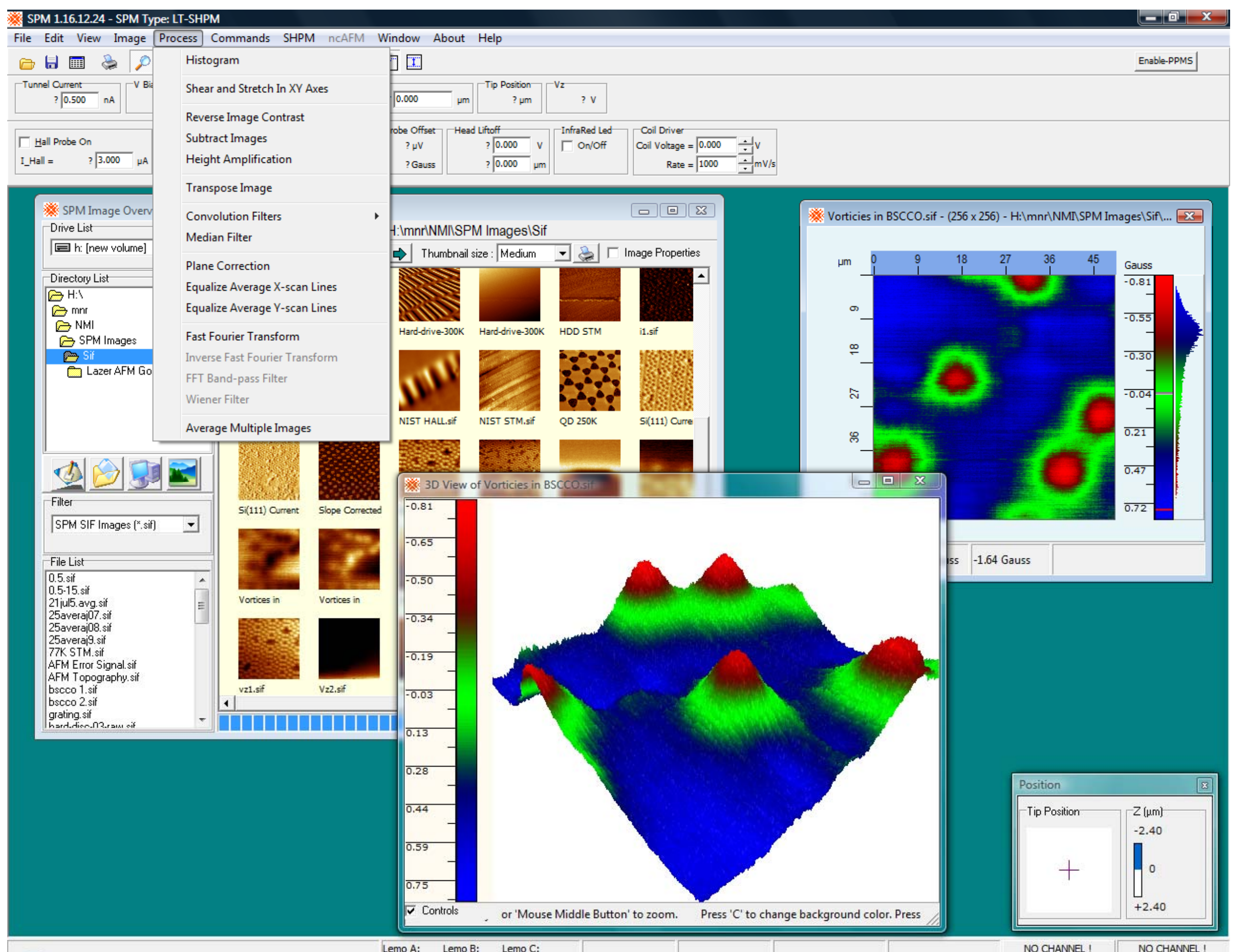

Figure 2.19: Screenshot of the SPM control program

Chapter 3 : Fabrication & Characterization

This chapter explains the details of the fabrication steps applied to the various heterostructure semiconductors and Bismuth thin film that are selected as appropriate materials to be used in production of Hall sensors for scanning Hall probe microscopy. The lines in the plots are meant to be a guide the eye through the Chapter.

3.1 Introduction

The Hall probe fabrication during this thesis work is mainly performed in Class 100 clean room facility located at Advanced Research Laboratories of Bilkent University, Physics Department. Fabrication of Hall probes, whatever the wafer is used, is composed of the sequential treatment of the wafer to shape with etching or deposition, either directly, or after lithographic patterning. The following stages are the main fabrication steps used through the fabrication. The fabrication order is not strictly as it is listed below. The aim of this chapter is to give an idea about the general production sequence. The details of the process steps specific to the materials used are given at the related sections. The wafers used in this study are either provided by the collaborated groups or acquired from the commercially wafer foundries.

3.2 Sample Preparation

The wafers had to be cut in to the appropriate sizes suitable with the mask design. Our first generation mask requires 5×5mm samples, whereas, the second generation mask needs 12×12mm sized samples. The wafer surface was spun with a photoresist and baked to protect from the debris during the cleavage or dicing. The samples with substrates having crystallographic orientation [100], (HEMT, PHEMT, InSb, SOI etc.)

were cut from the wafer by, first making a scratch along the crystalline direction of the wafer with a diamond scriber, then cleaved by pressing on the back side or by placing the sample on a glass slide just along the cut line and pressing the free side down, while holding the other part firmly on the glass. Wafers with substrates having crystallographic orientation [111], (GaN) on the other hand, have been diced completely with a Disco DAD321 dicer. These wafers are also spun by photoresist prior to cut process, to protect them from the cutting water of the blades and possible debris. Beside the debris or dust from scribing, pieces of wafers can commonly be contaminated by, dust from the surrounding environment, lint from the wipers and body oil of the user. Therefore, they have to be cleaned prior to use. There exist different cleaning procedures like the standard RCA cleaning procedure and its variations. In this work, pieces are cleaned by immersing into three separate beakers of acetone followed by three beakers of isopropanol. Note that each solvent was poured into its dedicated beaker, labeled accordingly, in order to prevent cross-contamination. Dipping into the alcohol is done before letting the acetone dry on the sample surface. Alcohol cleans any remnants of acetone and organic materials. No deionized (DI) water is used after the alcohol, as it evaporates more easily than water, leaving a dry surface. Ultrasonic agitation is also applied when necessary, however, with low power adjusted by a variable transformer or while the samples are in polypropylene beaker, which reduce the power by absorption compared to the glass. Otherwise GaAs based samples are easily broken. After the cleaning, the samples were blown dry with filtered ultra high purity nitrogen gas supplied directly from a liquid nitrogen tank. The cleaning process is repeated at the beginning of each step when necessary. Sometimes it was enough to squirt acetone followed by isopropanol and then blow dry the sample with nitrogen gas. Photoresist strippers can also be applied for the cleaning, when necessary. We have used AZ100 Remover, by Microchemicals GmbH, which was reported by the producer to be metal ion free. It has been observed that wafers having layers with aluminum content, like InAlAs, AlGaAs etc., are attacked by this stripper, if immersed for a long period of time. Mechanical cleaning using swabs with chemicals like photoresist strippers, acetone or isopropanol, may not be suitable for all wafers, as the swabs can

scratch the wafer surface. Oxygen plasma cleaning is another option to clean the organic remnants, especially the cross-linked photoresists. Although, this has some advantages over chemical cleaning methods, i.e. elimination of ion contamination, no attack to layers below the surface, the exposure time and dose should be arranged carefully, as it can still damage the surface with Oxygen ions [41, 42].

3.3 Active Area Definition

The first, and the most important, step of the fabrication starts with the definition of the active Hall cross. The performance of the sensor is mainly defined at this step. It is explained in related sections that the noise characteristics, the initial probe offset due to misalignments and the real spatial resolution are determined by the quality of the active Hall cross definition. The standard probe area defined by optical lithography was 1μm. The smallest physical width defined by optical lithography, on the other hand, was 0.5μm.

The process begins by cleaning the samples as explained above. Later, the samples are spun with desired positive photoresist, which is a photo sensitive polymer liquid that can that can be spread out onto a substrate as a thin film. It can be patterned with a desired shape using a mask, and developed into desired patterns for subsequent processing. This optical means of patterning in general called as *photolithography*. Note that the entire process of patterning is a *binary pattern process,* which means that there is no half defined pattern. As, none of the processes are done using full wafers, it was inevitable to have the edge beads, the accumulation or ridge of resist at the edges of the wafer during spinning process. Non circular, non-beveled and small wafer pieces increases the formation of the edge beads. Edge beads can be up to 30-40 times higher than the thickness of the resist film and can greatly decrease the lithographic resolution. Although there exists a class of chemicals called edge bead removers, it may just be enough to have the sides of the wafer wiped off by a swab wet by acetone. In this work,

when needed, a mask is used to expose the sides of the chips, with 1 mm width, leaving the middle part protected. Later, the remaining resist around the sides are carefully cleaned by swap wetting it by acetone. Dark erosion is low enough to use the photoresist film in the next photolithography step.

Different photoresists are used at this step including AZ-5214E, AZ-MIR726 and AZ-1505. In general, for probes having dimensions larger than 1μm, AZ5214E is good enough. However, when ≤1μm crosses are desired AZ-MIR701 or AZ-1505 has to be used. Film thicknesses depend on the viscosity of the photoresist and the spin speed. These two resist have lower viscosity compared to AZ-5214E, thus the thicknesses are smaller after the spin and their edge bead formation are lower. Both resists are designed to fabricate patterns down to ~0.3-0.4μm. Spun samples are prebaked on a hot plate to evaporate the remaining solvent in the resist film and to prevent it sticking to the mask. Then, the chips are exposed with Karl Suss MJB3 mask aligner, aligning them under the appropriate section of the quartz photomask. The mask aligner provides three degrees of freedom, X, Y and θ, to align the sample under the desired pattern. Our mask has no alignment markers, rather the patterns themselves are used for alignment. Contact lithography is used for this step in which the mask has a physical contact with the sample by means of the vacuum between the mask and the sample. Contact lithography has high resolution and high throughput, but the mask is contamination is also high and it may need to be cleaned for sequential use. Mask damage observed after intensive use is another drawback. Exposed samples are then developed by immersing them into the developing solutions. The developing process is stopped by rinsing the samples under deionized (DI) water for several seconds. The pattern transfer to the wafer is done by etching, either wet or dry. Individual process details for the corresponding photoresist used are given in Table 3.1. Etching process is used to separate the pads which forms the Hall cross by removing the active region (2DEG) of the wafer. Hence the depth of etch is determined by the depth of the 2DEG or the quantum well (QW). Wet etchants are usually isotropic. So, side etch has to be considered carefully. Side etch can also be helpful by decreasing the physical dimensions, but it can also completely destroy the

Hall cross. If the shape is not properly defined due to the optical proximity during the exposure, the side etch will enhance the problems in the definition. Optical proximity is a complex phenomena [43]. The easiest way to cope with is to use thinner resist and completely remove the edge beads. Keep in mind that, 2DEG is also depleted a certain distance laterally beyond the physical dimensions set by the vertical etching. The size of this depletion region can be of the order of the depth of the 2DEG [44]. Thus the electrical width of the probe can be smaller than its physical width, which increases the spatial resolution. However, if the depletion is too much and the probe is small, or the electron gas is very deep, than the sensor may not work due to insufficient carrier concentration in the sensor.

Table 3.1: Process parameters of the photoresists used in active area definition

	AZ-5214E	**AZ-MIR701**	**AZ-1505**
Spin Speed & Time	10,000 rpm., 40s	6,000 rpm., 40s	4,000 rpm., 40s
Thickness	~1µm	~0.8µm	~0.5µm
Prebake	50s at 110°C	60s at 90°C	50s at 100°C
Exposure Dose	240mJ	150mJ	150mJ
Post-expose Bake	-	60s at 100 °C	-
Development	KOH based AZ-400K:DI / 1:4	2.8% TMAH based AZ-MIF726 single puddle	2.8% TMAH based AZ-MIF726 single puddle
Hard Bake	2min. at 120 °C	2min. at 120 °C	2min. at 120 °C
Tone	Positive / Image Reversal	Positive	Positive

Dry etch is another option and was usually used for this step during this study. A Leybold LE321 Reactive Ion Etcher (RIE) is available in our Clean Room facility. RIE, an ion assisted etch method, is preferred because it has less undercut, better process control and the isotropy can be controlled. Etching rate and isotropy are dependent on

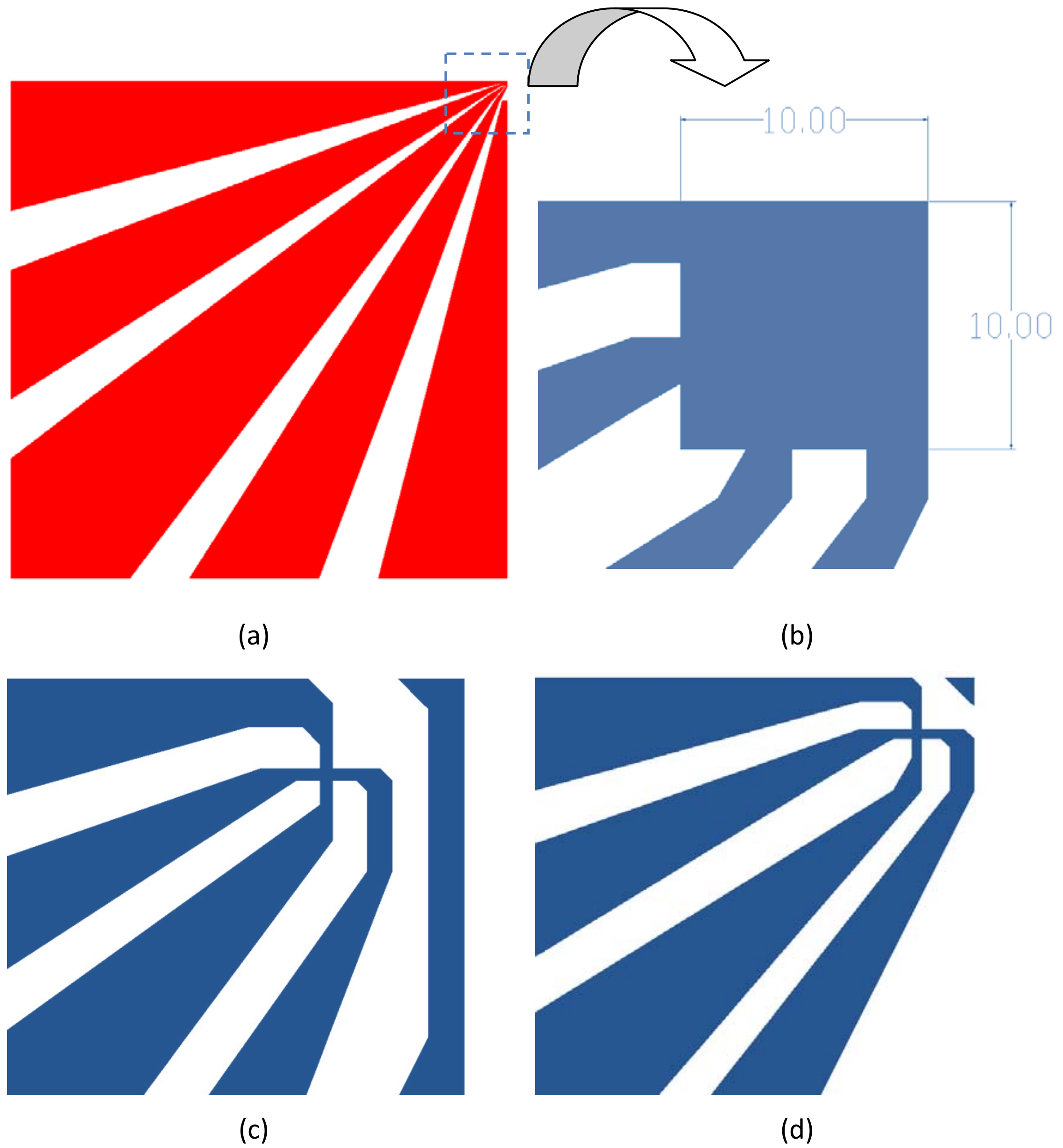

Figure 3.1: Mask designs for Hall cross definition. The whole chip with ohmic pad extensions (a), close up appearance 10μm × 10μm e-beam/FIB template (b), and two different designs of 1μm Hall crosses (c) & (d) are shown. In first generation mask (c), Hall cross and tip separation is 14μm, whereas, in second generation mask (d) this distance is reduced to 8.5μm. The distances are measured from the center of the cross to the mesa corner. Reduction due to side etch is not included.

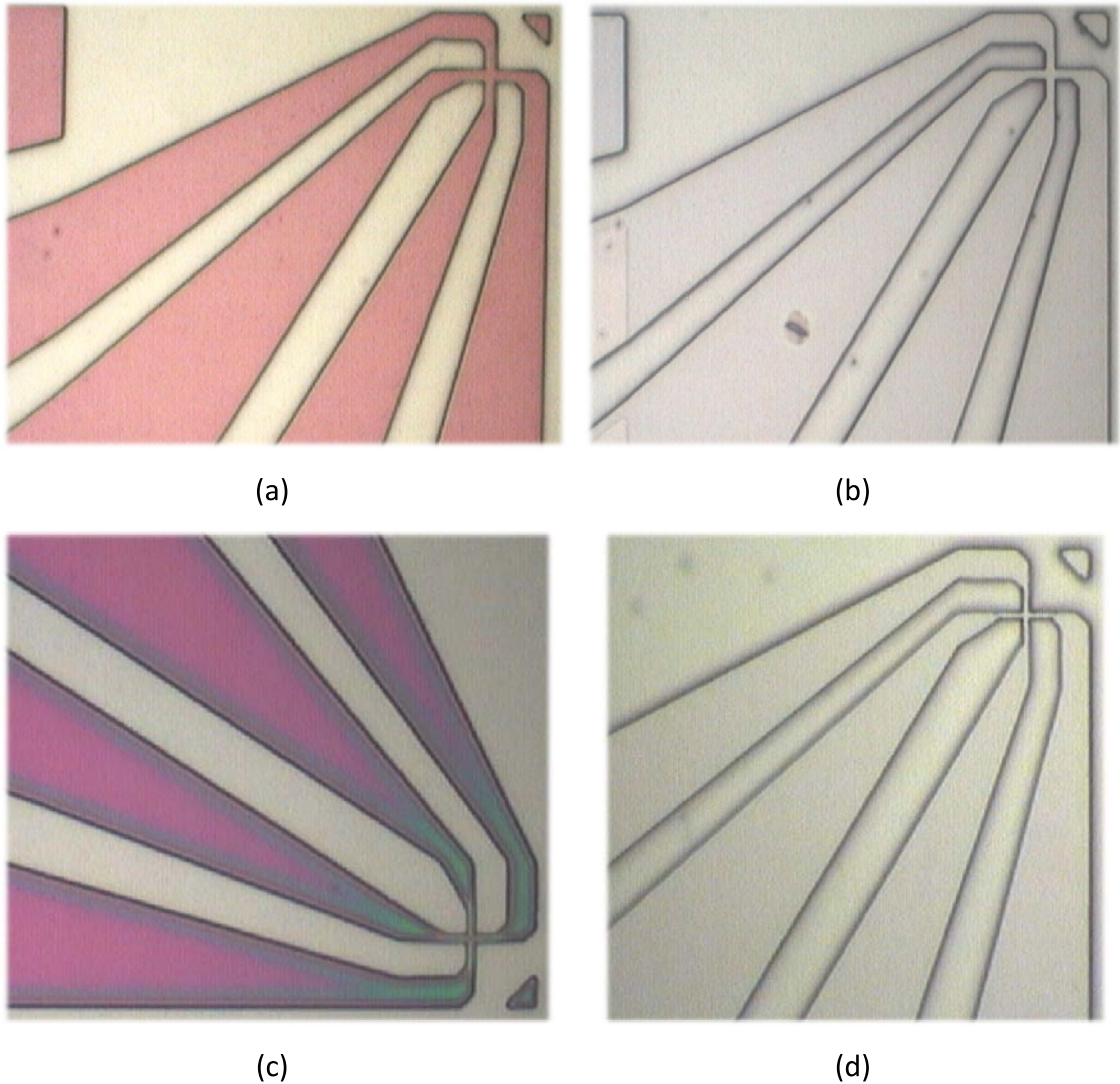

Figure 3.2: Examples of Hall cross definitions. A 1μm Hall probe after the develop (a) and when etched (b) is shown. Similarly (c) & (d) show developed and etched probes, respectively, where the probe size is 0.5μm. Given sizes are physical. 1μm probe defined using AZ-MIR701 whereas 0.5μm one is using AZ-1505. In both cases etching is done by CCl_2F_2 plasma with an etch depth of ~1.2μm

the process pressure of the gas. Low pressure means relatively lower etch rate, however, the anisotropy is high (etch is more physical), and the plasma damage is lower due to

lower kinetic energy of ions. For the thin film materials, the active area definition etch should be done until the substrate is reached. The active area can also be defined by lift-off process. For this case, image reversal of the AZ-5214E is used. A positive resist has positive slope 75-85º. When AZ 5214E is processed to have image reversal, this slope is reversed. Thus, final result will be a negative wall profile ideally suited for lift-off. To have the image reversal, the spun samples are first exposed for 15s at 6mW with mask, baked on the hot plate at 120ºC for 2 minutes and flood exposure is done for 45s.
If the probes will be defined by e-beam lithography, the current and voltage leads must still be electrically isolated from each other. These pads become wide towards the sides of the chip, so that, they provide enough space for bonding. It is not practical to define a huge area with e-beam. Therefore, this separation should again be done using optical lithography. This procedure also defines an area small enough to further pattern with e-beam or Focused Ion Beam (FIB) lithography.

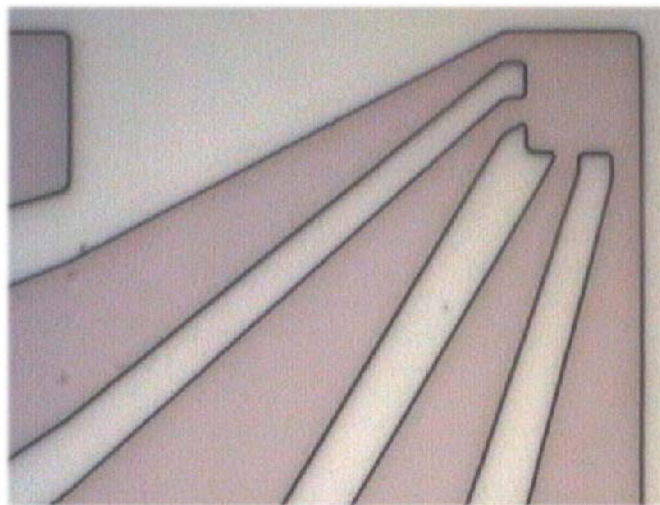

Figure 3.3: A 10μm × 10μm area isolated by etching for further e-beam process. The four pads have to be separated further until a Hall cross with desired size is obtained. The isolated lead, which appears on the upper left side of the image, is the tip pad. If needed it has to be connected to the corner of the active region where an isolated tip can be fabricated.

3.4 Mesa Step Definition

To scan with high resolution the probe must be in the closest position to the sample. In other words, the active area of the probe must be as close as possible to the specimen surface. To maintain this, a mesa is defined with optical lithography, whose corner serves as a crude STM or AFM tip. Hall probe chip is tilted by 1-1.5º with respect to the sample, prior to scan, to ensure the mesa corner is in the closest point to the specimen. The depth of the mesa etch should be such that no part of the chip must be closer than the corner of the mesa after the desired tilt.

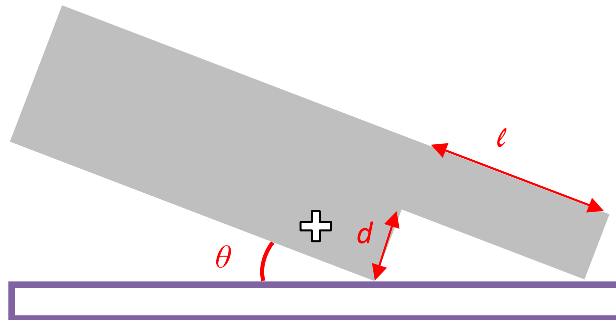

Figure 3.4. Schematic representation of Hall probe alignment.

The required depth of the mesa etch can be calculated considering the parameters given in the Figure 3.4, where l is the length of the wafer remained after the individual chips are diced off the die, d is the depth of the mesa and θ is the inclination of the probe with respect to the sample. Usually $l \leq 30\mu m$ and $\theta \leq 2^{\circ}$. From the same figure we see that $d > l \times tan\theta$ condition must be satisfied to have the mesa corner at the highest position. Accepting these maximum values, d_{min} is ~1µm. For the fabrications, depth of mesa etch was around 1.5µm.

For this step, AZ-5214E is spun at 6,000 rpm, resulting in a thickness around 1.3µm. Prebake is done on a hotplate at 110ºC for 50s. Exposure is performed to maintain a

dose level of 240-300mJ and, developed in 1:4 mixture of AZ-400K:DI. Hard bake is done at 120ºC for 2 minutes. Samples are then etched either by wet etchant using H_2SO_4, H_2O_2 and DI mixture with a ratio 1:8:40 or with RIE. Used etchant has an etch rate of ~25nm/min. at 25ºC. To have a stable etch rate over time first, DI and acid are mixed and left for stabilization. As this mixture is exothermic, immediate addition of peroxide right after the acid in water decreases the peroxide concentration in the mixture which, decreases the etch rate as well. The peroxide added after 10 minutes and the solution left over for another 10 minutes after stirred well. When the wet etch is performed, the side etch also has to be considered, due to its isotropic nature. Two different masks, optimized with respect to the type of etch, wet or dry, have been used.

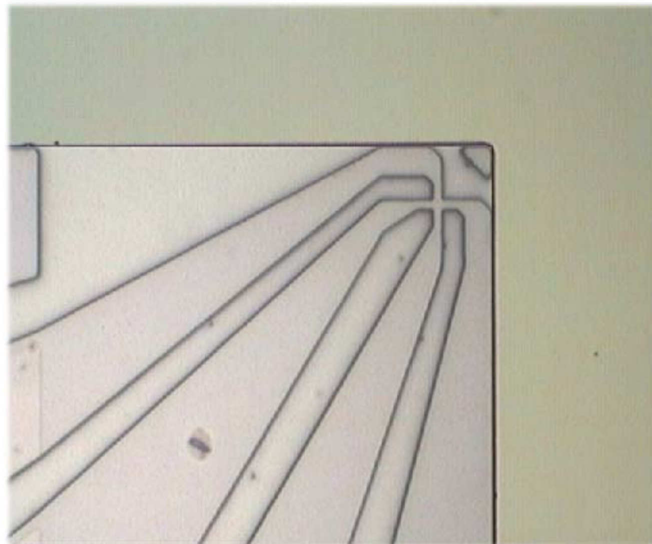

Figure 3.5: Mesa etch.

3.5 Recess Etch

When the probes are aligned while they are upside down, there is a possibility of bond wires to touch the surface and short circuit the signals. To prevent this, sides of each individual chip has to be deeply etched. The process steps are:

1. Spin AZ-5214E at 6000 rpm, for 40s,
2. Soft bake on a hot plate at 110ºC for 50s,
3. Expose for 60s at 5mW power,
4. Develop in 1:4 mixture of AZ-400K:DI
5. Hard bake at 120ºC for 2 min,
6. Immerse into HCl, H2O2, DI (4:10:55 by volume) mixture, for 1hr,
7. Rinse under DI for several seconds,
8. Clean with acetone and isopropanol.

As the etch time is long, the area around the Hall cross is further covered by photoresist, simply by placing a small drop using an injector. The mask shown in Fig. 3.6a is in zig-zag shape to prevent the undercut as the etch rates are different in different crystallographic directions, which results in different slopes. The etch depth is ~55µm after 1 hour. The bonding is later done on these lower parts of the edge after the Ohmic contacts.

3.6 Ohmic Contact Metallization

Ohmic contacts are necessary in order to have electrical connection to the active area. However the contact has to be done away from the active region in the sense that the operated region is not affected by the effects of annealing the contacts. In other words the contact must not, in any way, play role in the operation of the device, in our case the Hall sensor. Placement of a metal in intimate contact with a semiconductor does not necessarily show an ohmic behavior. It may be necessary to have the metals directly in contact with the regions of the semiconductor having the high doping density. These layers can be several tens of nanometers below the surface. To reach these layers the metals must be diffused by thermal means. Impurity type, that is the doping type, has to be considered while choosing the metal. AZ-5214E, being the only image reversal

photoresist available, is used. Negative wall slope obtained by reversal help to lift off the resist covered parts. Another, possible method, for easy lift off without image

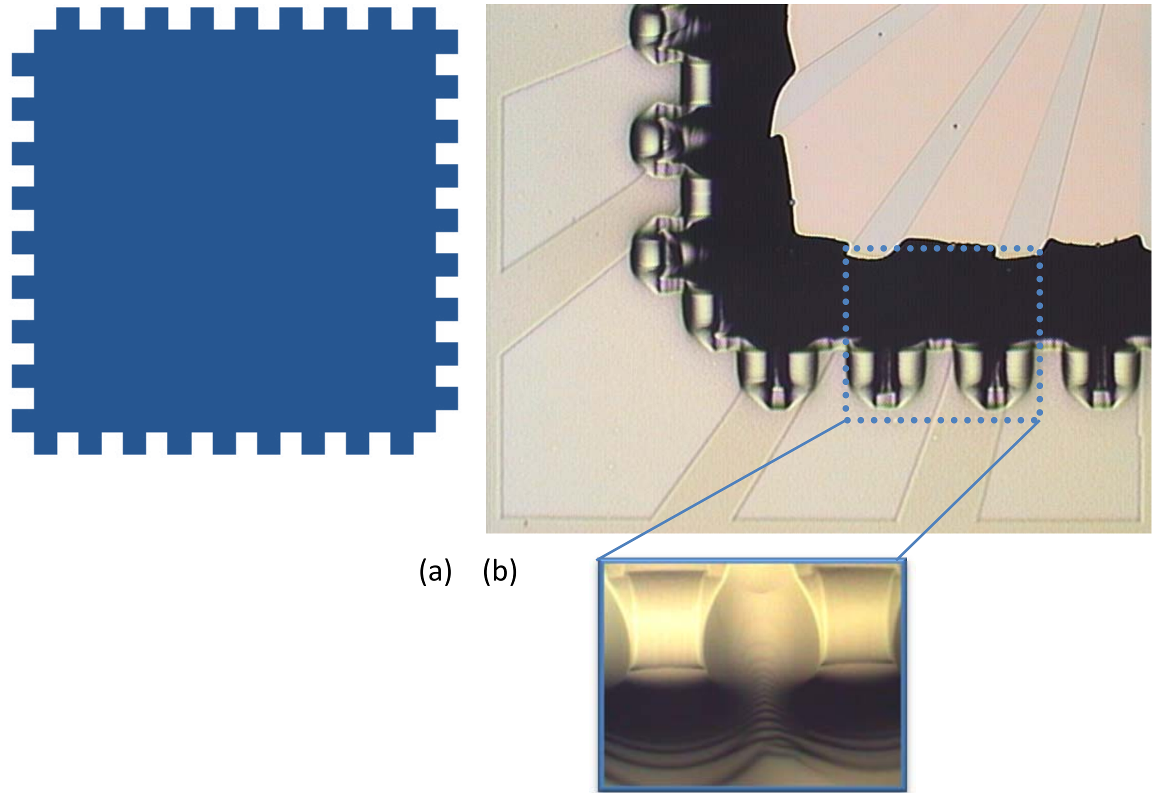

Figure 3.6: Recess etch mask design (a), and etched wafer (b).

reversal, is to immerse the samples in chlorbenzol for several minutes prior to development. Chlorbenzol hardens the top part of the photoresist film. While developing hardened parts has lower dissolution rate, which creates a mushroom like shape around the edges of the pattern allowing the developer to penetrate relatively easier. Similar hardening can also be obtained by a very short flood exposure before the real exposure done by the mask. Cleaned samples are spun at 6000 rpm for 40s, soft baked at 110ºC for 50s. After proper alignment exposure done for 15s at 6mW, image reversal bake performed at 120ºC for 2min. and finally flood exposure done for 45s. Exposed samples are developed in 1:4 ratio AZ-400K:DI, rinsed with DI to stop the

development and blown dried by nitrogen. Samples are immersed in to HCl solution diluted by DI with volumetric mix ratio of 1:5, for a few seconds, to clean the native oxide of the wafer, which may decrease the Ohmic contact quality, rinsed and then blow dried. All samples are placed on a microscope slide using vacuum compatible polyimide 3M tape and loaded carefully in to Leybold L560 thermal evaporator, ensuring they are parallel with respect to the boats. Evaporation materials are placed in tungsten boats whose thicknesses are 125μm. Only two materials can be evaporated in a single run. The deposition chamber is pumped down to $\sim 4\times10^{-6}$ mbar. Deposition parameters, evaporation rate, final thickness etc., set on Inficon deposition controller. Current directed to the desired boat while the sample is not on that particular boat. Time allowed not contaminate the samples while the possible organic remnants are burnt and degassed first. Sides of the holder are masked with aluminum foil to further protect the samples from cross contamination since the system has no shutter. When the desired evaporation rate reached the holder automatically brings the sample over the boat, which can be done manually too. Evaporation rate monitored with 6MHz crystal oscillator connected to the deposition controller. When the evaporation is finished the chips are taken out and immersed into acetone immediately for the lift-off. Acetone dissolves the resist that masks the areas where no metal is wanted and the metal on top of that resist film goes away. The process can be enforced or fastened up by squirting a stream of acetone with an injector. The rule of thumb for an easier lift of is, not to exceed the total metal film thickness, more than 1/3 of the photoresist thickness. In the worst case, ultrasonic agitation can also be applied. However, this is not the best option and must be done very carefully. In the case where the gold is the Ohmic metal, a thin layer (~5-10nm) of Ti or Cr is evaporated to increase the surface adhesion. It has been observed that, during the fabrication, Cr has better adhesion properties than Ti, probably due to the fast oxidization of Ti even while we were evaporating it.

If the recipe does not contain a rapid thermal process (RTP) step after the Ohmic contact metallization, next step can begin. RTP is done under inert gas environment to prevent oxidation. In this work N_2 or 95%N_2 + 5%H_2 mixture is used. Due to different

diffusion rates of materials in multilayer contacts, voids may be generated, which is the evidence of material loss. In addition, the spike formation increases the surface roughness. This effect is known as Kirkendall effect (Fig. 3.7b) [45]. A nickel layer, known as wetting layer evaporated on top of the Au/Ge used for GaAs 2DEG contacts for instance, with 10-30nm thickness, reduces the bubble up formation and helps alloy to diffuse.

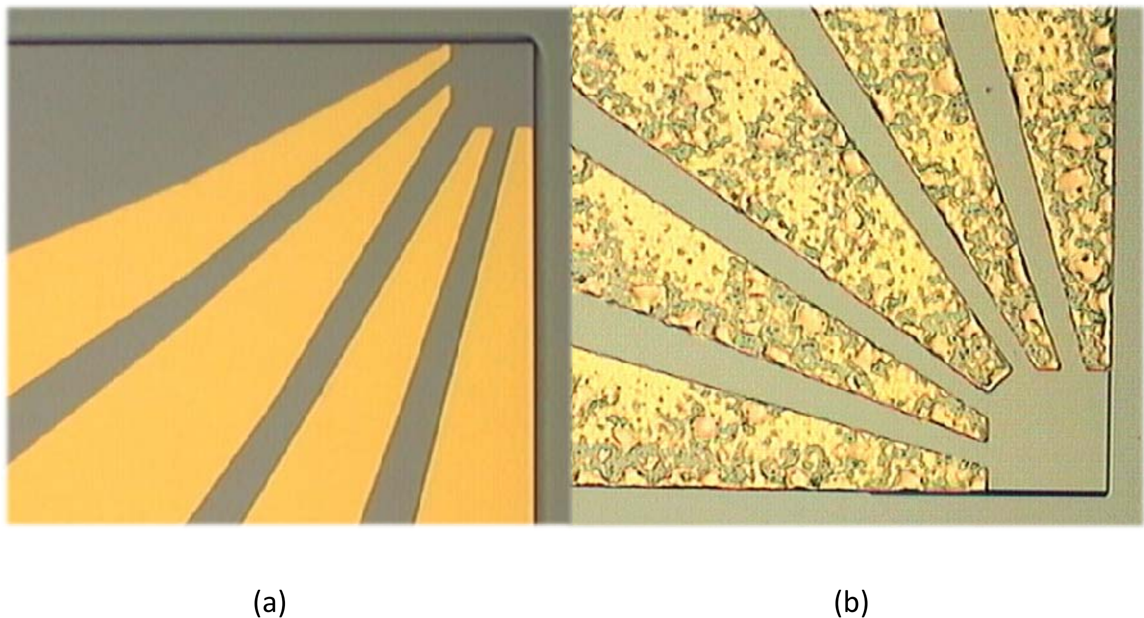

(a) (b)

Figure 3.7: Ohmic contacts without (a) and with (b) RTP. The Kirkendall effect after RTP can be seen in part (b). The RTP process was done at 450ºC for 45 sec under forming gas (95%N_2, 5%H_2) environment. An Ohmic metallization was done to a 2DEG HEMT GaAs sample evaporating 27nm Ge/ 54nm Au/ 6nm Ni /100nm Au.

3.7 STM Tip Metallization

If STM feedback is chosen to bring the sensor into close proximity of the sample, the corner of the mesa step is turned into a crude STM tip. The designated part of the corner, which is electrically separated from the Hall cross, is covered by a thin layer of

gold. The fabrication starts by spinning AZ 5214E at 6000 rpm. Aligned wafer is exposed for 45s at 6 mW and developed. Following the similar steps of ohmic contact metallization 10nm Cr / 50 nm Au is evaporated to define the tip.

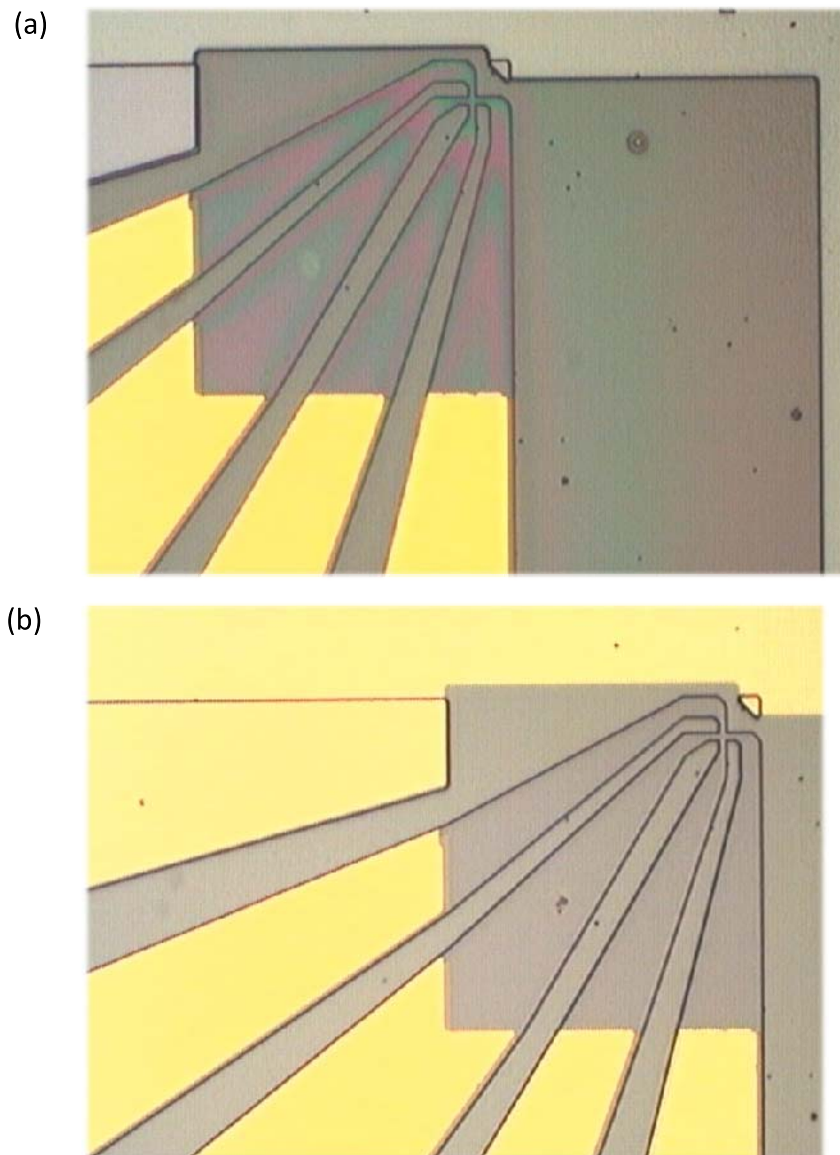

Figure 3.8: Tip definition lithography (a) and the tip after lift-off (b) 10nm Cr /50nm Au evaporated for the tip. Connection between the tip lead and the tip is maintained via mesa etch.

3.8 Metallization for Bonding

Sometimes, it might be necessary to further coat the pads with gold to make the wire bonding easier. This is usually needed if the metal is diffused too much after RTP and bonding is difficult. There is no need to cover all the pads again with metal it will be enough to process the regions of the where the bonding is done. For that purpose the mask shown in Fig.1 is designed. That step is optimized according to image reversal exposure of AZ5214E.

3.9 Packaging

When the fabrication process is completed, the wafers are diced in to individual chips. To do this, chips are spun by photoresist for protection, placed on a UV curable tape and placed on the vacuum chuck of the Disco DAD321 dicer. Right after the optical camera assisted adjustment, wafers are diced all the way down. The piece of tape, which has the diced chips, is exposed to UV light to release the chips. Separated chips are then cleaned by acetone, followed by isopropanol and finally blow dried by nitrogen. They are later inspected under zoom microscope against any problems. Individual chips are then placed on a non magnetic sensor holder made from gold plated printed circuit board (PCB).Gluing is either done by super glue or a low temperature compatible epoxy. An ultrasonic wedge bonder is used to connect the pads to the PCB. Bonding is done from the chip to the PCB pads in order not to damage the chip with excess power applied to break the wire. Gold wires having 12µm diameter are used. Tested chips are stored in vacuum or inert gas desiccators.

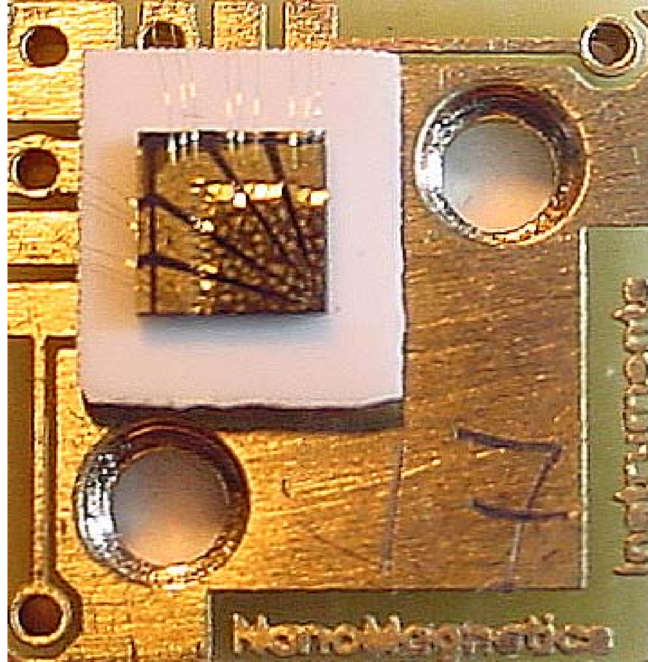

Figure 3.9: Diced & packaged Hall probe.

3.10 GaN Hall Probes for SHPM

Some parts of the thesis work discussed in this section is accepted for publication, “Variable Temperature-Scanning Hall Probe Microscopy (VT-SHPM) with GaN/AlGaN Two-Dimensional Electron Gas (2DEG) Micro Hall Sensors in 4.2-425K range, Using Novel Quartz Tuning Fork AFM Feedback”, R. Akram, M. Dede, and A. Oral in IEEE Transactions on Magnetics, Institute of Electrical and Electronics Engineers, Inc.

3.10.1 Introduction

The developments in technology find many applications in our everyday life by introducing practical devices that are even not dreamed a few decades ago. Nowadays,

carrying a cell phone or using a high speed wireless internet spot is something usual. The era started by the semiconductor device technology makes all these to happen. Although today's telecommunication devices relies on the Si and GaAs based materials [46] it has been estimated that the developments in high power, high frequency electronics devices and the demands presented by the military applications shows that wide bandgap materials, like GaN, will be dominating in production [47]. GaN appear to be one of the most promising materials for applications in high frequency and power electronics because of the structural and electronic characteristics. Its high breakdown voltage and high power density, high temperature tolerances and high thermal conductivity are the first few properties that can be listed [48, 46]. These general properties lend themselves to exploitation in nearly any electronic device with special applications in high power electronics, high frequency applications and use in hostile conditions (such as high temperature probes). Commercial GaN based LEDs and Lasers are currently available, more devices will become available in the future.

GaN has been chosen for fabrication of Hall probes, mainly because its active layer is only 20nm below the surface, which gives opportunity to reduce the size of the Hall probes. Another attraction was its high heat resistance and physical strength.

3.10.2 Fabrication

The AlGaN/GaN two dimensional electron gas (2DEG) material semiconductor wafers used in our experiments are grown by rotating disc MOCVD on Si (111) [49]. The structure of the wafer, as shown in Fig. 3.9 starts with a high resistivity Si (111) substrate with a resistivity of 10 kΩ-cm. On top of this substrate, first, proprietary stress mitigating transition layer of 1.1μm is grown in order to minimize the stress and cope with the lattice mismatch. This is followed by 1μm thick layer of undoped GaN, which forms a 2DEG at the interface of $Al_{0.26}Ga_{0.74}N$ layer. Finally, a cap layer for protection purposes composed of thin (20Å) layer of GaN is grown on the wafer. The room

temperature sheet carrier concentration and electron mobility of the 2DEG induced at the heterointerface are 2 x 10^{12} cm^{-2} and 1,500 cm^2/Vs, respectively.

Micro Hall probes with effective dimension of 1μm x 1μm have been fabricated using optical lithography in a Class 100 clean room environment. Device fabrication process consists of the following steps which are:

1. Hall Probe Definition: Definition of active "Hall cross" patterned by reactive ion etching (RIE) using CCl_2F_2 gas plasma. 5 mm x 5 mm pieces of the material are spun by AZ 5214E resist at 6000 rpm for 40s, exposed to 200 mJ and developed in AZ400K:DI (1:4) solution.
2. Formation of the Mesa: Samples are spun by AZ 5214E resist at 6000 rpm for 40s, exposed to 200 mJ and developed in AZ400K:DI (1:4) solution. 1.2-1.5 μm depth is obtained by CCl_2F_2 gas plasma.
3. Ohmic Contact Metallization: Thermal evaporation of Ti/Al/Ti/Au to get the Ohmic contacts; followed by rapid thermal processing (RTP) in a nitrogen atmosphere at 850°C for 30 sec. right after the lift off done by immersing samples in acetone.

In this study 32.768kHz Quartz crystals tuning forks with dimensions ($l \times w \times t$) of prongs are, 3.81mm × 0.34mm × 0.62mm resulting in stiffness of 29 kN/m, have also been used. In order to integrate these force sensors in SHPM for AFM feedback, they are extracted from their cans and the leads have been replaced with a non magnetic wiring. Furthermore these Quartz tuning forks are glued, by super glue, to a 10mm × 10mm printed circuit board sensor holder, compatible with the scanning head of the SHPM system, with one prong free configuration. Wiring is done by 12μm gold wires using an ultrasonic wedge bonder. The wires are carefully placed not to touch the quartz crystal tuning fork leads. Details of the operation of Quartz Crystal feedback SHPM is described in the preceding chapters.

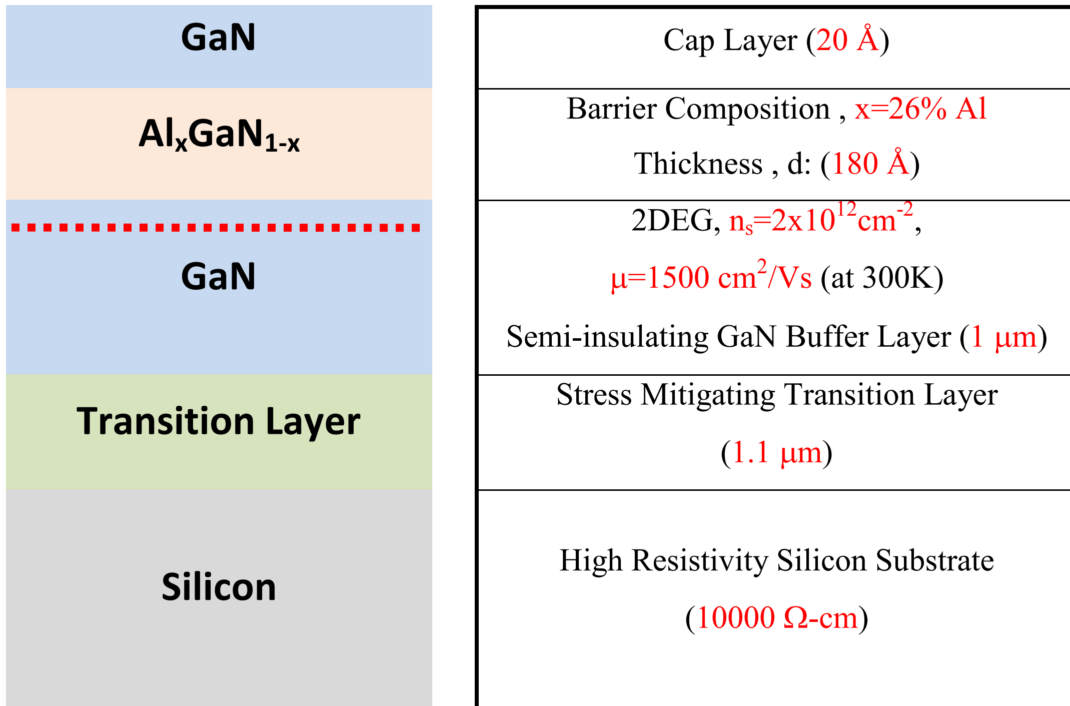

Figure 3.10: Schematic diagram of the layer configuration of the AlGaN/GaN heterostructure used

3.10.3 Characterization

The physical limitations introduced by the elevated temperature are one of the strongest motivations for switching to wide band gap materials. As the temperature is increased the thermal degradation mechanism starts to diminish the functionality of the Hall devices. Any semiconductor is consists of free charge carriers even if there is no dopant atoms added during the growth. Thus under any circumstances there will be thermally excited electrons and holes in the lattice. These are called the intrinsic carriers and their concentration is related to the temperature as given in the Eq.3.1 [50].

$$n_i = \sqrt{N_C N_V} e^{-E_G/2k_B T} \tag{3.1}$$

where N_C and N_V are the effective electron and hole density of carriers, respectively in inverse cubic centimeter (cm^{-3}); E_G is the bandgap energy of the semiconductor in electron volts (eV), k_B is the Boltzmann constant (8.62×10^{-5} eV/K) and T is the temperature in Kelvin (K). Hence the intrinsic carrier concentration computed in terms of cm^{-3}. From this basic formula it is possible to predict that at any given temperature the free carrier concentration of a wide bandgap semiconductor having bandgap energy of ~3 eV, like SiC or GaN; will be smaller than of the silicon whose bandgap energy is 1.1 eV.

Usually the silicon wafers have doping densities of 10^{14} to 10^{17} cm^{-3}. These values are far larger than the room temperature intrinsic carrier concentration which is around 10^{10} cm^{-3}. However, as the temperature goes beyond 300K, concentration of these intrinsic charge carriers will start to increase or comparable to the device doping levels. As the doping levels are selected according to the specific needs of the device, this increase will start to violate the design rules and the device will become useless or its sensitivity will be decreased.

Another important drawback of the temperature increase will show itself due to the increase in the thermal vibration energy of the lattice atoms. As the thermal vibrations increase the possibility for a carrier to collide with the lattice, namely the lattice scattering will also increase. That will lead to a significant decrease in carrier mobility. Consequently, decrease in mobility will increase the resistivity and the amount of the maximum current will be decreased accordingly, reducing the sensitivity further.

The temperature dependent characterization of the 1µm sized GaN probes are done over a wide temperature range starting from 4.2K temperature up to 150ºC. Another study [51] shows some characterization results using 100µm sized probes up to 600ºC starting from room temperature. In this work characterization for magnetic response is done by applying external magnetic field with a coil and by measuring the Hall Voltage response to this known field strength. The value of Hall coefficient, R_H is obtained from the slope of the magnetization (B-H) curve. As shown in Fig. 3.11, value of R_H also depends on the Hall current and two regimes can be formed in terms of the applied current bias (I_H).

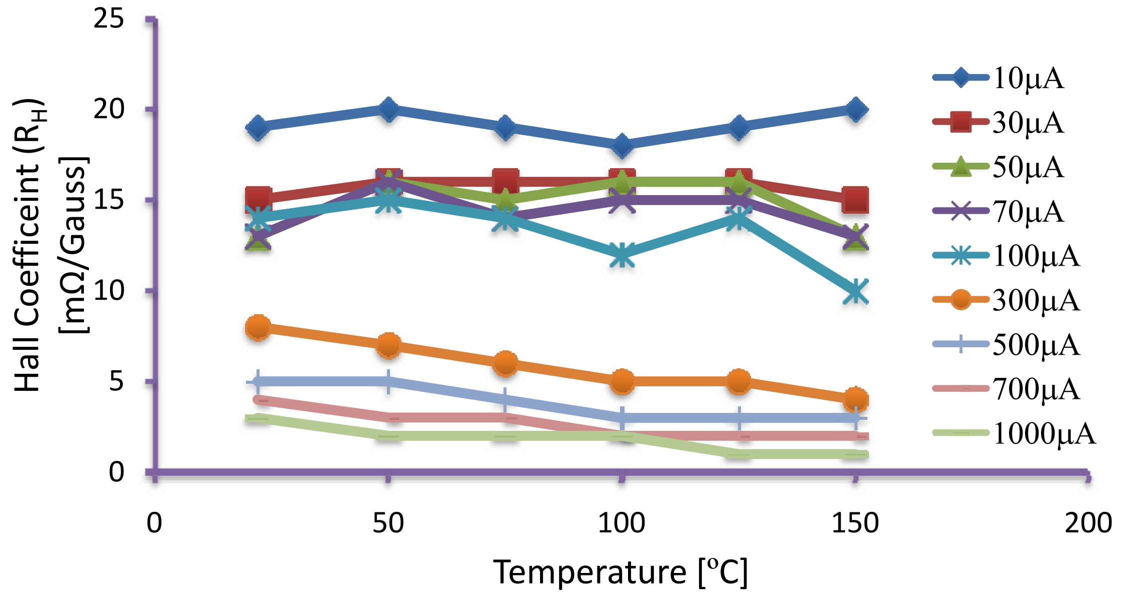

Figure 3.11: Effect of Hall current on Hall coefficient, R_H., as a function of the temperature.

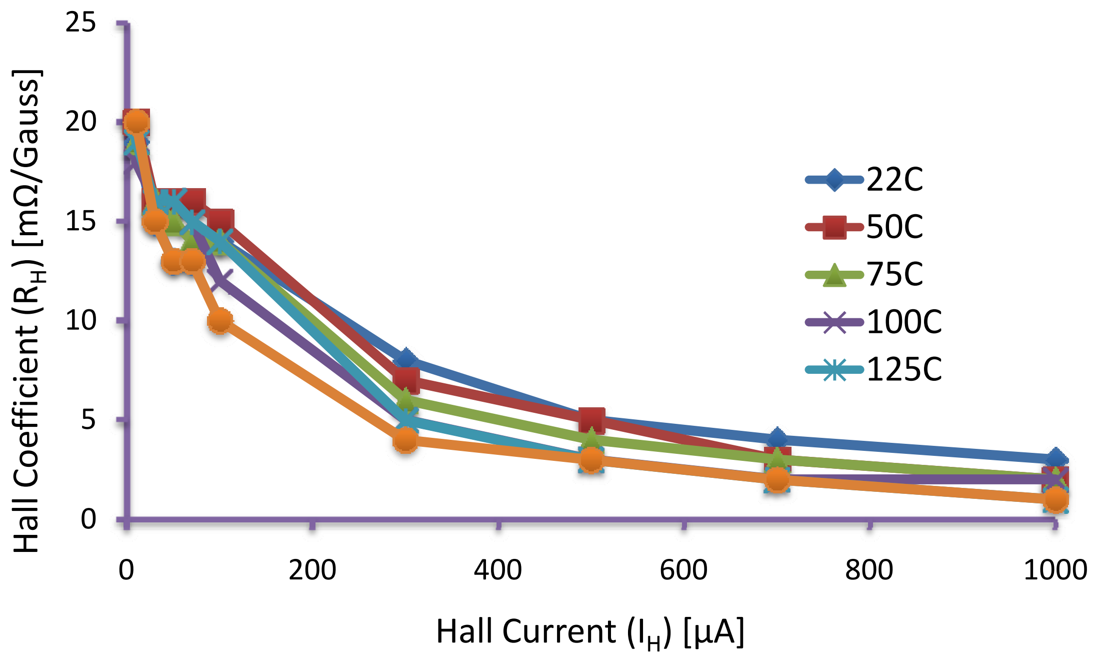

Figure 3.12: Effect of Temperature on Hall coefficient, R_H. as a function of the Hall current, I_H.

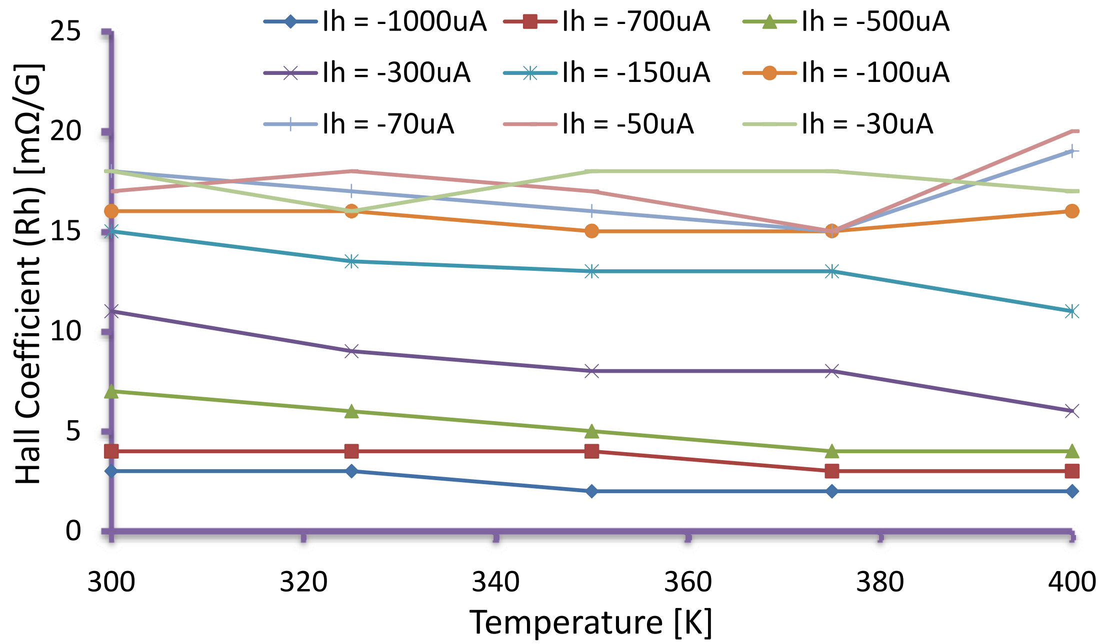

Figure 3.13: Hall coefficient for negative drive currents at high temperatures.

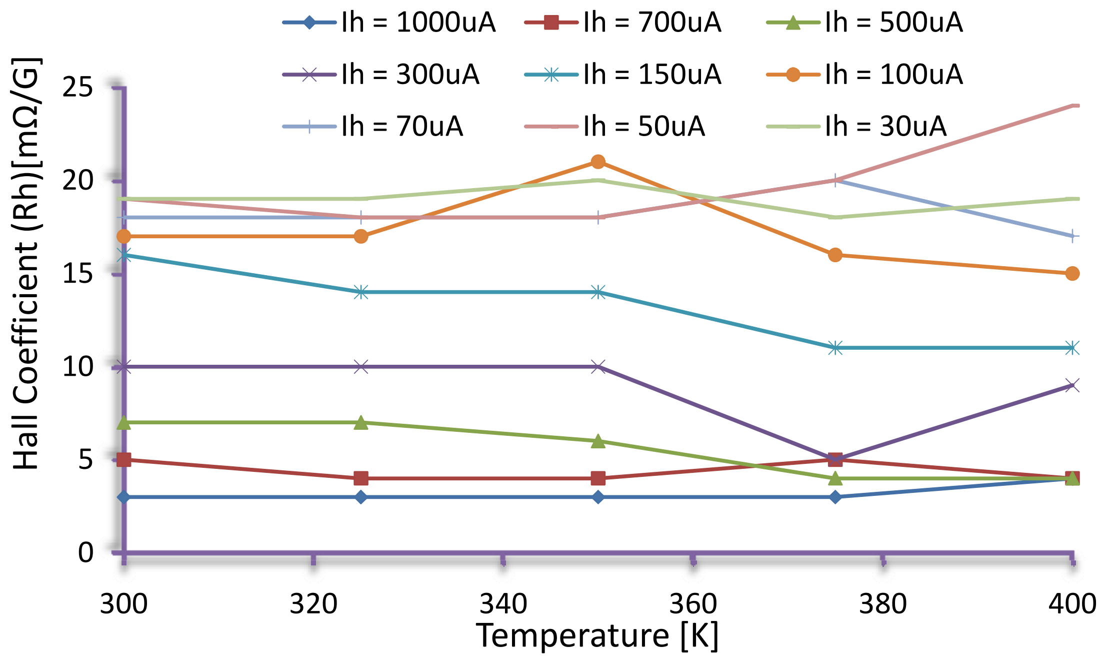

Figure 3.14: Hall coefficient for positive drive currents at high temperatures

At high Hall current bias, R_H is more affected by the temperature. This is more significant with the current values over 100 μA. (Fig. 3.12). The detailed inspection of the Hall coefficient at elevated temperature values can be seen for both negative and positive Hall current values as shown in Fig. 3.13 and Fig. 3.14 respectively.

Dependence of Hall voltage (V_H) is also examined with respect to the Hall current (I_H) by varying the temperature from 22ºC to 150ºC. As shown in Fig.3.15, linear relations can be observed between V_H vs. I_H characteristics. As the same external magnetic field is applied, all the time of the measurement, the change in the linear relationship between the passed current and gathered Hall voltage is govern by the Hall coefficient. It is observed that two different regions of slope exist. One can define a dynamic resistance, $r_{H,}$ mimicking the ohms law, which is the slope of V_H vs. I_H curve, $r_H \triangleq V_H / I_H$. At 300K as shown in Fig. 3.16, dynamic resistance of low current, $I_H < 100\mu A$, regime r_{HLC} is 510Ω and dynamic resistance of high current, $I_H > 100\mu A$, regime r_{HHC} is found to be 62Ω. It is speculated that this decrease in the r_H value is due to that there might be opening of new conduction channels by applying high current causing an increase in the number of parallel paths. This has been further investigated by increasing the temperature. An increase in temperature from 300K to 425K shows that r_{HLC} increases by 29.4% and r_{HHC} decreases by 50% which further supports the previously stated argument that the increase in the number of channels by increasing Hall current (Fig. 3.16). The noise spectral density measurements of GaN Hall probes are given in Fig. 3.17; where, an increase in white noise level can clearly be seen. Increase in the bias current cause an increase in the number of carrier which adds more noise due to Joule heating in the Hall sensors.

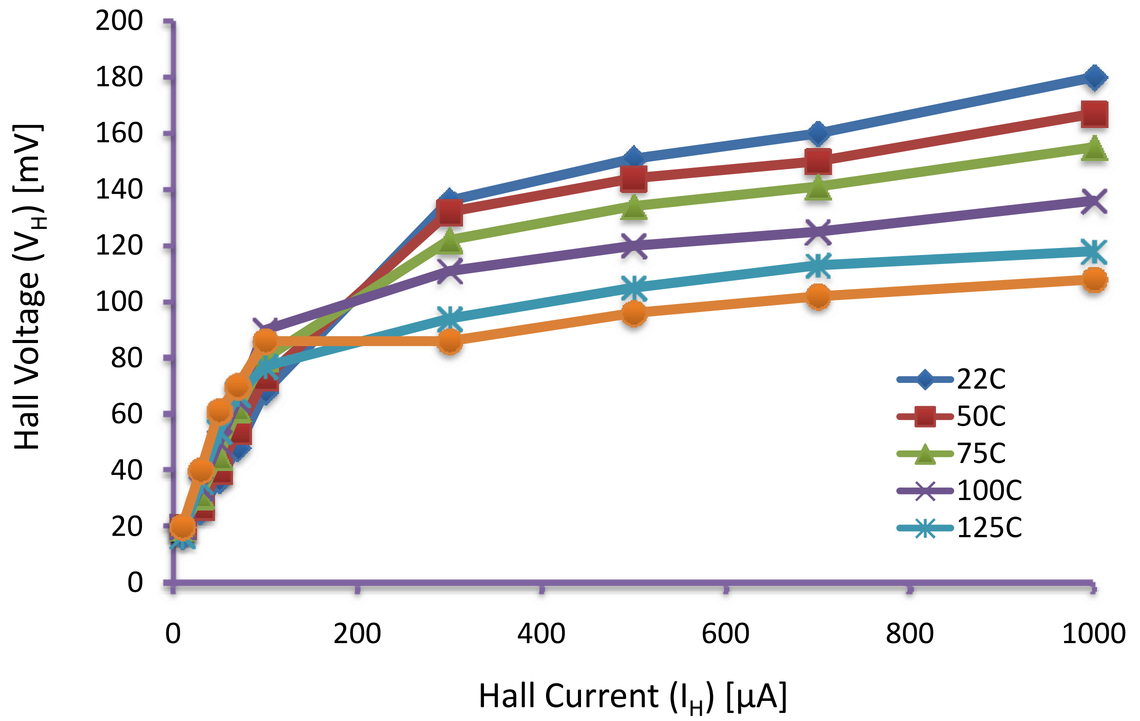

Figure 3.15: Hall voltage (V_H) is measured as a function of Hall current (I_H), varying the temperature from 22ºC to 150ºC

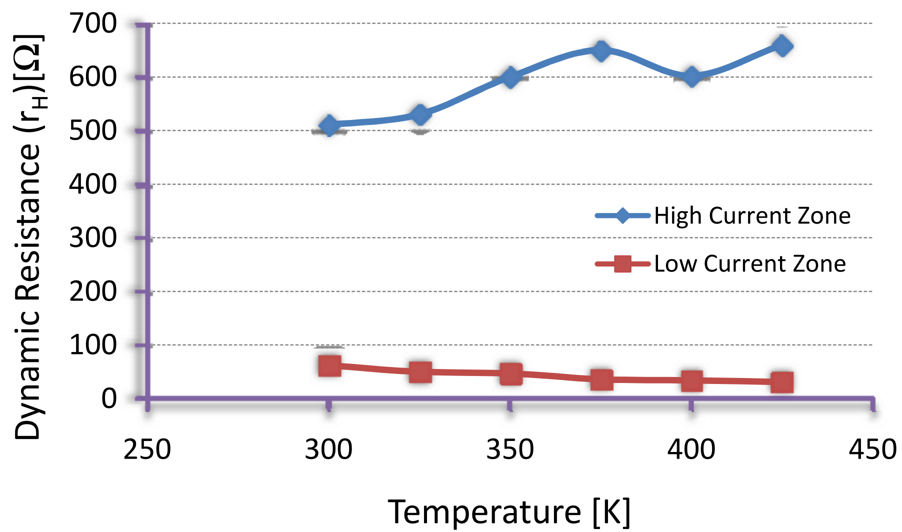

Figure 3.16 Effect of temperature on the dynamic resistances for low current (r_{HLC}) and high current (r_{HHC}) regions.

3.10.4 Experiments

During the experiments, the scanning sensor remains at high temperatures for long period of times. Run time effects on V_H vs. I_H and R_H vs. I_H characteristics under high temperature environments have been investigated. The results showed no significant change in the values, (Fig. 3.18) suggesting a safe use of these Hall probes in scanning systems over a long time in harsh conditions. The Hall coefficient is decreased with the

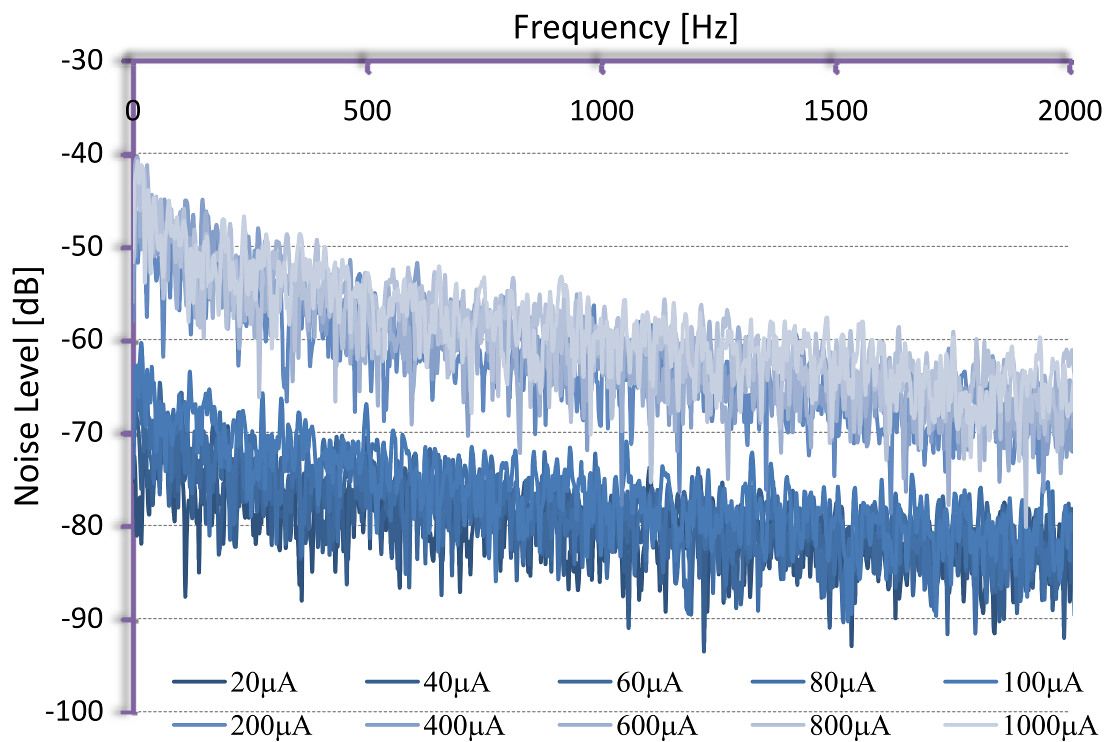

Figure 3.17: Noise power spectrum of GaN probes at 300K for different drive currents.

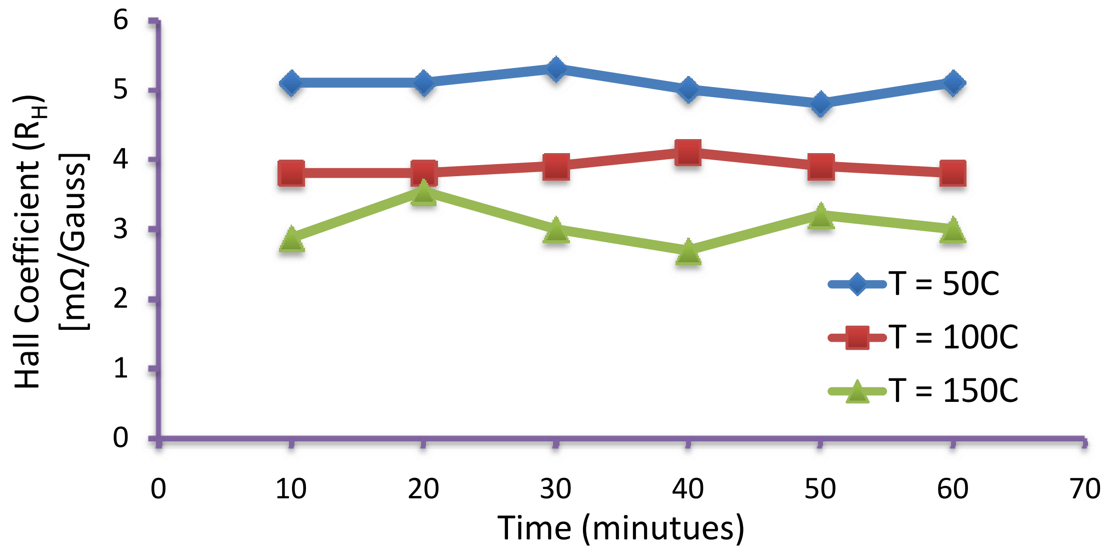

Figure 3.18: Hall coefficient stability over time at different ambient temperatures

increased temperature due to the increase in the effective carrier density due to the inversely proportional relation. The response measured through the sensor, that is, the Hall voltage generated by the externally applied magnetic field is also decreased by increasing the temperature. This is mainly due to the increase in serial resistance and consequential increase in thermal noise (Johnson noise) and the decrease in the Hall coefficient (Fig. 3.19 & Fig. 3.20).

Hall sensor is lithographically positioned 12µm away from corner of a deep etch mesa, which serves as a crude AFM tip. During the scan the sample is tilted ~1°- 1.5° with respect to Hall probe chip ensuring that the corner of the mesa is the highest point. The sensor assembly is dithered at the resonance frequency of the tuning fork with the dedicated split section on the scan piezo tube and controlled using a digital Phase Locked Loop (PLL) circuit. The frequency shift Δf, measured by the PLL circuit is used for AFM feedback to keep the sensor sample separation constant with the feedback loop. As the combined sensor approaches to the surface, the resonant frequency of the sensor shifts due to tip sample interaction.

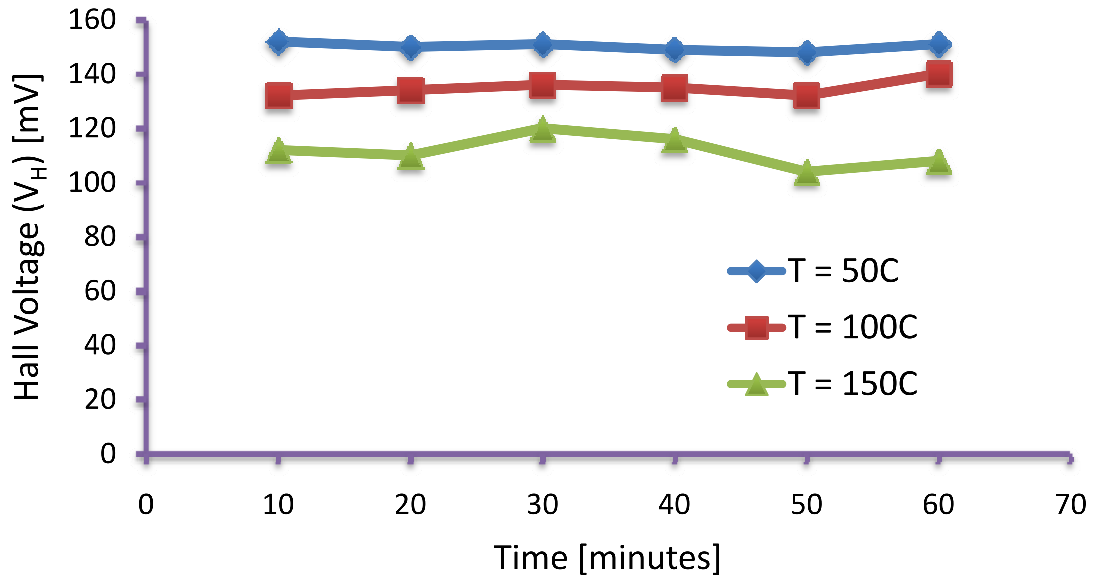

Figure 3.19: Hall voltage stability over time at different ambient temperatures.

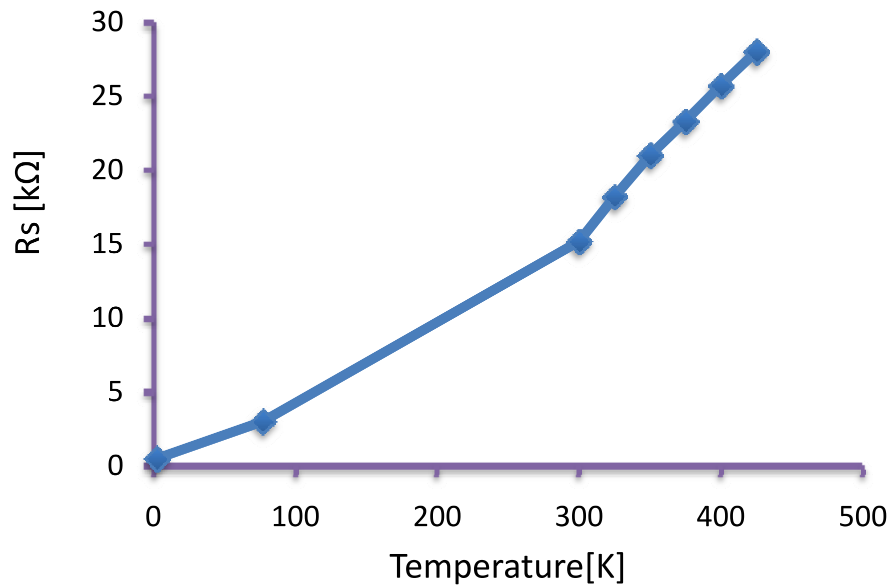

Figure 3.20: Serial resistance measured at different ambient temperatures.

In order to scan at low temperature the microscope is mounted in to a stainless steel tube that serves as variable temperature insert (VTI), which is flushed several times and filled with 1-1.5 Atm of helium gas at 300K, which serves as heat exchange gas, and cooled down to 4.2K gradually at a rate of ~3K/min. simply by slowly dipping in to the dewar. The Hall sensor was driven with 500μA DC current and the series resistance of the Hall sensor was 0.5kΩ, The resonance frequency and the quality factor were 17,780 Hz and Q~60 at the indicated temperature. Experiments at 77K were also performed applying similar preparation conditions, except liquid nitrogen was used as a cryogen. LN_2 experiment performed separate from LHe, mainly because of the cost of the LHe and practical difficulties in temperature control. The resonance frequency and the quality factor were 17,630 Hz and Q~97, and 16,944 Hz and Q~305 at 77K and 300K, respectively.

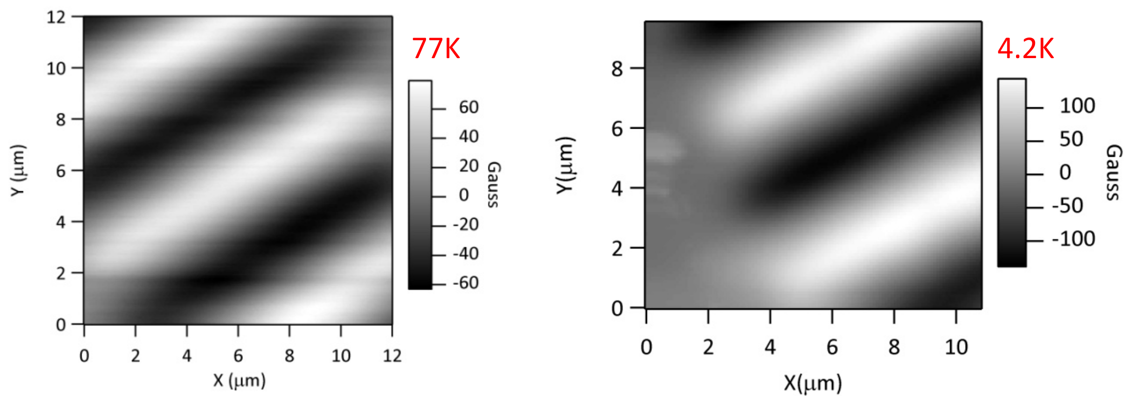

Figure 3.21: SHPM image of hard disk sample at Liquid helium temperature (4.2K) & Liquid Nitrogen Temperature (77K) obtained with GaN Hall probe.

In order to investigate the high temperature operation of these GaN micro Hall probes, a low noise heater stage has been embedded in to the LT system. This stage is obtained simply winding a wire non-inductively around the aluminum sample holder. However, the wire is twisted prior to the winding in order to cancel the magnetic field generated by the coil. Heat profile of the coil and the attached sample holder is first calibrated

with respect to the passed current using a DS600 analog temperature sensor, which has accuracy of 0.75ºC in the temperature range of -40ºC to 125ºC.

As R_H is high at low currents one can argue that the experimental results would be better if the applied current is set to a lower value instead of 500 µA. However, if compared carefully, increasing the applied current from 10µA, where R_H is 19mΩ/Gauss, to 500µA where R_H is 5mΩ/Gauss, at room temperature, comes a 98% increase in current where as decrease in R_H is just ~74%. Hence there is an overall gain in Hall signal at high bias currents! Therefore, it was useful to use high currents rather than low currents as the aim was to increase the sensitivity of the SHPM system.

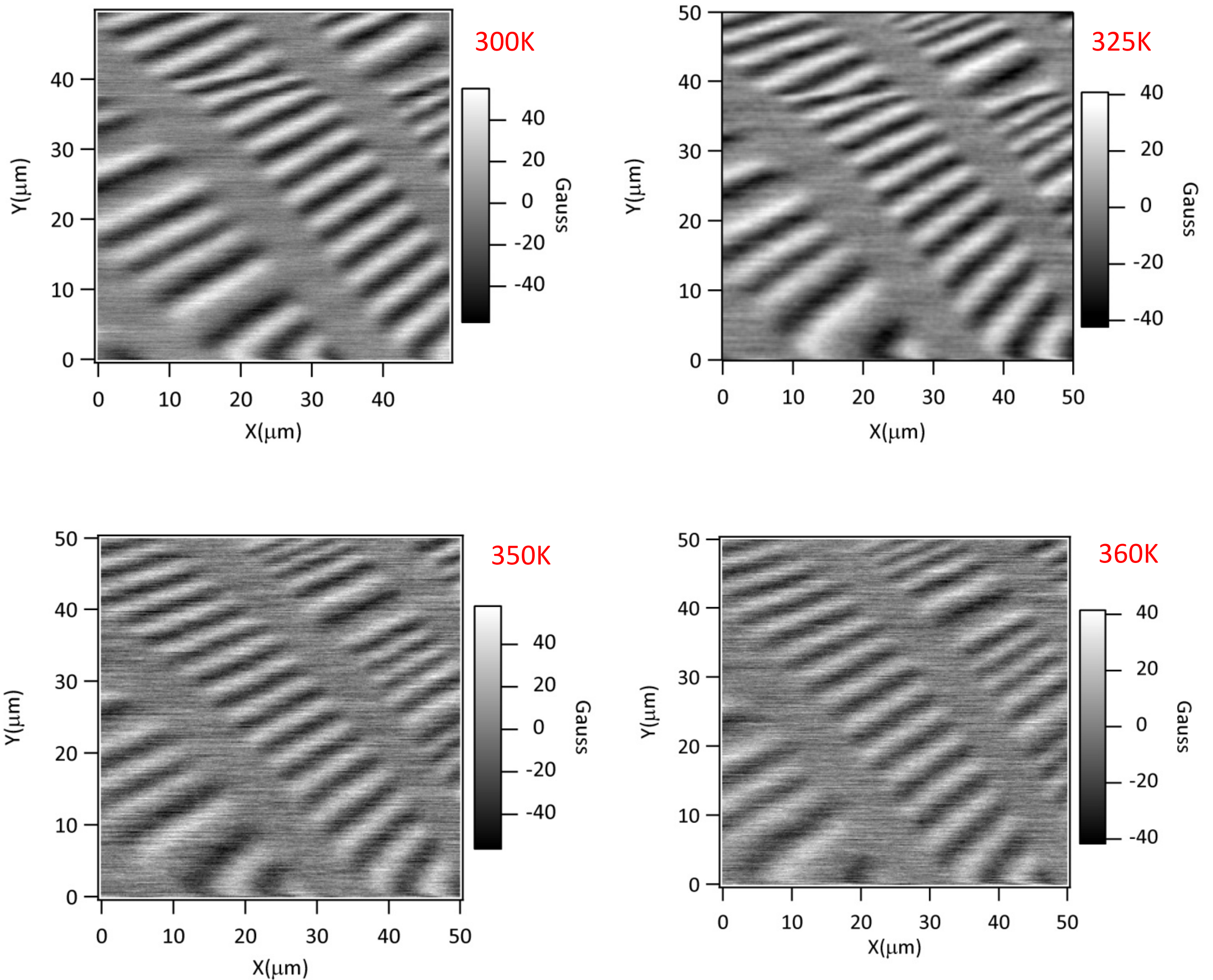

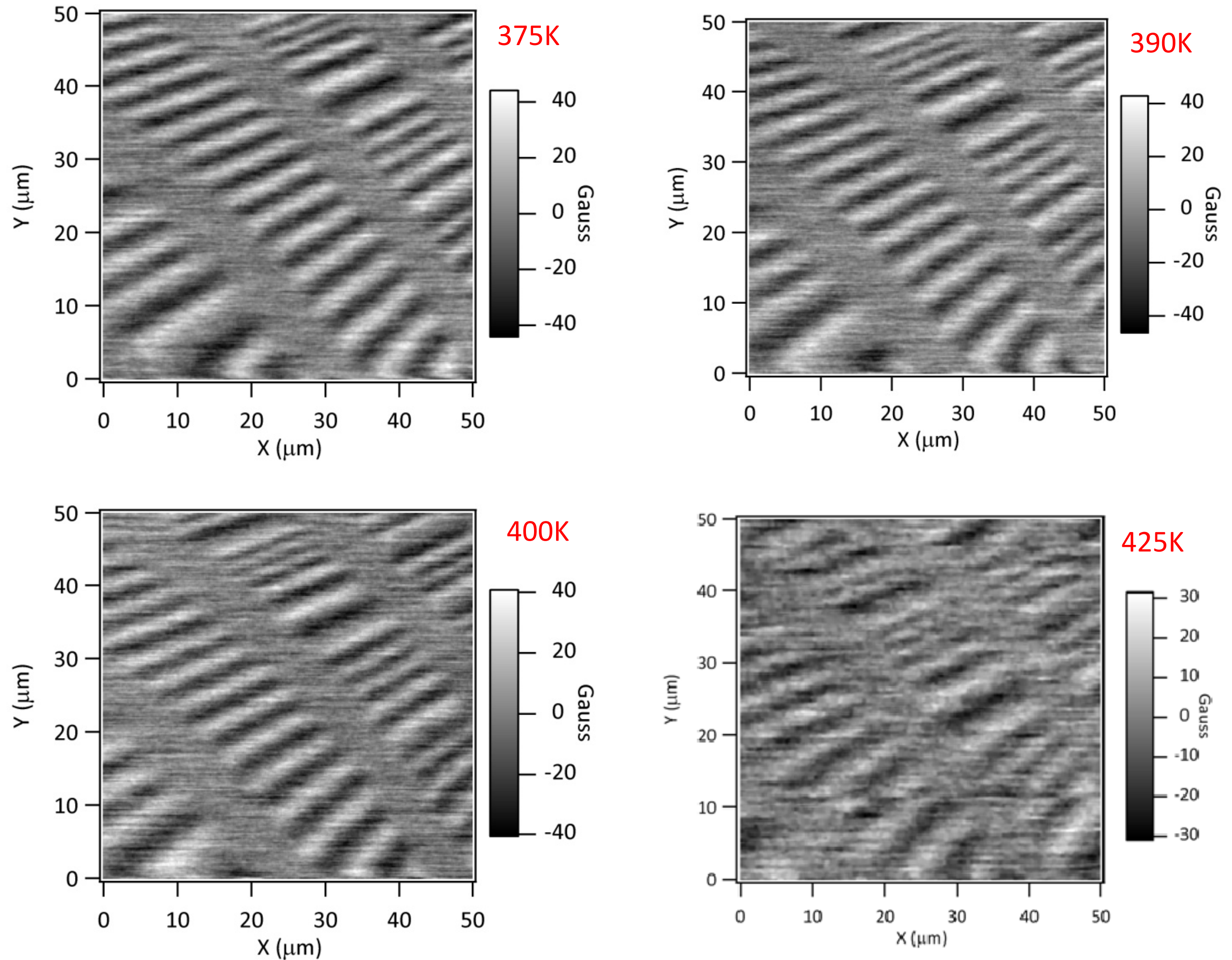

Figure 3.22: SHPM image of hard disk sample at high temperatures. Scanning speed was 5μm/s. Distortions at 425K are most probably to be due to degradation of epoxy between the HP and tuning fork.

In a recent work from Sandhu group [52], SPM with AlGaN/GaN based micro Hall probes with dimensions of 2×2μm has been demonstrated using STM feedback at high temperatures, up to 375K. The results shown in Fig. 3.22 confirm the success of AFM feedback tracking system with micro Hall probes up to 425K. Even though a relatively heavy mass is attached at the end of tuning fork, usually a quality factor, Q, 150-220 is obtained even at atmospheric pressures. Despite more or less the planar geometry, the viscous damping is not a big problem due to high stiffness of the force sensor.

The observed distortions in the scanned images at high temperatures are considered to be not mainly due to performance of the Hall probe but it is due to problems related with the used glue to fix the scanning PZT and the probe holder, and degradation of the sample. The resonance frequency and quality factor of the quartz crystal tuning fork changes with the temperature as shown in Fig. 3.23, however this change is still much less than the conventional silicon AFM cantilevers.

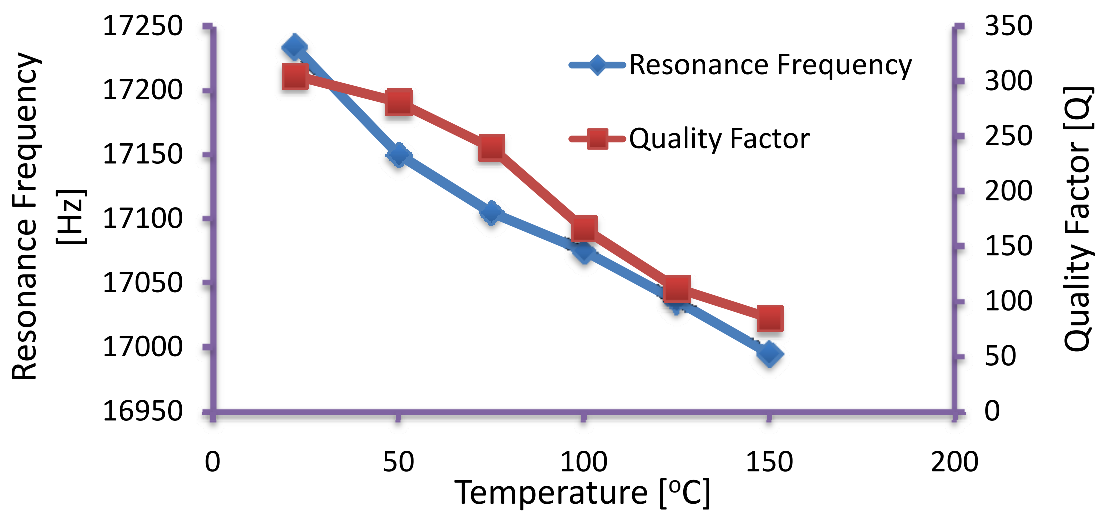

Figure 3.23: Effect of environment temperature on the resonance frequency and quality factor of the quartz tuning fork.

No significant change on the electrical properties of Hall Probes has been observed during the experiments as displayed in Fig. 3.24 and Fig. 3.25. GaN/AlGaN Hall probes can even work in the contact mode operation even at high temperature without getting damaged physically. Usually due to the physical contact of the probe to the sample, a scratch may develop over time; which sometimes can cause malfunction of the probe. This is not observed with the GaN sensors even when experimental accidents happened when there were strong forces enough to break the tuning fork. Chemical stability due to small bond length between the constituent atoms supports the use of the material under harsh environments.

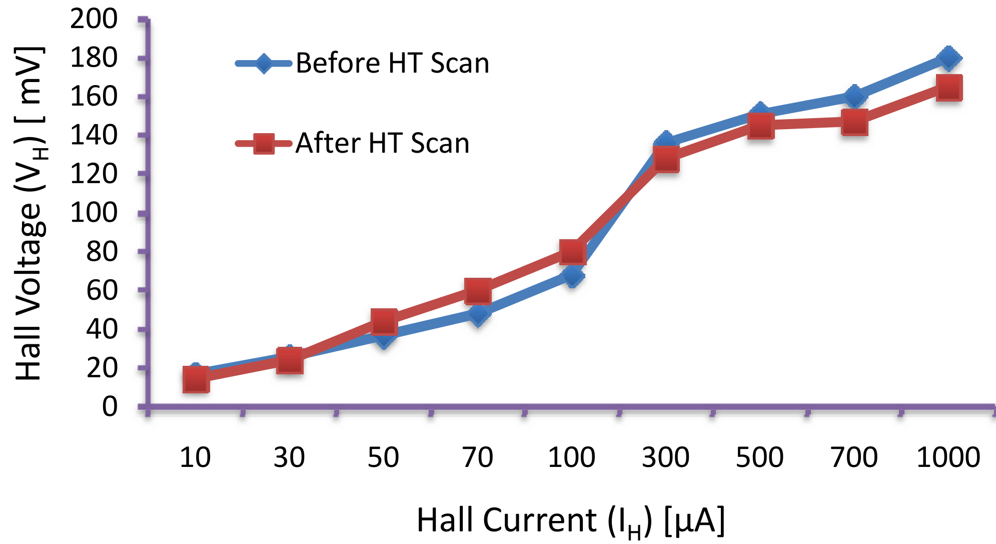

Figure 3.24: Stability comparison with respect to the electrical characteristics before and after the scan.

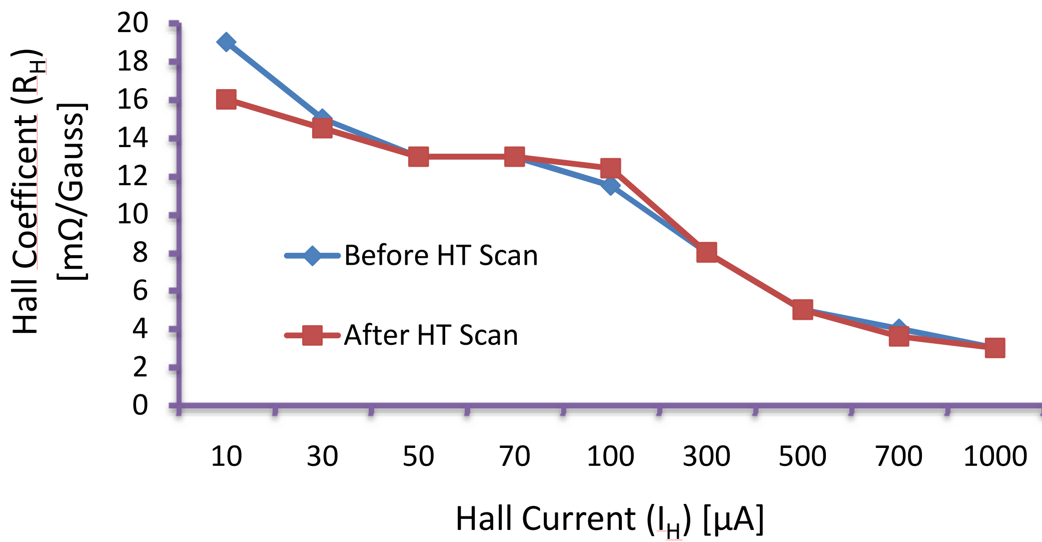

Figure 3.25: Stability comparison with respect to the electrical characteristics before and after the scan.

3.11 InSb Based Quantum Well Hall Sensors

3.11.1 Introducion

Further development of the Hall probes requires development of new materials for the fabrication of high sensitivity elements at the nanometer scale. Techniques employing the micro or nano fabricated Hall elements have an increasing place in biosensors and biomedical applications in addition to the imaging. Especially for the biological applications where high sensitivity is essential, magnetic detection levels are the key concern about the selection of the method. Scanning quantum interference devices (SQUID) has the highest level of magnetic sensitivity among the local probing techniques. However, it is also known that due to the materials used in the sensing elements, SQUID can only operate under cryogenic temperatures, which is the major drawback for the medical applications. Thus, when flexibility is needed in terms of the temperature, the best choice becomes the Hall devices again. To compete with other magnetic local microscopy techniques, the required improvements have to be done by eliminating the factors that limit the detection capability of the Hall sensors. Absolute magnetic sensitivity and the noise levels are the two most important parameters in terms of the sensitivity enhancement [53]. The critical physical requirements are the high electron mobility and an ultra-thin conducting layer very close to the material's surface. Indium Antimonide (InSb), belongs to a class of electronic material called "III-V compound semiconductor", can have high mobility and nano-sized conductive channels with a suitable application of the selective doping profiles. In fact, InSb has the highest electron mobility and the saturation velocity (Table 3.2) of any known commonly used semiconductor. [54]. InSb/AlInSb quantum well (QW) structures gaining importance over the conventional semiconducting materials, like GaAs, due to their large electron spin effects, namely the g-factor, and the small effective electron mass, $m^*=0.014m_0$ [55, 56]. In this work, the micro-Hall devices are fabricated from InAlSb/InAsSb/InAlSb heterostructures are investigated in terms of their

magnetoresistive properties and imaging performances at elevated temperatures up to 125ºC.

Table 3.2: Typical Channel Electron Properties at 295K [54]

	Si	GaAs	$In_{53}Ga_{47}As$	InAs	InSb
Electron Mobility ($cm^2V^{-1}s^{-1}$ $n_s=1\times10^{12}/cm^2$)	600	4,600	7,800	16,000	30,000
Electron Saturation Velocity (10^7cm/s)	1.0	1.2	0.8	3.5	5.0
Energy Band-gap (eV)	1.12	1.42	0.72	0.36	0.18

3.11.2 Fabrication

The InAlSb/InAsSb/InAlSb heterostructure wafer used has the layer structures as shown in the Fig. 3.26. Electrical conduction is confined to a 30nm wide InAsSb quantum well. Fabrication, starting with the dicing of the wafer in to 12 mm × 12 mm pieces, has the following steps.

1. Hall Probe Definition: Samples are spun at 5000 rpm with AZ-1505 positive photoresist to obtain ~0.5μm resist thickness. Exposure done for a dose level of 150 mJ and development performed using AZ-MIF726, single puddle developer. Etching done by CCl_2F_2 plasma for an approximate depth of 0.9 μm. The RIE parameters are summarized in Table 3.3. Note that it may not be necessary to obtain such a deep etch level, instead an etch depth which clears the InAsSb layer would be enough to separate the devices. However, we preferred to continue until the substrate is reached to make sure the probe is well isolated. The similar approach is reported by Orr *et al*. [57] while isolating the devices in order to eliminate the pad to pad conduction in the barrier layers. At the end, probes whose physical size is 1μm are obtained.

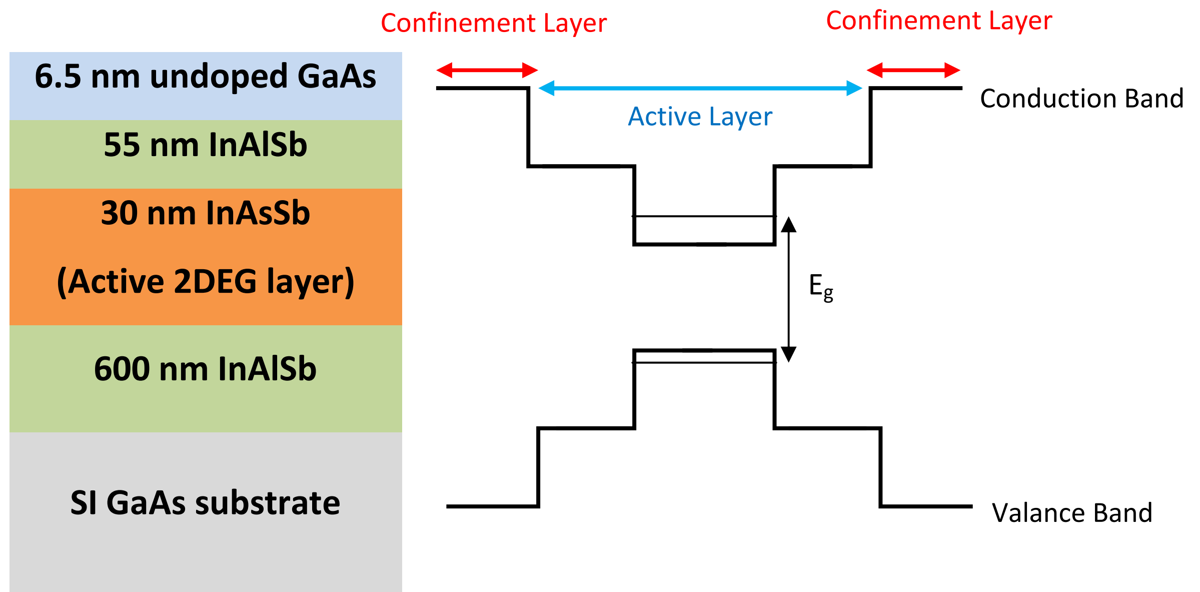

Figure 3.26: InSb quantum well wafer structure and band diagram.

2. Mesa Etch: Samples are spun by AZ-5214E photorezist at 7000 rpm for a thickness of ~1.2 µm. Exposure done at 5 mW for 45sec. and the samples are developed in 1:4 AZ-400K:DI mixture. Etching done with CCl_2F_2 plasma and a final depth of ~1.4 µm is obtained.
3. Ohmic Contact Metallization: Samples are spun by AZ-5214E at 7000 rpm and image reversal exposure is done. Developed samples are placed in the box coater and 10 nm. Cr / 150 nm. Au is thermally evaporated under the base pressure of 4×10^{-6} bar. Lift off is done immersing the samples in acetone and squirting the solvent when necessary. Ti/Au ohmic contact is also reported. [56, 57]. Note that in either case the ohmic metal is Au; Cr or Ti is used to improve the surface adhesion of the material to stick the gold. In this study Cr is preferred due to its observed better adhesion properties. Indium metal contact is also reported [53].

Later, the chips are diced in to the individual sensors and each sensor is glued by super glue on top of the 32.768kHz quartz crystal tuning forks with dimensions (l × w × t) of prongs are, 3.81mm × 0.34mm × 0.62mm. The stiffness of the forks was 29kN/m. The tuning forks are extracted from their cans and their leads have been replaced with

Table 3.3: RIE etch parameters for InSb

Gas Flow Rate	**:**	20 sccm.
Base Pressure	**:**	~10^{-6} mbar.
Process Pressure	**:**	4 µbar.
RF Power (from above)	**:**	100 Watt
Etch Rate	**:**	nm./min.

non magnetic wiring. Then the quartz tuning forks are glued, by super glue, to a 10mm × 10mm printed circuit board sensor holder, compatible with the scanning head of the SHPM system, with one prong free configuration. Wiring is done by 12 µm gold wires using an ultrasonic wedge bonder. The wires are carefully placed not to touch the wirings used to carry the signals from the prongs and the prongs themselves.

3.11.3 Characterization

The 300K electron mobility and sheet carrier concentration were 36,500 cm^2/Vs and $2.5\times10^{11}cm^{-2}$, respectively. The theoretical Hall coefficient calculated from the indicated sheet carrier density, 0.25Ω/G, is in a good agreement with values indicated in the Fig. 3.27 for the bias current values low enough not to heat the sample. The current sensitivity is found to be 2,640 V/A/T, which is about an order of magnitude greater than GaAs pseudomorphic devices. From the same figure it is obvious that, at elevated temperatures, regardless of the applied current, there will be a decrease in Hall coefficient due to the increase in the total sheet carrier densities. This increase is also shown by Orr *et al*. [57] for the QW samples having different conduction channel widths. A rapid increase in carrier concentration has been observed above 100K while mobility starts to decrease as a consequence. The same behavior is also observed by Kunets *et al*. [53]. Nevertheless, for current values above 300 µA, the heating caused by

the applied current will dominate the environment temperature and the close values of Hall coefficients will be reached whatever the temperature is.

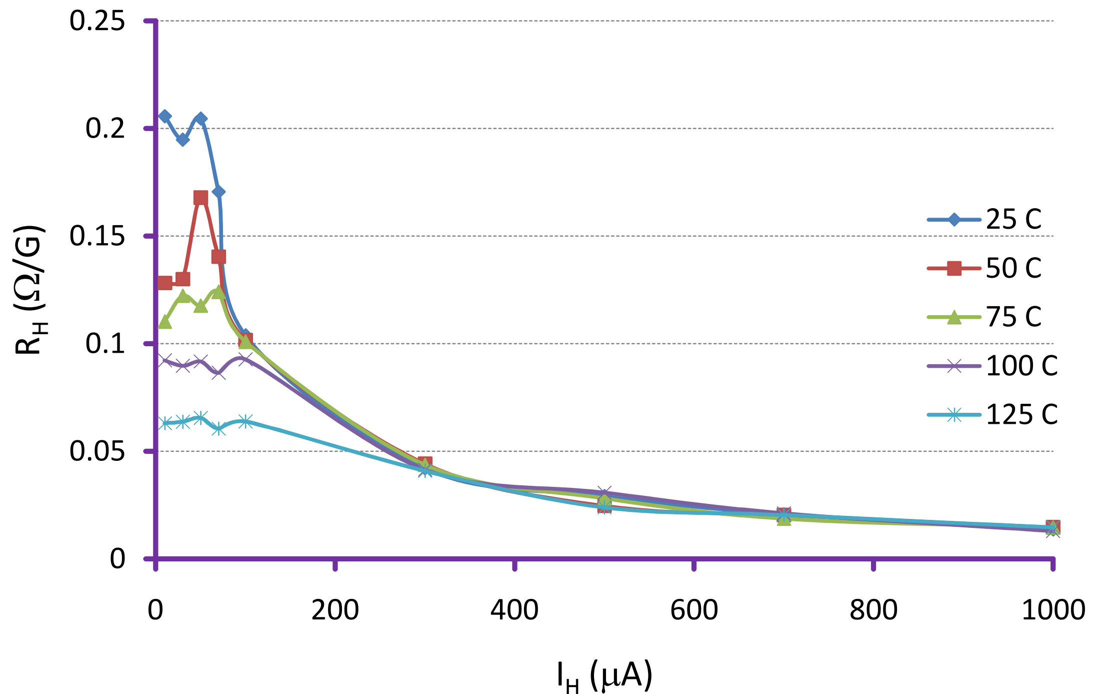

Figure 3.27: Change of Hall coefficient (R_H) as a function of different drive currents with respect to the temperature for 1μm × 1μm. sized Hall probe.

It is essential, for a Hall sensor, to know the noise levels as the ultimate aim is to employ it in a magnetic field measurement application. For this reason, the noise power spectrum (Fig. 3.28) is measured and examined carefully. The probes are offset nulled right after the bias current is applied. The Hall voltage which is amplified with the low noise amplifier is fed to a Textronix TDS1002B digital scope and the fast Fourier transform (FFT) of the signal is acquired in the range of 0 to 1250 Hz with 1 Hz increments and is averaged 10 times to get the final values. From the chart we see that the 1/f noise is the dominating noise component for low and mid range frequencies as shown in Fig. 3.27. Another important component is the Johnson noise. It can be seen that the noise level is increasing as a result of the high electric field created in the active

region of the sensor which heats the electrons gas. This is observable after as current bias values exceeds 70 µA. The overall noise levels are higher than the values reported by Kunets *et al*. [53], but in that study the size of the Hall element had size of 35 µm × 200 µm (with × length). One must note that both of the noise components, 1/f noise and Johnson noise, depend on the size of the device [58].

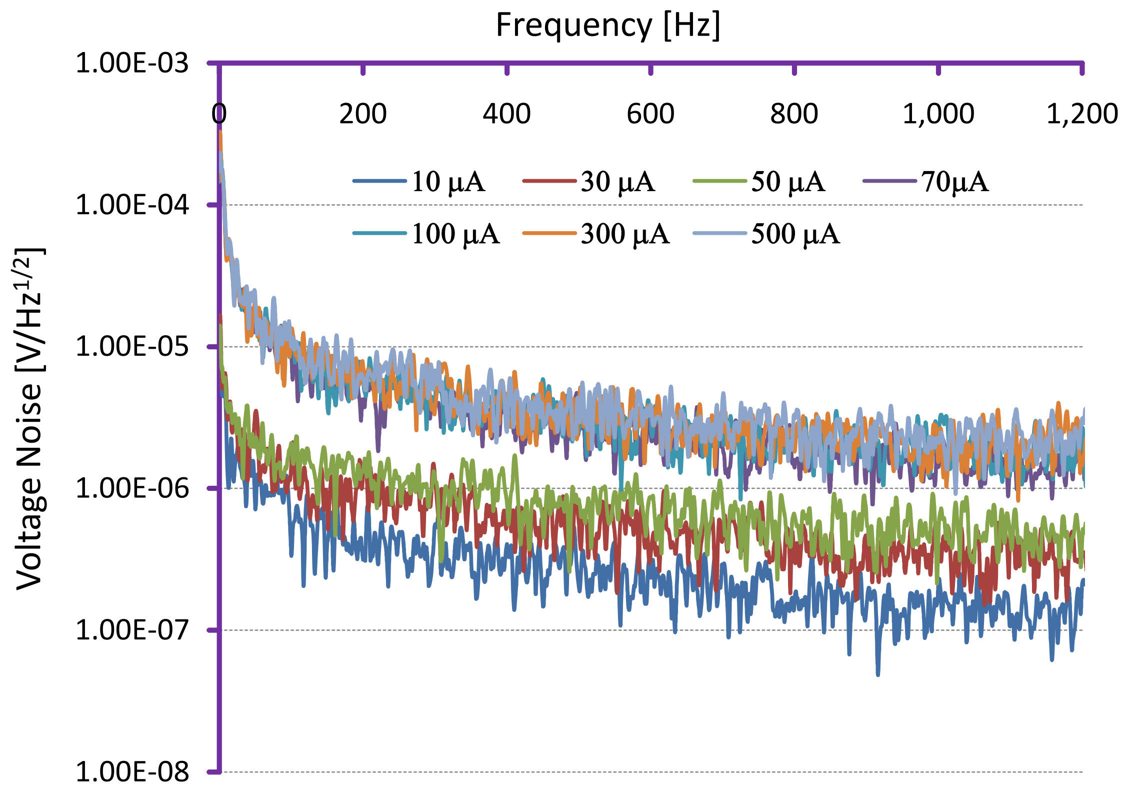

Figure 3.28: Noise spectrum of InSb QW Hall probes at 300K for different bias currents.

Unlike most of the conventional semiconductors, this sample of InSb QW exhibits an opposite behavior of the temperature dependence of its serial resistance as shown in Fig. 3.29. Although, increase in temperature adds extra energy to the electrons in the valance band and free them to join the other carriers, increasing the carrier

concentration. The electron-phonon scattering increases the serial resistance at the same time due to lower mobility. On the contrary, in that sample, increase in the total number of the carriers suppress the effects coming from the electron scattering due to the high mobility even at elevated temperatures. However, there could be a limit to that decrease in serial resistance if the temperature is further increased probably due to the degradation of the semiconductor which is not studied.

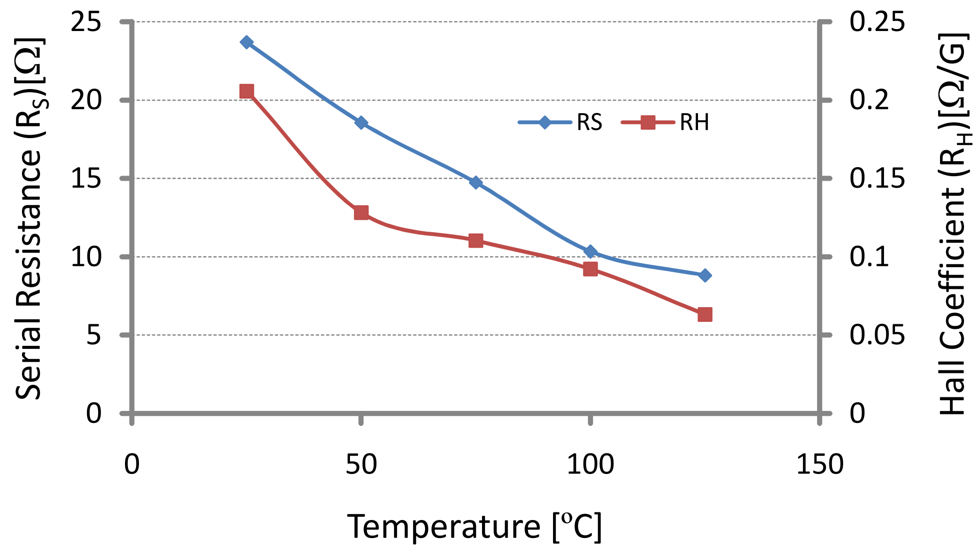

Figure 3.29: Change of Hall coefficient (R_H) and the serial resistance (R_S) as a function of the temperature for fixed drive current I_H=100 μA

3.11.4 Experiments

During the scan the sample is tilted ~1°- 1.5° with respect to Hall probe chip ensuring that the corner of the mesa is the highest point. The sensor assembly is dithered at the resonance frequency (Fig. 3.30) of the combined sensor with the dedicated split section on the scanner piezo tube and controlled using a digital Phase Locked Loop (PLL) circuit. The frequency shift Δf, measured by the PLL circuit is used for AFM feedback

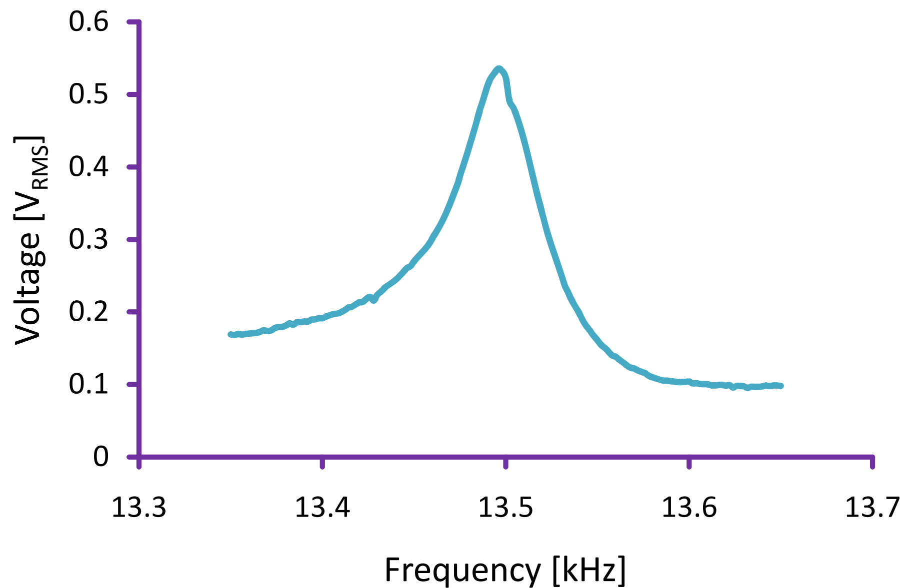

Figure 3.30: Resonance frequency curve of the 32.768kHz quartz crystal tuning fork loaded with 1.25 mm. × 1.25 mm. × 0.5 mm. InSb QW Hall sensor.

to keep the sensor sample separation constant with the feedback loop. The first sample to be examined was a piece of hard disk sample. The probe is offset nulled before the approach. When the sample is brought to the close proximity of the sensor head the scan is initiated. Scan result is given in Fig. 3.31. Phase shift, frequency shift, RMS and the topography data are also simultaneously gathered together with the magnetic image, however are not shown here as no interest is given. Later, a demagnetized NdFeB permanent magnet sample is used for SHPM scan. Due to roughness of the sample scan is performed by lifting the head of the scanner above the sample for 1V. Indicated lift off level corresponds to 240 nm gap between the sample and the corner of the chip which serves as an AFM tip. The image in Fig. 3.32 shows the domain patterns on the sample.

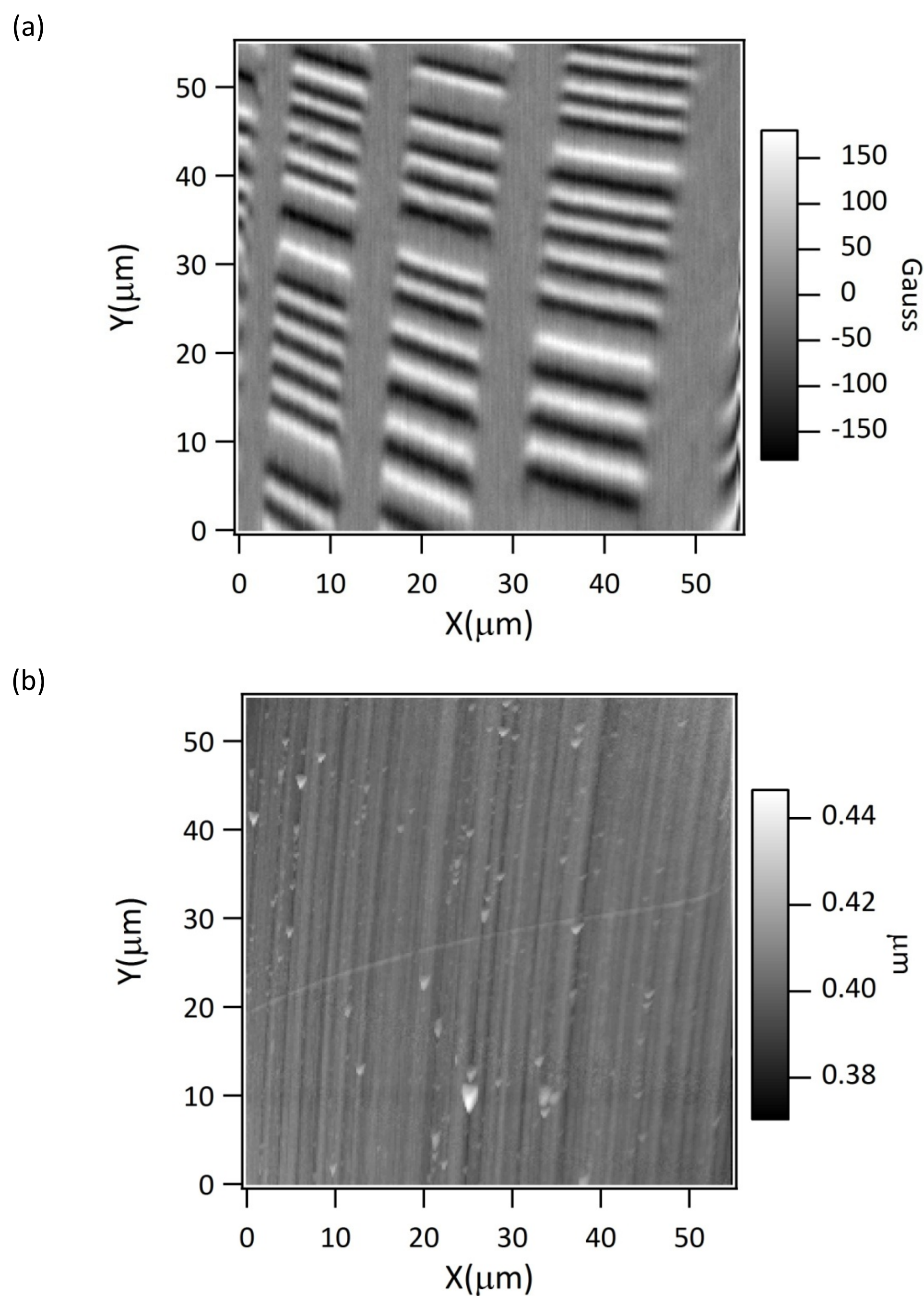

Figure 3.31: HDD SHPM scan image obtained at room temperature. The magnetic field profile (a) and the surface topography (b) obtained simultaneously. The scan parameters are; area: 55µm × 55µm, speed: 5µm/sec., resolution: 256×256 pixels, mode: AFM tracking

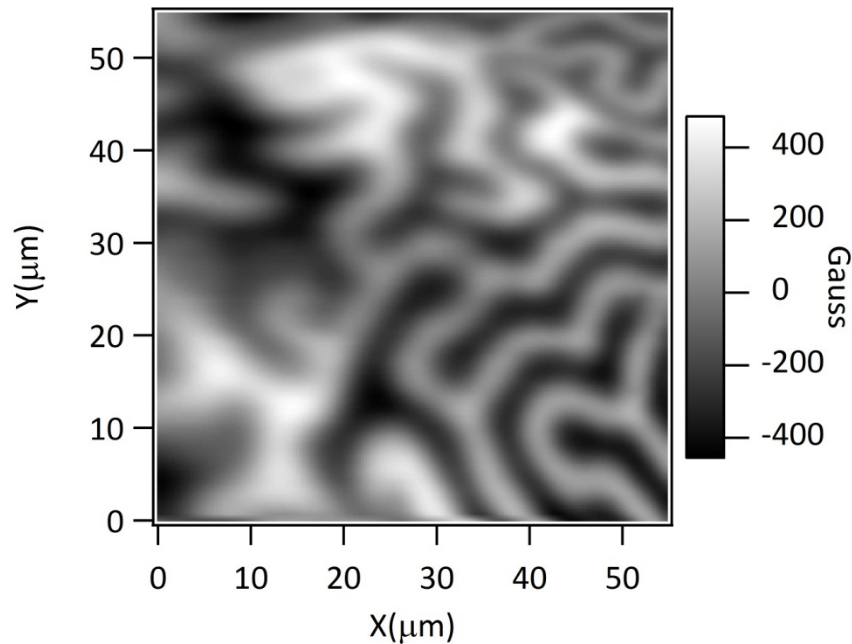

Figure 3.32: NdFeB permanent magnet image scanned at room temperature. The scan parameters are; area: 55μm × 55μm, speed: 5μm/sec., resolution: 256×256 pixels, mode: lift off

In order to investigate the high temperature properties, a low noise heater stage has been embedded in to the LT system whose details are given in GaN section. The hard disk sample is scanned at 25ºC and then, the temperature is gradually increased to 125ºC with 25ºC steps. At each step an image is acquired to check the performance. It has been observed that starting from 50ºC, the glue used to fix the QTF and the sensor starts to give up. This distorts the quality of the images as the parts starts to separate from each other as shown in Fig. 3.33 a&b. At high temperatures the same effect is observed among the other parts of the microscope as well. The chip holder and the scanner piezo appeared to be separated after a number of scans. It can also be observed, comparing the images, that there exist a thermal drift.

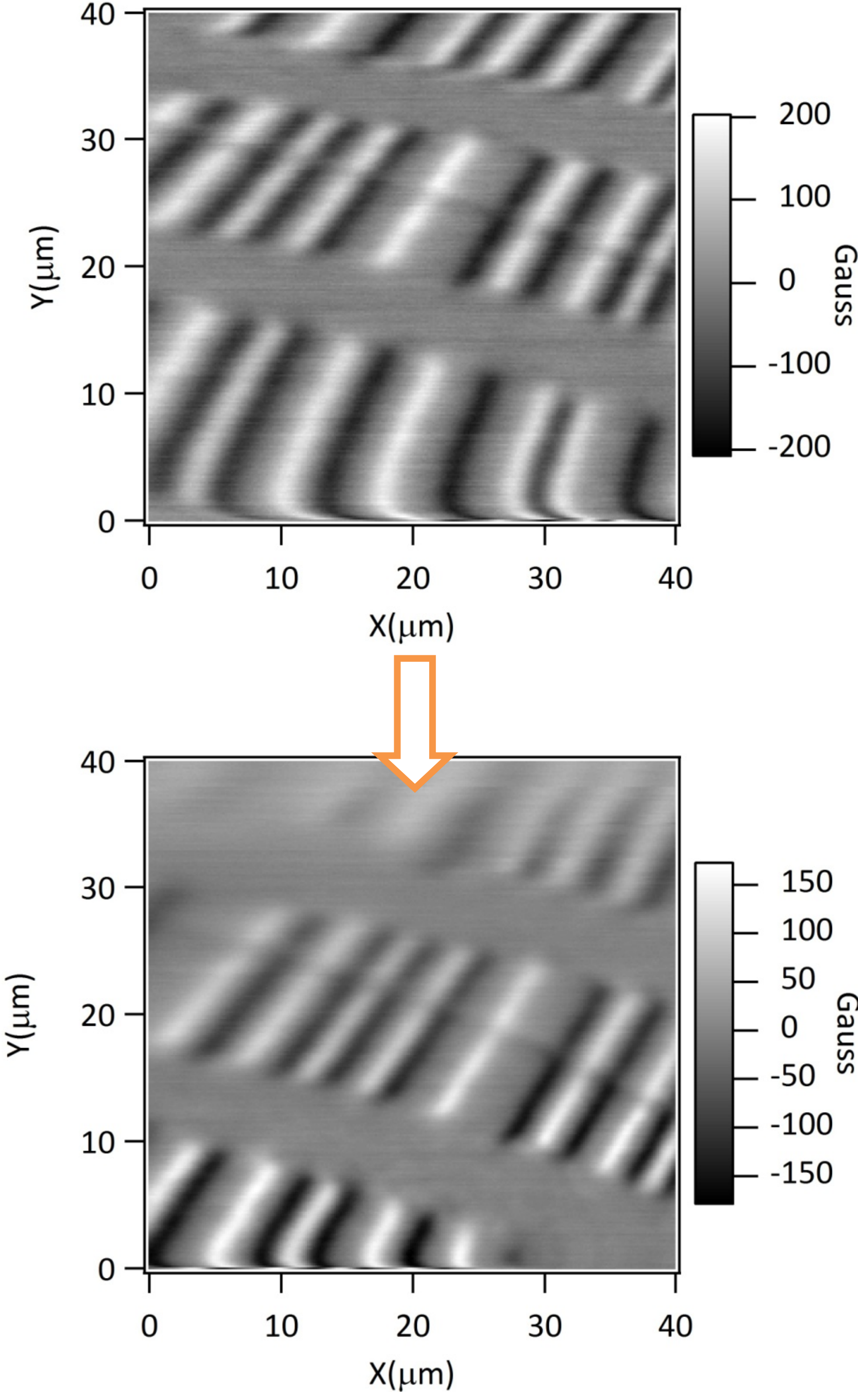

Figure 3.33: High temperature scan of Hard disk sample (a) 25ºC (b) 125ºC

3.12 SOI Hall Sensors for SHPM

3.12.1 Introduction

Silicon Hall sensors are widely used in many applications ranging from the high end industrial applications to everyday solutions. In industry, for example, they can be found in systems for the measurement of speed and rotation. In the automobiles, Hall sensors can be found in systems such as ABS, speed meters, electric windows, doors, headlights, the engine and the gearbox. Silicon is the obvious choice of material for the sensors as it is the most established semiconductor technology. It is also important to note that the silicon Hall sensors, unlike most of the other sensors, are CMOS compatible [59]. On the other hand, some specific problems occur in silicon Hall sensors. If the silicon crystal is stressed, due to the piezo resistive nature of the silicon [60], piezoresistive signals can sometimes be well above the magnetic Hall voltage signals [59]. Another problem for a magnetometer using silicon Hall sensors is its offset and, even more important, the drift of the sensor offset. The perfect Hall sensor does not develop an output voltage when a magnetic field is absent. In practice, however, all Hall sensors have offset voltage as a result of the fabrication steps, material inhomogenities, the mechanical construction of the sensor or the environmental conditions, like mechanical stresses, temperature variations and aging [61]. The biggest contribution comes from the mechanical stress [62]. This offset can be nulled by means of calibration or using appropriate dedicated electronic circuits with wide dynamic range as long as the offset is constant. But this is not the case, as mechanical stresses, temperature variations and aging cause the sensor offset to fluctuate. Continuous spinning current method [63] has been reported to compensate the problems caused by the offset. In this method, the structure is designed in such a way that current and Hall voltage leads are continuously switched, which compensates the offset by accumulating the magnetic signal along different directions. The magnetic signal accumulated along different directions of the arms. It is also suggested that, preferred orientations of the

Hall sensor with respect to the crystal the same direction but measured by different leads [62]. Improvements, however, can be achieved by the use of silicon on insulator (SOI) technology. Only a thin silicon layer insulated by an oxide layer is used instead of the whole silicon wafer. This leads to a higher current density in the active Hall element and to a reduction of the piezoresitive effect [59]. In addition to this, it has been reported that [64], when the Hall devices are integrated, using the CMOS technology, to mixed mode electronic layouts, that are used for energy measurements for example, a switching noise injected by the substrate can severely affect the resolution of the devices and the silicon-on-insulator (SOI) technology offers several advantages for the mixed-signal circuit design. Two techniques are used while implementing the Hall sensors in to SOI integrated circuit design. These are partially depleted (PD) [65] and a fully depleted (FD) [66] SOI technology.

In this study SOI micro hall sensors for SHPM imaging, which offer an ease in fabrication due to compatibility with CMOS fabrication process, have been investigated. This compatibility also makes it suitable to fabricate sub-micron Hall sensors on AFM cantilevers with integrated front-end electronics for a number of applications.

3.12.2 Fabrication

Silicon on Insulator wafers with n-type device and p-type handle layer has been used for the Hall sensor fabrication. The layer configuration of the wafer is follows;

a) A 3μm device layer of n-type Silicon(100) with resistivity of 0.005-0.02 Ω-cm and carrier concentration of 1×10^{18}- 2×10^{19} cm^{-3},
b) 2μm buried oxide (box) layer of thermal SiO_2,
c) 500μm thick layer of p-type Silicon handle layer with resistivity 20-50 Ωcm.

Micro Hall probes with effective dimension of 1µm x 1µm have been fabricated using optical lithography in a Class 100 clean room environment. Device fabrication process consists of four major steps which are summarized as follows:

1. Thinning the device layer down to few hundred nanometers by reactive ion etching (RIE) using mixture of SF_6 and O_2 gas plasma. This procedure aims to obtain a thin top layer with low resistivity, in order to inspect capability of sub micron device fabrication. Thinning the wafer, as it is expected to achieve, relatively lower carrier concentration which will lead to an increase in the Hall coefficient (Fig 3.34). At the end, random thicknesses of top Si have obtained due to the ±500nm thickness variation of the device layer throughout the wafer.
2. Active "Hall cross" patterning by using RIE. 5 mm×5 mm. pieces of the material are spun by AZ 5214E resist at 6000 rpm for 40 sec., exposed to 200 mJ of UV light and developed in AZ400K:DI (1:4) solution. Etching is performed with RIE using SF_6 and O_2 mixture.
3. Formation of the mesa by etching through the SiO_2 layer ~1.5µm by using RIE with mixture of CHF_3 and O_2 gas plasma,
4. Thermal evaporation of Ti/Au (50Å/1000Å) Ohmic contacts, and rapid thermal processing (RTP) in a nitrogen atmosphere at 400°C for 30s.

On a 5mm × 5mm chip, four Hall sensors are micro-fabricated at a time and they are diced to a size of 1mm × 1mm × 0.5mm to be used in SHPM application. Hall probes with a wide range of thicknesses from ~250nm to ~550nm have been produced and studied during this work. Electrical connections have been established with 12µm gold wires using ultrasonic wedge bonder.

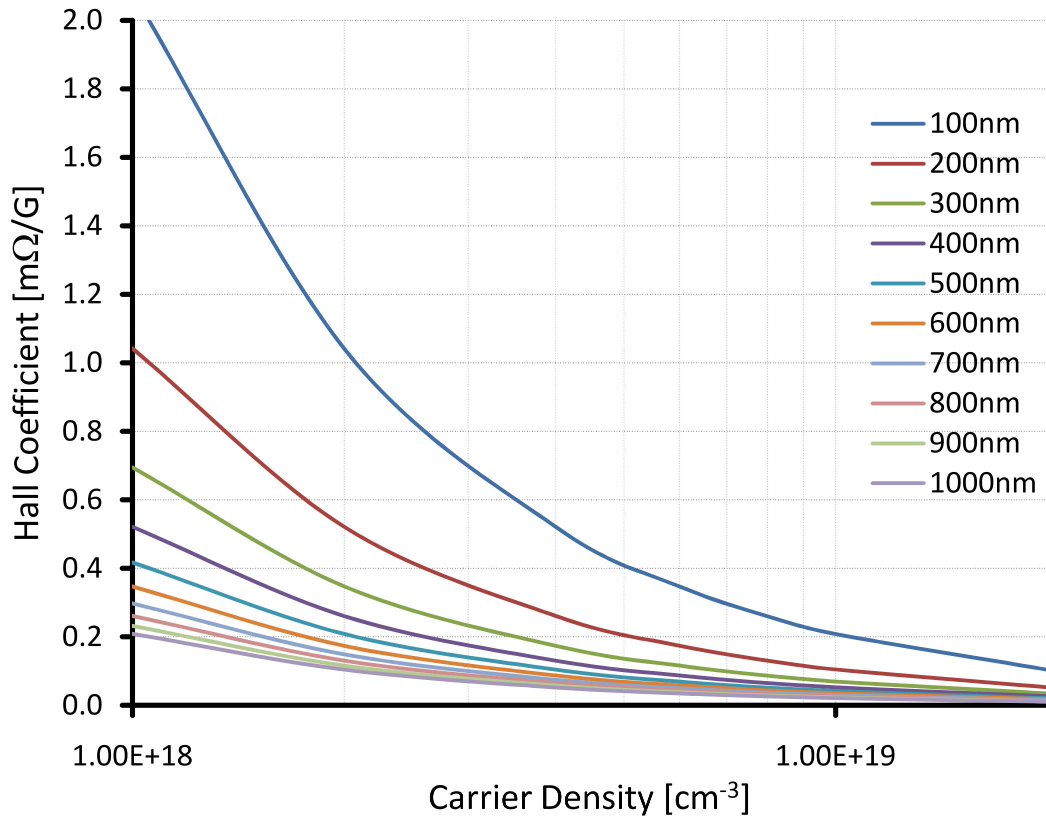

Figure 3.34: Effect of material thickness on Hall coefficient with respect to the carrier density, calculated based on the parameters of the used SOI wafer.

3.12.3 Characterization

Probes, having different active device layer thicknesses, are characterized by measuring electrical, magnetic and noise figures between 25-150ºC. The noise determines the minimum detectable magnetic field, Si Hall probes' noise have been carefully characterized. The probes are offset nulled right after the bias current is applied. The Hall voltage generated by the sensor is amplified with the low noise pre-amplifier with a gain of 1,001. The output of the amplifier is fed to a Textronix TDS1002B digital scope and the fast Fourier transform (FFT) of the signal acquired with 1.23303 Hz increments for 1,024 points, and are averaged 10 times to get the final values. It has been found

that sensitivity is strongly affected by the geometry of the hall probe as it can be seen in Fig. 3.35. By decreasing the thickness of the hall cross, we cause unintentional defects in the geometry of the hall cross, which might be due to inhomogeneity of the wafer or depletion of the carriers and leaving us with more dependence on the defective layers. For the observed *1/f* noise an ensemble of microscopic fluctuations might be assumed. The correlation between frequency dependent noise and the speculated, however counterintuitive, depletion of carriers is not clear.

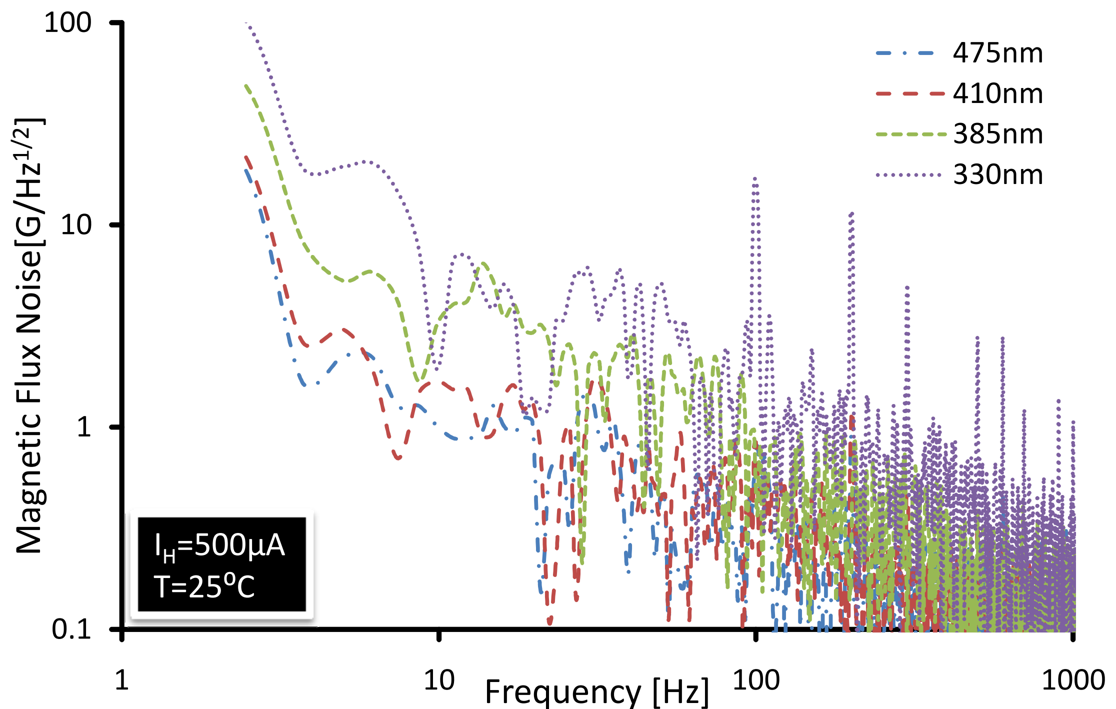

Figure 3.35: Effect of device thickness on the magnetic flux noise spectrum vs. frequency at 25°C with fixed bias current of 500µA.

Fig. 3.36 shows the effect of bias current on the noise spectra, representing an increase in the noise level by increasing the bias current. Increase in the bias current cause an increase in the number of carrier which adds more noise due to Joule heating in the Hall sensors, which cause an increase in the noise floor level. While on the other hand an

increase in the temperature leads to a slight decrease in the noise level for a fixed bias current value of 500μA as shown in Fig. 3.37. Comparing both tendencies, one might expect that the increase in temperature should do the same effect, of increasing the environmental temperature, as the result should be an increase in the number of free carriers. Probably as the bias current value was already high, the effect of the temperature on the overall noise could not clearly be seen. A better comparison might require use of lower current values.

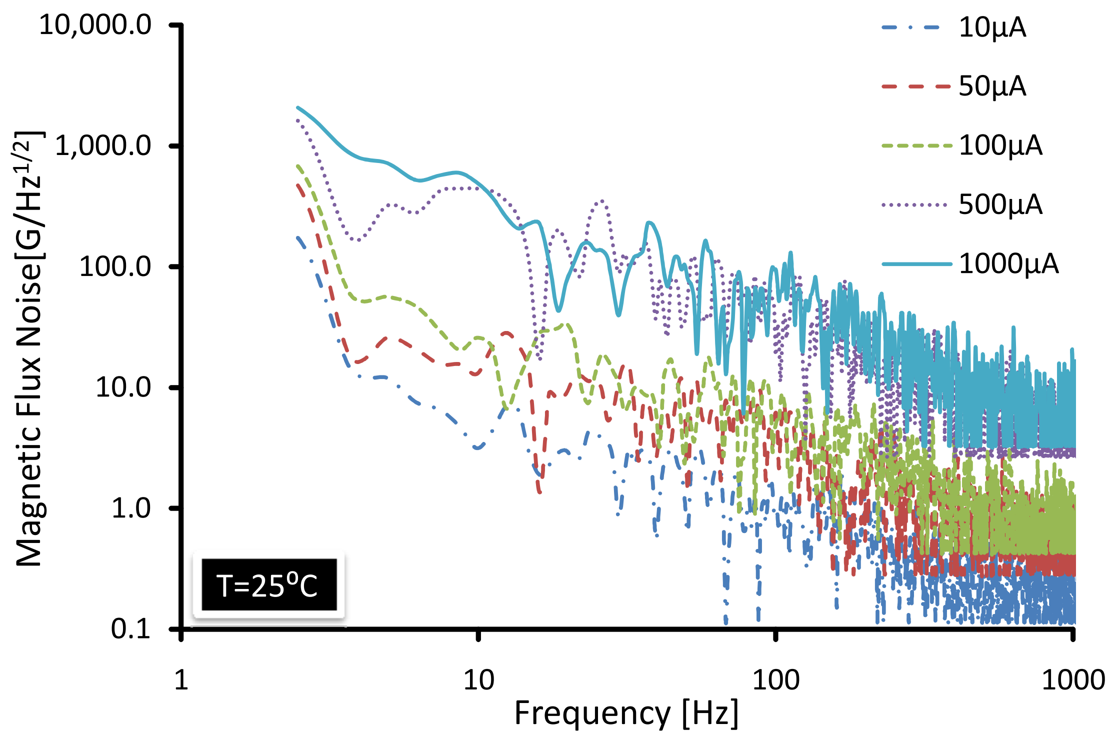

Figure 3.36: Effect of bias current on the magnetic flux noise spectrum vs. frequency at 25°C.

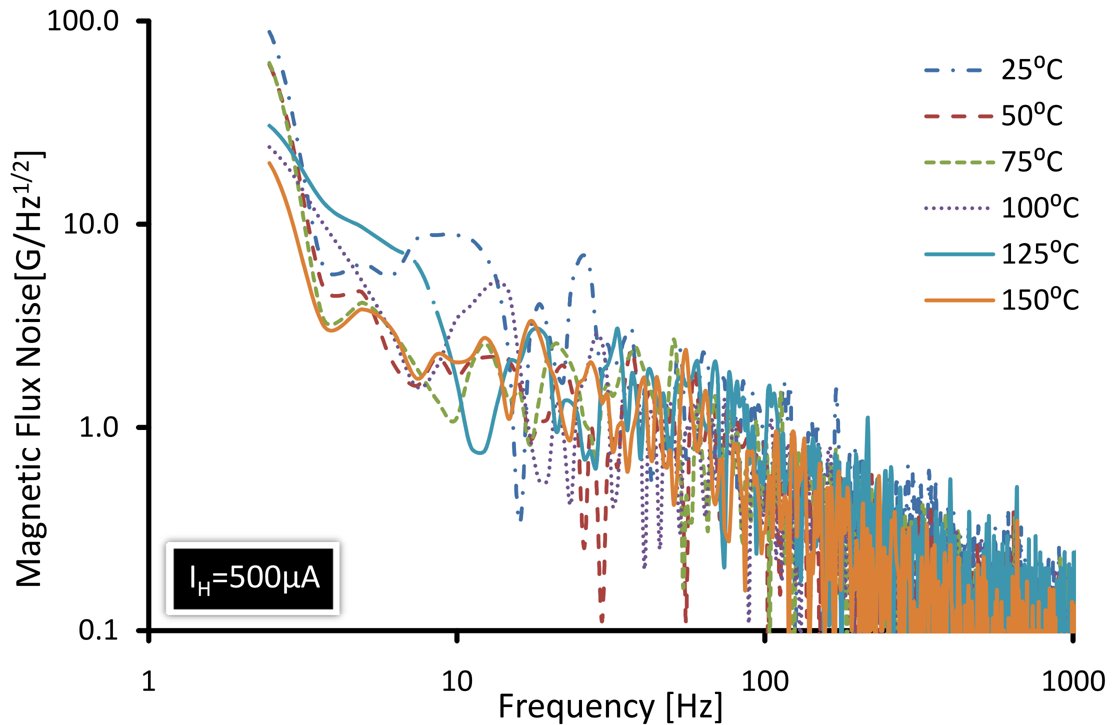

Figure 3.37: Effect of the temperature on the magnetic flux density noise spectrum vs. frequency with fixed bias current of 500µA.

Hall Sensors have been characterized for Hall voltage (V_H) vs. Hall current (I_H) under different temperatures for different thicknesses of the Hall devices. As shown in Fig. 3.38 and Fig. 3.39, linear relations can be observed between V_H vs. I_H characteristics with a two different dynamic resistances (slop of V_H vs. I_H curve, r_H V_H / I_H) values. These two regions can be distinguished as a low current regime ($I_H \leq 100\mu A$) and high current regime ($I_H \geq 100\mu A$). Value of dynamic resistance in low current region (r_{HLC}) is higher than in high current region (r_{HLC}). The typical value of r_{HLC} in low current regime is 35mΩ and in high current regime it is found to be r_{HHC} = 530µΩ at 25ºC. Under an increase in the temperature from 25ºC to 150ºC conditions, r_{HLC} increases from 34.9mΩ to 139mΩ and r_{HHC} from 0.53mΩ to 1.3mΩ. This behavior can be due to an increase of the number of channels by increasing the bias current or temperature. In order to

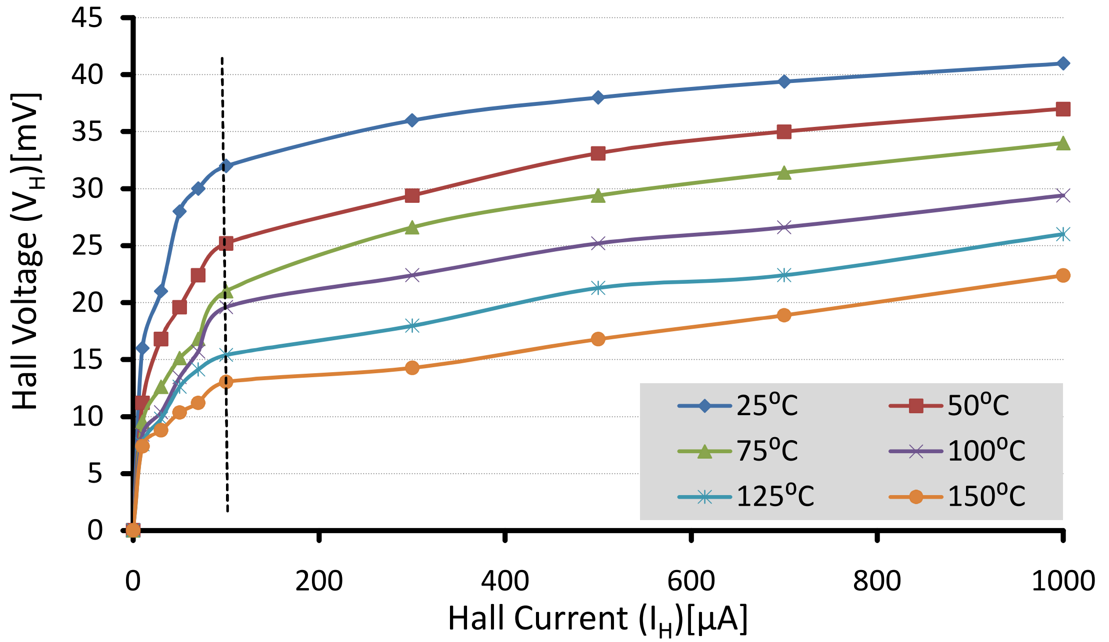

Figure 3.38: Effect of Temperature on the V_H vs. I_H characteristics. r_{HHC} and r_{HLC} is the dynamic resistance defined as the slope of curve in high current (I_H> 100μA) and low current (I_H<100μA) regime.

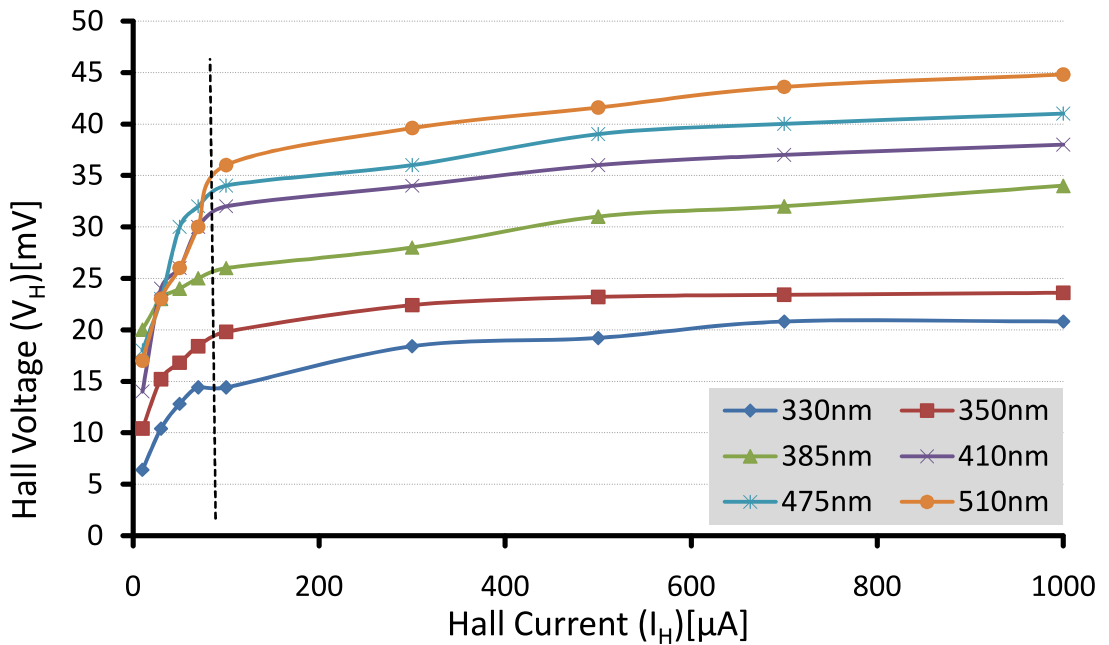

Figure 3.39: Effect of device thicknesses on the V_H vs. I_H characteristics.

investigate the effect of the minimum possible thickness or in other words the ultimate hall probe size, effective thicknesses of 250nm to 500nm have been tested. It has been seen that for our samples Hall effect has not been seen for the thickness less than 300nm. This is speculated to be due to irregularities, local thickness variations, in the etched hall probes and decrease in the carrier concentration.

Hall probes have been also characterized for their magnetic characteristics by applying magnetic field with external coil and by measuring the response to calculate the value of Hall coefficient, R_H. As shown in Fig. 3.41 and 3.42, value of R_H also depends on the applied current and two regimes can be formed as in the case of V_H vs. I_H characteristics. It has been observed that by increasing the temperature, R_H value also increases. It can be speculated that the increase in temperature cause an increase in the series resistance more than carrier concentration (Fig. 3.40) which leads to a decrease in the mobility; so as a cumulative effect an increase in R_H is observed. A systematic increase in the value of R_H by increasing the thickness of the hall cross confirms the above statement that carrier concentration plays an important role and should be considered for designing a proper nano Hall probes. A small discrepancy at high thicknesses (t_{eff} > 450nm) in the results presented in Fig. 3.42 is mainly due to improper etch of hall cross which is due to non homogeneity of the SOI wafer.

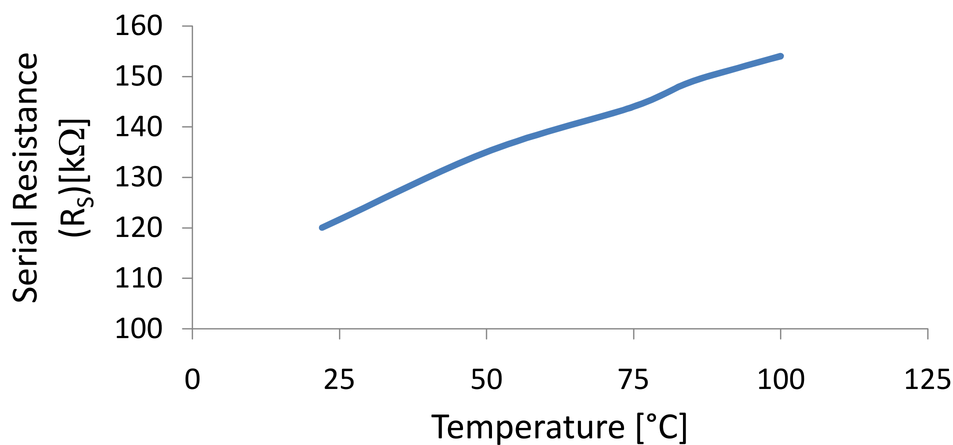

Figure 3.40: Change of series resistance R_s with respect to temperature for a Hall device thickness of 405nm.

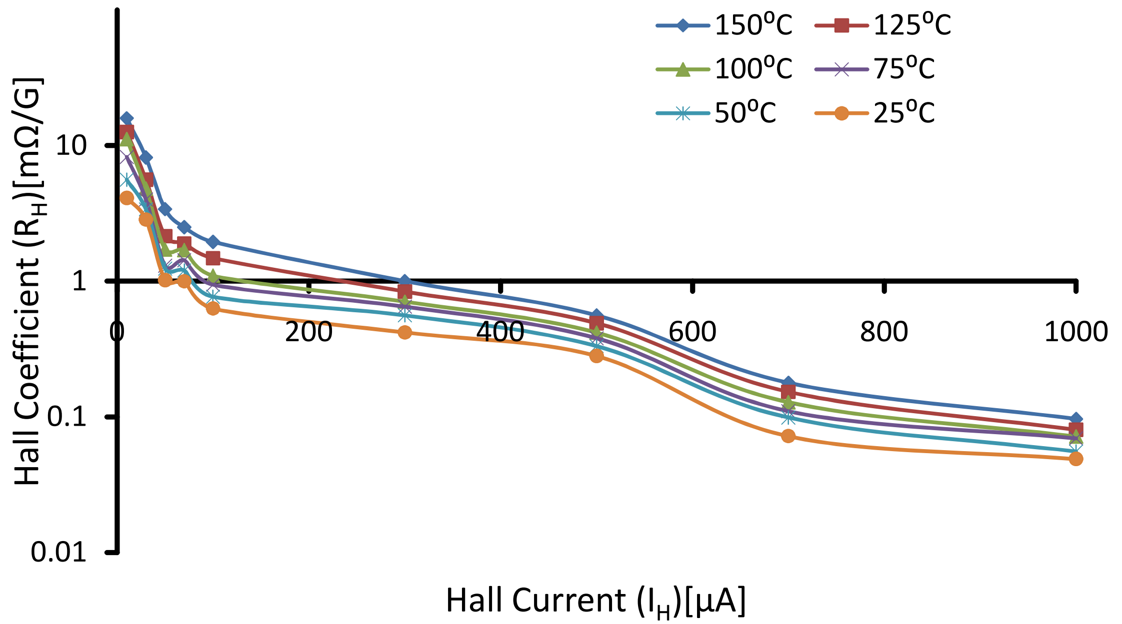

Figure 3.41: Effect of Temperature on the Hall coefficient vs. Hall current.

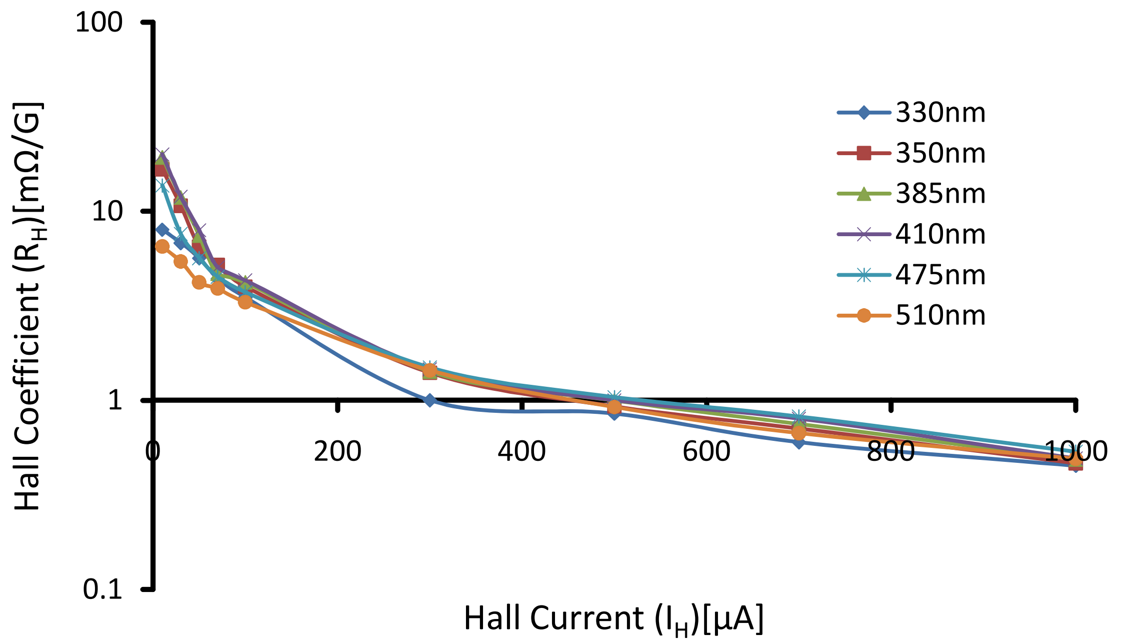

Figure 3.42: Effect of device layer thickness on the Hall coefficient vs. Hall current characteristics.

3.12.4 Experiments

The first experiments are conducted at room temperature using both, STM and AFM feedback, Fig 3.43. In both cases the sample is tilted ~1°- 1.5° with respect to Hall probe chip ensuring that the corner of the mesa is the highest point. In AFM feedback, as the sensor approaches to the surface, the resonant frequency of the sensor shifts due to the tip-sample forces. The sensor assembly is dithered at the resonance frequency with the dedicated split section on the scan piezo tube using a digital Phase Locked Loop (PLL) circuit. The frequency shift measured by the PLL circuit is used for AFM feedback to keep the sensor sample separation constant with the feedback loop. In the case of STM feedback, the sample is biased with -100mV voltage. The tunneling current between the sample surface and the gold coated corner of the mesa is maintained at a constant level by the by the feedback electronics during the scan. The microscope can be operated in two modes: AFM tracking and lift-off mode. In our SHPM experiments we have used an AFM tracking mode with a Δf = +10Hz. Moreover the same system can detect AFM topography and the frequency shift signal generated by the PLL at the same time. The same operation modes are also valid for the STM feedback. Even though a relatively heavy mass is attached at the end of tuning fork, we usually get a relatively high quality factor, Q ~150-220 even at atmospheric pressures. Despite more or less the planar geometry, the viscous damping is not a big problem due to high stiffness of the force sensor.

In order to investigate the potential high temperature operation of these Si micro hall probes, a non-inductively wound low noise heater stage has been embedded at the LT system. Fig. 3.44 shows magnetic image of HDD sample obtained in AFM tracking mode from 25ºC to 100ºC with a scanning speed of 5µm/s, pixel size of 256 x 256 and scan area of 50µm x 50µm. The Hall sensor was driven with 500µA DC current, the series resistance of the Hall sensor was 139kΩ, 144kΩ, 148kΩ and 155kΩ at 25ºC, 50ºC, 75ºC and 100ºC respectively.

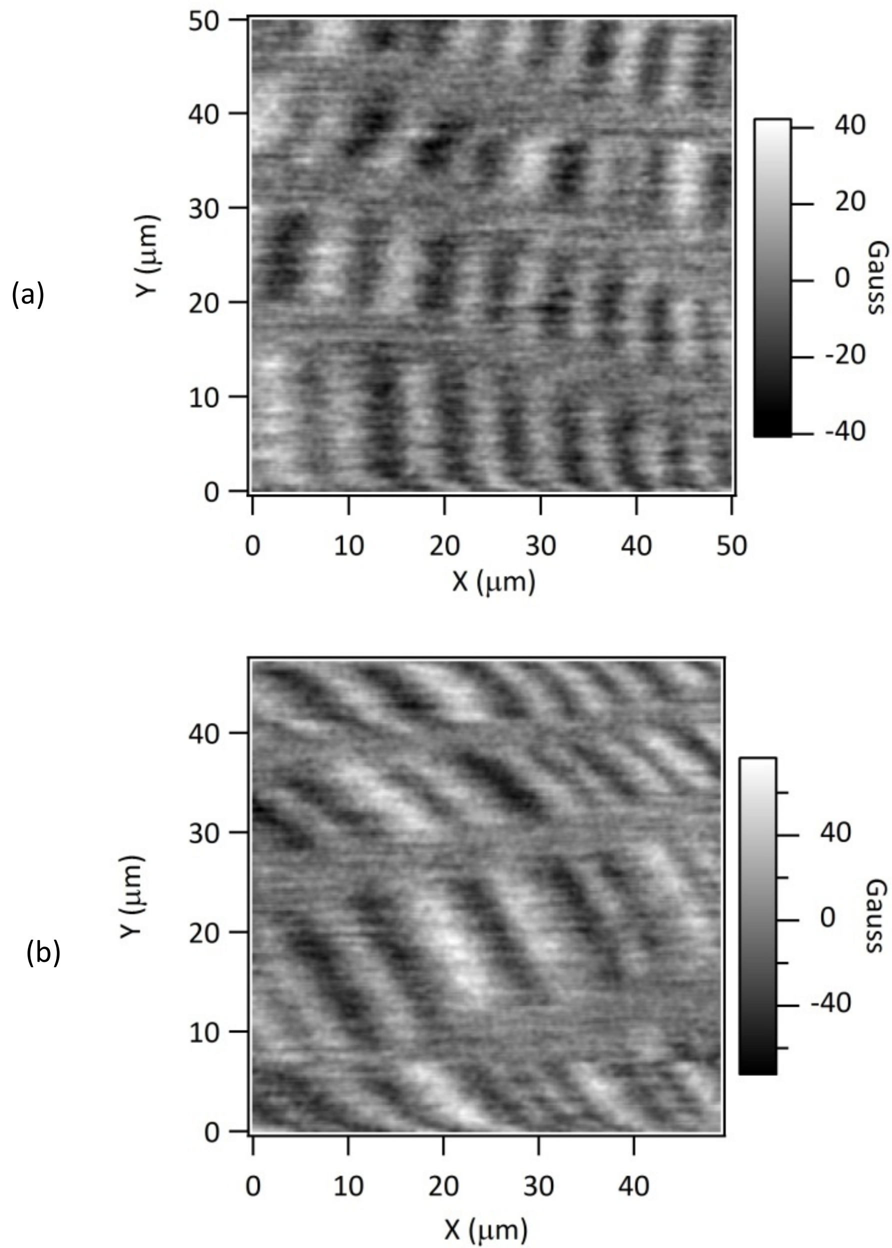

Figure 3.43: SHPM image of hard disk sample using (a) QTF AFM and (b) STM feedback at 25°C, with scanning speed of 5μm/s. Device thickness was 405nm.

In AFM mode the resonance frequency and the quality factor of quartz tuning fork were 15.745 Hz and ~140, 15.740kHz and ~ 130, 15.738kHz and ~119, and 15.732kHz and ~

115 at 25°C, 50°C, 75°C and 100°C respectively. The trend in the change of the resonance frequency with respect to the temperature increase is shown in Fig. 3.45.

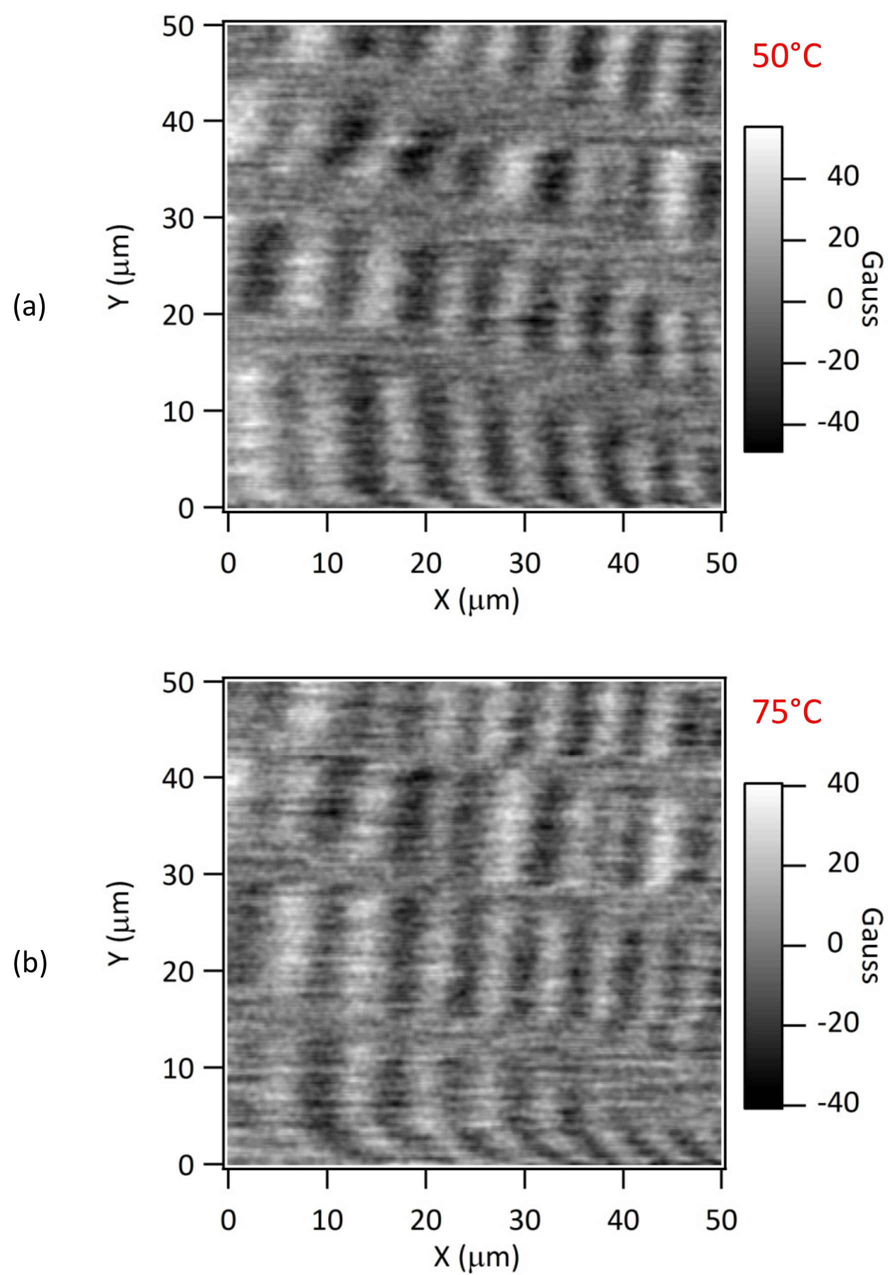

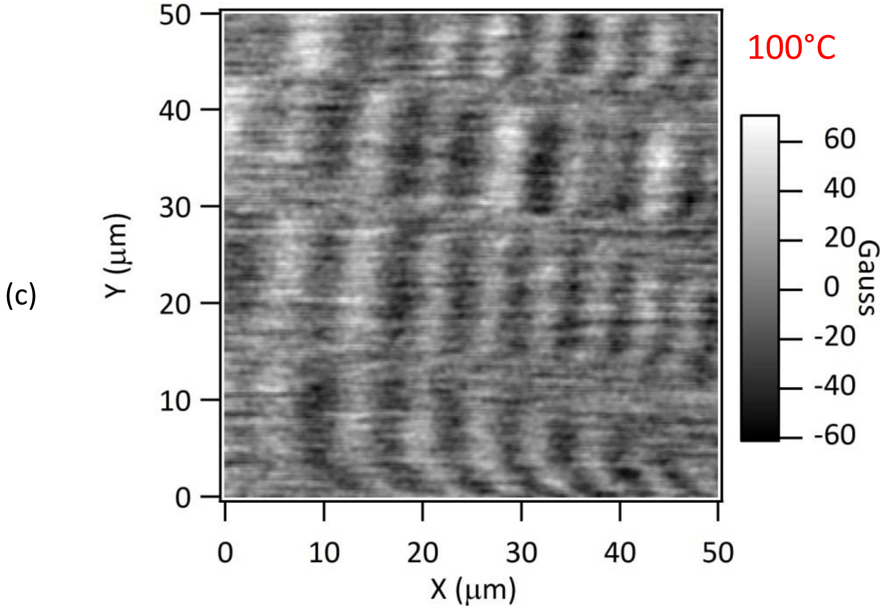

Figure 3.44: SHPM image of hard disk drive sample at high temperatures (50-100°C) using QTF AFM feedback.

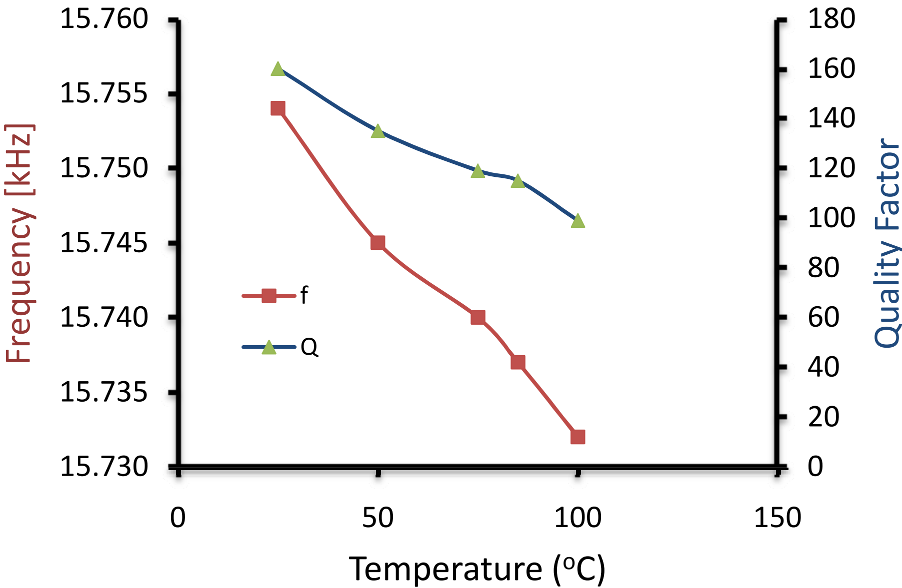

Figure 3.45: Change in resonance frequency and the quality of the quartz crystal tuning fork loaded by a 1 mm × 1mm × 0.5 mm Si Hall probe.

3.13 Bismuth Thin Film Hall Sensors

Some parts of the studies discussed in this section is published as “50nm Hall Sensors for Room Temperature Scanning Hall Probe Microscopy, Adarsh SANDHU, Kouichi KUROSAWA, Munir DEDE and Ahmet ORAL, Japanese Journal of Applied Physics Vol. 43, No. 2, 2004, pp. 777–778.” The Japan Society of Applied Physics

3.13.1 Introduction

Bismuth is a white, crystalline, brittle semi-metal found in solid form in nature, whose symbol in periodic table of elements is Bi. It has extremely low melting point, 271.3ºC and the thermal conductivity is lower than any metal, except mercury. Bismuth is the most diamagnetic of all metals. It exhibits a very large magnetoresistance. The earliest application of Bismuth Hall sensors goes back to 1962 when Broom *et al*. [67] used a 100µm Hall cross to scan superconducting tin and lead films to measure trapped flux. Later in 1971 Goren *et al.* [68] reported a 4µm sized probe used to measure flux penetration in superconducting films. This study was the first two dimensional SHPM image obtained by scanning the probe a few micron above the sample. The first Bi Hall probe defined by e-beam lithography technique presented by Brawner *et al.* [69] in 1993. In this study 2×4µm sized Hall sensor was defined by e-beam lithography patterning and standard lift off techniques after thermal evaporation of 150nm Bi film. This probe was used to make precision measurements of the critical state profiles in single crystals of $YBa_2Cu_3O_{7-y}$, superconductors. During the measurement 0.3mA DC drive current is applied to Hall sensor. Although e-beam lithography was applied in this study, the Hall probe size was still not sub-micron. Miniaturization of Bismuth Hall sensors simultaneously demonstrated by Chong *et al*. [70] using e-beam patterning and Sandhu *et al*. [71] by using Focused Ion Beam (FIB) milling in 2001. Chong *et al*. presented a ~400nm sized Bi Hall probe fabricated, by thermal evaporation followed by lift off on top of a pyramidal cantilever with 70nm thick Bi film. Sandhu *et al*., on the

other hand, reported a ~120nm sized Hall probe FIB milled out of 70nm Bi film thermally evaporated on semi-insulating GaAs substrate. Most of the applications of Bi Hall sensors were demonstrated by Sandhu group [72-74] of Tokyo Institute of Technology including the demonstration of smallest bismuth Hall probe [31] in collaboration with our group. Other studies are also present on bismuth for Hall device applications [75, 76].

The motivation reported by the above groups behind the use of Bismuth includes, the galvanometric properties of nano structures patterned out of Bismuth, like the low electron density, long mean free path and the extra large extension of the electron wave function [77], the smaller serial resistance compared to GaAs/AlGaAs probes and, negligible surface charge depletion effects [71]. I would to add, with practical concerns, its ease of availability as a material and its ease of processing as a thin film compared to InSb thin films and other III-V semiconductor heterostructures.

3.13.2 Fabrication & Characterization

Fabrication of Bi Hall probes consist of sequences from optical lithography which are followed by e-beam lithography or focused ion beam (FIB) milling. The process begins with dicing and cleaning of semi insulating (SI) GaAs wafers. Wafers are diced into either 5×5 mm or 12×12 mm pieces depending on the mask set used. Practically both masks have similar outputs, except the second generation mask designed to yield 64 individual chips and requires 12×12 mm wafer pieces whereas, first generation mask can only provide 4 chips on a 5×5 mm piece. Remaining fabrication steps, although they are the same, have different order of application depending whether the fine patterning of the Hall cross will be done by e-beam lithography or FIB. If the final patterning will be performed by FIB then, the following scheme is followed for the fabrication.

1. Mesa step definition is done first by spinning the samples at 6,000 rpm for 40s. Soft bake is done at 110ºC for 50s on a hot plate. Exposure is performed using a KarsSuss MJB3 mask aligner at a dose level of 240mJ. Developed samples, immersing in 1:4 AZ-400K:DI, are *not* hard baked as dry etch with RIE hardens the resist. Dry etch is preferred because of its anisotropy. CCl_2F_2 gas with 20sccm flow rate and 4μbar process pressure is used to obtain the plasma with 100W RF power applied to the specimen. Samples are etched for ~15min to achieve 1.6-1.8μm mesa depth. Etched samples are immersed immediately into acetone and exposed to low power ultrasonic agitation. This step is critical to completely clean the resist. It has been observed that if the samples are tried to be cleaned by squirting the acetone and if there exists some residual photoresist film after the squirting has stopped, it becomes virtually very difficult to completely clean the samples. Later, samples are squirted on by isopropanol and blow dried by dry nitrogen gas.

2. Recess etch is done by spinning the samples at 6,000 rpm for 40s Soft bake is done at 110ºC for 50s on a hot plate. Exposure is performed with a dose level of 300mJ. Developed samples are dipped into 4:10:55 volumetric mix of $HCl:H_2O_2:DI$ for 1hr to get ~55μm etch depth around edges. Cleaning is done by acetone and isopropanol.

3. For the Ohmic contact metallization, the samples are spun at 7,000 rpm for 40s by AZ5214E photoresist. After the soft bake, image reversal lithography is done first exposing the samples with the mask for 15 s at 6mW, baking for 2 min at 120ºC on hot plate, and then finally flood exposing for 45s. Developed samples are loaded into evaporation chamber. The evaporation system is pumped down to $\sim 4\times10^{-6}$ mbar approximately in 1hr. 10nm Cr and 150nm Au are deposited by thermal evaporation. Samples are then immersed into acetone beaker and lift off is done by squirting acetone using a glass injector.

4. An image reversal lithography is performed just like the procedure above, this time to obtain 10×10μm area consist of thin layer of bismuth just at the edge of the mesa. The samples are again loaded to the thermal evaporator, this time only Bi is placed to its dedicated boat. Bi pieces used for the evaporation immersed in to 1:5 HCl:DI mixture to clean the oxide layer and the organic dirt. It has been observed that if this procedure is not done a black residual substance remain in the boat after the bismuth has completely evaporated. This material could also contaminate the coated wafer. After the lift off, the samples were ready for FIB etching. The evaporation of Bi is left to the last stage, first to prevent it from getting oxidized during the fabrication, and second not to damage the Bi film during repeated processes of resist spin or cleaning. Note that, no material was evaporated before Bi to enhance the surface adhesion.

5. Tip metallization. A triangular portion right at the corner of the mesa is defined as an STM tip by evaporation of 10nm Cr / 50nm Au by thermal evaporation of the materials followed by lift off in acetone. For the patterning AZ-5214E resist spun at 7,000 rpm and exposed for 45s at 6mW.

Wafers were diced in to individual chips after the fabrication and mounted on non-magnetic PCBs. The electrical connections maintained by gold wires, 12μm in diameter, using ultrasonic wedge bonder. Note that it is preferred to dice and package the chips before the FIB done so that testing of processed chips done immediately.

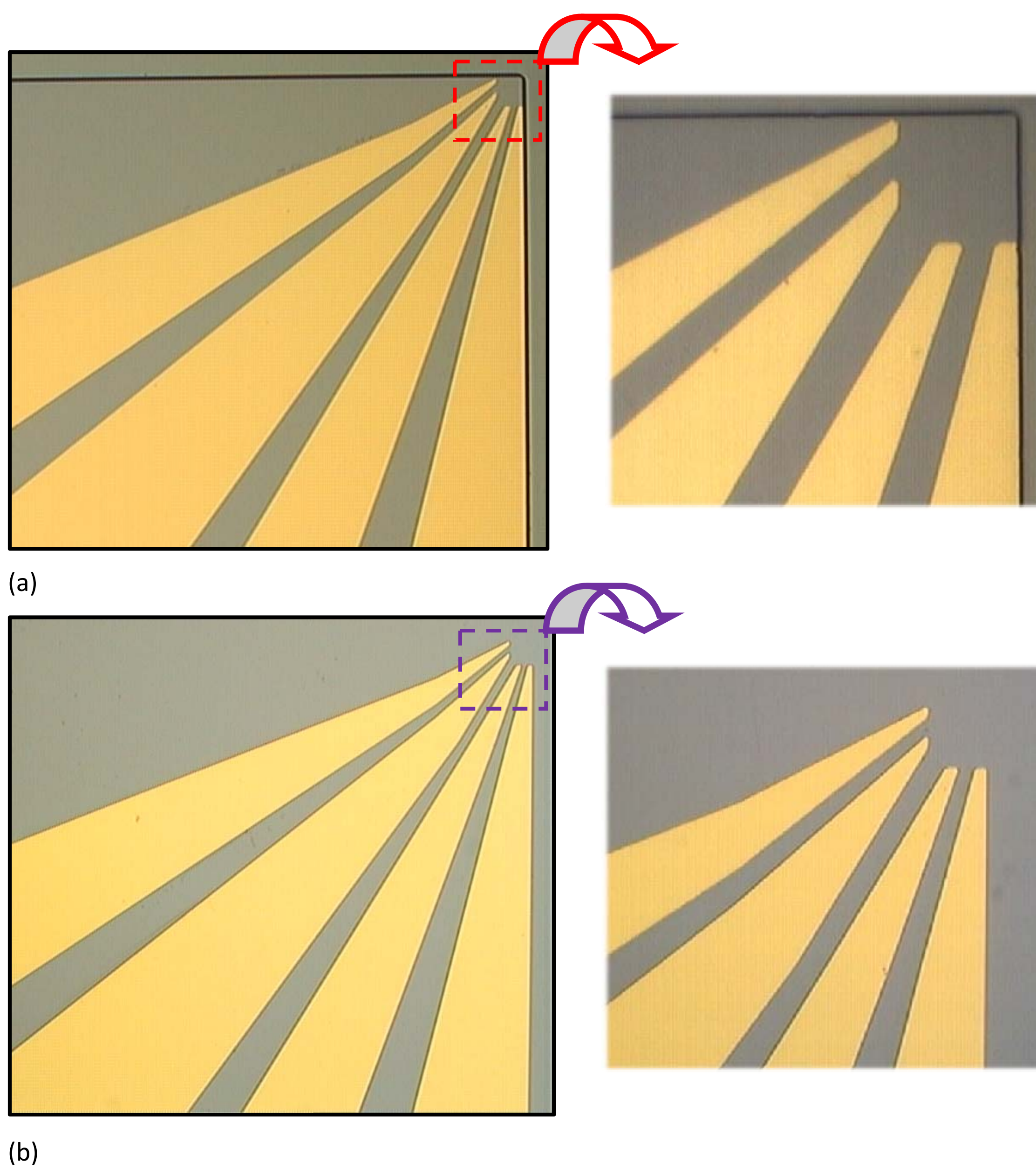

Figure 3.46: Ohmic contact metallization with (a) and without (b) mesa step.

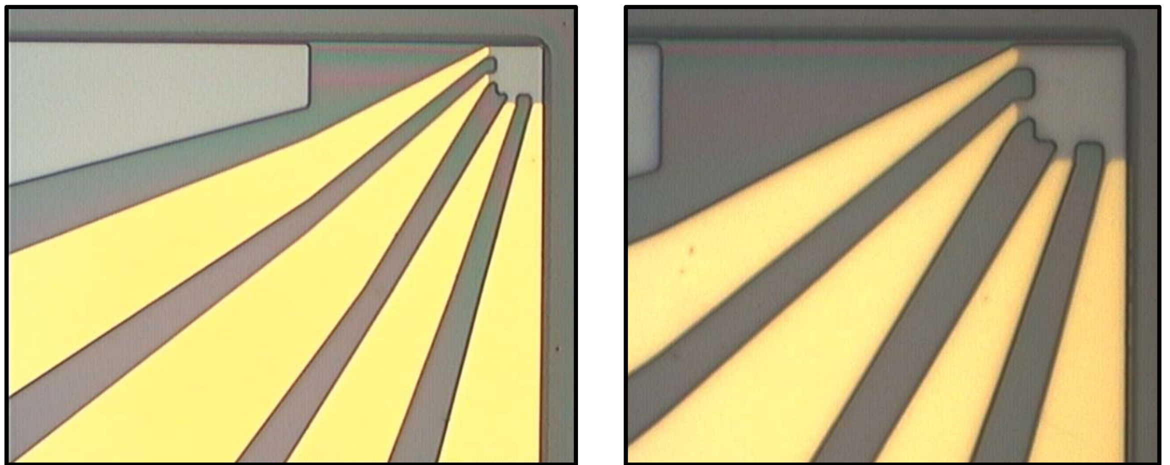

(a)

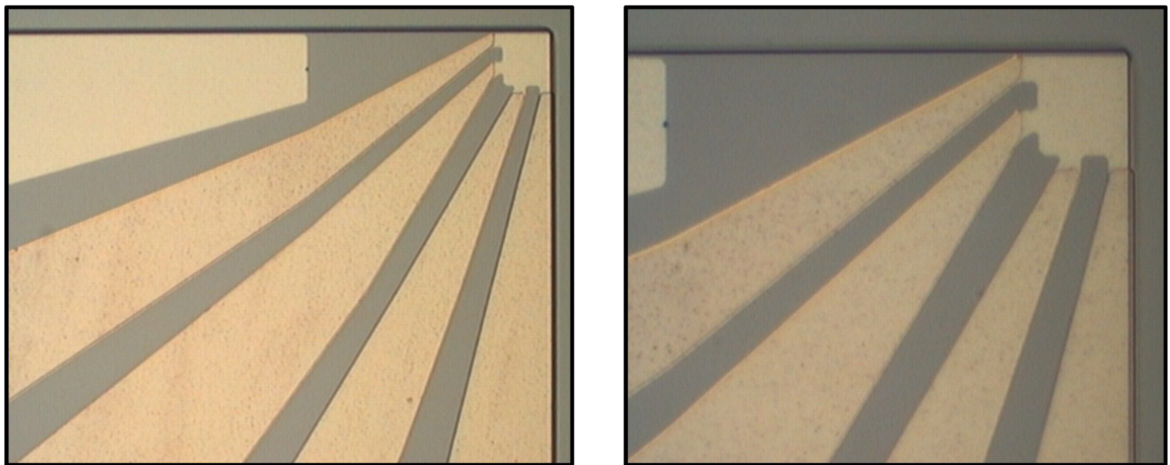

(b)

Figure 3.47: Image reversal lithography for active area definition (a) and the thin film obtained by thermal evaporation followed by lift off (b).

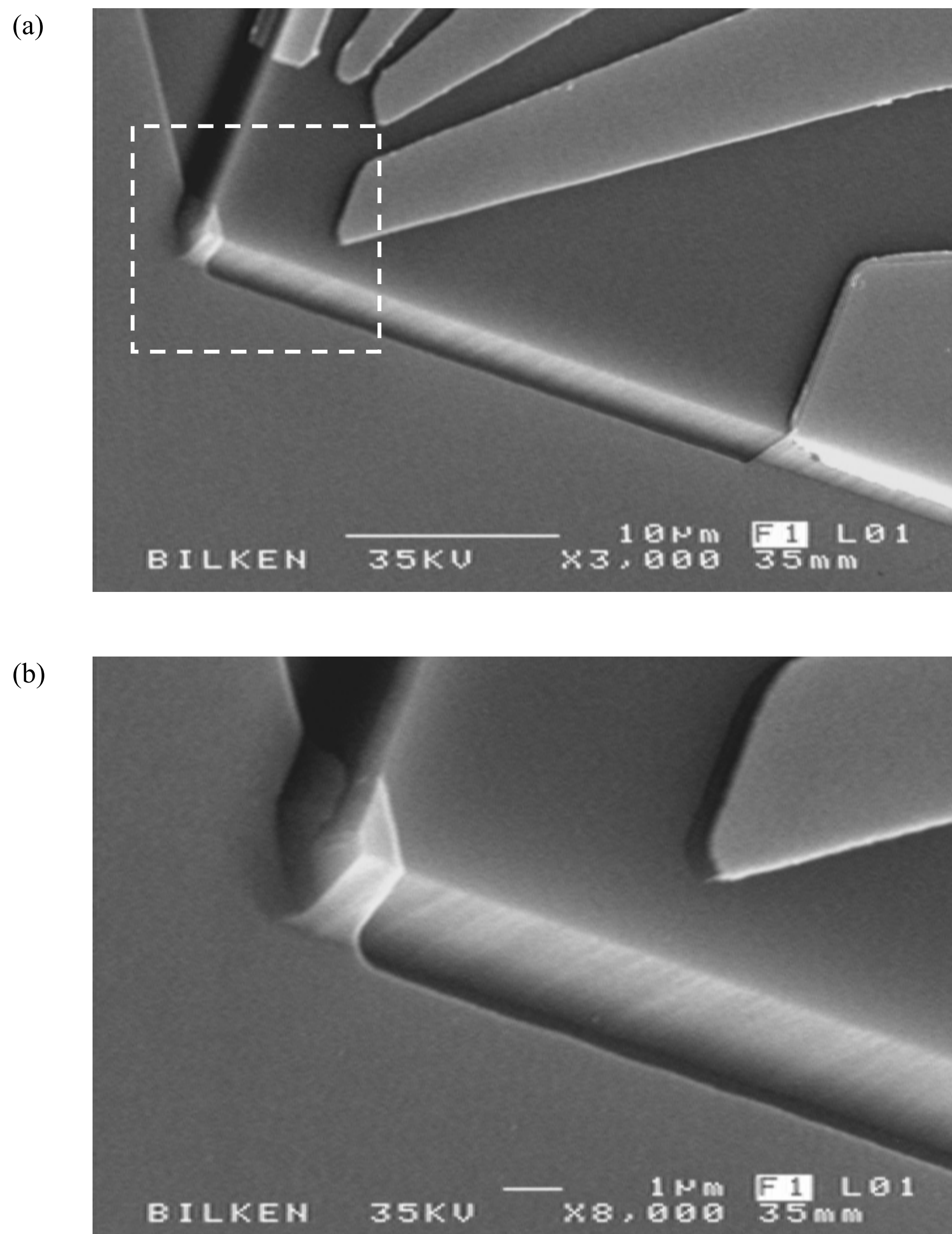

Figure 3.48: STM tip metallization.

Collaborating with Sandhu group at Tokyo Institute of Technology, prepared chips were sent to Hitachi Science Systems Ltd. located at Tsukuba, Japan. FIB Milling was done by a Hitachi FB-2100 FIB system. 50×50 nm Hall sensor structures were patterned as shown in Fig.3.49 [31] with ion currents and acceleration voltage of $25A/cm^2$ and 40kV respectively.

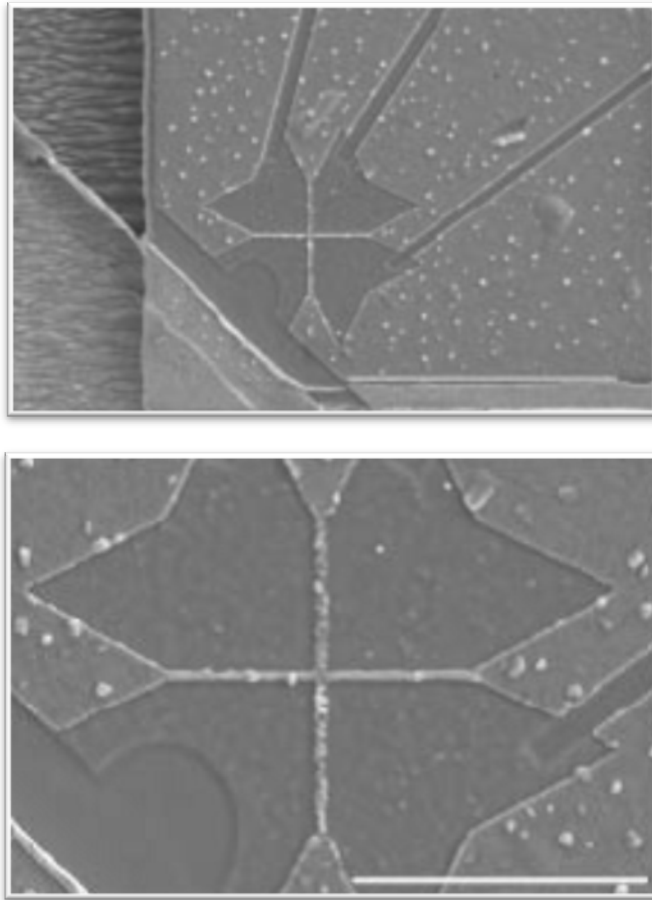

Figure 3.49: SEM images of FIB patterned typical 50nm × 50nm Bi Hall probe. The STM tip Hall cross center distance is ~4μm.

The room temperature Hall coefficient and the serial resistance of the probes were measured to be 4×10^{-4} Ω/G and 9.1 kΩ respectively. Biased with a DC Hall drive current Hall sensors' noise was measured with a spectrum analyzer. The minimum noise

level of ~1.4 G/√Hz was obtained at a 43μA Hall current. After characterization, the probe is used to scan a 5μm thick Bi crystalline substituted iron garnet film at room temperature in the lift-off mode. The stray field distribution over the sample is imaged using a RT-SHPM at Tokyo. An area of 8μm × 8μm is scanned for an image with 110G dynamic z-range as shown in Fig.3.50. This was the first demonstration of 50nm sized Bi Hall probes at room temperature. The bias current leak to STM tip prevented the proper positioning of the probe over the sample. The image is not clear as the sample-probe separation was high.

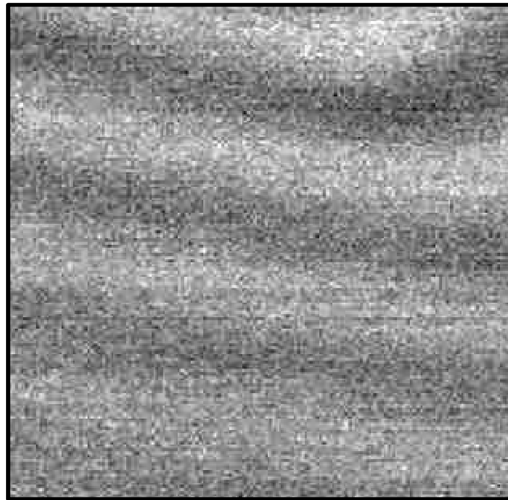

Figure 3.50: RT-SHPM image of Bi substituted iron garnet sample obtained by 50nm sized Bi Hall probe. Image size is 8×8μm and the vertical scale from bright to dark is ±55G

A further study on miniaturization of Bi Hall probes with FIB was done at the National Center of CNR-INFM S3 in University of Modena, Italy, collaborating with Prof. Marco Affronte and his group at the Department of Physics of the same institution. A FEI Strata^{TM} DB 235 FIB system is used during milling. Samples were placed on the dedicated holder for loading into the chamber. All sample surfaces were grounded by aluminum tape and conductive carbon paste to prevent charge accumulation at the

surface as shown in Fig 3.51. When this was not done the charging prevents obtaining a good focus which directly affects the writing quality as shown in Fig.3.52. FIB milling was done with 30kV acceleration voltage and 24pA beam current. Beam current decreased down to 10pA for finer definitions. Writing time was optimized to remove the thin film and not to accumulate Ga on the material as displayed in Fig. 3.53. Several probes with cross size around ~100µm were fabricated. Smaller sizes were not tried to increase the FIB yield. Some of the patterning results obtained from the fabrication is shown in the Figure 3.54 & 3.55.

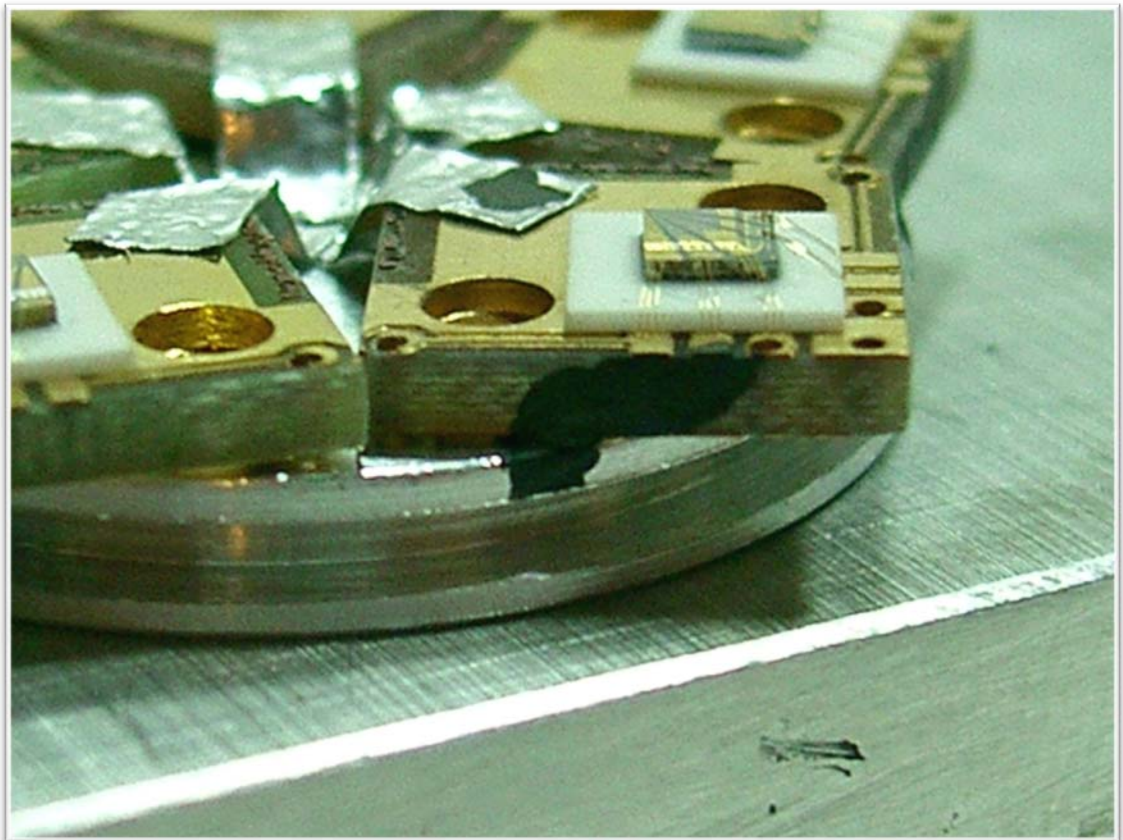

Figure 3.51: Mounting Hall sensors on a 1” sized sample holder. PCBs were mounted by double sided carbon tape. Grounding between the top layer of the PCBs and the holder was obtained by aluminum tape pieces and carbon paste.

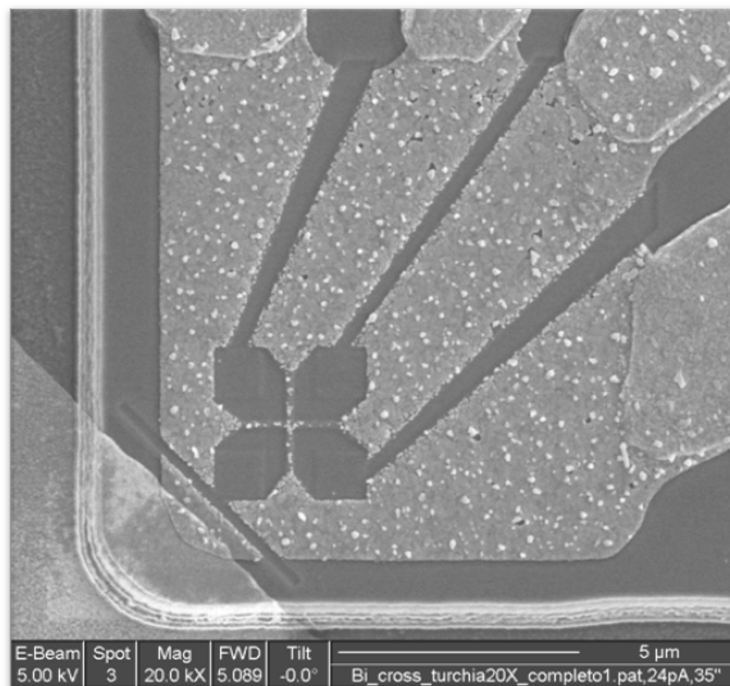

Figure 3.52: Effect of charging. The line definitions were not sharp as the beam profile could not be adjusted sharp enough and had a wide Gaussian shape.

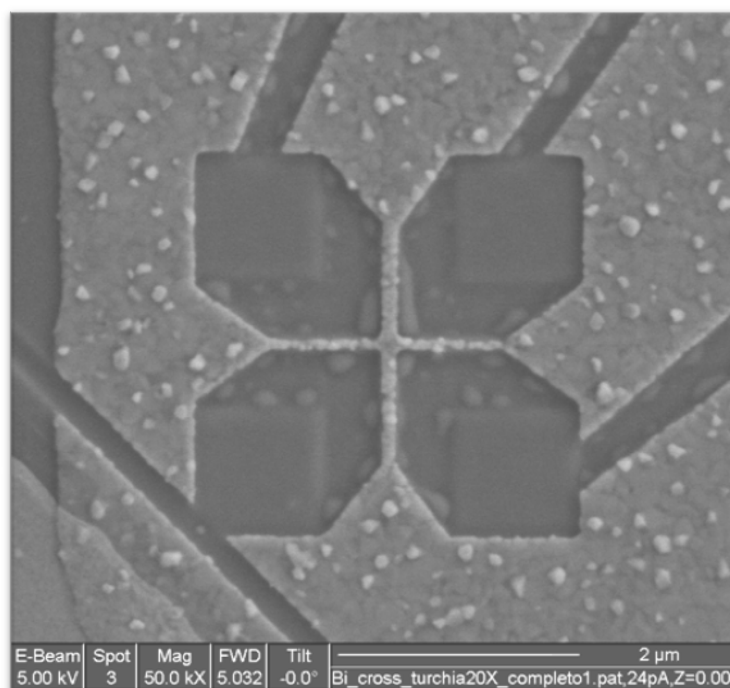

Figure 3.53: Accumulation of Gallium on the surface due to overexposure. Bubble formation around the exposed areas is the sign of accumulation.

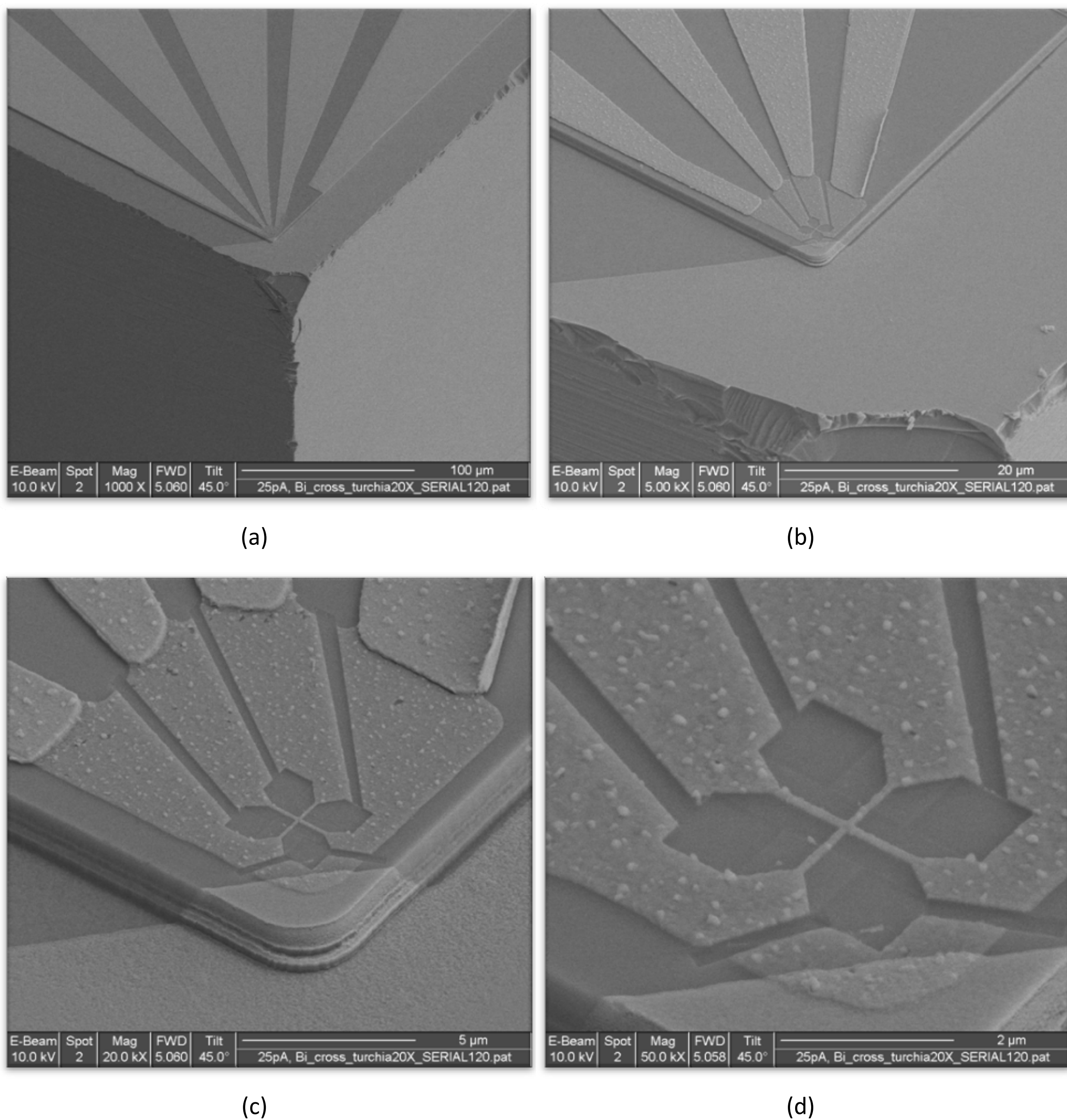

Figure 3.54: Images of a typical FIB patterned Hall probe at ×1000 (a), ×5000 (b), ×20000 (c), and ×50000 (d) magnifications. Overall chip, mesa, Ohmic pads and the STM tip can be seen.

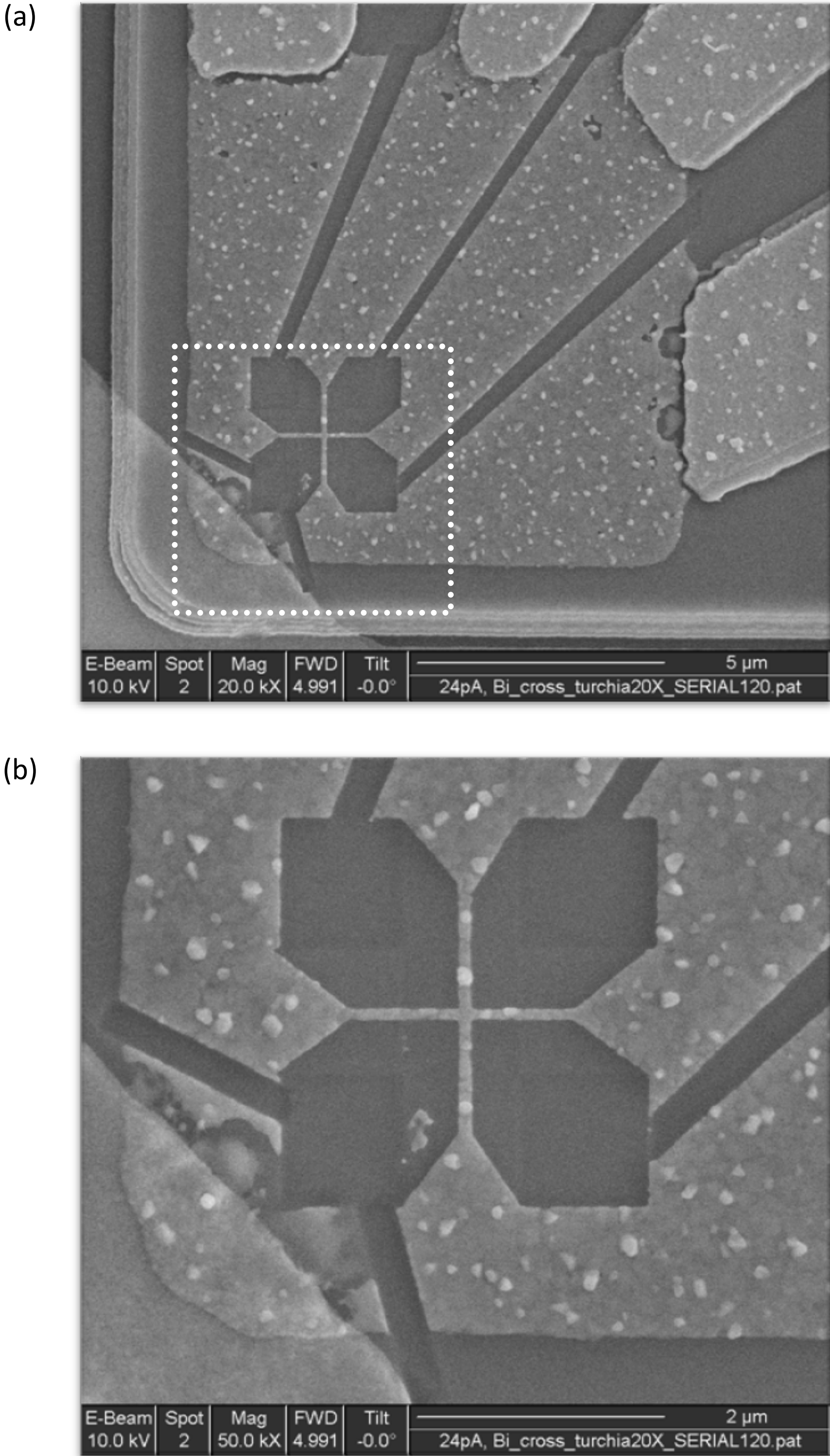

Figure 3.55: Image of FIB patterned Hall probe at ×20000 (a), with close up display of Hall cross (b)

The grounding from the chip to the PCB was maintained by the bonding wires. 5 packaged chips at a time could be loaded. Serial resistance of the probes measured to be ~3kΩ. Functionality test after the FIB patterning have been done by mounting the sensors on a micro Hall Gaussmeter of NanoMagnetics Instruments Ltd. A powerful magnet is brought close to the probe and the generated Hall voltage due to the magnet filed is observed by a Textronix TDS1002 scope. The change in the voltage sign depending on the pole of the magnet was the basic sign showing the probe had chance to work. The chips that passed this simple test mounted on an LT-SHPM inserted in to a physical property measurement system (PPMS) of Quantum Design Inc. that has a 5T superconducting magnet for further examination. A ramping field was applied with the PPMS coil and the response of the Hall sensor is observed through the scope at different temperatures starting from room temperature. The Hall coefficients calculated from the B-H curve measurements (Fig 3.56) show that there is an increase in R_H with decreasing temperature. This is due to the decrease in the total number of charge carriers due to lowered temperature.

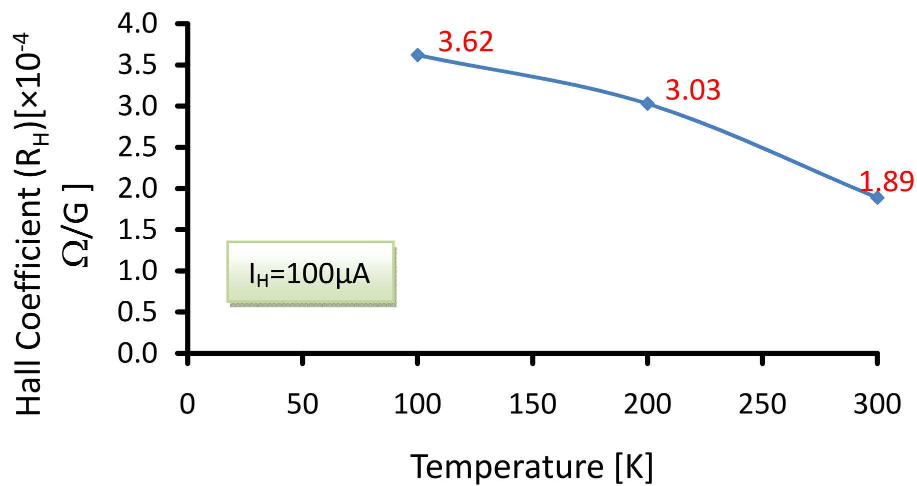

Figure 3.56: Temperature depended change in Hall coefficient of ~100nm sized Bi Hall probes.

Drive current dependent noise spectral densities of the probes at 200K and 100K were also measured. The Hall voltage signal after the low noise amplifier is measured by the TDS1002 scope and the FFT of the signal is recorded at 25kS/s sampling rate. A typical spectrum through the oscilloscope screen is given in Fig. 3.57.

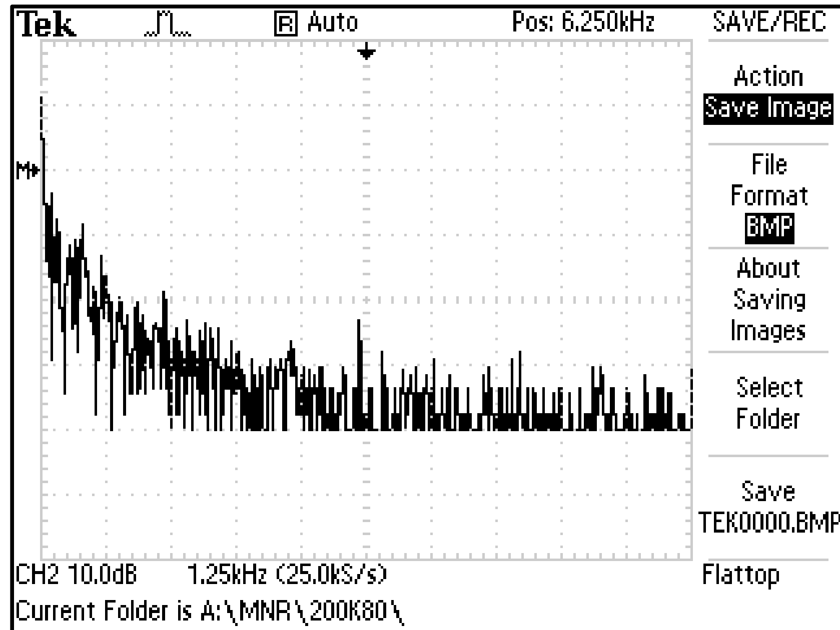

Figure 3.57: Noise spectral density pattern of the probes measured through the scope

Spectrum is measured and averaged 10 times at each drive current value. Vertical ranges were converted into Gauss and the noise spectra have been plotted at 200K, Fig. 3.58 and 100K, Fig. 3.59. Noise level is decreased by increasing the Hall currents at both temperatures in the range of the used current values. This was expected as the minimum detectable magnetic field is inversely proportional to the Hall current. The trend in the noise spectra shows that this decrease would continue up to some higher current, however the test is limited by 100µA. Johnson noise would be ~1.4 times smaller when the temperature is decreased from 200K to 100K, assuming the other parameters remains the same. But, there is a little increase in the overall noise level for high frequencies as the temperature is decreased to 100K. The reason for this could be

the decrease in the electron mobility at low temperature due to boundary scattering in polycrystalline bismuth, although number of carriers decreasing by lowering the temperature [78]. This tradeoff results in equilibrium and the minimum detectable magnetic field floor becomes almost the same for both temperatures as shown in Fig. 3.60 & 3.61. It is noticeable that the noise figures become less frequency dependent at high frequencies as the temperature is decreases. In other words, the *1/f* corner frequency shifts towards the lower frequencies. These set of probes could not be used for scanning due to the high current leakage to the STM tip, which overrides the feedback.

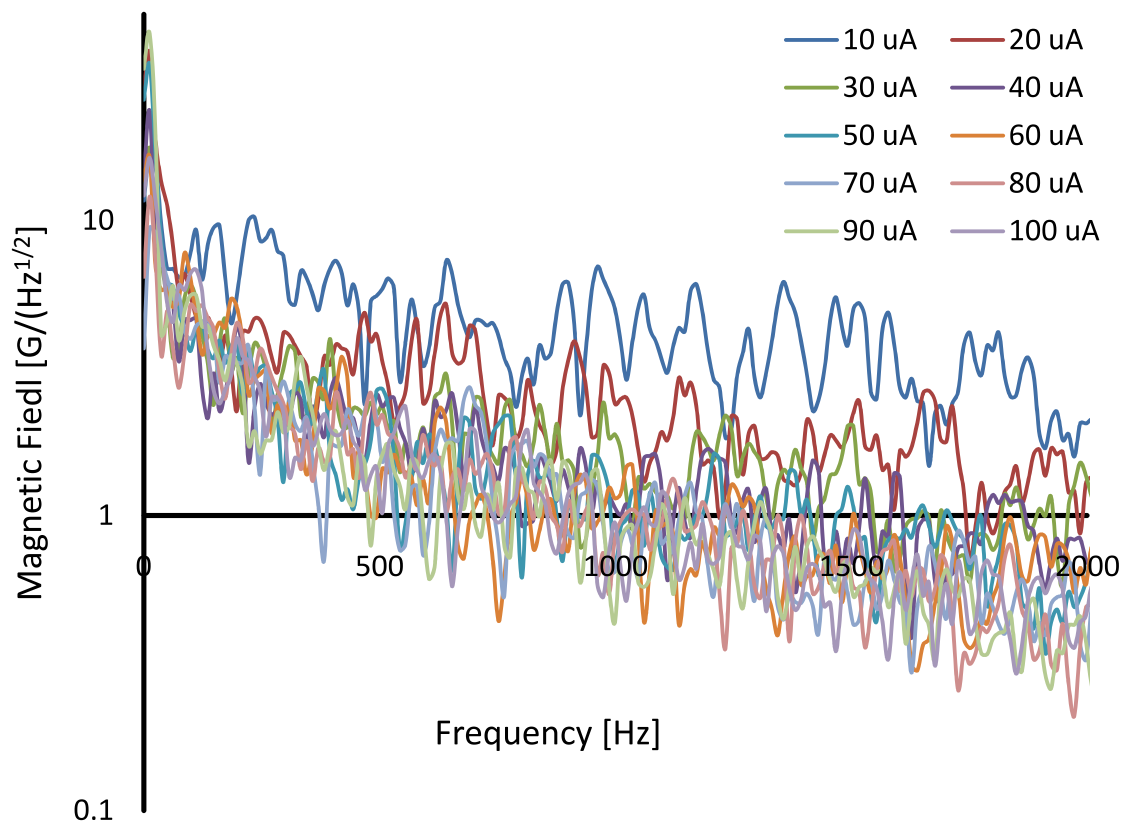

Figure 3.58: Noise spectrum of the ~80nm thick ~100nm sized Bi hall probe at 200K as a function of the frequency.

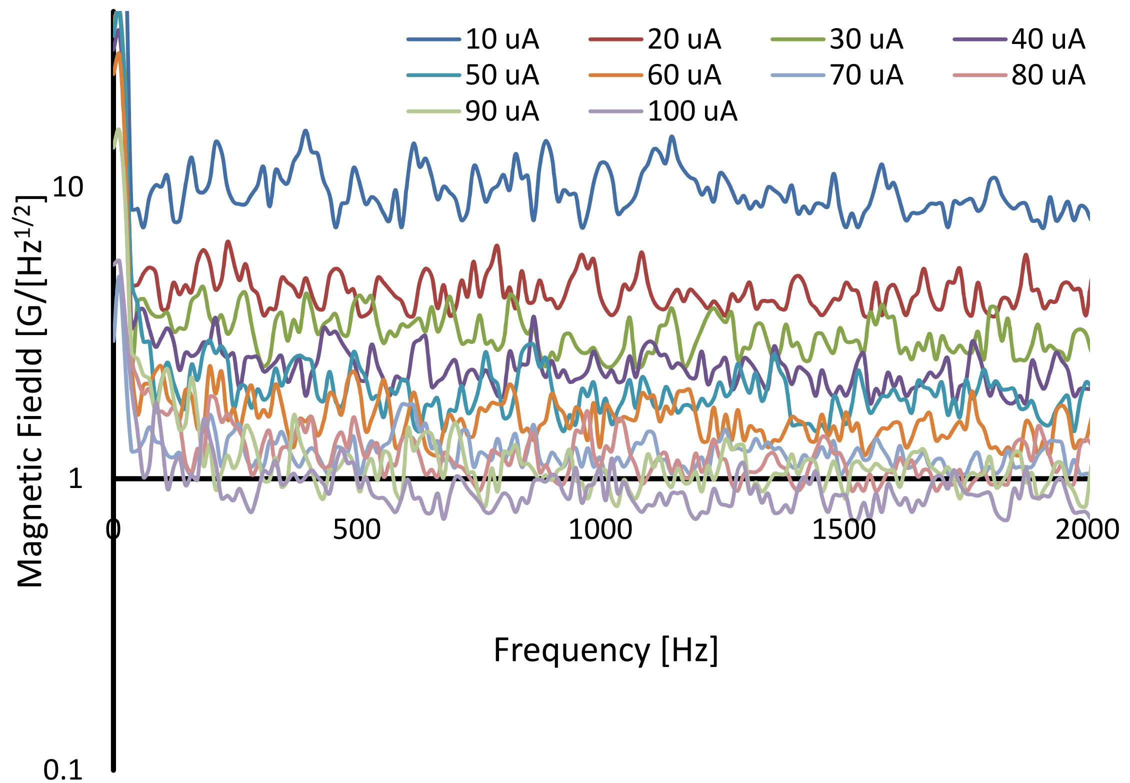

Figure 3.59: Noise spectrum of the ~80nm thick ~100nm sized Bi hall probe at 100K as a function of the frequency.

The other patterning method used in this thesis is the e-beam lithography. Electron beam (e-beam) lithography is a direct, maskless, method used to create very small structures in the resist, that can subsequently be transferred onto the substrate after the selective removal of either exposed(positive) or non-exposed (negative) regions of the resist. Electron beam lithography is not diffraction limited at the wavelength of the light used by optical lithography. This method gives the ability to produce much smaller structures. For the miniaturization using e-beam patterning, only Ohmic contact metallization and recess etch is done before the e-beam lithography step. Fine structures are then defined by e-beam lithography followed by thermal evaporation and lift off of

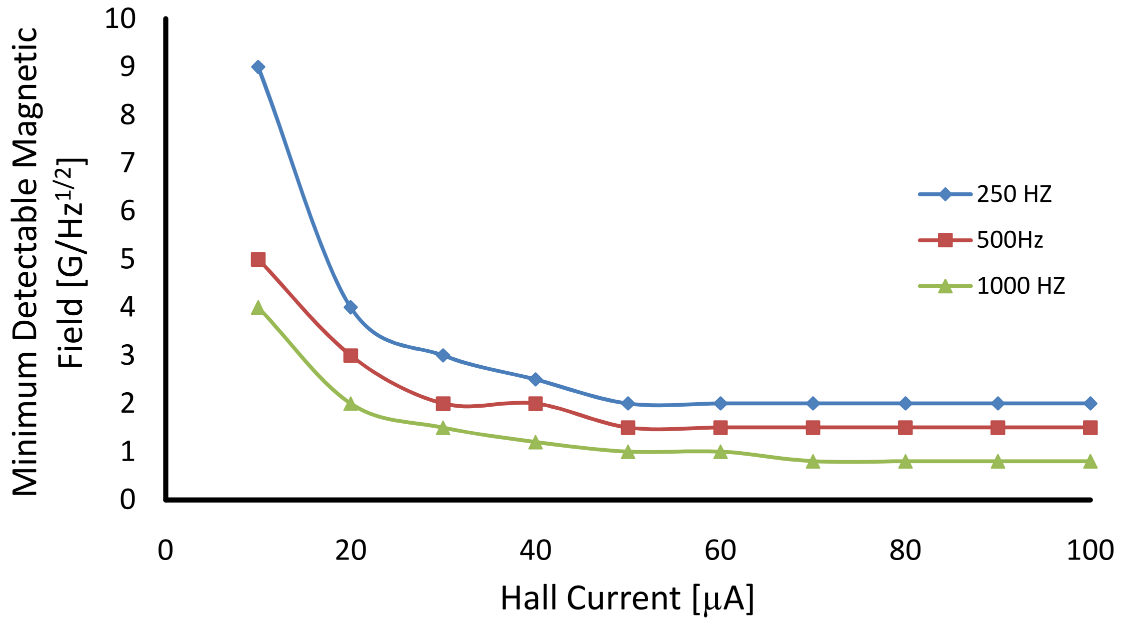

Figure 3.60: Minimum detectable magnetic field of ~100nm sized Bi probe as a function of the applied bias current at 200K

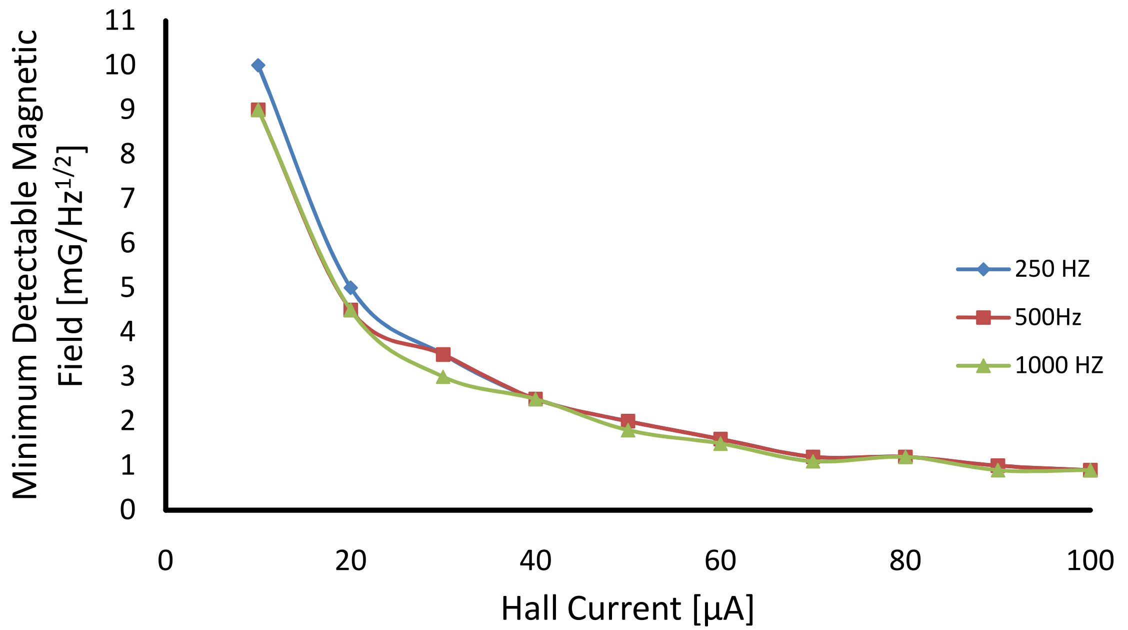

Figure 3.61: Minimum detectable magnetic field of ~100nm sized Bi probe as a function of the applied bias current at 100K

the bismuth thin film. Finally mesa step is microfabricated. The fabrication steps were conducted by this way because it was noticed that the mesa lithography causes the e-beam resist to spin non uniformly. Standard Polymethylmethacrylate (PMMA) formulated with 950,000 molecular weight resist dissolved in chlorobenzene was used for e-beam patterning. PMMA is most commonly used resist as a high resolution positive resist for direct write e-beam lithography as well as x-ray and deep UV microlithography processes. Cleaned samples were spun by PMMA at 1,000 rpm for 6s followed by6,000 rpm spin for 60s. PMMA is applied onto the chips continuously during the slow spin to obtain more homogeneous film with ~100nm thickness. Prebake was done at 160ºC for 2 hours in oven. A JEOL JSM6400 scanning electron microscope (SEM) with an attached e-beam pattern generator & beam controller was used for the lithography. This pattern generator is the first e-beam lithography system in Turkey and is a homemade system which was built by Dr. İsmet İnönü Kaya during his Ph.D. thesis [79]. The system consists of control electronics, an A/D converter and control software written in Pascal with a total cost of ~$1000. The program reads the solid object drawings from DXF file output of AutoCAD-10 & AutoCAD-14 software. The necessary information like size, corner points, and color etc., are read and used to adjust the expose parameters. Only solid rectangles are accepted. The color value of the drawings converted to the dose value. Index color 5 (blue) is defined as the base dose. If the solid rectangles are in color 5 than the set dose applied 1/1. If, for example, the shapes are white in color, that is index color 7, then set dose value is multiplied by 7/5 before that shape is exposed. Typical pattern design can be seen in Fig. 3.62. Samples were placed on the SEM holder and fixed using two brass leaf springs. All the electron-optical alignments of the SEM, gun tilt & shift, focus, astigmatism etc., were done to obtain a fine beam shape before the exposure. Adjustments were done at the probe current and extra high tension applied to accelerate the electrons values that will be used during the exposure. This was repeated whenever a new sample is loaded. Since it is nearly impossible to place the sample without tilt, each scan area on the chip will have to have small adjustments in focus. To do this, three distinct points were selected on the wafer and their 3D coordinates were introduced to the program. The lateral coordinates

(X&Y) contains the position information in chip plane, whereas the perpendicular (Z) coordinate is the focus value of that particular point. The software later can automatically calculates the fine focus parameter at any point of the defined plane and sends this information to the SEM. Alignment of the wafer was manually done with the aid of the cross hair on the screen.

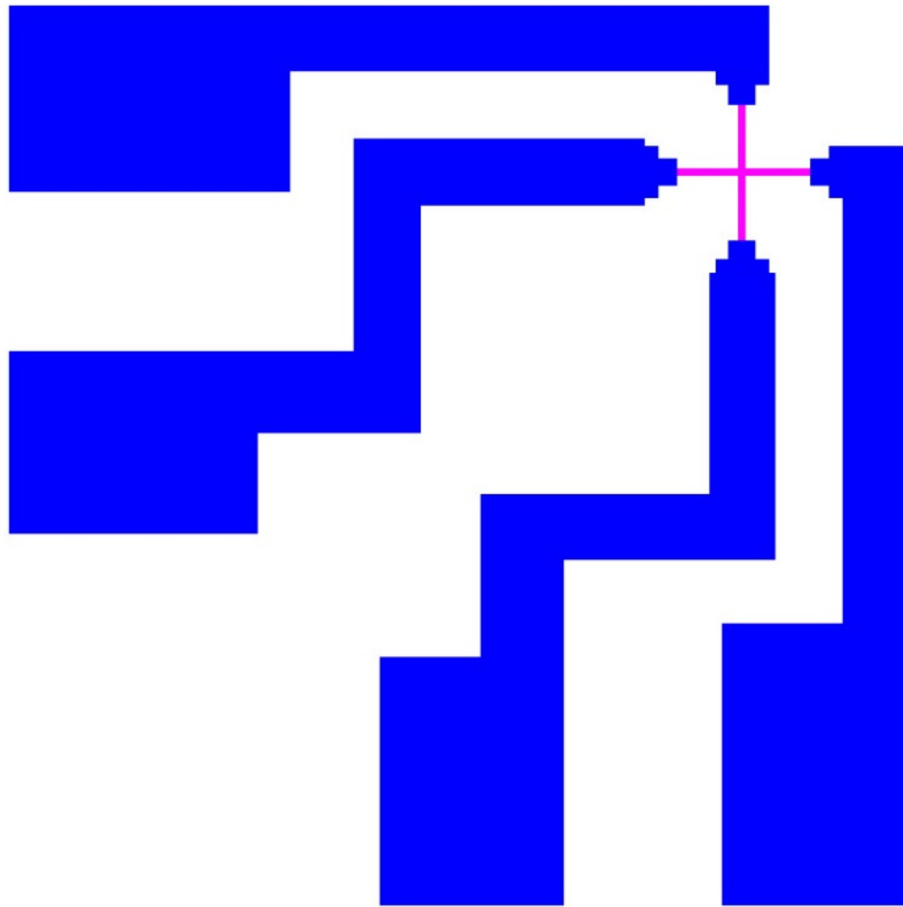

Figure 3.62: Solid drawing of the e-beam pattern designed for 100nm wide Hall probes. The shape composed of 23 individual rectangles. Different index colors gives ability to expose at different dose values in a single drawing.

The alignment has to be done quickly as the sample is also exposed during that time. Having the alignment is completed; beam blanking set on to protect the area from the

further exposure. Alignment of the sample was done at the same magnification in which exposure is done to prevent drifts and shifts due to the magnification change. The exposure parameters, dose & dot separation, were set through the software. Dot separation is the measure of the beam resolution and indicates the pixellization of the area. The minimum pixel size is determined by the field of view at that particular magnification and the resolution of the A/D converter. Our A/D converter has 12 bit resolution which means that it can divide the field of view in to 4096. Thus, if a 5nm dot separation is desired the maximum pattern size can be 20.48μm × 20.48μm. For bigger structures lower resolution has to be set. The physical limitation to the dot separation comes from the beam size obtained with the tungsten hairpin filament used in our SEM. The exposure was done at ~30pA probe current with 40kV extra high tension (EHT) voltage setting the base dose to 200μC/cm^2. The acceleration voltage value was the maximum achievable with our SEM. The EHT voltage set to highest and probe current to a relatively small value to increase the resolution. The value of the acceleration voltage is important because the current density and the sensitivity of the resist are depended on it. The resolution is less depended on the spot size but more on the scattered electrons. . There are two types of scattering taking place in the solid, which are elastic and inelastic scatterings. Collision of incident electrons with atoms in the material is an elastic scattering process, because of the huge mass difference of an electron and atom. When an electron undergoes with elastic scattering, it does not lose its energy immediately but change its direction. The incident electron will lose its energy while interacting with the other electrons in the material. During these inelastic scatterings with the material, electrons' beam energy is deposited into the material which is the e-beam resist.

Monte Carlo simulations show that he penetration depth of electron is known to increase when the EHT voltage is increased and the functional relationship is $V^{3/2}$[80]. At the acceleration voltage 10 kV or below the lateral spread of the electrons at the surface is almost the same as the penetration depth. At higher than 30 kV, the lateral spread becomes very small. Electron forward scattering is primarily dependent on incident electron energy and it is clear that electrons will have much less broadening

due to forward scattering when the EHT voltage is higher. Forward scattering gives rise to an intra-proximity effect meaning the scattered electrons will stay in the exposed pattern. On the other hand, the backward scattering gives rise to inter-proximity effect between the exposed patterns. Thus, the effect on the resist from the forward scattering is smaller than the backward one. So, if the EHT voltage is high, this will decrease the exposure of resist due to scattered electrons [81, 80]. The resist thickness is also important. Coulomb interactions, are also limits the resolution. Boersch effect where electrons repel each other in the beam direction causing energy spread among electrons which result in chromatic aberration; and Loeffler effect in which electrons repel/collide each other in the radial direction that causes trajectory change and energy spread among electrons resulting in chromatic and spherical aberration has to be considered [82].

Exposed samples were developed in 1:3 methyl isobutyl ketone (MIBK): isopropanol mixture for 60s. Development time was calculated as 30s, plus 30s for each 100nm resist thickness. Samples are dipped in to isopropanol for another 60s to stop the development and blow dried with nitrogen. Chips were loaded into evaporation chamber and the pumped down for a vacuum level of $\sim 4\times 10^{-6}$mbar. ~30 nm bismuth film was deposited by thermally evaporation and ~100nm Hall crosses defined by liftoff after the evaporation. The thickness of the film is held thin for easy lift off and to examine the effects of the film thickness, since decreasing the cross size below 50nm require to have the film thickness <50nm as well. Although some of the probes exhibited reactions to the applied magnetic fields, generally the noise was too high. The serial resistances were measured to be ~700kΩ which is very high compared to the previous results. The high resistance is probably due to the small thickness of the film. Note that the bismuth evaporates to a polycrystalline film. It is possible that for a certain small thickness the scattering due to the boundaries of the crystalline structures creates such a high resistivity considering the width of the Hall crosses is also small. In a similar study, Petit *et al.* [76] compared the average noise densities of bismuth probes with different thicknesses. In this study probes with 29nm film thickness has minimum 1000nm width

while the probes with 78nm and 152nm Bi film thickness studied down to ~50nm. This could have the same reasoning supporting the idea above. El-Sayed reported considerable increase of resistivity in thermally evaporated Bi thin films thickness less than 35nm [83]. He attributed the variation of resistivity at small thicknesses to the increase in the concentration of grain boundaries due to the decrease in crystallite size, and increase in lattice defect density and the internal strain which, we believe is a further evidence of our prediction.

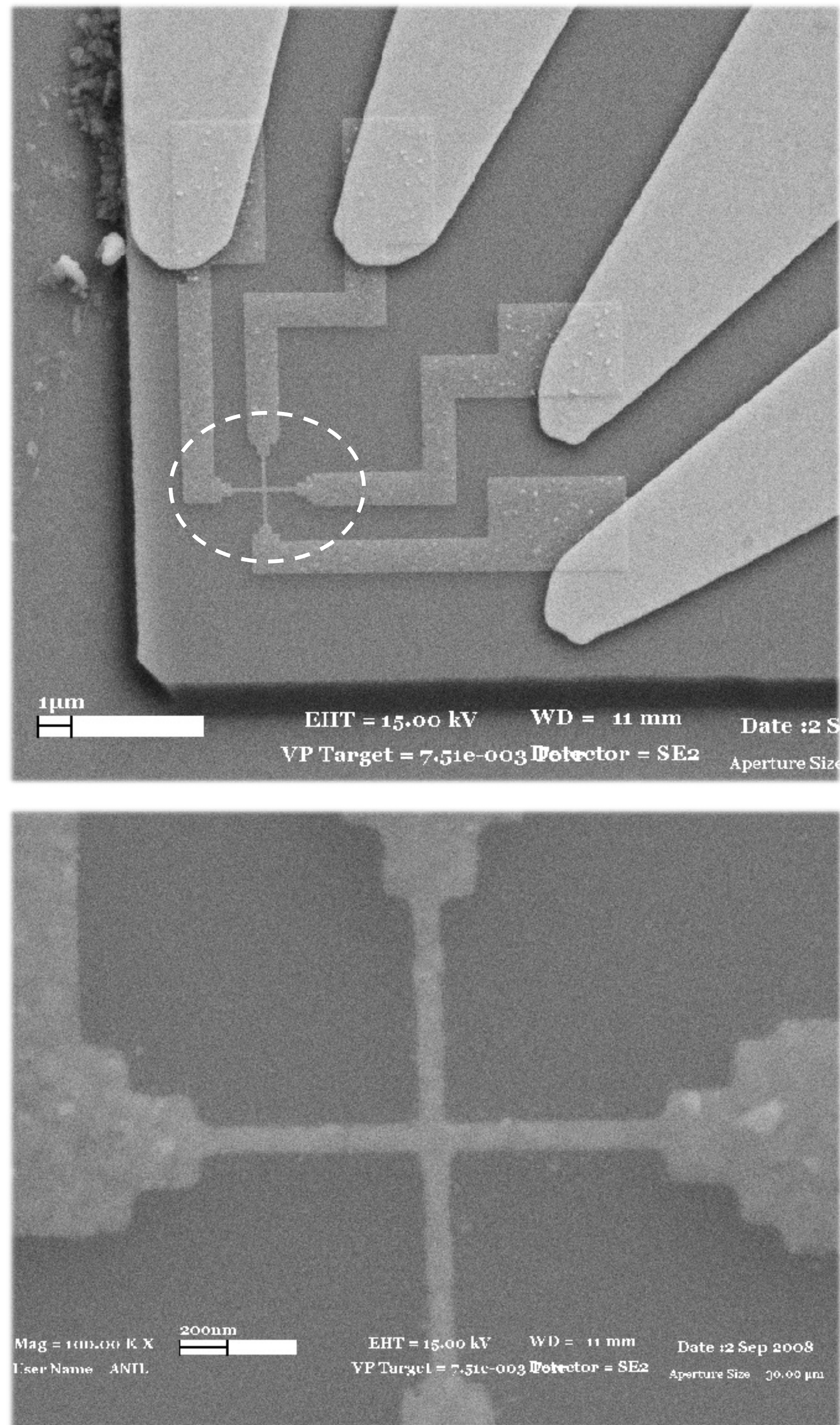

Figure 3.63: 100nm Hall probe fabricated by e-beam lithography and Bizmuth thermal evaporation & lift-off.

Chapter 4 : Quartz Crystal AFM Feedback for SHPM

A new approach to image the non-conductive magnetic samples employing quartz crystal tuning forks will be presented in this Chapter. Tuning fork-Hall probe integration, characterization and imaging at various temperatures using different samples will be described.

Some parts of the studies discussed in this section is published as "Scanning Hall Probe Microscopy (SHPM) Using Quartz Crystal AFM Feedback, M. Dede, K. Urkmen, O. Girisen, M. Atabak, A. Oral,I. Farrer, and D. Ritchie, Journal of Nanoscience and Nanotechnology Vol:8 no:2, pp. 619–622, 2008". Copyright 2008 The American Scientific Publishers.

4.1 Introduction

Although the first Hall microscopes were demonstrated by Goren and Tinkham using step motors [68], the technique is improved further in 1992 when a GaAs/AlGaAs Hall probe is integrated with an STM tip to track the surface with STM feedback [29]. This brought the opportunity to resolve the magnetic field profile of the samples with much greater accuracy and resolution compared to its predecessors. Due to its physical nature, tunneling phenomena requires a certain level of conductivity of the inspected material so that the electron can tunnel through the vacuum or air barrier overcoming the energy barrier. But, not all of the samples are conductive and not all samples can be covered with a thin layer of metal to achieve certain surface conductivity, sufficient enough to have the tunneling. So, this brings a significant limitation to the possible samples for inspection. The solution came in 1986 when Binnig, Quate and Gerber

invented the first Atomic Force Microscope (AFM) [6] which enabled the detection of atomic scale features on a wide range of insulating surfaces that including, biological samples, and polymers. The first combination of AFM and SHPM was shown by Chong *et al*. in 2001 [70]. In this study a Hall sensor is patterned by e-beam lithography and bismuth lift off on an AFM cantilever, which is fabricated from Si_3N_4 membrane. The cantilever was resonated at its resonance frequency by a dither piezo and a laser beam was focused onto the cantilever to measure its vibration. Heterodyne interferometer detection method has been used for detection. The room temperature resonance frequency and the Q values of the free oscillating cantilever were 157kHz and 600 respectively.

In a similar study, Mouaziz *et al*. [75] incorporated bismuth Hall sensors on a photo-plastic cantilevers made by SU-8 photoresist. For a rectangular cantilever of dimensions 500×100×10μm (length×width×thickness), the resonance frequency and the estimated spring constant were 17 kHz and 1 N/m respectively. A relatively small Q factor, 30, has been reported, which was measured in air.

Brook *et al.* [38, 39], however, applied the idea of piezoresistive cantilevers to GaAs/AlGaAs 2DEG materials. The advantage of the piezoresistive cantilever method shown in this study was indicated as that Hall sensor and the cantilever were fully integrated on one chip which requires no external displacement sensing element. This brings the design simplicity of the displacement detection system which is accepted as the major advantage, while working in a low-temperature environment where the size of the scanner unit is. As the ultimate idea was to obtain a Hall sensors having high level of magnetic field sensitivity, the design and the material selection of the cantilever had to be done accordingly. For the fabrication of a low-noise Hall probe a high-mobility $Al_{0.3}Ga_{0.7}As$/GaAs two dimensional electron gas (2DEG) required to be grown at the surface. Thus, the n-$Al_{0.4}Ga_{0.6}As$ layer of the grown wafer selected as the piezoresistive sensing element since the Al content of the material could be adjusted to maximize the piezoresistive coefficient. The chip was mounted to the end of a piezo actuator and the

piezoresistive response was detected using a lock-in amplifier. The resonance frequency of cantilevers with 1nm oscillation amplitude reported to be between 18–21 kHz and *Q* factors were 300–500 at open atmosphere conditions. The cantilever dimensions were 400×150×6μm (length×width×thickness).Although sophisticated, the approach has its own difficulties. First of all, wafers can be used for this application are limited due to the design considerations. Not any available material, like the ones presented in Chapter 3, can directly be used. In addition to that, the cantilever is fragile due to its material. Extreme care should be given while cleaning even a sample, nitrogen blow cleaning to remove dust particles can easily break the cantilever.

All the mentioned studies have relatively complex fabrication steps and especially fabrication of cantilevers requires a huge effort. However, the opportunities brought by the use of AFM feedback cannot be disregarded. Thus solution lies in a much simpler method that will unify the process simplicity with versatility. The answer, we proposed, was to use the quartz crystal tuning fork as the force sensor. Quartz crystal force sensors have been used in Scanning Probe Microscopy (SPM) for a wide range of applications [84]. They have also been used to track the sample surfaces in Scanning SQUID Microscopy [85], where the SQUID chip is glued directly on the quartz tuning fork. The method was also realized by Karrai *et al*. [86], who took advantage of mechanical resonance of a piezoelectric tuning fork to control the tip-sample distance in a near field scanning optical microscope. They are also have used in magnetic force microscopy (MFM) [87] and alternating gradient magnetometry (AGM) [88].

Quartz crystal oscillators have been used as frequency standards in electronic instruments, digital clocks and watches. They provide time standards with extremely high accuracy at a very low cost. Their simplicity and accuracy has encouraged the application of quartz resonators as sensors. Crystal quartz has highly stable elastic properties with very low hysteresis which make it suitable for mechanical resonator sensors with a frequency dependent on applied stress. Quartz also has the advantage of being piezolelectric which enables the vibration to be maintained and measured by a

simple electrical drive circuit. This brings the opportunity of not using any external optical system for force detection, which simplifies the design considerations tremendously. Tuning fork sensors do not suffer from resonance shift which is a problem in silicon based cantilevers [89]. Also, the dithering amplitude of tuning forks is much smaller than the conventional cantilevers due to its low spectral noise density, which is around 100fm/√Hz [90].

Tuning forks are usually used by attaching a tiny sharp metal tip to the end of one of the prongs of the fork. Later, the measurements are done by driving the fork at constant amplitude and observe the changes in frequency shifts, while bringing it to the sample surface. To be useful, the change in the fundamental resonance of the fork should be measured accurately. This can be done with two different methods [89]. In the first method the tuning fork is excited by a dither piezo driven at a fixed frequency, measuring the amplitude changes due to tip-surface interactions [89, 91]. In the other method [86], however, fork is shaken at its mechanical resonance frequency using a Phase Locked Loop(PLL) system by a help of the dither piezo. One of the In the first method, when the fork is close to the sample surface a reduction in this oscillation amplitude gives the measure of the forces acting up on the tip attached to the end of the fork. Thus, if this amplitude signal is fed to the feedback control electronics, while the sensor is moved over the sample, the mapping of the topography is achieved. This can simply be done by using a lock-in amplifier. The piezo is dithered at the resonance of the cantilever to have maximum amplitude with a sinusoidal drive voltage either by the internal frequency generator of the lock-in amplifier or with an external frequency generator. The amplitude signal measured by the lock-in amplifier from the mechanical movement of the tuning fork is used as the error signal. If the outputs of the lock-in are offset nulled when the probe is away from the surface, later any change in this amplitude, excluding the disturbances, can be fed in to electronics to control the feedback at a set value of amplitude decrease. This amplitude decrease is usually the full width at half maximum value of the initial amplitude. In spite of many advantages stated above, two critical drawbacks of the tuning fork reported in its practical use.

These are high stiffness and slow response. Stiffness is not a big problem if Q can be increased. In order to overcome the slow response problem, a phase-locked-loop (PLL) detection scheme was suggested [92]. Proposed by Giessibl *et al.* [93] the method is based on the frequency modulation method, which measures the shift in the resonance frequency of the tuning fork. We have employed a phase-locked loop (PLL) which outputs a voltage proportional to frequency shift (Δf) of the quartz crystal tuning fork.. While the combined sensor is approached to the surface, the resonant frequency of the sensor shifts because of tip-sample forces. The frequency shifts measured by the PLL is used for AFM feedback to keep the sensor-sample separation constant with the feedback loop. The SHPM Control Electronics is modified to detect AFM topography and the phase signal generated by the PLL, along with the magnetic field image.

4.2 Sensor Preparation

The hall sensors are fabricated with the methods described in related sections of Chapter 3. Commercially available quartz crystal tuning forks (QTF) are first extracted from their hermetically sealed cans. This is simply done by carefully squeezing the end of the can by a pair of long nose pliers. The electrical leads were detached using a soldering iron. These leads are magnetic. Afterwards, they are fixed on a sensor holder made out of 10×10mm printed circuit board(PCB) using a low temperature compatible epoxy and electrical contacts to the quartz crystal are then soldered. The Hall sensor chip, whose dimensions are 1mm × 1mm × 0.5mm, then attached, using either low temperature compatible glue or super glue depending on the application, at the end of free prong of 32.768 kHz or 100kHz quartz crystals, which are used as force sensor. While attaching the chip it was placed to the end of the probe as much as possible not to affect the stiffness of the cantilever. However, due to the mass of the chip the resonance frequency shifts towards the smaller values. Used glue can also affect the resonance properties of the tuning fork. In our case the mass of the attached chip is far bigger than the mass of

the glue. Nevertheless excess use of glue was avoided. The electrical connections to the Hall sensor is established using 12µm sized gold wires.

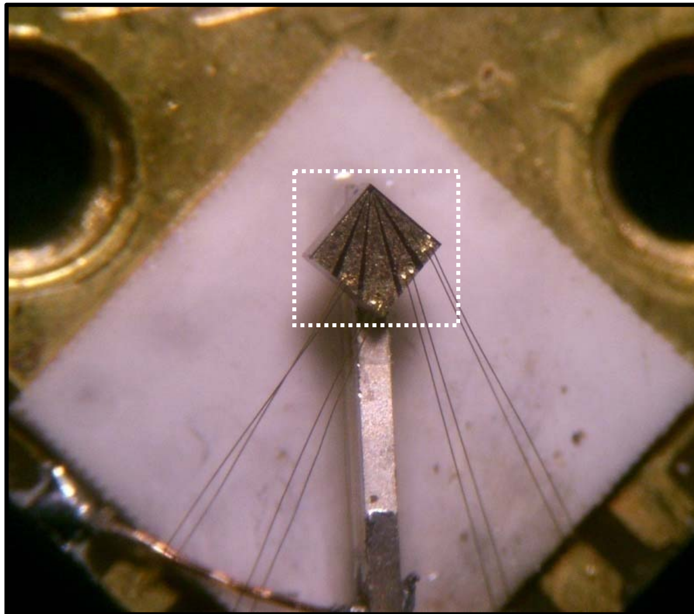

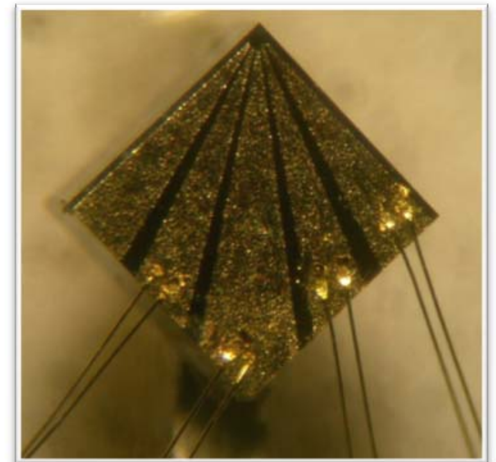

(a)

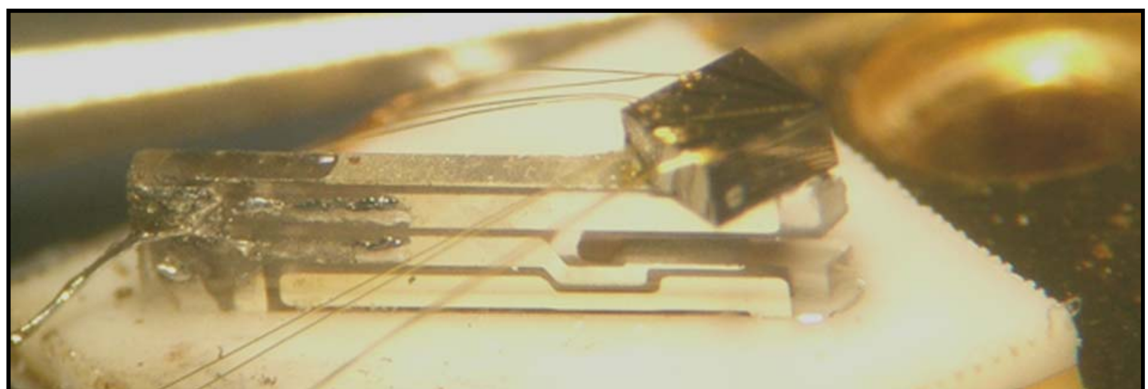

(b)

Figure 4.1: Top (a) ands side (b) view of the quartz tuning fork Hall probe combined sensor after packaging.

4.3 Characterization

In order to investigate the loading effect of Hall probe chip on the resonance frequency of the quartz tuning fork detailed calculations have been done. A vibration of the Quartz crystal can be considered as a driven damped oscillator. The problem can be simplified by considering the motion of a prong as a fixed-end and free-end cantilever model. Therefore, the motion of a prong can be considered as a 1-dimensional driven oscillator [92]. These calculations were done based on two simplest models; Simple Harmonic Oscillator (SHO) and Cantilever Beam Theory (CBT). Calculations done were based on a tuning fork with central frequency of 32,768Hz. According to calculations based on these two models, the combination of HP with QTF gives a typical resonance frequency of 31.7kHz (SHO model) and 21.2kHz (CBT model). Further studies were done by using the computer simulation program, COSMOS DesignStar, these QTF's were investigated for different mounting techniques as shown in Fig. 4.5. The first 5 vibration modes were calculated for both mounting types (Fig. 4.6 & 4.7) however, the torsional and lateral vibration modes are not interesting for our application so the rest of the text will consider only the related modes. It has been observed under unloaded (no Hall probe attached to QTF) condition when both prongs are free then we have two modes of operation, namely symmetric (both prongs are vibrating up and down in phase) with 16.581 kHz, (close to CBT model) and Asymmetric (prongs are 180º out of phase while vibrating up and down) with 31.729 kHz (close to SHO). Effect of fixing one prong showed up as an elimination of the asymmetric mode and we get single frequency of 17.595kHz. Simulation results after adding Hall probe to the QTF show similar results as in the case of free prong as we can observe the presence of both type of resonance frequencies; 17.138kHz (symmetric mode) and 31.4kHz (asymmetric mode) and under one prong fixed condition we have single frequency at 17.6kHz. These values are in close agreement with the calculated values from CBT (symmetric mode) and SHO (asymmetric mode) models. The slight discrepancy in the theoretical results,

(a)

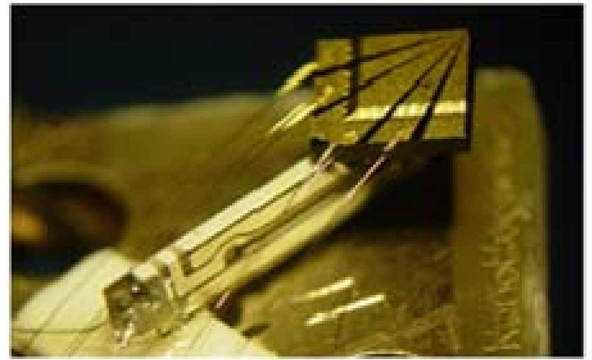

(b)

Figure 4.2: One prong free (a) and two prongs free (b) configurations of combined sensors.

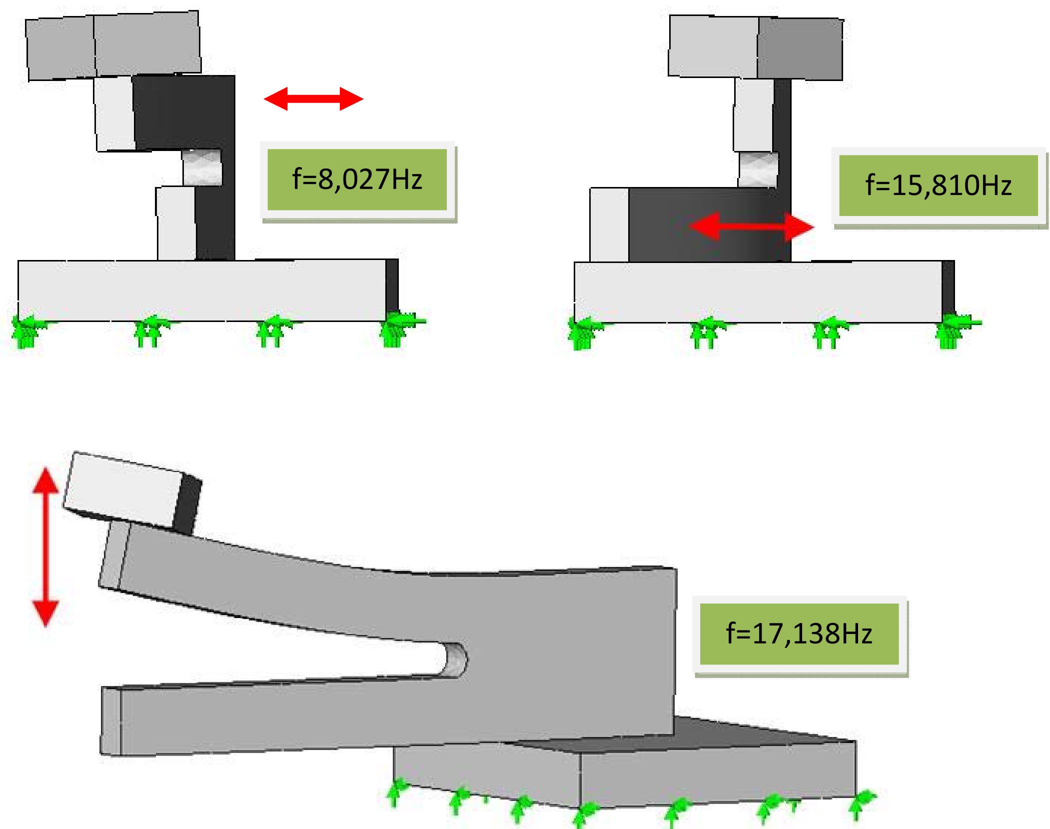

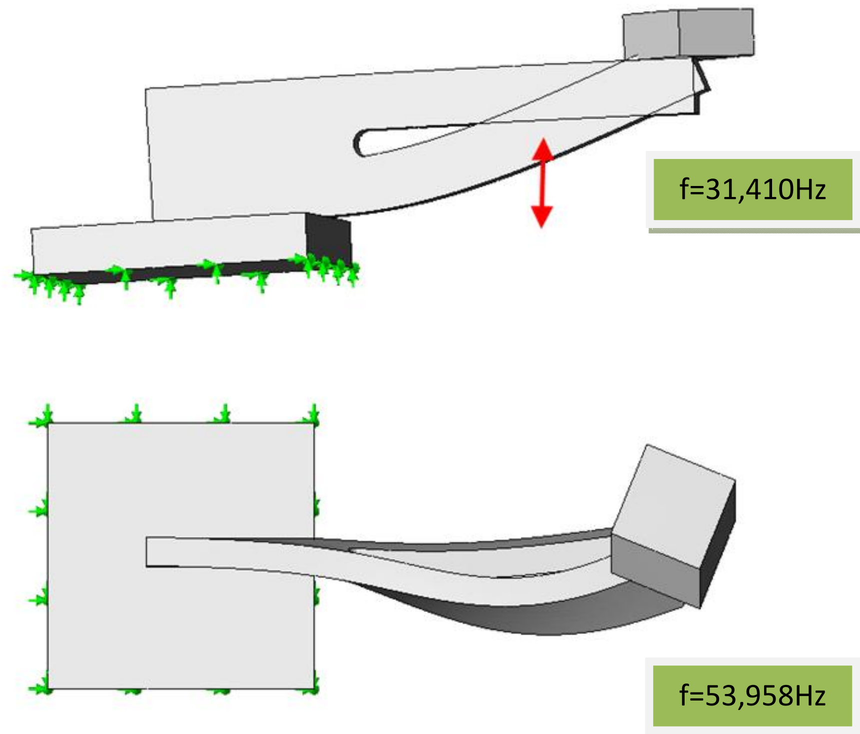

Figure 4.3: First 5 vibration modes of two prongs free configuration obtained by finite element analysis.

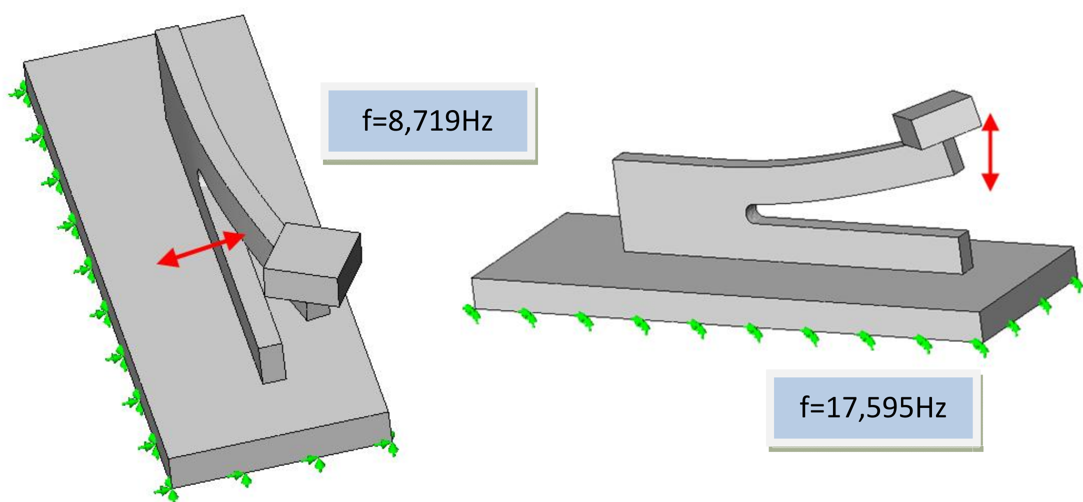

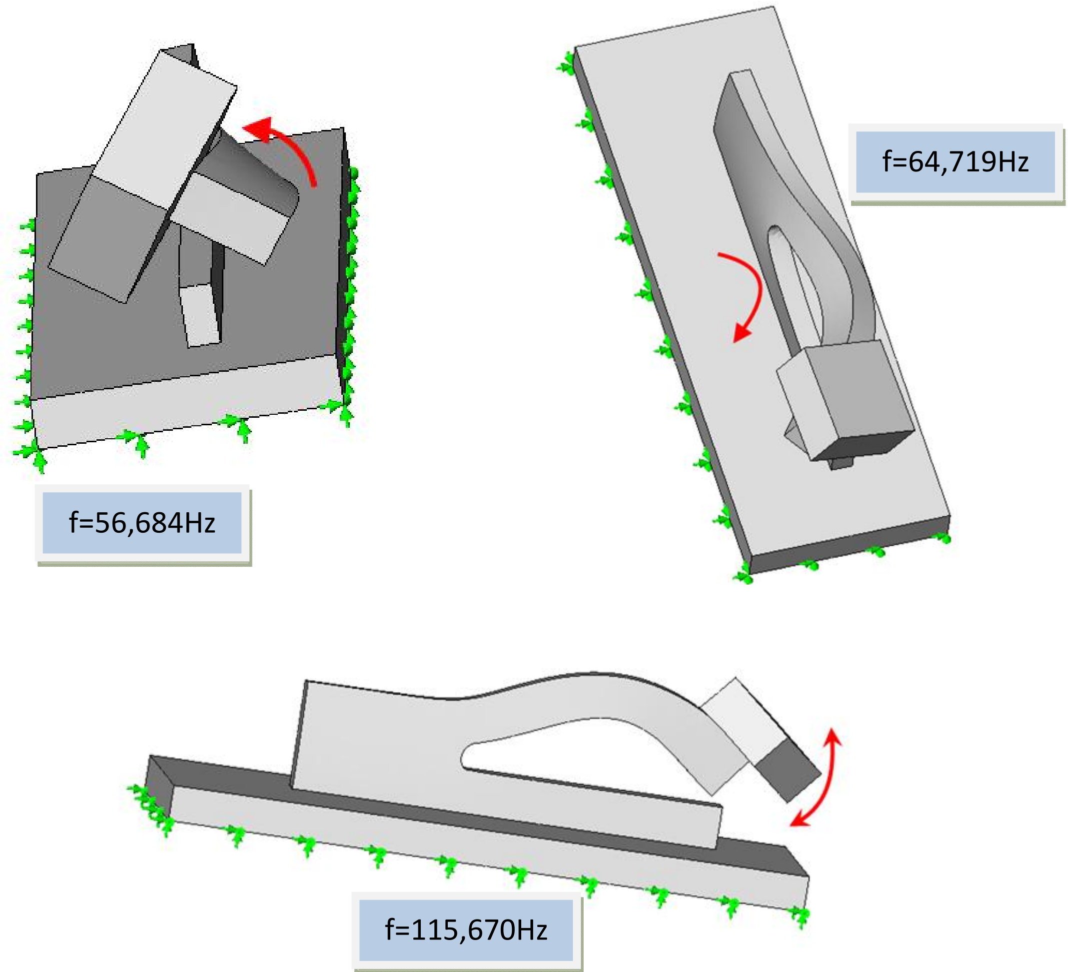

Figure 4.4: First 5 vibration modes of one prong free configuration obtained by finite element analysis.

simulation and given specification is due to the simplicity of the model used where the effect of bonding wires, weight of the glue and effect of ambient environment has not been included in the calculation. In order to confirm these results a real probe has been attached to the tip of the QTFs. They have been prepared using both configuration (one prong fixed and both prongs free). Frequency response of QTF has been measured using a simple I-V converter with a gain of $1.5x10^7$V/A, as the sensor assembly was dithered with the special excitation part integrated at the scanner piezo. From Fig. 4.5 it is clear

that when both prongs are free we have two resonance frequencies around 17.035kHz and 31.535kHz but when one of the prongs was fixed, we get a single resonance frequency around 17.84kHz with much higher amplitude. A slight discrepancy from the calculated and simulated results is probably due to the mass of glue and the position of the HP has not been included at the calculations and simulation. There are two peaks around ~3 kHz or ~6 kHz, as seen in Fig. 4.5. This is due to the resonance frequency of the whole scanner assembly. Two different systems with 2” and 3” long scan piezo tubes have been used. Based on the above results, we can conclude that for stable operation one prong of the QTF should be fixed. Under such condition we are close to symmetric mode and this can be easily explained by using the cantilever beam theory. The study is summarized in Table 4.1.

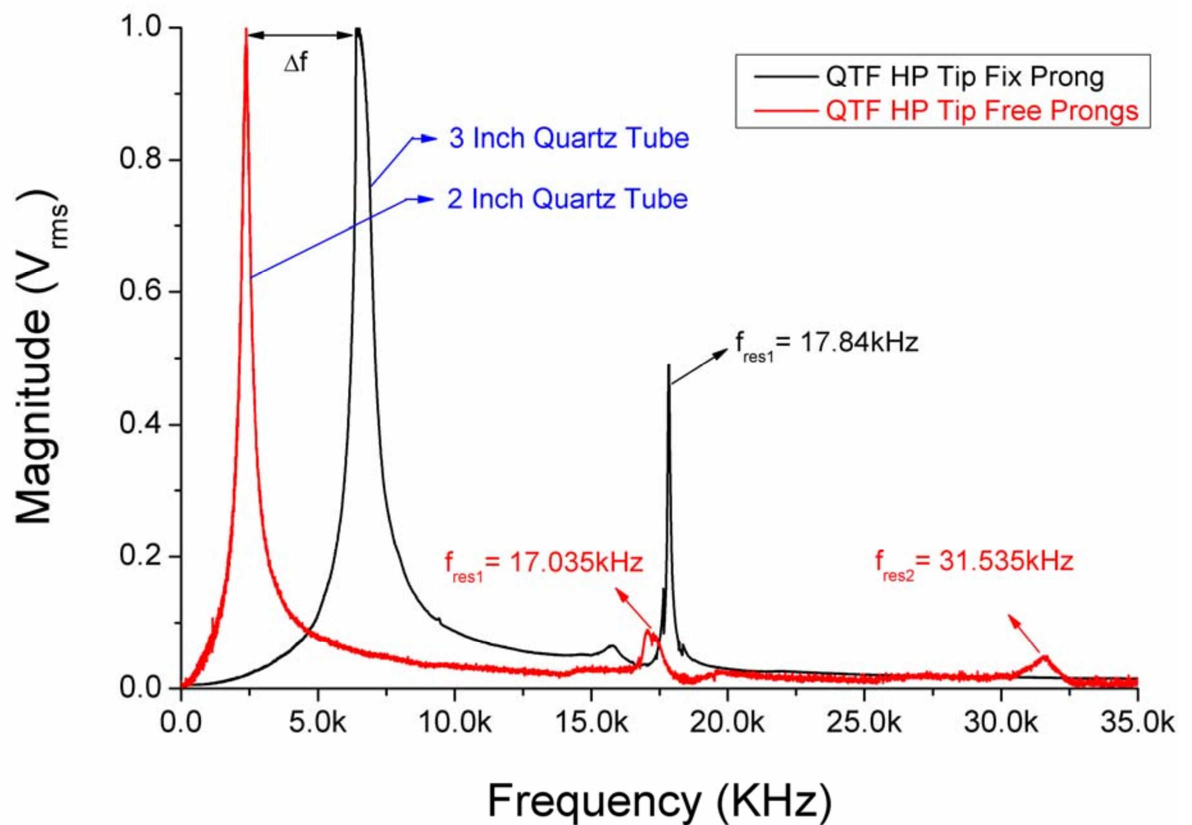

Figure 4.5: Frequency response of 32kHz Quartz Tuning fork with integrated Hall probe under fix prong and free prong configuration. The effect of scan piezo is also shown.

Table 4.1: Summary of the used parameters and calculation / simulations results for QTFs.

Dimensions of Quartz Tuning Fork

	Width	Length	Thickness	Mass of Cantilever
Tuning Fork	0.34mm	3.81mm	0.62mm	2.13mg
	Width	Length	Thickness	Mass of Hall Probe
Hall Probe	1mm	1mm	0.475mm	1.11mg

Calculation

Theoretical Models	Simple Harmonic Oscillator	Cantilever Beam theory
Effective Mass	$M_{SHO} = \frac{m_c M_t}{m_c + M_t}$ = 0.73mg	$M_{CBT} = M_t + 0.24 m_c$ = 1.62mg
Resonance Frequency	$f_{SHO} = \frac{1}{2\pi}\sqrt{\frac{k}{M_{SHO}}}$ = 31.7kHz	$f_{CBT} = \frac{1}{2\pi}\sqrt{\frac{k}{M_{CBT}}}$ = 21.2kHz

Simulation

Vibration Mode	Symmetric	Asymmetric
Both prongs are free	17.14kHz	31.41kHz
One prong is free	17.6kHz	0

4.4 Experiments

1μm sized Hall sensors that are microfabricated in a Class 100 clean room using optical lithography were used for these experiments. The semiconductor wafers used were MBE grown P-HEMT and AlGaAs/GaAs two dimensional electron gas (2DEG) materials. The carrier concentrations of the samples were 2.1×10^{13} cm^2 for P-HEMT and 3.6×10^{11} cm^2 for 2DEG wafers. The mobility of both samples was around 6,000 $cm^{2/}$Vs at 300K.

Two different tuning forks were used. The dimensions ($l \times w \times t$) of the quartz crystals' prongs were, $3.81\times0.34\times0.62$mm for 32.768 kHz and $1.72\times0.32\times0.4$mm for the 100kHz tuning forks, resulting in stiffness of 29 kN/m and 200 kN/m, respectively. Initially 32.768 kHz quartz crystals and sensor chip sizes of 2.5×2.5×0.5mm (~17mg) were used. This combination gives a typical resonance frequency of ~5-6 kHz for the sensor. Even though this low frequency, sensors have worked reasonably well and some images were obtained. It was desirable to increase the resonance frequency of the combined sensor for faster scan rates. Therefore, the final chip sizes were reduced to 1×1×0.5mm (~2.7mg) by dicing and employed smaller and stiffer 100 kHz tuning forks, which produced a much higher, ~29-33 kHz resonance frequency. The sample is tilted ~1.25º with respect to the probe prior to the experiment (Fig. 4.6). Tuning of the fork was done, using the control software, when it was away from the surface as shown in Fig4.7. The PLL card takes care of the entire operation. The oscillator output of the PLL card is connected to the dither section of the piezo scanner. By this way the end of the scan piezo is dithered to excite the quartz crystal. Amplified signals from quartz crystal are the input signal of PLL. PLL card measures frequency shift of this signal and feed it to the External input of the feedback controller card at the SHPM Controller Electronics. The controller keeps the Δf constant during the entire scan.

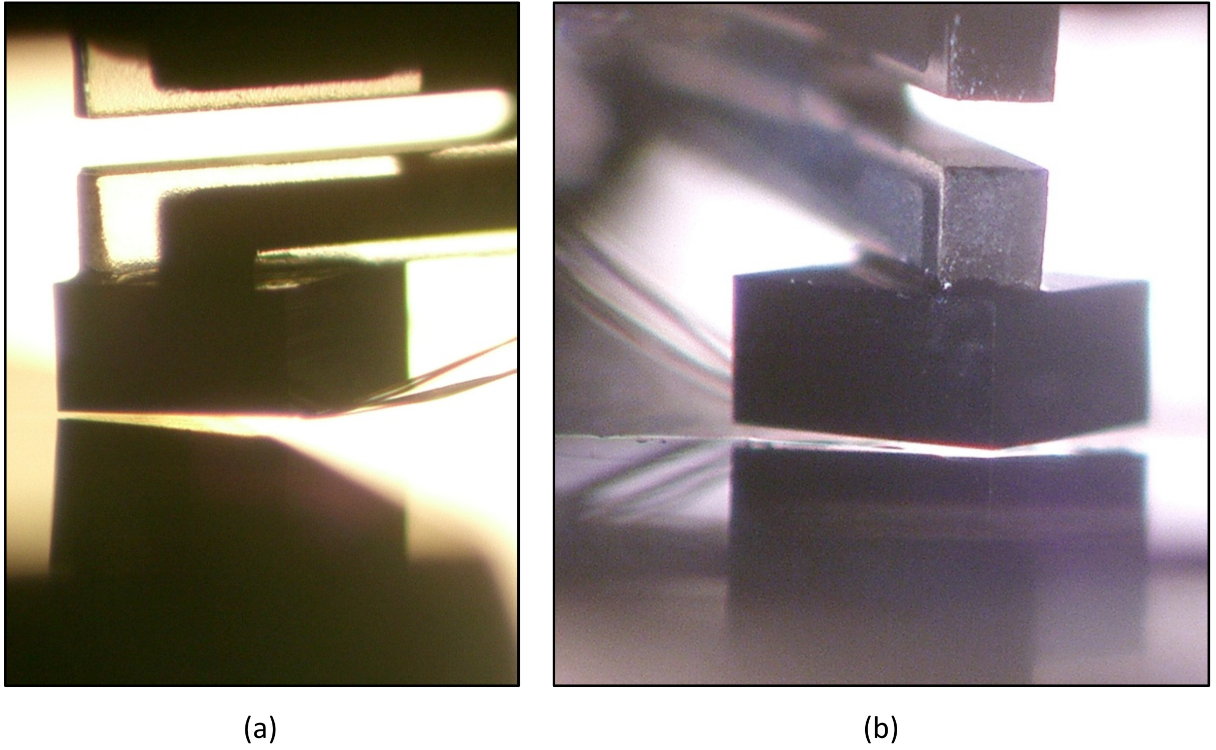

Figure 4.6: Side view (a) and corner view (b) of the sample-probe alignment

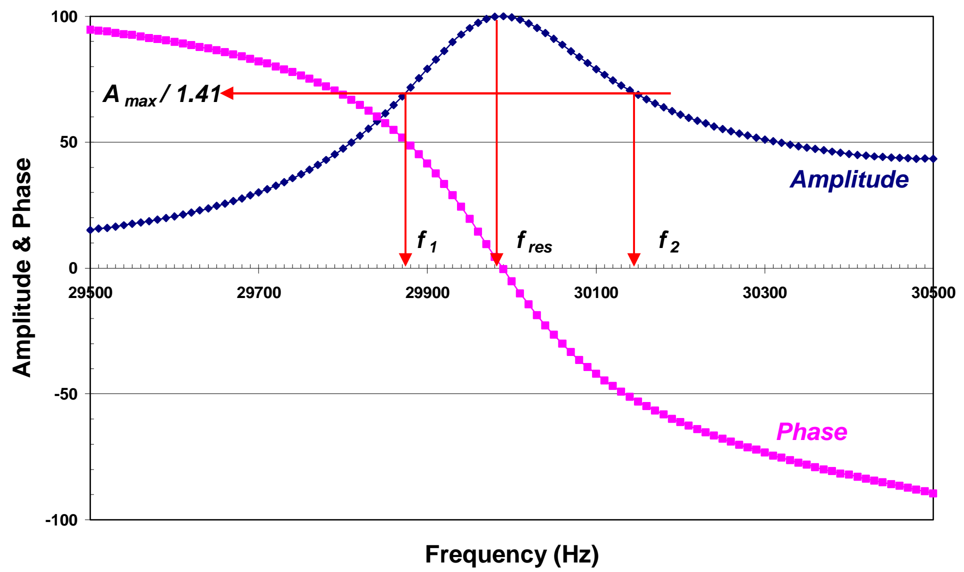

Figure 4.7: Autotune curves of the tuning forks.

The magnetic domains and topography of the Iron Garnet thin film crystal and NdFeB demagnetised magnet were imaged to show the performance of the microscope at room temperature. A sensor with 32.768 kHz tuning fork and a 2.5×2.5×0.5mm size P-HEMT Hall sensor chip was used, giving a resonance frequency of 5,297 Hz. The Hall coefficient of the sensor was R_H ~ 3 mΩ/Gauss and a series resistance of R_s ~ 3kΩ at 300K. The oscillation amplitude was ~50nm with a Q ~ 230. The AFM feedback is established with +15 Hz frequency shift. The Hall sensor biased with 300μA current and a low noise DC amplifier was used to detect Hall voltage. The scan speed was 2μm/s. Fig. 4.8a & b show AFM Tracking SHPM images of Iron garnet and NdFeB demagnetised magnet samples obtained at 300K respectively.

We have also imaged a hard disk sample at 300K with the Quartz Crystal AFM feedback using 100kHz tuning fork combined with a smaller 1×1×0.5mm size 2DEG Hall sensor chip. The resultant resonance frequency of the combined sensor was 35,620 Hz. The Hall coefficient of the sensor was R_H ~ 0.175 Ω/Gauss and a series resistance of R_s = 55kΩ at 300K. The oscillation amplitude was ~50nm with a Q ~ 200. The AFM feedback is established with +5Hz frequency shift. The scan speed was 2μm/s. The Hall sensor was driven with a 3 μA DC Hall current and a low noise DC amplifier is used to detect Hall voltage. Fig.4.9 show simultaneously obtained SHPM and AFM images of the sample. Even though the corner of the mesa, which serves as the tip, is a not very sharp one, we can obtain topographic features with a relatively good resolution.

The 2DEG Hall sensor chip was also used for low temperature imaging of the HDD sample and a single crystal BSCCO(2212) high-T_c superconductor sample [94] at 4.2K. The sample space was filled with 1Atm of Helium exchange gas at 300K and cooled down to 4.2K. The Hall sensor was driven with 20μA DC current, the series resistance of the Hall sensor was ~2kΩ at 4.2K. The resonance frequency and the quality factor were 36,031 Hz and ~450 respectively. Figure 4.10 shows magnetic image of HDD sample

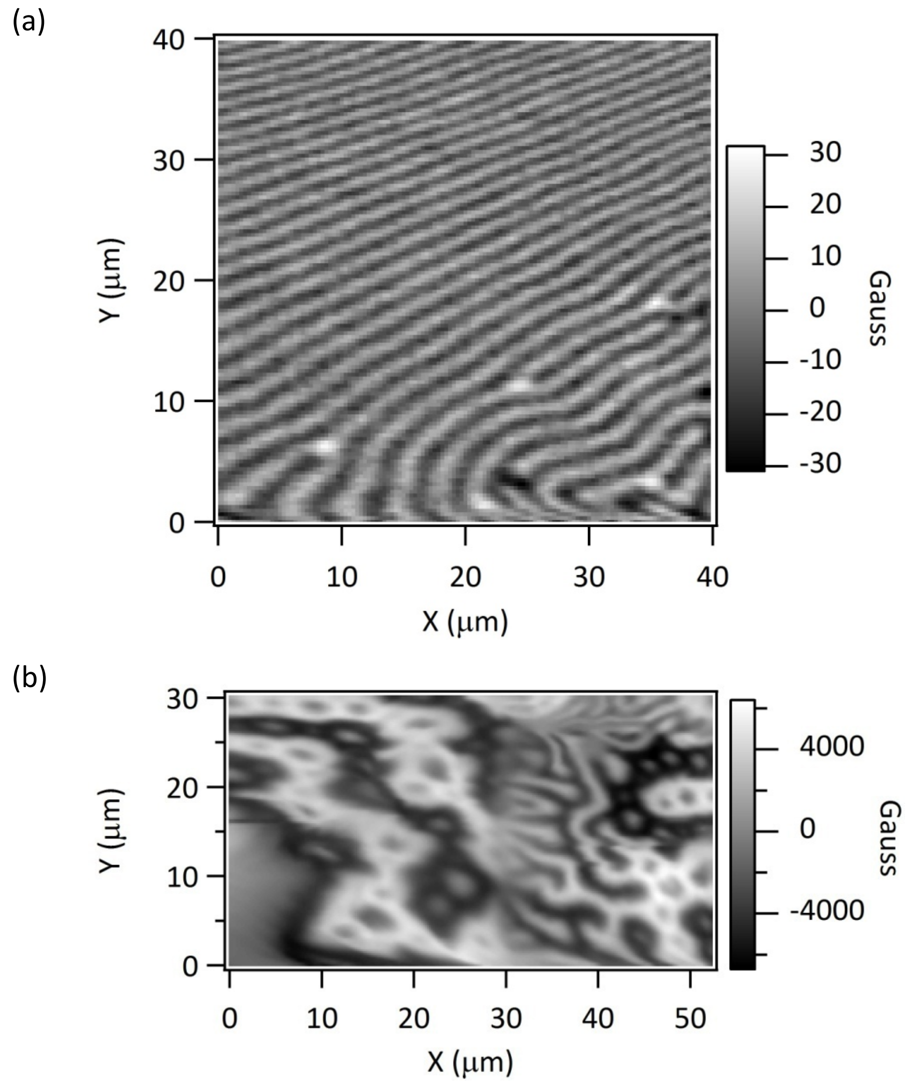

Figure 4.8: SHPM image of (a) iron garnet crystal and (b) NdFeB demagnetised magnet obtained in AFM Tracking mode at 300K. Size of the images and vertical scale of the images are (a) 40×40μm & 62 Gauss and (b) 52×30μm & 12,868 Gauss, respectively

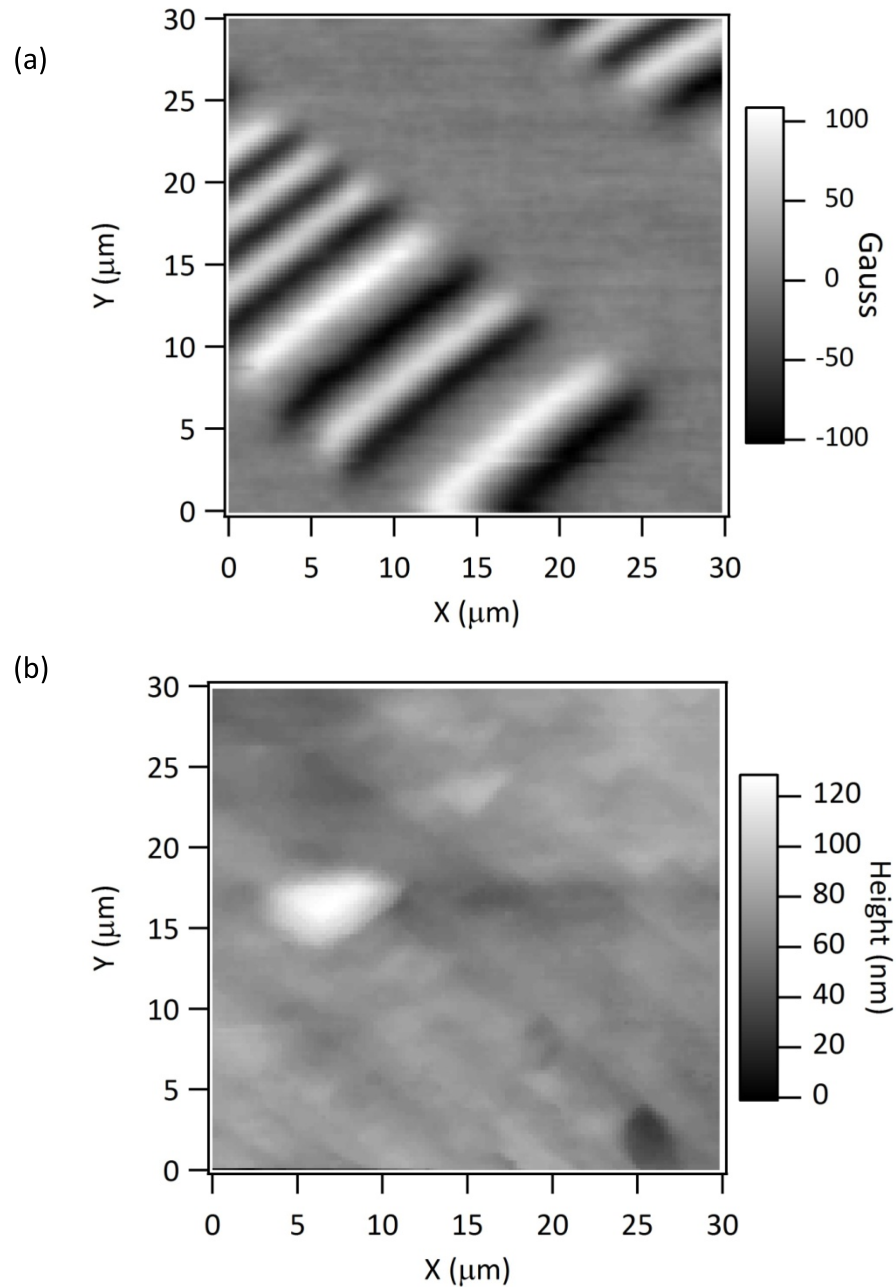

Figure 4.9: SHPM image of (a) Hard disk specimen and (b) simultaneously obtained topography at 300K. Size of the images are 50×50μm and vertical scales are (a) 209 Gauss and (b) 127nm. Vertical scale for the topography shows the relative values.

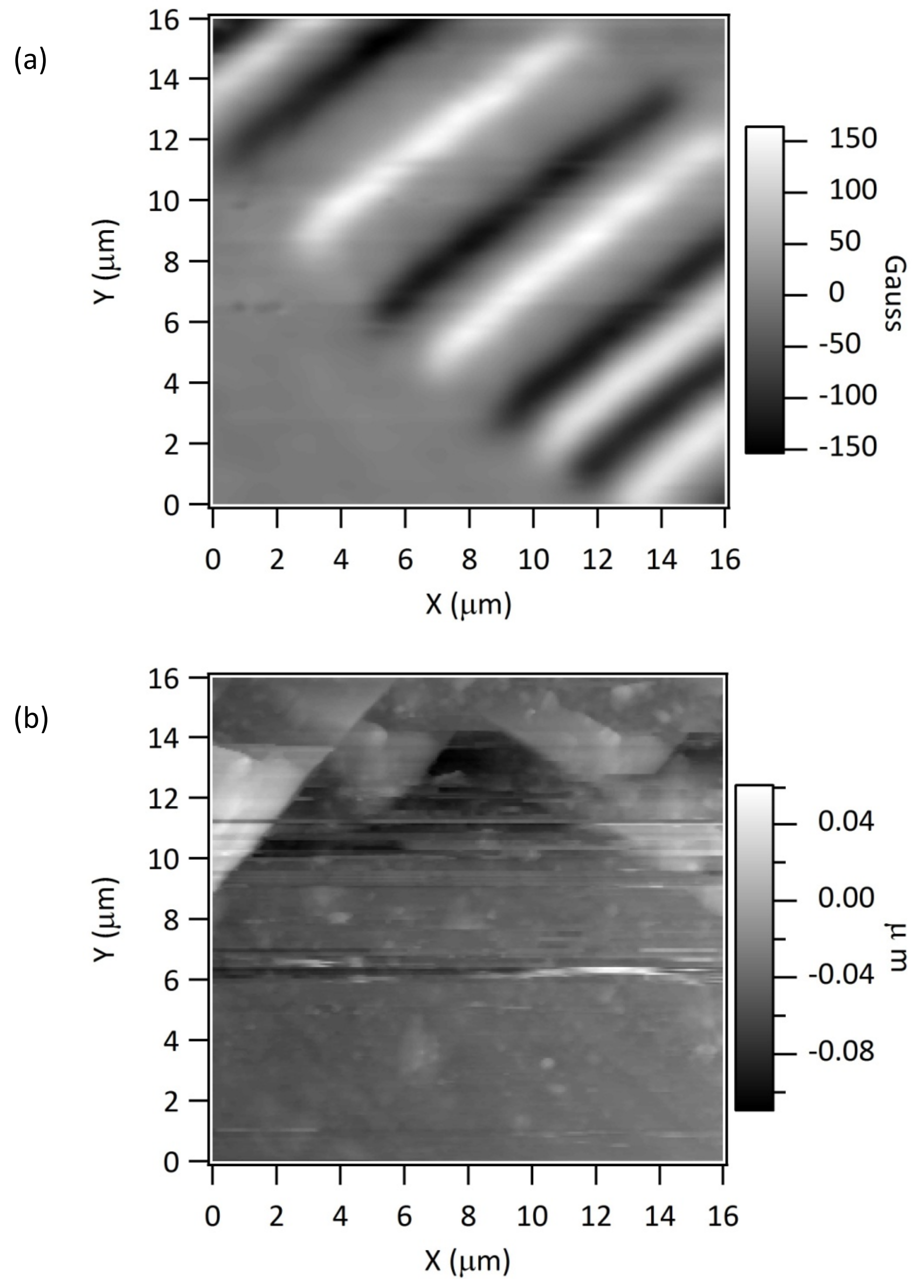

Figure 4.10: SHPM image of Hard disk specimen gathered by AFM tracking at 4.2K. Sizes of the images are 16 μm × 16μm and vertical scales are 312 Gauss and 170nm for magnetic (a) and topographic (b) images respectively.

obtained in AFM Tracking mode at 4.2K (Fig. 4.11). The single crystal BSCCO (2212) sample was field cooled down to 4.2K under the external magnetic field of 0.28Oersted. The sensor is first brought into close proximity of the sample using the AFM feedback. Then, it has been retracted 250 nm above the surface. The surface has been scanned keeping the height constant and the magnetic image shown in Figure 4.14 has been acquired. The images were averaged to decrease the effect of *1/f* noise. Individual vortices can clearly be seen in the SHPM image.

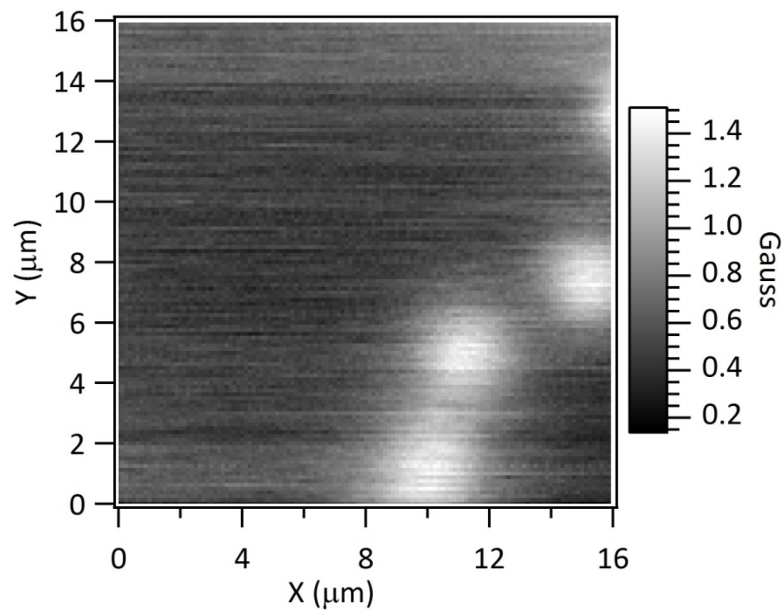

Figure 4.11: SHPM image of single crystal BSCCO 2212 specimen at 4.2K obtained in lift-off mode. Scan area is 16×16µm and vertical scale is 1.65 Gauss. Image shown is the average of 25 images.

Chapter 5 : Hall Probe Gradiometry

This chapter shows the first demonstration of a novel Hall gradiometer and its application to obtain all the spatial components of the magnetic field over a hard disk sample with 700nm spatial resolution.

5.1 Introduction

In the original configuration proposed by Edwin Hall, the Hall sensors usually, has the form of a plate, on the surface of the chip, fitted with four contacts. By the methods of integrated circuit technology, such a plate can be merged in to the chip surface, which is named as the "horizontal" configuration as shown in Figure 5.1 [95], in which the Hall device is *only* sensitive to the magnetic field perpendicular to the chip plane. In the simplest case there exist, a square plate of n-well in a p-type doped semiconductor. When a current is passed through the contact on the dedicated pair of the n-well, consequential voltage is built up due to the perpendicular component of the applied magnetic field. This voltage is measured through the other pair of contacts. Some applications, on the other hand, may require simultaneous measurement of the all three vector components, B_x, B_y and B_z, of the magnetic field **B** with a high spatial resolution on the specimen. The first novel device employing the Hall probes for the parallel field detection has suggested by R.S. Popovic [96]. The motivation was to introduce a sensor capable of measuring the magnetic fields parallel to the chip surface, produced by the standard integrated circuit fabrication methods. The difficulty about the integration was the placement of the ohmic contacts for each pad forming the Hall element. To solve this, a Hall plate with the current carrying axis placed vertical to the chip plane is fabricated as shown in Fig. 2.2. In this configuration, due to the placement, the device is named as “vertical Hall effect device”. The device geometry is designed such that all the contacts become available at the top surface of the chip. The substrate, or the device

layer, is an n-doped silicon wafer surrounded by a p-doped region to isolate the sensor element. The contacts are ion implemented regions with higher doping concentrations with respect to the substrate. Note that this device is still one dimensional (1D) as the only measurable component of the magnetic field is the one perpendicular to the bias current. By putting together two such devices, the two-dimensional sensor (2D) is obtainable. In this cross-shaped device, as shown in Fig 5.3, the four output current electrodes are connected together.

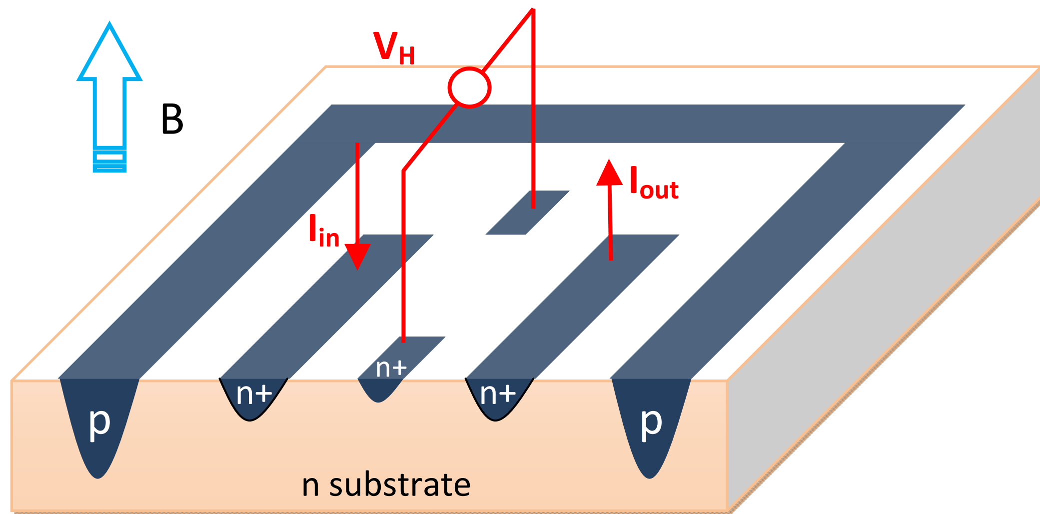

Figure 5.1: A Hall plate in the integrated circuit technology. A magnetic field perpendicular to the chip surface generates a Hall voltage between the two voltage electrodes of the Hall sensor [95].

The voltage differences between the sensing contacts of each branch are directly proportional to the corresponding magnetic field components in two different directions. With such a sensor, it is now possible to measure the magnitude of a magnetic field in the X-Y plane. It is also possible to place these devices in an array, having more than two sensing elements for each direction or in different angular orientation. The operation principle and the sensitivity of the device is essentially unaffected by this unusual geometry. The 1D Hall device is similar to the JFET transistor, and the effective device thickness can be altered by applying negative voltage to the p-doped isolation ring [96].

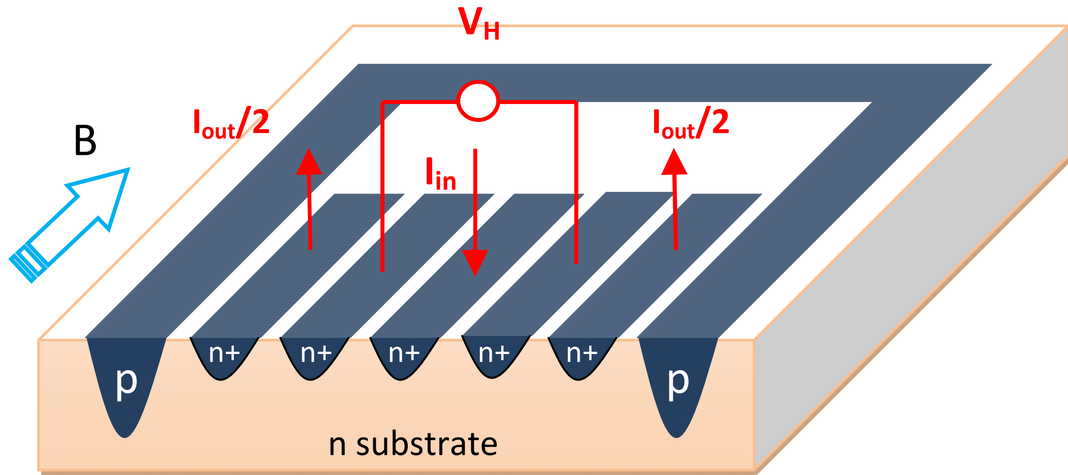

Figure 5.2: Cut through of a 1D integrated vertical Hall device. This sensor is sensitive to a magnetic field parallel to the chip surface [95].

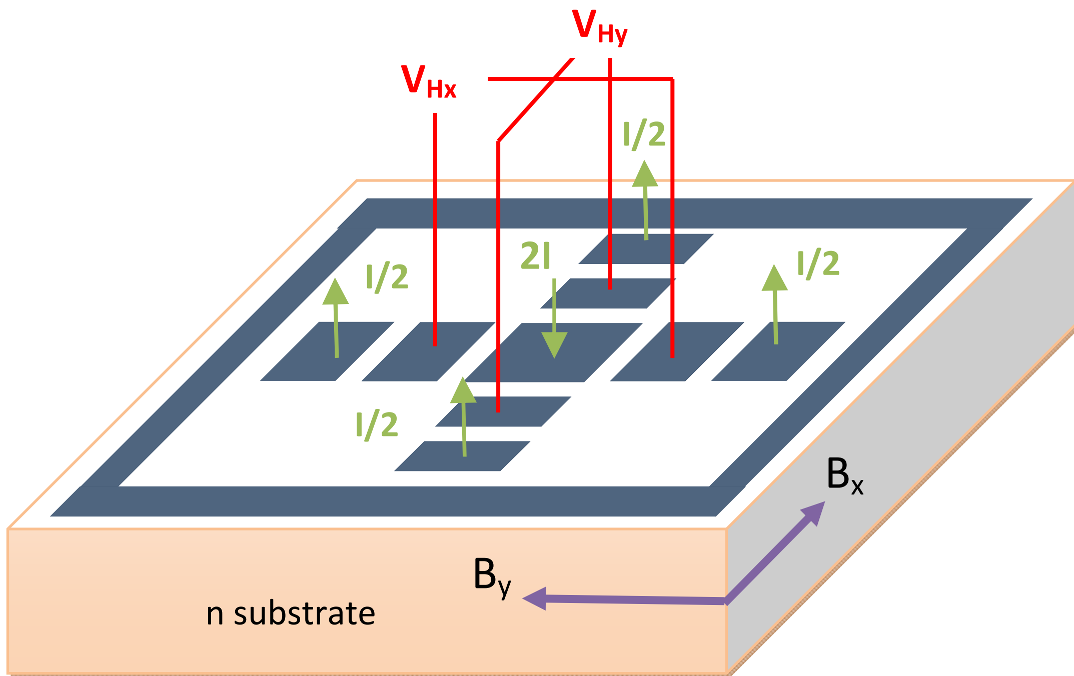

Figure 5.3: Two vertical Hall sensors placed in a cross shape (2D), used to measure a magnetic field in X and Y directions.

Following the same idea, one horizontal and one 2D vertical Hall elements can be placed together to obtain a 3D version, which can detect all three spatial components of the external magnetic field. Different orientation and positions are possible [97] for the Hall sensors due to flexibility of the production method employed. To combine the elements in order to have a 3D sensor, two different approaches have been reported [95, 98, 99]. The first approach is to place unidirectional (1D) individual elements in a perpendicular manner to each other [100, 99]. This is called the "hybrid micro system" [95, 99]. Since the assembling the parts is difficult, alignment and angle errors may arise [95, 101]. Also, due to the huge measurement volume, local measurements are difficult and some corrections have to be applied to the acquired data. It should be noted that the term "hybrid" should not be confused with the applications where a Hall probe and readout integrated circuit (IC) are brought together on a single chip [102].
The other possibility consists of a one-chip microsystem where various sensitive parts are integrated on a single substrate [95, 99, 103]. These kinds of combinations have been demonstrated in the recent years in a number of studies. The main problem with this layout, reported by different groups [98, 104, 105, 99], is the cross coupling between the XYZ channels. The cross coupling (CC) is a parasitic effect observed in a channel when the external magnetic fields are applied in the other two perpendicular directions. Possible sources of it are the geometrical miss-alignments during the fabrication, temperature gradients, and different magnetoresistance behavior of the material in different directions [98]. In other words, its occurrence is related to all of the physical phenomena that create a distribution irregularity in current or potential in the active region of the device. To reduce this effect, various tricks can be applied; simultaneous measurement of magnetic field vector by separation of the outputs [106], amperometric mode of operation [98], and calibration of the CC [104]. Another important criterion is the spatial resolution of the 3D probe systems. The reported spatial resolutions are of the order ~100µm or higher [98, 101, 106, 104]. The smallest reported size is ~50µm [103].

Another approach has been utilized by Gregusova *et al.* [107]. In his work a pyramidal structure having individual Hall sensors on three adjacent facets and at the top is fabricated. The fabrication basically consists of the following steps [108]:

a) Three dimensional micromachining of planar GaAs substrate to reveal pyramids confined to specific facets,
b) MOCVD overgrowth of a III-V semiconductor heterostructure across the wafer including the pyramids and its side walls,
c) Device processing to form the Hall probes on the overgrown semiconductors on the facets.

The complicated process details can be found elsewhere [109, 107, 108]. The pyramids, where the Hall probes are placed, have 30° tilted facets. The reported active area, which is the key for the spatial resolution, of the individual Hall probes is ~5μm × 5μm. Unlike the previous methods summarized above, each Hall device is sensitive to the perpendicular component of the magnetic field only. The scanning is performed using stepper motors over the designated area and the data is processed in order to get the all the components of the magnetic field transforming the values from the Hall probe coordinates to the Cartesian coordinates of the field [110]. Local mapping of the field over a scanned area is also shown by this method [107] where a spatial resolution of 5μm is achieved.

5.2 Novel Hall Probe Gradiometry

The gradiometry in the general sense describes the method used to measure the variation of a physical quantity in space. In our case it is the magnetic field variation over the sample. From Figure 5.4 it can be seen that if a different voltage value is measured through terminals $V_{1\text{-}2}$ and $V_{3\text{-}4}$ due to the presence of an external magnetic field up on the Hall array, this indicates a field variation along the current axis. The magnitude of the voltage difference can be used to quantify this variation. This is a one

dimensional first order gradiometer configuration. Number of terminals can be increased but the separation between them should be as much as the width of the Hall crosses.

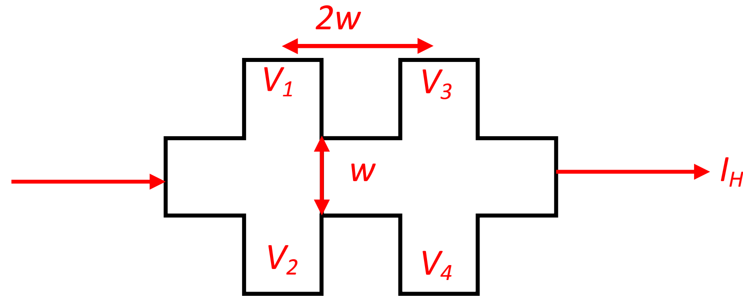

Figure 5.4: Hall gradiometer.

The method used in this study, however, is completely different than the methods described above. There is no need for the complex design principles or the growth requirements. Any semiconducting material suitable for a Hall effect device is applicable with a simple fabrication process. The spatial resolution is just defined by the width of the Hall cross, thus the limitation only comes from the fabrication capability or from the material properties, such as the surface charge depletion after certain size. In fact, probes with ~50nm spatial resolution has already been shown [31], which can readily be employed to measure the three dimensional magnetic fields using that method.

The low noise amplifier is modified such that, the current and voltage signals can be passed through any four leads of the Hall cross. The restriction of having the current and the voltage leads to be mutually perpendicular to each other is eliminated. If the current flow does not follow a straight path as shown in Fig. 5.5, we still observe the Hall effect, which we may call the bending resistance [111, 112]. As the current flows at any particular point along the path, the magnetic force F_M is perpendicular to the direction of motion. In uniform magnetic field however, the Hall voltage would be equal to zero. But, if the magnetic field distribution across the device is spatially non-uniform and nonsymmetrical along the gradient axis, there will be a finite voltage developed at the

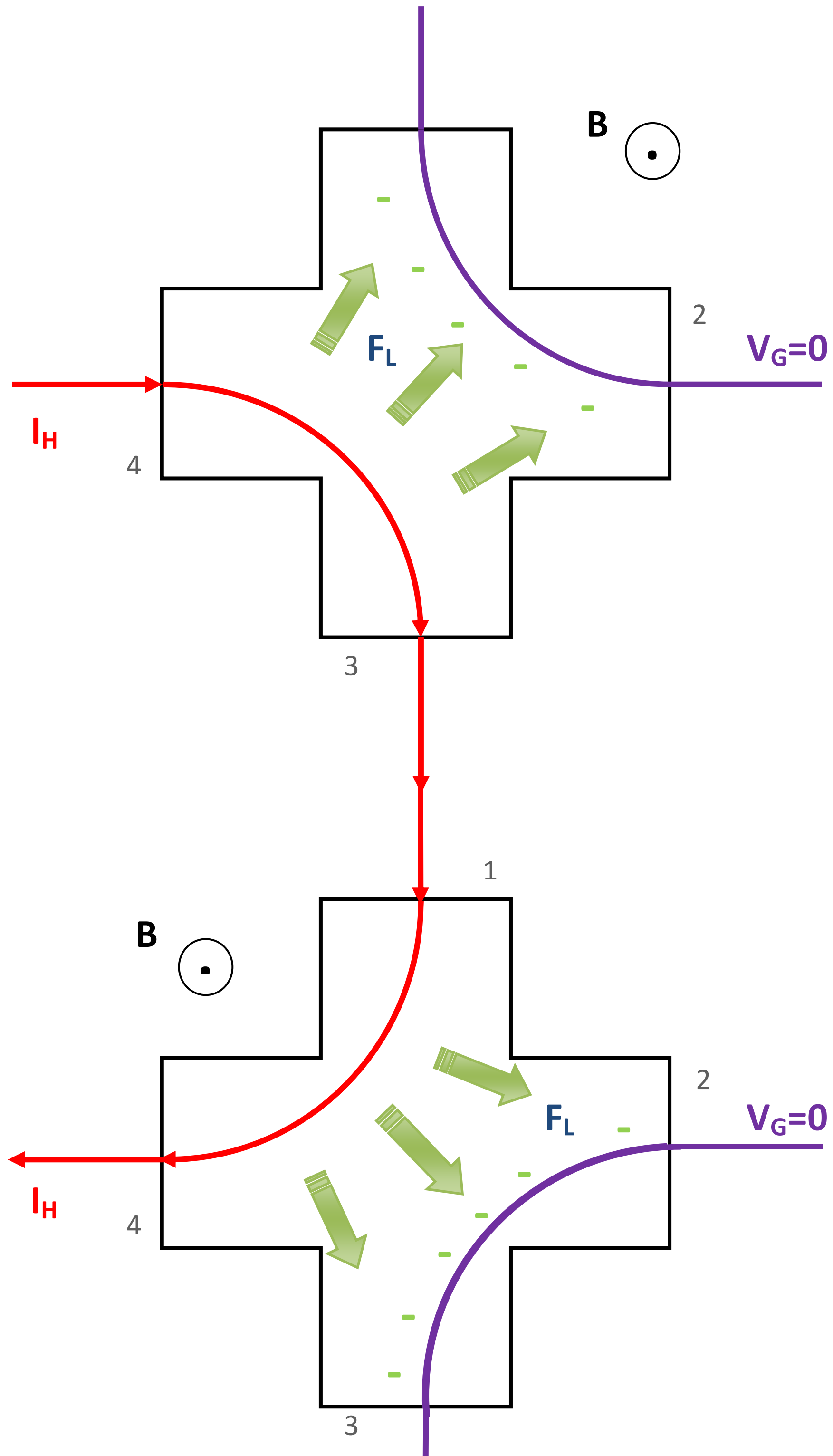

Figure 5.5: Hall effect with non-perpendicular current and voltage leads with different configurations under uniform magnetic field.

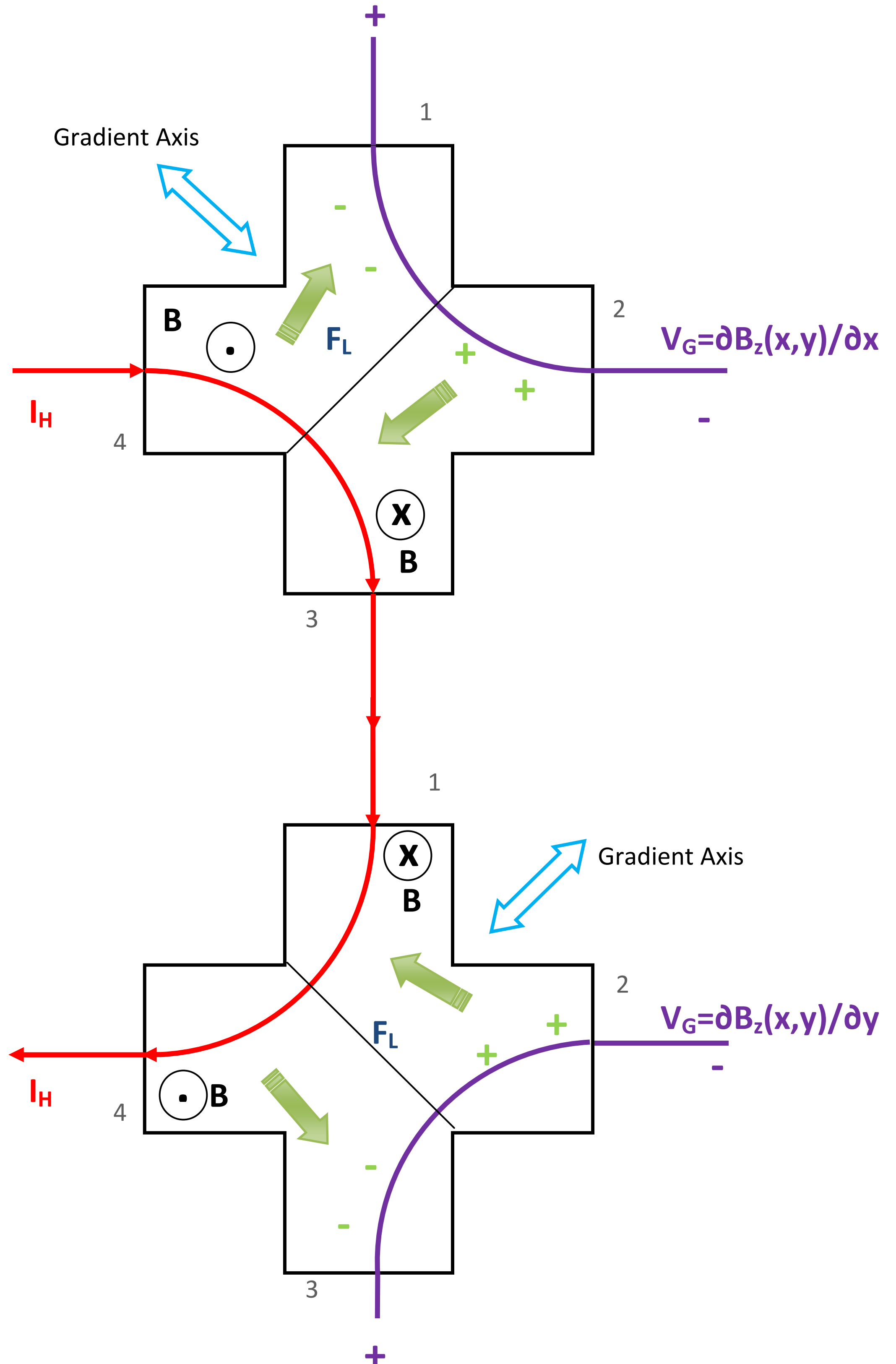

Figure 5.6: Hall effect with non-perpendicular current and voltage leads with different configurations under non-uniform magnetic field.

voltage terminals. The lateral electric field $\vec{E}$ generated to balance the magnetic force is not uniform across the device; in other words, it has a gradient along the device. As a result, the measured potential is the derivative of the perpendicular magnetic field in the active region of the Hall cross. Depending on the current flow path the derivative about to different diagonals of the Hall cross is measured as shown in Fig. 5.7 with the non-perpendicular current and voltage leads with different configurations and the field gradient axis. This has been accidentally observed by Bath University group [113] during an SHPM experiment, where the voltage and current leads were mixed up. The orientation of the sensor over the magnetic field distribution of the measured sample is important. In our setup the probe has a fixed position with respect to the quadrants of the scanner piezo. Thus, the orientation of the probe is not changing during the scan which is placed by 45º with respect to the X&Y scan directions. On the other hand the sample can be aligned in any desired rotational angle with respect to our Hall sensor.

We wanted to investigate the origin of this signal and perhaps we may be able to use it in various applications. In the experiments a hard disk sample is imaged with a 1μm size PHEMT Hall probe in LN_2 environment to minimize the thermal drift. First, an image is obtained using the normal Hall sensor configuration, where current and voltage leads were perpendicular to each other. The scan performed with a speed of 5μm/s at 256 pixel resolution, applying a 500μA DC drive current to the probe in the AFM tracking mode. Figure 5.8 shows the SHPM image of the Hard Disk sample resolving individual bits. The Hall sensor alignment and the lead configurations are given at the right hand side of the figure.

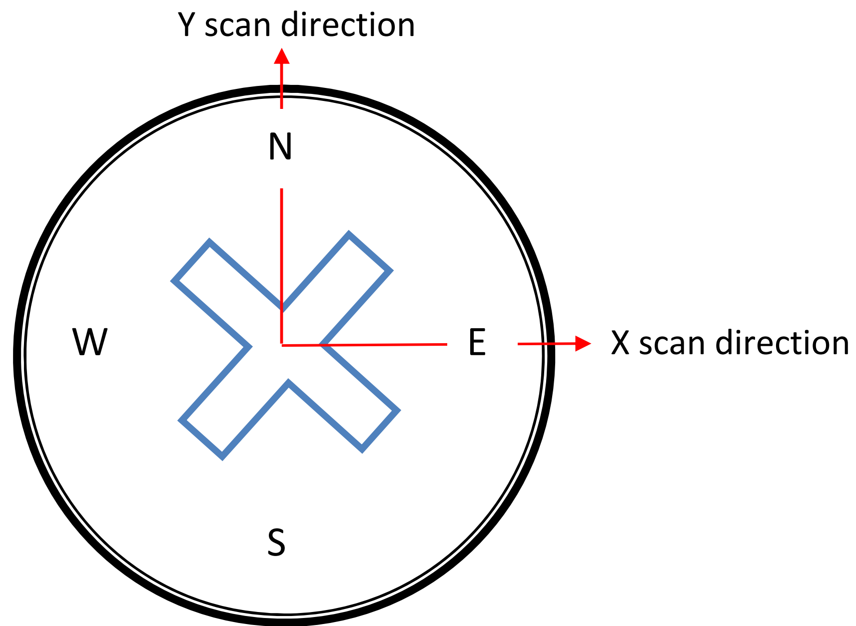

Figure 5.7: Orientation of the Hall sensor, over the sample, with respect to the scan direction of the microscope: Hall cross has 45° alignment.

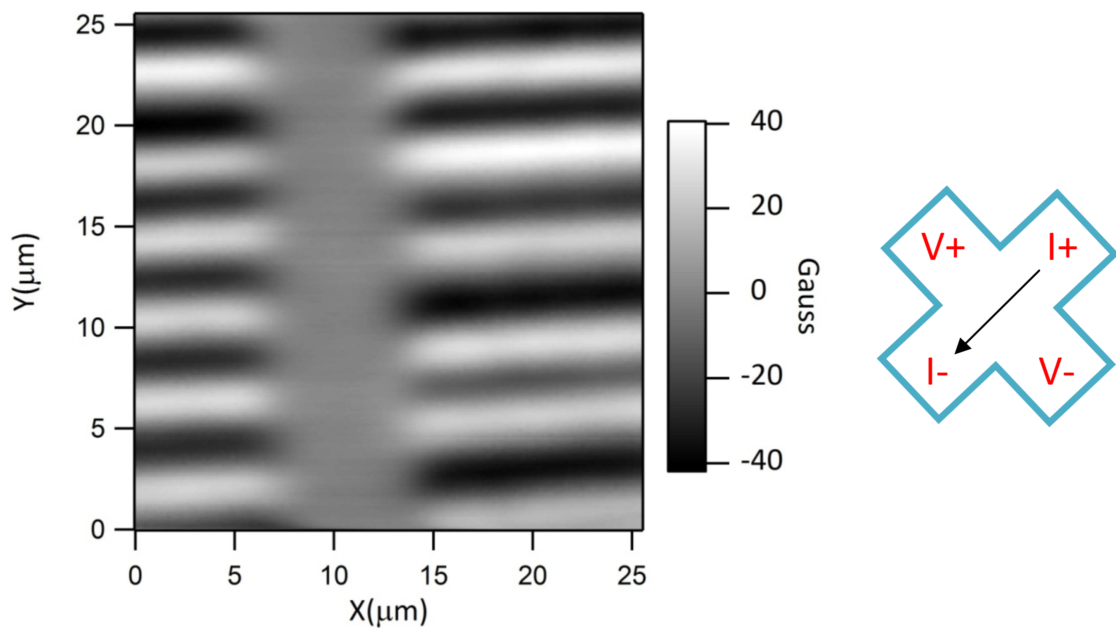

Figure 5.8: SHPM scan of a Hard disk sample at 77K with normal Hall sensor configuration of mutually perpendicular current and voltage leads. Hall cross diagram shows the relative alignment of the probe over the sample and the leads' positions.

The magnitude of the Hall voltage signal is stored in a 256×256 matrix. Hence, matrix arithmetic operations can be applied on the acquired image. Equipped with these, the rows are differentiated along the *y* direction to obtain $\partial \mathbf{B_z}/\partial \mathbf{x}$, and columns are differentiated to get $\partial \mathbf{B_z}/\partial \mathbf{y}$ along the *x* direction using forward differences method. The results are shown in Fig 5.9 and Fig 5.10 which are calculated $\partial \mathbf{B_z}/\partial \mathbf{x}$ and $\partial \mathbf{B_z}/\partial \mathbf{y}$ respectively. Immediately after obtaining the standard SHPM image, drive current direction is changed to the proper leads so that the $\partial \mathbf{B_z}/\partial \mathbf{x}$ and $\partial \mathbf{B_z}/\partial \mathbf{y}$ images can be obtained. To have a healthy comparison, the probe was not pulled back off the surface while the switch positions on the amplifier are changed. The Hall probe was driven by smaller, 100μA current, as it was not possible to properly offset null the probe. The other scan parameters are held the same as in the case of normal scan. Images obtained as a result of these experiments and the current/ voltage lead configurations are shown in Fig. 5.11 and 5.12. The results are in perfect agreement with the calculated ones, except the field values are not absolute since the probe is offset nulled at the presence of the field.

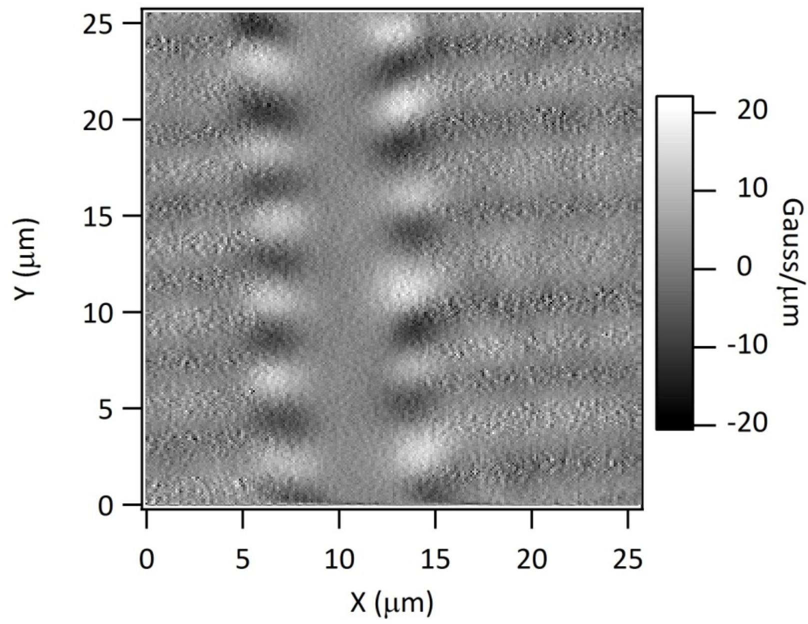

Figure 5.9: Calculated $\partial \mathbf{B_z}/\partial \mathbf{x}$ from the measured $\mathbf{B_z(x,y)}$ data matrix by forward differences.

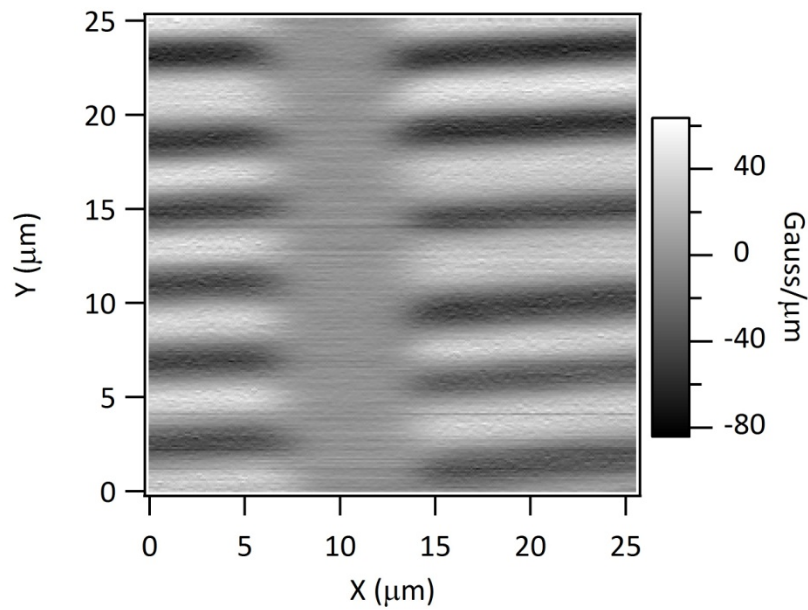

Figure 5.10: Calculated $\partial \mathbf{B_z}/\partial \mathbf{y}$ from the measured $\mathbf{B_z(x,y)}$ data matrix by forward differences.

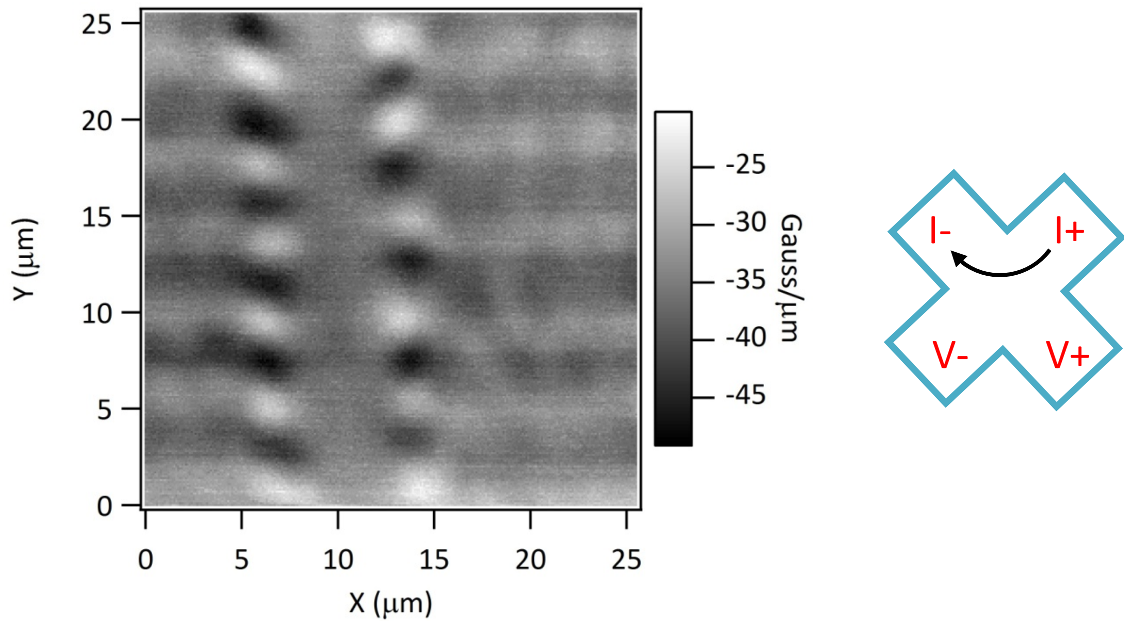

Figure 5.11: SHPM scan of a HDD at 77K with Hall sensor configuration shown in the diagram. The image represents $\partial \mathbf{B_z}/\partial \mathbf{x}$ due to the relative positions of current and voltage leads

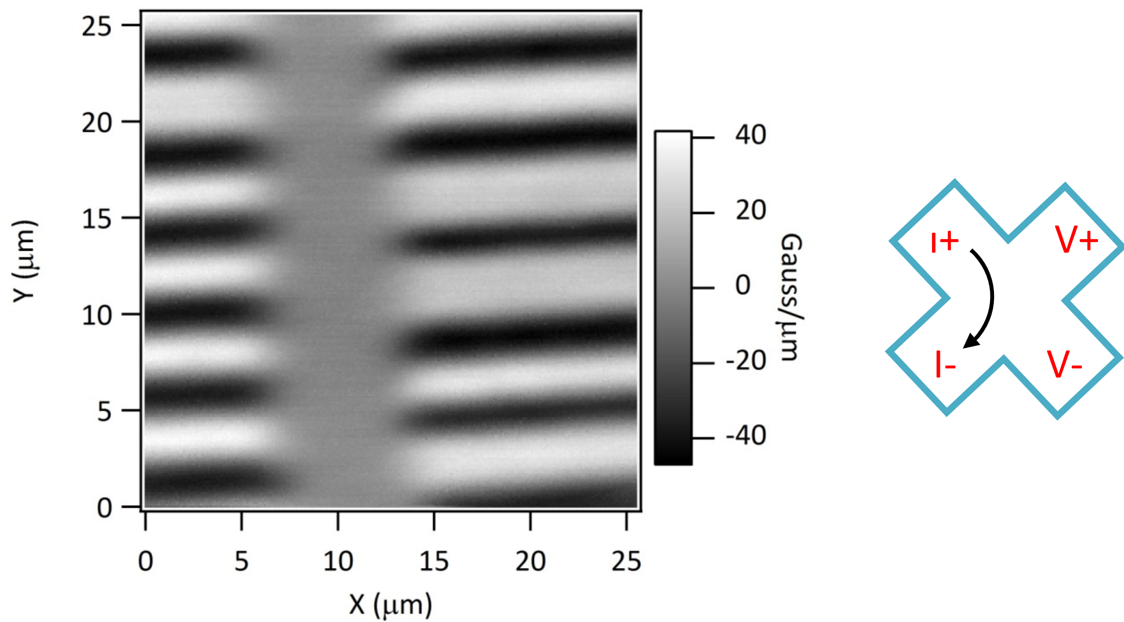

Figure 5.12: SHPM scan of a HDD at 77K with Hall sensor configuration shown in the diagram. The image represents $\partial \mathbf{B_z}/\partial \mathbf{y}$ due to the relative positions of current and voltage leads.

5.3 Three Dimensional Magnetic Field Imaging

As different sample orientations are scanned, different images are obtained in lateral derivative, which was actually expected as the gradient of the field changes in the space. One may argue that since we can calculate the local gradient of the $\mathbf{B_z(x,y)}$ along $\boldsymbol{x}$ and $\boldsymbol{y}$ directions, why should we bother imaging in this obscure way? On the other hand this measurement mode clearly gives us the local gradient of the $\mathbf{B_z(x,y)}$, which can be used in a number of applications like gradiometry etc.

A more important ramification is the possibility of calculating in-plane components, $\mathbf{B_x(x,y)}$ and $\mathbf{B_y(x,y)}$ of the magnetic field if we *measure* $\mathbf{B_z(x,y)}$, $\partial\mathbf{B_z(x,y)}/\partial\mathbf{x}$ and $\partial\mathbf{B_z(x,y)}/\partial\mathbf{y}$ across the space. If we start with the Maxwell equation derived from Ampere's law [114],

$$\vec{\nabla} \times \vec{B} = \varepsilon_0 \mu_0 \vec{J} + \varepsilon_0 \mu_0 \frac{\partial \vec{E}}{\partial t} \tag{5.1}$$

In a source free region the equation simplifies to,

$$\vec{\nabla} \times \vec{B} = 0 \tag{5.2}$$

which can be written, in open form, as

$$\left(\frac{\partial}{\partial x}\hat{\imath} + \frac{\partial}{\partial y}\hat{\jmath} + \frac{\partial}{\partial z}\hat{k}\right) \times \left(B_x\hat{\imath} + B_y\hat{\jmath} + B_z\hat{k}\right) = 0 \tag{5.3}$$

from which we can get,

$$\left(\frac{\partial B_z}{\partial y} - \frac{\partial B_y}{\partial z}\right)\hat{\imath} - \left(\frac{\partial B_z}{\partial x} - \frac{\partial B_x}{\partial z}\right)\hat{\jmath} + \left(\frac{\partial B_y}{\partial x} - \frac{\partial B_x}{\partial y}\right)\hat{k} = 0 \tag{5.4}$$

To satisfy the equation each vector component must individually be equal to zero.

$$\left(\frac{\partial B_z}{\partial y} - \frac{\partial B_y}{\partial z}\right) = 0 \quad (5.5)$$

$$\left(\frac{\partial B_z}{\partial x} - \frac{\partial B_x}{\partial z}\right) = 0 \quad (5.6)$$

$$\left(\frac{\partial B_y}{\partial x} - \frac{\partial B_x}{\partial y}\right) = 0 \quad (5.7)$$

The first two equations can be solved in terms of the parameters we measure at the beginning of the problem. Hence we can write,

$$\left(\frac{\partial B_z}{\partial y} - \frac{\partial B_y}{\partial z}\right) = 0 \quad (5.8)$$

$$\Rightarrow \frac{\partial B_z}{\partial y} = \frac{\partial B_y}{\partial z} \quad (5.9)$$

$$B_y = \int_z^{\infty} \frac{\partial B_z}{\partial y} dz \quad (5.10)$$

Hence if we measure or obtain $\partial \mathbf{Bz}/\partial \mathbf{y}$ as a function of z, then we can calculate the $\mathbf{B_y}$ at this specific z. The SHPM data should be obtained at increasing sample-sensor distances, until the signal decays to zero or below the noise levels. A similar equation can be written for $\mathbf{B_x}$ as well,

$$B_x(x, y, z) = \int_z^{\infty} \frac{\partial B_z(x,y,z')}{\partial x} dz' \quad (5.11)$$

As, it is not possible to integrate the equations analytically, we have to compute them numerically from the measured data.

$$\int_z^{\infty} f(z')\, dz' \cong h\left[\sum_{j=1}^{n} f(jh)\right] \quad (5.12)$$

The situation can visualized with the aid of Fig. 5.13 given below. While we can measure the quantitative value of the perpendicular magnetic field, $\mathbf{B_z}$, at the closest sample-sensor position, this is not exactly the case for the derivatives. The change in magnitude at a particular point for, $\partial \mathbf{B_z}(x,y,z)/\partial \mathbf{x}$ and $\partial \mathbf{B_z}(x,y,z)/\partial \mathbf{y}$ is not necessarily a decrease with increasing sample-sensor separation. However, the overall dynamic field will decrease with increasing probe-sample separation.

Note that we do not need to have an infinite sum as the field value $f(jh)$ will decay after a certain value of jh that can be set as the finite upper limit n. Thus, $\partial \mathbf{B_z}(x,y,z)/\partial \mathbf{x}$ and $\partial \mathbf{B_z}(x,y,z)/\partial \mathbf{y}$ are acquired at different heights (z_i) until the field decays to zero, carefully recording the values. A fixed incremental separation $\boldsymbol{h}$ is used between the scans for ease of calculation.

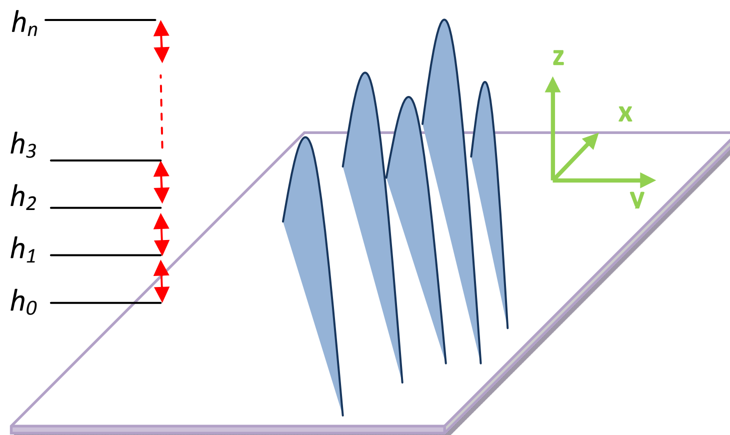

Figure 5.13: Visualization of incremental scan for $B_z(x,y,z)$, $\partial B_z(x,y,z)/\partial x$ and $\partial B_z(x,y,z)/\partial y$

While the sample is scanned the surface is never perfectly smooth. In addition to this, some inclination angle can unintentionally be given, while mounting the sample. For this reason, while the sample is scanned with a liftoff, this distance must be applied throughout the sample evenly. The magnetic force microscopy (MFM) techniques, where the magnetic and interaction forces have to be separated, can be applied to this

case. Hence, while the forward scan is conducted using the feedback following the surface texture; the backward scan is performed following the same texture, however this time, by adding the required lift-off value at each pixels. By this procedure, the value of ***h*** is held fixed throughout the whole scan area. Fig 5.14 shows the image of Hard disk with the forward scan, (a) while the probe is in closest proximity of the sample, and backward scan (b) while the probe is lifted off by 3.5µm. The decay of the magnetic signal when the probe is lifted off by 3.5µm away from the surface can clearly be seen and obviously this distance can be accepted as the upper limit of the integration while calculating the $\mathbf{B_x}$ and $\mathbf{B_y}$. This value is within the range of retraction capability of the used scanner piezo at room temperature. But, unfortunately, the effect of the thermal drift is also high at room temperature and it is virtually impossible to scan the same portion of the HDD by giving successive offsets, which is required to integrate $\partial \mathbf{B_z}/\partial \mathbf{x}$ or $\partial \mathbf{B_z}/\partial \mathbf{y}$. Fig 5.15 shows this effect. At each level of 0.5µm offset, three images, B_z, $\partial B_z/\partial x$ and $\partial B_z/\partial y$, had to be recorded. Each image requires ~40 minutes to be scanned. Hence, approximately two hours spent at each level. As a result, the experiments had to be done at low temperature to eliminate the thermal drift, which unfortunately reduces the scan area of the piezo tube in X, Y and Z directions. To satisfy both requirements, the stick-slip coarse approach mechanism is used to successively pull the Hall sensor off the sample. The motion of the puck is first calibrated for a given voltage pulse. Then appropriate numbers of pulses were applied in order to lift-off the sensor from the sample. We adjusted the voltage pulses applied to the piezo to provide 250nm backward steps. Overall 26 scans are performed, starting from the closest proximity of the sample, with 250nm steps, until the probe is 6.5µm away from the sample in height. At each height level, $\mathbf{B_z}(x,y)$, $\partial \mathbf{B_z}(x,y)/\partial \mathbf{x}$ and $\partial \mathbf{B_z}(x,y)/\partial \mathbf{y}$ were imaged. The thermal drift is insignificant at 77K as evident in Fig 5.16. $\partial \mathbf{B_z}/\partial \mathbf{x}$ and $\partial \mathbf{B_z}/\partial \mathbf{y}$ images are used to integrate $\mathbf{B_x}$ and $\mathbf{B_y}$ respectively using the method described above. Figures 5.17-5.19 show the $\mathbf{B_z}$, $\mathbf{B_y}$ and $\mathbf{B_x}$ fields of an Hard disk sample.

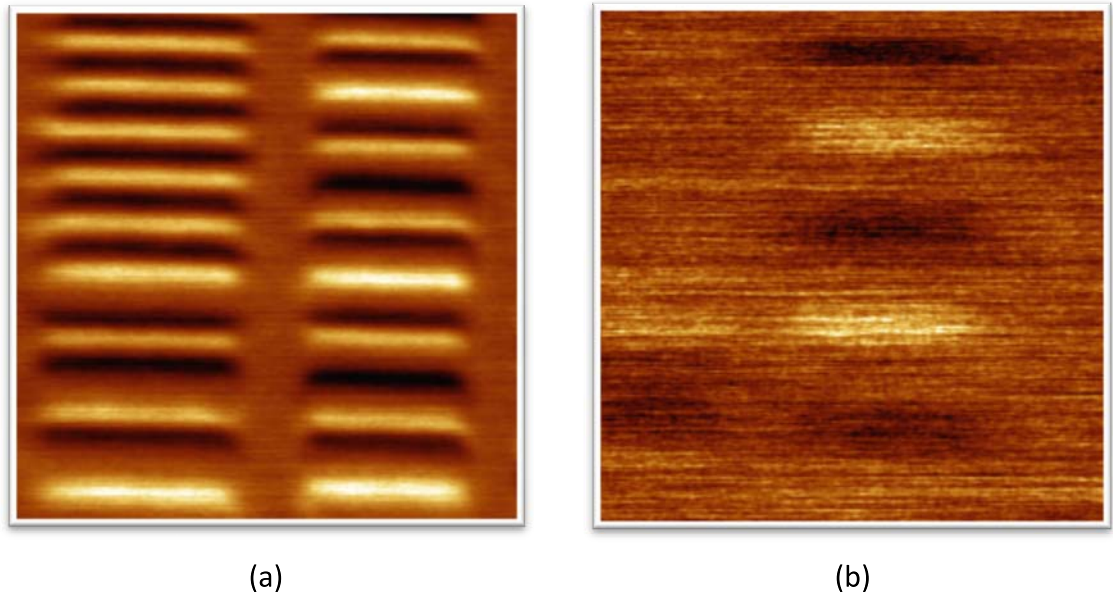

(a) (b)

Figure 5.14: SHPM image of Hard disk sample, (a) forward scan (in the tunneling range) and (b) backward scan (3.5µm away from the surface). Both images were obtained with STM feedback. Scan speed was 5µm/s, resolution set to 256 × 256 pixels, -100mV bias voltage applied to the sample and the tunneling current of 1nA maintained during the scan.

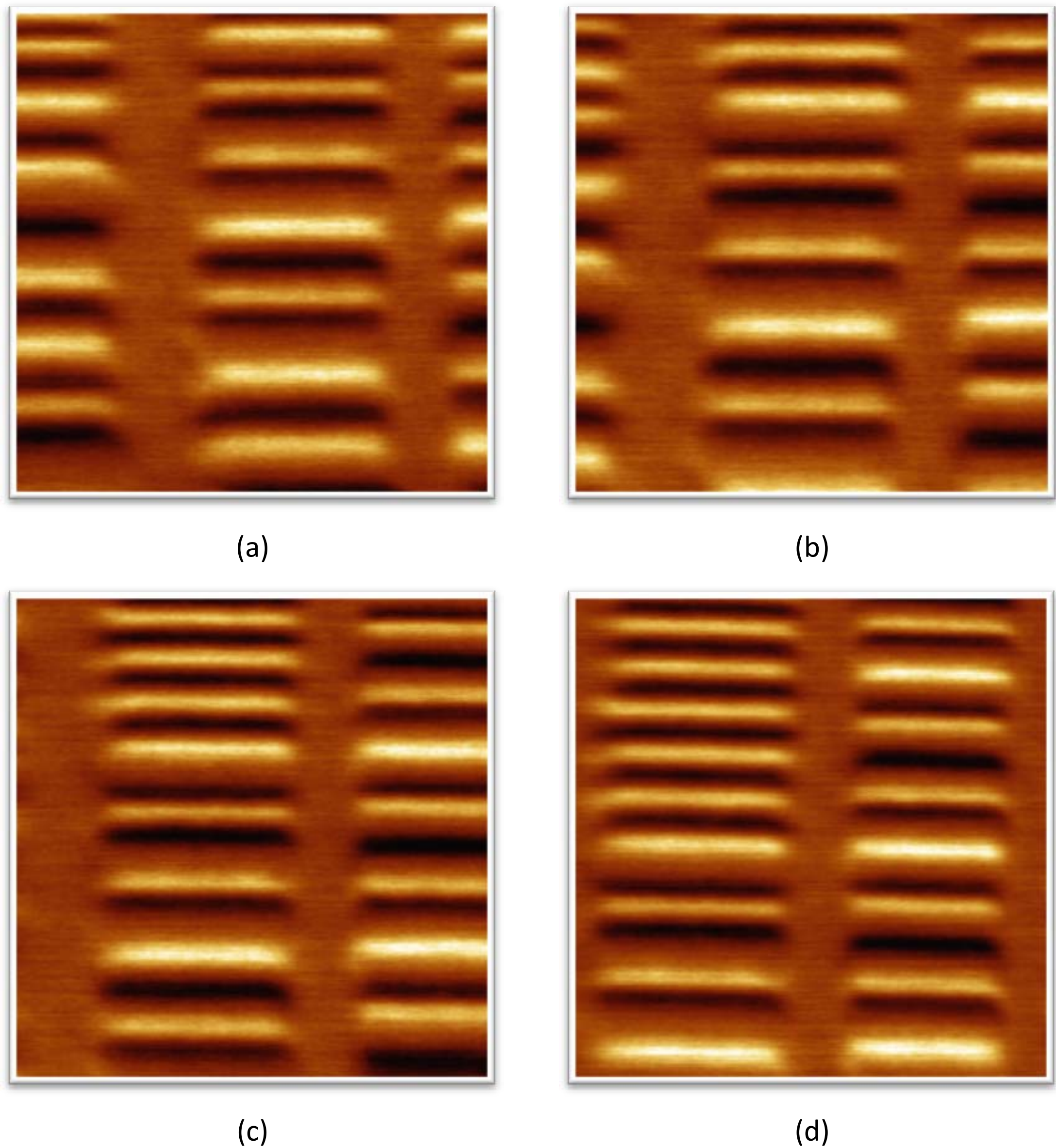

Figure 5.15: SHPM images of Hard disk sample obtained at room temperature showing effect of the thermal drift. Pictures are the forward scans of probe above the sample with a height of (a) 0.5µm, (b) 1.5µm, (c) 2.5µm, (d) 3.5µm respectively. Field decay is not seen as the offset is only given during the backward scan. Approximately 4 hours of time passed between the shown images. The shift is towards the bottom left corner. All images were obtained with STM feedback using a 1µm PHEMT sensor. Scan speed was 5µm/s, resolution set to 256 × 256 pixels, -100mV bias voltage applied to the sample and the tunneling current of 1nA maintained during the scan.

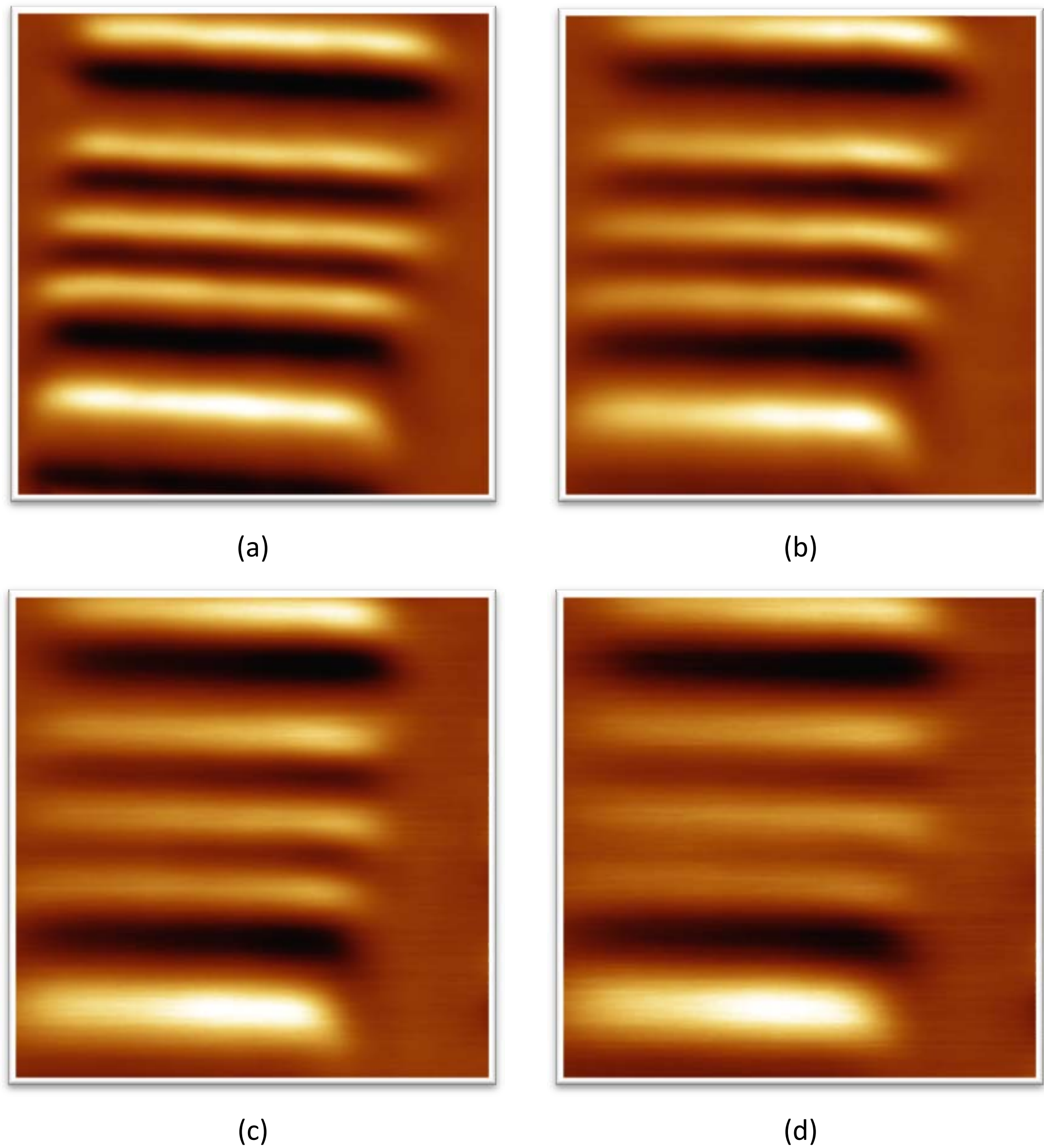

Figure 5.16: SHPM images of Hard disk sample obtained at 77K showing effect of the thermal drift. Pictures are the scans of probe levels above the sample with a height of (a) 0.25 µm, (b) 1.25µm, (c) 2.5µm, (d) 3.75µm respectively. Approximately 10 hours passed between the first and the last images. There is a very little drift which becomes insignificant after thermal stabilization. All images were obtained using a 1µm PHEMT sensor. Scan speed was 5µm/s, resolution set to 256 × 256 pixels. The decay of the magnetic field can also be seen as the sensors moves away from the sample.

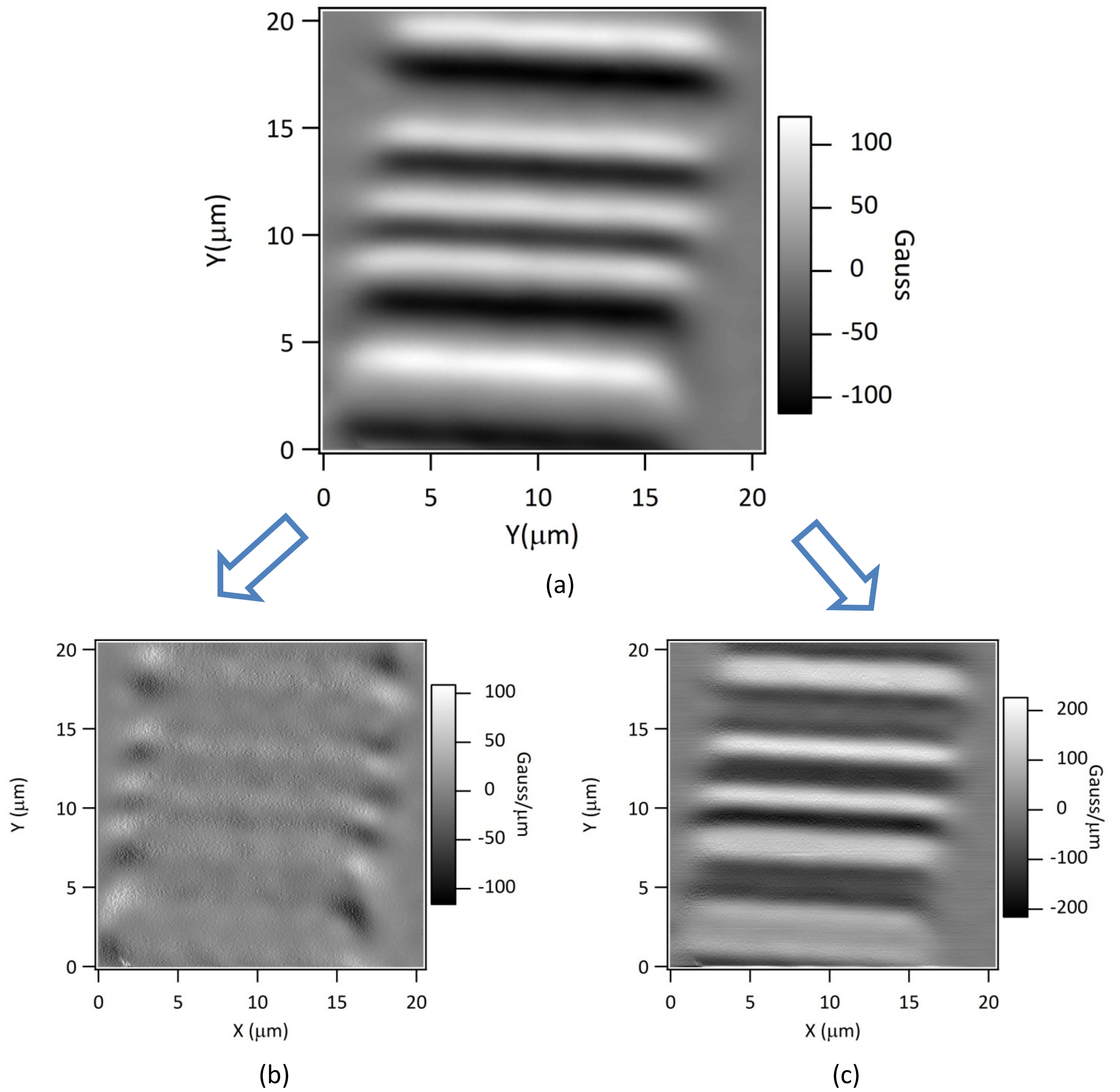

Figure 5.17: SHPM image of Hard disk sample, shows the $\mathbf{B_z}$ of the field (a), obtained at 77K in the feedback tracking zone. Image was obtained using a 1µm PHEMT sensor. Scan speed was 5µm/s, resolution set to 256×256 pixels. $\partial \mathbf{B_z}(x,y)/\partial \mathbf{x}$ (b) and $\partial \mathbf{B_z}(x,y)/\partial \mathbf{y}$ (c) are calculated from $\mathbf{B_z}$ image by differentiating rows and columns of the image matrix respectively.

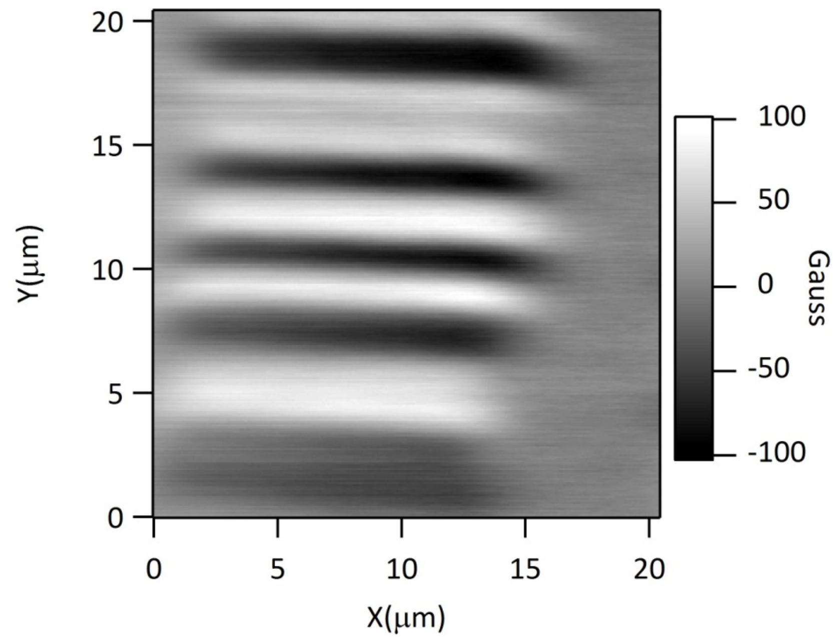

Figure 5.18: $\mathbf{B_y}$ field calculated by integrating $\partial \mathbf{B_z}/\partial \mathbf{y}$ over a finite range. Each image file used in calculation was obtained using the same 1μm PHEMT sensor. Scan speed was 5μm/s, resolution set to 256×256 pixels. The increments along the z-direction, $\boldsymbol{h}$, is set to 0.25μm in the range of [0, 6.5μm].

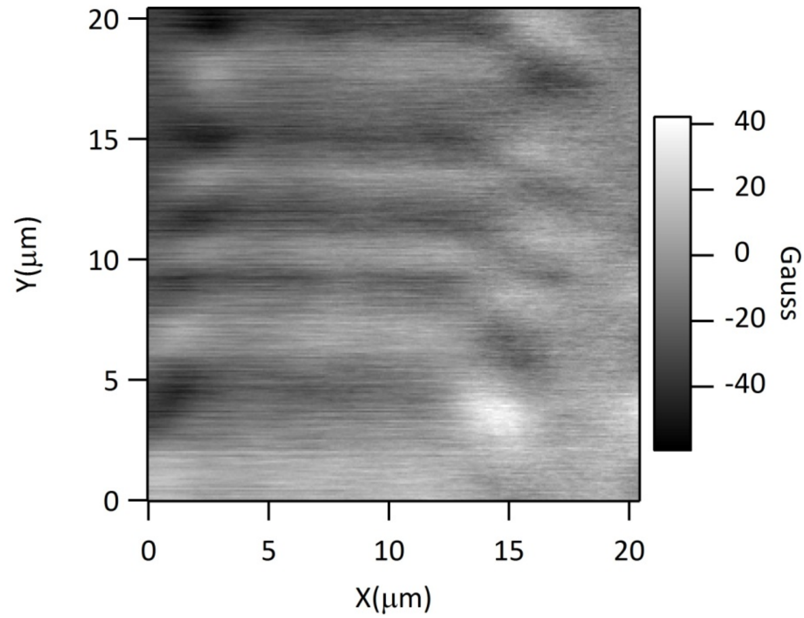

Figure 5.19: $\mathbf{B_x}$ field calculated by integrating $\partial \mathbf{B_z}/\partial \mathbf{x}$ over a finite range. Each image file used in calculation was obtained using the same 1μm PHEMT sensor. Scan speed was 5μm/s, resolution set to 256×256 pixels. The increments along the z-direction, $\boldsymbol{h}$, is set to 0.25μm in the range of [0, 6.5μm].

Chapter 6 : Conclusions

Hall probes with effective physical sizes of 50nm-1000nm were fabricated and characterized in a wide temperature range starting from 4.2K up to 425K using different semiconductor heterostructures, GaN, SOI, GaAs, InSb and Bismuth semi-metal thin films for Scanning Hall Probe Microscopy (SHPM).

Process steps are optimized for different material systems. Second generation optical masks were designed to increase the resolution and production yield of the probes and used successfully. InSb Quantum Well (QW) structure found to be the most promising material for room and high temperature applications due to its high carrier mobility even at elevated temperatures. Its room temperature sensitivity was also very good. Smaller sizes down to ~30nm with this structure may also possible. GaN however was the most appropriate material for extremely harsh environments due to its physical strength. No damage due to scratch was observed with this material; these probes seem to be indestructible. Bismuth, although promising for small sized, <50nm, Hall probes, needs to be further processed to obtain single crystalline film before further miniaturization. GaN Hall sensors were demonstrated to operate up to 125ºC in SHPM. Higher temperature operation seems to be limited by the glue and other instrumental factors, not by the Hall sensor itself.

During this thesis Silicon On Insulator (SOI) Hall sensors have also been developed for SHPM. Thickness dependent characteristics of SOI wafer has been studied as function of temperatures.

Quartz crystal tuning fork AFM feedback demonstrated for the first time for SHPM over a large temperature range. Its performance has been analyzed in detail and

experiments carried with 1µm×1µm Hall probes has been successfully shown for a hard disk sample in the temperature range of 4.2K to 425K. Other samples, NdFeB demagnetized magnet, Bi substituted iron garnet and, single crystal BSCCO(2212) High Temperature superconductor, were also scanned with this method to show the applicability of the method over a wide range of specimens. By this method complex production steps proposed in the literature to inspect the non-conductive samples was avoided.

A novel Scanning Hall probe gradiometer has also been developed and a new method to image x, y & z components of the magnetic field on the sample surface has been demonstrated for the first time with 1µm resolution for the first time. 3D field distribution of a Hard Disk sample is successfully measured at 77K using this novel approach to prove the concept. At this stage our new method gives ×40 spatial resolution improvement over the alternative methods. Furthermore, the resolution can be increased further, by at least a ×20, using smaller Hall sensors, down to 50nm or smaller. This new gradiometer can also be used to detect the existence of superparamagnetic or ferromagnetic nanoparticles with a much simpler experimental setup.

Bibliography

[1] A. Hubert, and R. Schäfer, *Magnetic domains : the analysis of magnetic microstructures,* Springer, Berlin ; New York, 1998.

[2] S. J. Bending, *Local magnetic probes of superconductors,* Advances in Physics, vol.48, pp.449-535, 1999.

[3] E. Beaurepaire, *Magnetism : a synchrotron radiation approach,* Springer, Berlin, 2006.

[4] E. N. Kaufmann, *Methods in materials research: a current protocols publication,* Wiley, New York, 2000.

[5] G. Binnig *et al.*, *Surface Studies by Scanning Tunneling Microscopy,* Physical Review Letters, vol.49, pp.57-61, 1982.

[6] G. Binnig, C. F. Quate, and C. Gerber, *Atomic Force Microscope,* Physical Review Letters, vol.56, pp.930-933, 1986.

[7] E. Hall, *On a New Action of the Magnet on Electric Currents,* American Journal of Mathematics, vol.2, pp.287-292, 1879.

[8] G. J. Stoney, *Of the "Electron", or Atom of Electricity,* Philosophical Magazine, vol.38, pp.418-420, 1894.

[9] J. J. Thomson, *Cathode Rays (Reprinted from The London, Edinburgh, and Dublin Philosophical Magazine and Journal of Science, Fifth Series, October 1897),* Philosophical Magazine Letters, vol.87, pp.303-326, 2007.

[10] R. A. Millikan, *A new modification of the cloud method of determining the elementary electrical charge and the most probable value of that charge,* Phys. Mag, vol.XIX, pp.209, 1910.

[11] R. A. Millikan, *Elementary Electric Charge and the Avagadro Constant,* Physical Review, vol.II, pp.109, 1913.

[12] N. Robotti, *Thomson,J.J. At the Cavendish-Laboratory - the History of an Electric Charge Measurement,* Annals of Science, vol.52, pp.265-284, 1995.

[13] J. C. Maxwell, *A treatise on electricity and magnetism,* Clarendon press, Oxford,, 1873.

[14] D. Jiles, *Introduction to magnetism and magnetic materials,* Chapman and Hall, London ; New York, 1991.

[15] H. Hauser, G. Stangl, and J. Hochreiter, *High-performance magnetoresistive sensors,* Sensors and Actuators A-Physical, vol.81, pp.27-31, 2000.

[16] C. H. Moller *et al.*, *Extraordinary magnetoresistance effect in a microstructured metal-semiconductor hybrid structure,* Applied Physics Letters, vol.80, pp.3988-3990, 2002.

[17] S. A. Solin *et al.*, *Enhanced room-temperature geometric magnetoresistance in inhomogeneous narrow-gap semiconductors,* Science, vol.289, pp.1530-1532, 2000.

[18] H. D. Chopra, and S. Z. Hua, *Ballistic magnetoresistance over 3000% in Ni nanocontacts at room temperature,* Physical Review B, vol.66, pp.-, 2002.

[19] F. Bitter, *On Inhomogeneities in the Magnetization of Ferromagnetic Materials,* Physical Review, vol.38, pp.1903-1905, 1931.

[20] http://www.sims.berkeley.edu/research/projects/how-much-info-2003/

[21] I. D. Mayergoyz *et al.*, *Magnetic imaging on a spin-stand,* Journal of Applied Physics, vol.87, pp.6824-6826, 2000.

[22] R. Akram, *Fabrication and Optimization of RF-SQUID and SQUID Integration Assembly For High Resolution Magnetic Imaging Systems*, Thesis (Ph D), Bilkent University, 2005

[23] B. W. Gardner, *SQUID measurements of magnetic vortices in very underdoped yttrium-barium-copper-oxide*, Thesis (Ph D), Stanford University, 2004

[24] T. Hayashi, M. Tachiki, and H. Itozaki, *SQUID probe microscope combined with scanning tunneling microscope,* IEEE Transactions on Applied Superconductivity, vol.17, pp.792-795, 2007.

[25] T. Hayashi, M. Tachiki, and H. Itozaki, *STM-SQUID probe microscope,* Superconductor Science & Technology, vol.20, pp.S374-S379, 2007.

[26] L. Hao *et al.*, *Spatial resolution assessment of Nano-SQUIDs made by focused ion beam,* IEEE Transactions on Applied Superconductivity, vol.17, pp.742-745, 2007.

[27] Y. Martin, and H. K. Wickramasinghe, *Magnetic Imaging by Force Microscopy with 1000-a Resolution,* Applied Physics Letters, vol.50, pp.1455-1457, 1987.

[28] J. J. Saenz *et al.*, *Observation of Magnetic Forces by the Atomic Force Microscope,* Journal of Applied Physics, vol.62, pp.4293-4295, 1987.

[29] A. M. Chang *et al.*, *Scanning Hall Probe Microscopy,* Applied Physics Letters, vol.61, pp.1974-1976, 1992.

[30] NanoMagnetic Inst. Ltd., www.nanomagnetics-inst.com

[31] A. Sandhu *et al.*, *50 nm Hall sensors for room temperature scanning Hall probe microscopy,* Japanese Journal of Applied Physics Part 1-Regular Papers Short Notes & Review Papers, vol.43, pp.777-778, 2004.

[32] O. A. Mironov *et al.*, *Microminiature Hall probes based on n-InSb(Sn)/i-GaAs heterostructure for pulsed magnetic field applications up to 52 T,* Physica B-Condensed Matter, vol.346, pp.548-552, 2004.

[33] A. Oral, S. J. Bending, and M. Henini, *Real-time scanning hall probe microscopy,* Applied Physics Letters, vol.69, pp.1324-1326, 1996.

[34] B. L. Blackford, *A Simple Self-Propelled 2-Dimensional Micropositioner,* Review of Scientific Instruments, vol.64, pp.1360-1361, 1993.

[35] J. Tapson, and J. R. Greene, *A Simple Dynamic Piezoelectric X-Y Translation State Suitable for Scanning Probe Microscopes,* Review of Scientific Instruments, vol.64, pp.2387-2388, 1993.

[36] R. B. Dinner, M. R. Beasley, and K. A. Moler, *Cryogenic scanning Hall-probe microscope with centimeter scan range and submicron resolution,* Review of Scientific Instruments, vol.76, pp.103702, 2005.

[37] T. Schweinbock *et al.*, *Scanning Hall probe microscopy with shear force distance control,* Journal of Applied Physics, vol.87, pp.6496-6498, 2000.

[38] A. J. Brook *et al.*, *Integrated piezoresistive sensors for atomic force-guided scanning Hall probe microscopy,* Applied Physics Letters, vol.82, pp.3538-3540, 2003.

[39] A. J. Brook *et al.*, *Micromachined III-V cantilevers for AFM-tracking scanning hall probe microscopy,* Journal of Micromechanics and Microengineering, vol.13, pp.124-128, 2003.

[40] M. Dede *et al.*, *Scanning Hall Probe Microscopy (SHPM) using quartz crystal AFM feedback,* Journal of Nanoscience and Nanotechnology, vol.8, pp.619-622, 2008.

[41] K. Aoki, S. Uekusa, and H. Katsumata, *Oxygen plasma damage in GaAs directly exposed to surface-wave plasma,* Japanese Journal of Applied Physics Part 1-Regular Papers Short Notes & Review Papers, vol.41, pp.5762-5768, 2002.

[42] C. Lee, H. W. Kim, and S. Kim, *Organic contaminants removal by oxygen ECR plasma,* Applied Surface Science, vol.253, pp.3658-3663, 2007.

[43] N. B. Cobb, *Fast optical and process proximity correction algorithms for integrated circuit manufacturing*, Thesis (Ph D), University of California Berkeley, 1998

[44] J. W. Guikema, and Stanford University. Dept. of Physics.,*Scanning hall probe microscopy of magnetic vortices in very underdoped yttrium-barium-copper-oxide*, Thesis (Ph D), Stanford University, 2004., 2004

[45] S. K. Ghandhi, *VLSI fabrication principles : silicon and gallium arsenide,* Wiley, New York, 1994.

[46] H. Okumura, *Present status and future prospect of widegap semiconductor high-power devices,* Japanese Journal of Applied Physics Part 1-Regular Papers Brief Communications & Review Papers, vol.45, pp.7565-7586, 2006.

[47] Anon, *GaN early commercial opportunities lie in high power electronics,* Microwave Journal, vol.49, pp.69-69, 2006.

[48] U. K. Mishra *et al.*, *GaN-Based RF power devices and amplifiers,* Proceedings of the IEEE, vol.96, pp.287-305, 2008.

[49] T. G. P. Rajagopal, J.C. Roberts, J. D. Brown, T. Warren Weeks, E.L. Piner, K. J. Linthicum, *Large-Area, Device Quality GaN on Si Using a Novel Transition Layer Scheme,* Material Research Society Symposium Proceedings, vol.743, 2003.

[50] S. M. Sze, *Physics of Semiconductor Devices,* Wiley, New York, 1981.

[51] T. Yamamura *et al.*, *High sensitivity and quantitative magnetic field measurements at 600 degrees C,* Journal of Applied Physics, vol.99, pp.-, 2006.

[52] Z. Primadani, H. Osawa, and A. Sandhu, *High temperature scanning Hall probe microscopy using AlGaN/GaN two dimensional electron gas micro-Hall probes,* Journal of Applied Physics, vol.101, pp.09K105, 2007.

[53] V. P. Kunets *et al.*, *Highly sensitive micro-Hall devices based on Al0.12In0.88Sb/InSb heterostructures,* Journal of Applied Physics, vol.98, pp.014506-014506-014506, 2005.

[54] A. B. T. Ashley, L. Buckle, S. Datta, A. Dean, M. Emeny, M. Fearn, D. Hayes, K. Hilton, R. Jefferies, T. Martin, K. Nash, T. Philips, W. Tang, P. Wilding and R. Chau, in 7th International Conference on Solid-State and Integrated Circuits TechnologyBeijing, China, 2004), pp. 2253-2256.

[55] A. R. Dedigama *et al.*, *Current focusing in InSb heterostructures,* Physica E-Low-Dimensional Systems & Nanostructures, vol.34, pp.647-650, 2006.

[56] J. M. S. Orr *et al.*, *A surface-gated InSb quantum well single electron transistor,* New Journal of Physics, vol.9, pp.-, 2007.

[57] J. M. S. Orr *et al.*, *Electronic transport in modulation-doped InSb quantum well heterostructures,* Physical Review B, vol.77, pp.-, 2008.

[58] F. N. Hooge, *1/F Noise Sources,* IEEE Transactions on Electron Devices, vol.41, pp.1926-1935, 1994.

[59] H. Gruger, U. Vogel, and S. Ulbricht, *Setup and capability of CMOS Hall sensor arrays,* Sensors and Actuators A-Physical, vol.129, pp.100-102, 2006.

[60] G. S. Chung, *Thin Soi Structures for Sensing and Integrated-Circuit Applications,* Sensors and Actuators A-Physical, vol.39, pp.241-251, 1993.

[61] S. Bellekom, and P. M. Sarro, *Offset reduction of Hall plates in three different crystal planes,* Sensors and Actuators A-Physical, vol.66, pp.23-28, 1998.

[62] R. Steiner *et al.*, *Influence of mechanical stress on the offset voltage of Hall devices operated with spinning current method,* Journal of Microelectromechanical Systems, vol.8, pp.466-472, 1999.

[63] R. Steiner *et al.*, *Offset reduction in Hall devices by continuous spinning current method,* Sensors and Actuators A-Physical, vol.66, pp.167-172, 1998.

[64] M. Blagojevic *et al.*, *SOI hall-sensor front end for energy measurement,* IEEE Sensors Journal, vol.6, pp.1016-1021, 2006.

[65] P. L., H. Ballan, and M. Declercq, in EEE 2002 custom integrated circuits conferenceOrlando FL, USA, 12-15 May 2002), pp. 269-272.

[66] M. Blagojevic, M. Kayal, and D. De Venuto, *FD SOI Hall sensor electronics interfaces for energy measurement,* Microelectronics Journal, vol.37, pp.1576-1583, 2006.

[67] R. F. Broom, and E. H. Rhoderick, *Studies of the Intermediate State in Thin Superconducting Films,* Proceedings of the Physical Society, vol.79, pp.586-593, 1962.

[68] R. N. Goren, and M. Tinkham, *Patterns of magnetic flux penetration in superconducting films,* Journal of Low Temperature Physics, vol.5, pp.465, 1971.

[69] D. A. Brawner, and N. P. Ong, *Scanning Hall Microprobe Measurements of Magnetization Profiles in* $YBa_2Cu_3O_{7-Y}$ *Single-Crystals,* Journal of Applied Physics, vol.73, pp.3890-3902, 1993.

[70] B. K. Chong *et al.*, *Scanning Hall probe microscopy on an atomic force microscope tip,* Journal of Vacuum Science & Technology a-Vacuum Surfaces and Films, vol.19, pp.1769-1772, 2001.

[71] A. Sandhu *et al.*, *Bismuth nano-Hall probes fabricated by focused ion beam milling for direct magnetic imaging by room temperature scanning Hall probe microscopy,* Electronics Letters, vol.37, pp.1335-1336, 2001.

[72] A. Sandhu, and F. Handa, *Practical hall sensors for biomedical instrumentation,* IEEE Transactions on Magnetics, vol.41, pp.4123-4127, 2005.

[73] A. Sandhu *et al.*, *Direct magnetic imaging of ferromagnetic domain structures by room temperature scanning hall probe microscopy using a bismuth micro-hall probe,* Japanese Journal of Applied Physics Part 2-Letters, vol.40, pp.L524-L527, 2001.

[74] A. Sandhu *et al.*, *Room temperature scanning Hall probe microscopy using GaAs/AlGaAs and Bi micro-hall probes,* Ultramicroscopy, vol.91, pp.97-101, 2002.

[75] S. Mouaziz *et al.*, *Polymer-based cantilevers with integrated electrodes,* Journal of Microelectromechanical Systems, vol.15, pp.890-895, 2006.

[76] D. Petit *et al.*, *Room temperature performance of submicron bismuth Hall probes,* Iee Proceedings-Science Measurement and Technology, vol.151, pp.127-130, 2004.

[77] S. Mouaziz *et al.*, in TNT 2004 "Trends in Nanotechnology"Segovia, Spain, 2004).

[78] Y. Hasegawa *et al.*, *A method for analysis of carrier density and mobility in polycrystalline bismuth,* Physica B-Condensed Matter, vol.382, pp.140-146, 2006.

[79] İ. İ. Kaya,*Hot electron interactions in nanostructures*, Ph.D., Bilkent University, 1997

[80] S. Rizvi, *Handbook of photomask manufacturing technology,* Taylor & Francis, Boca Raton, 2005.

[81] M. A. McCord, *Electron beam lithography for 0.13 mu m manufacturing,* Journal of Vacuum Science & Technology B, vol.15, pp.2125-2129, 1997.

[82] J. A. Liddle *et al.*, *Space-charge limitations to throughput in projection electron-beam lithography (SCALPEL),* Microelectronic Engineering, vol.42, pp.155-158, 1998.

[83] N. Z. El-Sayed, *Physical characteristics of thermally evaporated Bismuth thin films,* Vacuum, vol.80, pp.860-863, 2006.

[84] F. J. Giessibl, *High-speed force sensor for force microscopy and profilometry utilizing a quartz tuning fork,* Applied Physics Letters, vol.73, pp.3956-3958, 1998.

[85] C. Veauvy, K. Hasselbach, and D. Mailly, *Scanning mu-superconduction quantum interference device force microscope,* Review of Scientific Instruments, vol.73, pp.3825-3830, 2002.

[86] K. Karrai, and R. D. Grober, *Piezoelectric Tip-Sample Distance Control for near-Field Optical Microscopes,* Applied Physics Letters, vol.66, pp.1842-1844, 1995.

[87] M. Todorovic, and S. Schultz, *Magnetic force microscopy using nonoptical piezoelectric quartz tuning fork detection design with applications to magnetic recording studies,* Journal of Applied Physics, vol.83, pp.6229-6231, 1998.

[88] M. Todorovic, and S. Schultz, *Miniature high-sensitivity quartz tuning fork alternating gradient magnetometry,* Applied Physics Letters, vol.73, pp.3595-3597, 1998.

[89] R. D. Grober *et al.*, *Fundamental limits to force detection using quartz tuning forks,* Review of Scientific Instruments, vol.71, pp.2776-2780, 2000.

[90] Y. Seo, P. Cadden-Zimansky, and V. Chandrasekhar, *Low-temperature high-resolution magnetic force microscopy using a quartz tuning fork,* Applied Physics Letters, vol.87, pp.-, 2005.

[91] G. M. King, J. S. Lamb, and G. Nunes, *Quartz tuning forks as sensors for attractive-mode force microscopy under ambient conditions,* Applied Physics Letters, vol.79, pp.1712-1714, 2001.

[92] Y. H. Seo, and S. B. Hong, *Quartz crystal resonator based scanning probe microscopy,* Modern Physics Letters B, vol.19, pp.1303-1322, 2005.

[93] F. J. Giessibl, *Forces and frequency shifts in atomic-resolution dynamic-force microscopy,* Physical Review B, vol.56, pp.16010-16015, 1997.

[94] T. Mochiku, and K. Kadowaki, *Growth and Properties of $Bi_2sr_2(Ca,Y)Cu_2O_{8+\delta}$ Single-Crystals,* Physica C, vol.235, pp.523-524, 1994.

[95] B. F. C.Schott, Blanchard, L. Chiesi, *Modern Integrated Silicon Hall Sensors,* Sensor Review, vol.18, pp.252-257, 1998.

[96] R. S. Popovic, *The Vertical Hall-Effect Device,* IEEE Electron Device Letters, vol.5, pp.357-358, 1984.

[97] Z. Randjelovic *et al.*, *A non-plate like Hall Sensor,* Sensors and Actuators A-Physical, vol.76, pp.293-297, 1999.

[98] K. Dimitrov, *3-D silicon Hall sensor for use in magnetic-based navigation systems for endovascular interventions,* Measurement, vol.40, pp.816-822, 2007.

[99] C. Schott, D. Manic, and R. S. Popovic, *Microsystem for high-accuracy 3-D magnetic-field measurements,* Sensors and Actuators A-Physical, vol.67, pp.133-137, 1998.

[100] E. Hirose *et al.*, *A new 3-axis magnetic field measurement system based on Hall elements,* IEEE Transactions on Applied Superconductivity, vol.14, pp.1814-1817, 2004.

[101] D. R. Popovic *et al.*, *Three-axis teslameter with integrated hall probe,* IEEE Transactions on Instrumentation and Measurement, vol.56, pp.1396-1402, 2007.

[102] M. Johnson *et al.*, *Hybrid hall effect device,* Applied Physics Letters, vol.71, pp.974-976, 1997.

[103] C. Schott, J. M. Waser, and R. S. Popovic, *Single-chip 3-D silicon Hall sensor,* Sensors and Actuators A-Physical, vol.82, pp.167-173, 2000.

[104] C. S. Roumenin, and S. V. Lozanova, *CMOS 2D Hall microsensor with minimal design complexity,* Electronics Letters, vol.43, pp.511-513, 2007.

[105] C. S. Roumenin, and D. I. Nikolov, *Five-contact silicon structure based integrated 3D Hall sensor,* Electronics Letters, vol.39, pp.1646-1648, 2003.

[106] C. Roumenin, K. Dimitrov, and A. Ivanov, *Integrated vector sensor and magnetic compass using a novel 3D Hall structure,* Sensors and Actuators A-Physical, vol.92, pp.119-122, 2001.

[107] D. Gregusova *et al.*, *Fabrication of a vector Hall sensor for magnetic microscopy,* Applied Physics Letters, vol.82, pp.3704-3706, 2003.

[108] D. Gregusova *et al.*, *Technology and properties of a vector hall sensor,* Microelectronics Journal, vol.37, pp.1543-1546, 2006.

[109] V. Cambel *et al.*, *Scanning vector Hall probe microscopy,* Journal of Magnetism and Magnetic Materials, vol.272-76, pp.2141-2143, 2004.

[110] J. Fedor *et al.*, *Scanning vector Hall probe microscope,* Review of Scientific Instruments, vol.74, pp.5105-5110, 2003.

[111] D. Grundler *et al.*, *Bend-resistance nanomagnetometry: spatially resolved magnetization studies in a ferromagnet/semiconductor hybrid structure,* Physica E-Low-Dimensional Systems & Nanostructures, vol.12, pp.248-251, 2002.

[112] F. M. Peeters, and X. Q. Li, *Hall magnetometer in the ballistic regime,* Applied Physics Letters, vol.72, pp.572-574, 1998.

[113] A. Oral, unpublished.

[114] J. D. Jackson, *Classical Electrodynamics,* Wiley, New York, 1999.